

ResearchOnline@JCU

This file is part of the following reference:

Boyle, Gregory (2015) *The modelling of non-equilibrium light lepton transport in gases and liquids*. PhD thesis, James Cook University.

Access to this file is available from:

<http://researchonline.jcu.edu.au/43770/>

The author has certified to JCU that they have made a reasonable effort to gain permission and acknowledge the owner of any third party copyright material included in this document. If you believe that this is not the case, please contact

*ResearchOnline@jcu.edu.au and quote
<http://researchonline.jcu.edu.au/43770/>*

The modelling of non-equilibrium light lepton transport in gases and liquids

Thesis submitted by

Gregory Boyle BSc(Hons)

in September (2015)

for the degree of Doctor of Philosophy

in the College of Science, Technology and Engineering

James Cook University



COPYRIGHT © GREGORY BOYLE, 2015.

Some rights reserved.

This work is licensed under Creative Commons
Attribution–Noncommercial–No Derivative Works license.

<http://creativecommons.org/licenses/by-nc-nd/3.0/au/>

Statement of access

I, the undersigned, the author of this thesis, understand that James Cook University will make it available for use within the University Library and, by microfilm or other means, allow access to users in other approved libraries. All users consulting with this thesis will have to sign the following statement:

In consulting this thesis I agree not to copy or closely paraphrase it in whole or in part without the written consent of the author; and to make proper written acknowledgement for any assistance which I have obtained from it.

Beyond this, I do not wish to place any restriction on access to this thesis.

(Gregory Boyle)

Date

Sources declaration

I declare that this thesis is my own work and has not been submitted in any form for another degree or diploma at any university or other institute of tertiary education. Information derived from the published and unpublished work of others has been acknowledged in the text and a list of references is given.

(Gregory Boyle)

Date

Statement of the contribution of others

I gratefully acknowledge the contributions detailed below.

Funding support was provided by the ARC Centre for Antimatter-Matter Studies, an Australian Postgraduate Award, and the James Cook University Graduate Research Scheme.

Editorial assistance for the overall thesis was provided by Prof. Ronald White and Madalyn Casey of James Cook University. Chapters 4-8 and Appendix A are each based on published papers, and editorial assistance was provided by all of the listed co-authors.

Contributions to the co-authored publications that form part of this thesis are as follows. Chapters 5-8 and Appendix A are based on publications in which I am first author. Chapter 4 contains results from a publication in which I am second author, wherein I provided Boltzmann equation simulations. W. J. Tattersall performed Monte Carlo simulation results for Chapters 4 and 6. J. Mitroy and Y. Cheng provided the theory and calculations with respect to scattering cross sections and z_{eff} in Chapter 5. R. P. McEachran provided the theory and calculations with respect to scattering cross sections and potentials in Chapter 7. R. D. White performed the Boltzmann equation calculations in Appendix A.

A more detailed discussion of the contributions from the co-authors is given at the beginning of each of the relevant chapters.

Acknowledgements

I have become indebted to countless people over the course of my PhD studies. I would like to give particular acknowledgement to the people listed below.

I am deeply grateful to my supervisor, Prof. R. D. White, for his constant patience, guidance and availability at all hours of the day or night. I wish to thank him for all the opportunities he has afforded me during my studies.

I would like to thank Prof. R. Robson and Prof. R. P. McEachran for many fruitful discussions, and for the benefit of their deep insight and expertise.

I am grateful to Prof. J. Mitroy for his wisdom, advice and motivation. His passing was a great loss to the physics community.

I would also like to thank S. Dujko and Z. Lj. Petrović for their support, particularly when responding to paper referees.

I am immensely grateful to Danny Cocks, Wade Tattersall and Madalyn Casey, without which this thesis would still be a distant prospect. Their assistance, discussions, calculations, editing and support have been invaluable. Particular thanks to Madalyn who has fought a war on two fronts as both colleague and housemate.

I am thankful to my brother, my parents and my grandparents for their unconditional love and encouragement.

To Sophie Gregory, thank you for your endless kindness and patience. It has meant so much to me.

I would like to thank my fellow students, past and present, for their friendship and advice throughout the course of this work. In particular, I would like to thank Tim Hicks and Michael Meehan.

Finally, I wish to acknowledge the financial support of the ARC Centre for Antimatter-Matter Studies, and James Cook University.

Abstract

An accurate quantitative understanding of the transport of light leptons, such as electrons and positrons, in dilute gaseous and soft condensed mediums is of interest to a number of technological applications, as well as from the perspective of fundamental physics research. In particular, this research has been directly applied to cross section set validation, is motivated by nuclear medicine, and will find application in liquid particle detectors and plasma medicine.

The connection between the microscopic description of matter, such as scattering cross sections, and macroscopic applications is usually made via Monte Carlo simulations or kinetic theory, which are often used in a complementary fashion. The fundamental kinetic equation considered in this work is Boltzmann's equation, which describes the evolution of the swarm particle phase-space distribution in time and space due to the influence of collisions with a background medium and external forces on the system. Following the work of White and co-workers [1] a full, multi-term, space-time Boltzmann equation solver has been developed for the first time for highly non-equilibrium electron and positron transport in dilute gases, dense gases and liquids. By simulating the evolution of the Boltzmann equation Green's function, the result from a single simulation can be used to model a wide variety of experimental configurations and applications including pulsed-Townsend, steady-state Townsend and other practical experimental devices.

Swarm experiments, which operate in the hydrodynamic regime, provide stringent tests on the accuracy and completeness of cross section sets, as well as a benchmark for the energy-dependent component of the numerical code. An investigation of benchmark model and real systems, including electron-neon, positron-helium and positron-molecular-hydrogen, have allowed us to assess and validate various scattering processes, as well as to comment on the consistency and accuracy of established cross sections with experimental measurements in the low-energy regime. A new collision operator for positron impact ionization was developed and systematically benchmarked as part of this.

A major focus of the present work is extending the kinetic theory formalism beyond dilute gases to dense gases, liquids and soft-condensed matter such as biological matter. The study of swarm transport in dense mediums is considerably more complex due to the density effects arising from the small interparticle spacings and highly correlated scattering centres. We have generalized the *ab initio* method of Lekner and Cohen [2, 3] overcoming several approximations which are no longer necessary in modern day transport and scattering theory. Liquid argon was chosen as the test bed for our calculations, and by including both coherent scattering effects and modifications to the electron-atom potential, a high level of agreement between the calculated and measured transport coefficients was achieved.

An investigation of the full spatio-temporal evolution of electrons in a model hard-sphere liquid successively demonstrated the periodic non-hydrodynamic phenomena expected, and was confirmed by independent Monte Carlo simulation. Finally, the spatio-temporal evolution of electron swarms in gas- and liquid-phase argon were compared. Striking differences were evident in the evolution of the distribution function components, which were a reflection of the reduced momentum-transfer and lack of a Ramsauer minimum in the liquid-phase when compared to the gas-phase cross sec-

tions. This highlights the problems with treating liquid systems as gaseous systems with increased density, with implications to various applications.

List of publications

This thesis contains content that has been published in the following journal articles:

[4] G. J. Boyle, R. D. White, R. E. Robson, S. Dujko and Z. Lj. Petrović. On the approximation of transport properties in structured materials using momentum-transfer theory. *New Journal of Physics*, **14**, 045011 (2012). doi:10.1088/1367-2630/14/4/045011.

[5] G. J. Boyle, M. J. Casey, R. D. White, Y. Cheng and J. Mitroy. Transport properties of electron swarms in gaseous neon at low values of E/N . *Journal of Physics D: Applied Physics*, **47**, 345203 (2014). doi:10.1088/0022-3727/47/34/345203.

[6] G. J. Boyle, M. J. Casey, R. D. White, and J. Mitroy. Transport theory for low-energy positron thermalization and annihilation in helium. *Physical Review A*, **89**, 022712 (2014). doi:10.1103/PhysRevA.89.022712.

[7] G. J. Boyle, W. J. Tattersall, D. G. Cocks, S. Dujko and R. D. White. Kinetic theory of positron-impact ionization in gases. *Physical Review A*, **91**, 052710 (2015). doi:10.1103/PhysRevA.91.052710.

[8] G. J. Boyle, R. P. McEachran, D. G. Cocks and R. D. White. Electron scattering and transport in liquid argon. *The Journal of Chemical Physics*, **142**, 154507 (2015). doi:10.1063/1.4917258.

[9] W. J. Tattersall, D. G. Cocks, G. J. Boyle, S. J. Buckman and R. D. White. Monte Carlo study of coherent scattering effects of low-energy charged particle transport in Percus-Yevick liquids. *Physical Review E*, **91**, 043304 (2015). doi:10.1103/PhysRevE.91.043304.

Contents

1	Introduction	1
1.1	Motivation and aims	1
1.1.1	Electron driven processes and applications	2
1.1.2	Positron driven processes and applications	3
1.1.3	Current status of modelling in soft-condensed matter	6
1.1.4	Aims of this study	7
1.2	Swarm experiments	8
1.2.1	Swarm measurements in dilute gases	9
1.2.2	Swarm measurements in dense gaseous and liquid phases	10
1.3	Kinetic theory of electron and positron swarms	10
1.3.1	The Boltzmann equation	11
1.3.2	Two-term vs. multi-term solutions	11
1.3.3	Transport in the hydrodynamic regime	12
1.3.4	Transport in the non-hydrodynamic regime	13
1.3.5	Kinetic modelling of lepton transport in dense gases, liquids and structured matter	14
1.3.6	Monte Carlo modelling of lepton transport in dense gases, liquids and structured matter	16
1.4	Structure of the thesis	16
2	Kinetic theory	19
2.1	Introduction	19
2.2	Multi-term Legendre polynomial expansion	20
2.2.1	Plane-parallel geometry	21
2.2.2	Hydrodynamic regime	22
2.3	Collision operators	24
2.3.1	Coherent scattering	25
2.3.2	Elastic collisional processes	27
2.3.3	Collisional excitation processes	30
2.3.4	Attachment, annihilation and positronium formation	32
2.3.5	Ionization processes	33
2.4	Transport properties and transport coefficients	34
2.4.1	Transport properties	34
2.4.2	Transport coefficients	35
2.5	Initial and boundary conditions	36
2.5.1	Initial energy distribution	36
2.5.2	Boundary conditions	37
3	Numerical techniques	38
3.1	Introduction	38
3.2	Operator splitting	38
3.3	Energy-space representation	39
3.3.1	Local vs. global approximations	39
3.3.2	Pseudo-spectral method	40
3.3.3	Finite difference method	46
3.3.4	Representation of cross sections	48
3.3.5	Representation of collision operators and h_l	48
3.4	Temporal representation	51

3.4.1	Asymptotic time behaviour	51
3.4.2	Temporal discretization	53
3.4.3	Temporally-adaptive energy mesh	54
4	Hydrodynamic benchmark systems	55
4.1	Introduction	55
4.2	Elastic collisions	56
4.2.1	Constant elastic collision frequency	56
4.2.2	Constant elastic cross section	57
4.2.3	Alternating electric field	58
4.3	Power-law loss processes	60
4.3.1	Convergence properties of finite difference and pseudo-spectral schemes	63
4.4	Excitations	64
4.4.1	Reid's ramp model	64
4.5	Electron impact ionization	66
4.5.1	Model of Lucas and Saelee	66
4.5.2	Model of Ness and Robson	66
4.6	Percus-Yevick hard-sphere model	68
4.6.1	Transport coefficients	71
4.7	Conclusion	74
5	Low-energy electron and positron transport in atomic gases	75
5.1	Introduction	75
5.2	Electron swarms in gaseous neon	76
5.2.1	Cross sections	77
5.2.2	Comparisons with transport data	79
5.2.3	Recommended low-energy momentum-transfer cross section	87
5.3	Positron swarms in gaseous helium	87
5.3.1	Cross sections	88
5.3.2	Positron diffusion and thermalization calculations	92
5.3.3	Positron annihilation in helium in an electric field	94
5.3.4	Recommended low-energy elastic and annihilation cross sections	97
6	Positron impact ionization in gases	98
6.1	Introduction	98
6.2	Positron impact ionization collision operator	99
6.2.1	Derivation	99
6.2.2	Legendre decomposition	101
6.2.3	Modified Frost-Phelps operator	102
6.3	Positron ionization benchmarking	102
6.4	Positron ionization energy-partitioning model	105
6.4.1	Test model	107
6.4.2	Model for positron impact ionization in H_2	107
6.5	Positrons in H_2	108
6.6	Conclusion	111
7	Electron scattering and transport in atomic liquids	112
7.1	Introduction	112
7.2	Electron scattering and transport in liquid argon	114
7.2.1	Scattering of electrons by argon gas	114
7.2.2	Screening of the polarization interaction	117
7.2.3	Effective potential in a liquid	119
7.2.4	Results	122
7.2.5	Impact of scattering anisotropy and the two-term approximation	126
7.3	Conclusion	129

8	Non-hydrodynamic space-time dependent transport	130
8.1	Introduction	130
8.2	Solution technique	131
8.2.1	Operator splitting	132
8.2.2	Configuration-space advection	132
8.2.3	Green's function solution	135
8.2.4	Numerical considerations and adaptive meshing	135
8.2.5	Transport properties	136
8.2.6	Reduced variables	137
8.3	Electron transport in a modified Percus-Yevick hard-sphere benchmark liquid model	138
8.3.1	Transport coefficients in the long-time limit	138
8.3.2	Space-time evolution of the phase-space distribution and its velocity moments	139
8.3.3	Steady-state Townsend configuration	140
8.4	Spatio-temporal relaxation of electrons in liquid argon	143
8.4.1	Cross sections, potentials and screening	144
8.4.2	Results	145
8.5	Conclusion	147
9	Concluding remarks	148
9.1	Summary	148
9.2	Recommendations for future work	149
A	Fluid modelling in dilute and dense atomic gases	151
A.1	Introduction	151
A.2	Fluid equations and momentum-transfer theory	152
A.3	Standard MTT	155
A.3.1	Drift velocity and mean energy	155
A.3.2	Diffusion coefficients	156
A.3.3	Benchmark model	157
A.3.4	Liquid argon	161
A.4	Modified MTT	163
A.4.1	Benchmark model	164
A.4.2	Liquid argon	167
A.5	Summary	170
	References	171

List of Figures

2.1	Schematic of the electric field direction and plane-parallel configuration-space geometry studied in this thesis.	22
2.2	Schematic of coherent scattering, where the incoming plane wave (with wave parameters \mathbf{k} and ω) is scattered from multiple scattering centres simultaneously into spherical outgoing waves (with wave parameters \mathbf{k}' and ω') through an angle χ . . .	26
3.1	The first five Chebyshev polynomials of the first kind, (3.11), on the interval $-1 < x < 1$	42
3.2	The first five Laguerre polynomials, (3.18)-(3.20), on the interval $0 < x < 15$	44
3.3	The first five Laguerre functions, (3.21), on the interval $0 < x < 35$	44
4.1	Variation of mean energy, ϵ , for model (4.9) over a range of reduced angular frequencies, ω/n_0 . Calculations have been performed with $U_\infty = 10$, $l_{\max} = 1$, and $N = 5000$	58
4.2	Variation of drift velocity, W , for model (4.9) over a range of reduced angular frequencies, ω/n_0 . Calculations have been performed with $U_\infty = 10$, $l_{\max} = 1$, and $N = 5000$	59
4.3	Variation of diffusion coefficients, $n_0 D_L$ and $n_0 D_T$, for model (4.9) over a range of reduced angular frequencies, ω/n_0 . Calculations have been performed with $U_\infty = 10$, $l_{\max} = 1$, and $N = 5000$	59
4.4	Convergence of RMS error with number of terms for finite difference, Chebyshev and Laguerre pseudo-spectral solutions for model (4.11).	64
4.5	The variation of the static structure factor with momentum exchange Δk for the Percus-Yevick model (with Verlet-Weiss correction) for various volume fractions, Φ	70
4.6	The energy variation of the structure-modified momentum-transfer cross section, Σ_m , for various volume fractions Φ , for a dense gas of hard spheres.	71
4.7	Mean energy, ϵ , for Percus-Yevick model (4.21) as a function of reduced electric field, E/n_0 , for a range of volume fractions, Φ	72
4.8	Drift velocity, W , for Percus-Yevick model (4.21) as a function of reduced electric field, E/n_0 , for a range of volume fractions, Φ	72
4.9	Transverse diffusion coefficient, $n_0 D_T$, for Percus-Yevick model (4.21) as a function of reduced electric field, E/n_0 , for a range of volume fractions, Φ	73
4.10	Longitudinal diffusion coefficient, $n_0 D_L$, for Percus-Yevick model (4.21) as a function of reduced electric field, E/n_0 , for a range of volume fractions, Φ	73
5.1	The mean energy (in eV) as a function of E/n_0 (in Td) for electron swarms in neon. The mean energy was computed using the SDpT cross section.	82
5.2	The relative difference, between calculated characteristic energies and the experimental data of the University of Rikkyo [10] group.	86
5.3	The elastic cross section, σ_T (in units of πa_0^2) for positron scattering for helium.	90
5.4	The momentum-transfer cross section, σ_m (in units of πa_0^2) for positron scattering for helium.	90
5.5	The annihilation parameter, z_{eff} for positron scattering for helium.	91

5.6	Temporal variation of $Z_{\text{eff}}(t)$ for positrons thermalizing in gaseous helium at a temperature of 293 K. The simulations are compared with the UCL experimental data [11] and the CH simulation [12]. The different initial distributions are characterised by varying distributions and average energies; Const v is a constant distribution in v space below the Ps-threshold; Const ϵ is a constant distribution in energy space below the Ps-threshold. See text for details.	93
5.7	Variation of $\epsilon(t)$ for positrons thermalizing in helium for different initial conditions. The temperature of the helium gas was taken as 293 K.	94
5.8	Comparison of steady-state $Z_{\text{eff}}(E/n_0)$ for thermalized positrons in helium at $T_0 = 293$ K. The curve labelled MP 2014 uses the MP cross section set. Also shown are experiments from the Toronto [13], UBC [14] and UCL [15] laboratories. Previous transport calculations are also depicted [12,16]).	95
5.9	The steady-state Z_{eff} and mean energy ϵ , for positrons thermalizing in helium at $T_0 = 293$ K under the action of a reduced electric field E/n_0 using the new cross section set.	96
6.1	Variation of mean energy, ϵ , with energy sharing fraction, Q , for PII model (6.21) at a reduced field of 800 Td.	105
6.2	Variation of mean energy, ϵ , with energy sharing fraction, Q , for EII model (6.21) at a reduced field of 800 Td.	105
6.3	Variation of the energy-fraction-partition function with impact energy, relative to the ionization threshold, and energy sharing fraction, Q , for parameters. (6.27) . .	107
6.4	Differential PII cross section for an impact energy of 100 eV, as a function of the energy sharing fraction, Q . KL 1998 is the experimental data of Kover and Laricchia [17] for the triply differential cross section for an impact energy of 100 eV and ejection angle of 0° . The model fit has been calculated with the parameters (6.28) and by assuming that the triply differential cross section is the same at all ejection angles.	109
6.5	Cross section set for positron scattering in H_2 . References are given in text.	109
6.6	Mean energy temporal relaxation of a positron swarm in H_2 at 293 K. The initial source distribution is uniform in speed space up to 1000 eV. The H_2 model ionization parameters are given in equation (6.28) and are compared with constant energy sharing fractions of $Q = 0.5$ and $Q = 1.0$	110
7.1	Cross sections for electron scattering from argon. The calculations described in this section, which use the non-local exchange interaction (solid line) are in good agreement with the recommended set of Buckman et al. [18]. A comparison with a calculation similar to that of Lekner [2] using a Buckingham potential (dotted line) shows loose qualitative agreement at the Ramsauer minimum, but quantitatively is incorrect. Also shown are the results from using two different effective models of a local exchange potential (thick dashed [19] and dash-dotted lines [20]) which do not agree with experimental measurement at all, as well as the cross section when exchange is included but polarization is neglected (thin dashed line).	117
7.2	Pair correlator for argon, as reported in Yarnell [21], measured in neutron scattering experiments. Also plotted, is the pair correlator calculated in the analytical Percus-Yevick approximation as used by Lekner [2].	118
7.3	The screening function $f(r)$ of the polarization interaction potential for scattering of an electron from a single argon atom in a bulk of density $n_0 = 0.0213 \text{ \AA}^{-3}$	119
7.4	Plots of the total effective potential V_{eff} felt by an electron when colliding with one atom in the liquid. Also shown are the components, V_1 and V_2 , which represent the direct potential of the atom and the contribution of the remaining atoms in the bulk respectively. The dashed vertical lines at $\sigma_{\text{core}}/2$ and r_m indicate the hard-core exclusion radius and the proposed collisional sphere respectively. Note that effects of exchange are not represented in this figure.	120
7.5	Elastic total and momentum-transfer cross sections for argon calculated from the phase shifts determined at a distance r^* . Our preferred choice for transport calculations in this work, $r^* = r_m$, corresponds to the solid line, the dashed lines are those corresponding to a variations $r^* = r_m \pm \frac{1}{16}a_0$ and the dotted line corresponds to a variation of $r^* = \sigma_{\text{core}}/2$	122

7.6	The drift velocity (top) and characteristic energy (bottom) of electrons in gaseous argon, calculated using the potentials and associated cross sections detailed in Section 7.2.1, and compared with available experimental data (Robertson [22, 23] at 90 K; Warren and Parker [24, 25] at 77 K; Townsend and Bailey [26, 27] at 288 K). The full non-local treatment of exchange considered here is compared to two forms of local exchange potentials (LocExA [19]; LocExB [20]) and to the case when the exchange interaction is neglected altogether. The background argon gas for the calculations was fixed at 90 K for determination of the drift velocity and 77 K for the characteristic energy.	124
7.7	Comparison of the measured drift velocities W and characteristic energies D_T/μ in gaseous and liquid argon, with those calculated from the various approximations to the cross sections. Experimental data (Robertson [22, 23] at 90 K; Miller et al. [28] at 85 K; Halpern et al. [29] at 85 K; Warren and Parker [24, 25] at 77 K; Townsend and Bailey [26, 27] at 288 K; Shibamura et al. [30] at an unmeasured liquid temperature). The various approximations used are: gas-phase only cross sections (Gas), gas-phase cross sections with coherent scattering (Gas+Coh), and liquid phase cross sections with coherent scattering effects (Liq+Coh). The results have been calculated using the full differential cross section and results are converged multi-term values. Experimental uncertainties are estimated at 2% for Robertson and less than 15% for Shibamura et al.	125
7.8	The momentum transfer cross sections in the gas-phase (Gas), liquid-phase (Liq) and their modifications when coherent scattering effects are included (+Coh). The recommended transfer cross section of reference [18] for a dilute gas is a combination of experimental measurements and theoretical calculations.	126
7.9	Comparison of the calculated drift and characteristic energy with variation in the distance r^* at which the phase shifts are determined. Experimental data is as detailed in Figure 7.7.	127
7.10	Differential cross sections in square angstroms for electrons in Ar for a) dilute gas phase, b) effective liquid phase including screening effects, and c) liquid phase cross section including coherent scattering effects $\Sigma(U, \chi)$	128
7.11	Percentage differences between the two-term and multi-term values of the characteristic energy for the gas and liquid phases using the full differential cross sections (solid lines), and percentage differences between the multi-term results with using only the momentum transfer cross section and the full differential cross section (dashed lines). All percentages are relative to the converged multi-term result using the full differential cross section.	128
8.1	Temporal evolution of the distribution function components for model (8.34) with $\Phi = 0$ (dashed lines) and $\Phi = 0.4$ (solid lines). The first row are $U^{\frac{1}{2}}f_0/n_0$ (eV^{-1}) contours while the second row are $ Uf_1/n_0 (\text{eV}^{-1/2})$ contours. The shaded contours indicate $Uf_1 < 0$. The four columns represent the times, $t^* = 0.2, 2, 20,$ and 200 respectively.	141
8.2	Temporal evolution of the spatially varying density and flux for model (8.34) with $\Phi = 0$ (dashed lines) and $\Phi = 0.4$ (solid lines). The four columns represent the times, $t^* = 0.2, 2, 20,$ and 200 respectively.	142
8.3	Spatial variation of the average energy and average velocity under SST conditions for model (8.34) with various volume fractions Φ	143
8.4	The momentum transfer cross sections in the gas-phase (dashed line) and liquid-phase (solid line) for electrons in argon.	144
8.5	Temporal evolution of the distribution function components for gas-phase (dashed lines) and liquid-phase (solid lines) argon. The first row are $U^{\frac{1}{2}}f_0/n_0(\text{eV}^{-1})$ contours, the second row are $ Uf_1/n_0 (\text{eV}^{-1/2})$ contours. The shaded contours indicate $Uf_1 < 0$. The three columns represent the times, $t^* = 1, 10,$ and 100 respectively.	146
8.6	Temporal evolution of the number density profiles for gas-phase (dashed lines) and liquid-phase (solid lines) argon. The three columns represent the times, $t^* = 1, 10,$ and 100 respectively.	147

A.1	The variation of the static structure factor with momentum exchange K for the Percus-Yevick model (with Verlet-Weiss correction) for various volume fractions, Φ .	157
A.2	The energy variation of elastic the collision frequency, $\tilde{\nu}_m$, for various volume fractions Φ , for a dense gas of hard spheres.	158
A.3	Variation of the swarm mean energy with reduced electric field, for various volume fractions Φ , for a dense gas of hard spheres. Fluid results are compared with those from a multi-term Boltzmann equation solution [1].	159
A.4	Variation of the swarm flux drift velocity with reduced electric field, for various volume fractions Φ , for a dense gas of hard spheres. Fluid results are compared with those from a multi-term Boltzmann equation solution [1].	159
A.5	Variation of s , as defined in (4.20), with reduced electric field, for various volume fractions Φ , for a dense gas of hard spheres.	160
A.6	Variation of the transverse diffusion coefficient with reduced electric field for various volume fractions Φ , for a dense gas of hard spheres. Fluid results are compared with those from a multi-term Boltzmann equation solution [1].	161
A.7	Variation of the longitudinal diffusion coefficient with reduced electric field for various volume fractions Φ , for a dense gas of hard spheres. Fluid results are compared with those from a multi-term Boltzmann equation solution [1].	161
A.8	Variation of the swarm mean energy with reduced electric field, for dilute gaseous and liquid argon at 84 K. Fluid results are compared with those from a multi-term Boltzmann equation solution [1] and Monte-Carlo simulation [31].	162
A.9	Variation of the swarm flux drift velocity with reduced electric field, for dilute gaseous and liquid argon at 84 K. Fluid results are compared with those from a multi-term Boltzmann equation solution [1] and Monte-Carlo simulation [31].	162
A.10	Variation of the swarm mean energy with reduced electric field, for various volume fractions Φ , for a dense gas of hard spheres. Fluid results are compared with those from a multi-term Boltzmann equation solution [1].	165
A.11	Variation of the swarm flux drift velocity with reduced electric field, for various volume fractions Φ , for a dense gas of hard spheres. Fluid results are compared with those from a multi-term Boltzmann equation solution [1].	165
A.12	Variation of the reduced effective electric field, E_{eff} , with reduced electric field for various volume fractions Φ , for a dense gas of hard spheres.	166
A.13	Variation of the transverse diffusion coefficient with reduced electric field for various volume fractions Φ , for a dense gas of hard spheres. Fluid results are compared with those from a multi-term Boltzmann equation solution [1].	166
A.14	Variation of the longitudinal diffusion coefficient with reduced electric field for various volume fractions Φ , for a dense gas of hard spheres. Fluid results are compared with those from a multi-term Boltzmann equation solution [1].	167
A.15	Variation of the swarm mean energy with reduced electric field, for dilute gaseous and liquid argon at 84 K. Fluid results are compared with those from a multi-term Boltzmann equation solution [1] and Monte-Carlo simulation [31].	167
A.16	Variation of the swarm flux drift velocity with reduced electric field, for dilute gaseous and liquid argon at 84 K. Fluid results are compared with those from a multi-term Boltzmann equation solution [1] and Monte-Carlo simulation [31].	168
A.17	Variation of the reduced effective electric field, E_{eff} , with reduced electric field, for dilute gaseous and liquid argon at 84 K. Fluid results are compared with those from a multi-term Boltzmann equation solution [1] and Monte-Carlo simulation [31].	168
A.18	Variation of the transverse diffusion coefficient with reduced electric field, for dilute gaseous and liquid argon at 84 K. Fluid results are compared with those from a multi-term Boltzmann equation solution [1] and Monte-Carlo simulation [31].	169
A.19	Variation of the longitudinal diffusion coefficient with reduced electric field, for dilute gaseous and liquid argon at 84 K. Fluid results are compared with those from a multi-term Boltzmann equation solution [1] and Monte-Carlo simulation [31].	169

List of Tables

4.1	Transport coefficients for model (4.1) with varying l_{\max} and T_0 . ‘An.’ refers to the analytic value to 5 significant figures found from equations (4.2)–(4.4). Calculations have been performed with $U_\infty = 12$ and $N = 5000$	56
4.2	Transport coefficients for model (4.5) with varying l_{\max} and T_0 . ‘Two-term.’ refers to the two-term approximation analytic value to 5 significant figures found from equations (4.6)–(4.7). ‘White’ refers to the value quoted in [32]. Calculations have been performed with $U_\infty = 6$ and $N = 5000$	57
4.3	Cycle-averaged ($\bar{\epsilon}$, $n_0\overline{D_T}$, and $n_0\overline{D_L}$) and RMS (W_{RMS}) values of the transport coefficients for model (4.9) at various applied reduced angular frequencies. ‘White’ refers to the value quoted in [33]. Calculations have been performed with $U_\infty = 10$, $N = 5000$ and $l_{\max} = 1$	59
4.4	Transport coefficients for model (4.10) with varying a and p . Note the values in square brackets are the corrected values for those given by Ness and Robson [34]. Calculations have been performed with $l_{\max} = 1$, and $N = 5000$	61
4.5	Transport coefficients for model (4.10) with varying p and l_{\max} . Calculations have been performed with $N = 5000$	62
4.6	Transport coefficients for Reid’s ramp model, (4.10), with varying E/n_0 . ‘M’ refers to the moment method of Ness and Robson [34], ‘POR’ the cubic spline method of Pitchford et al. [35, 36], ‘McM’ the relaxation method method of MacMahon [37], ‘FEM’ the finite element method of Segur et al. [38], ‘PDM’ the path differential method of Segur et al. [38], ‘Reid’, ‘Brag’, ‘Skull’ and ‘Penet’ the Monte Carlo results of Reid [39], Braglia et al. [40], Skullerud [38] and Penetrante [36] respectively. The accuracy of the various methods are included in brackets when known. Calculations have been performed with $l_{\max} = 5$ and $N = 5000$	65
4.7	Transport coefficients for Reids ramp model, (4.12), with varying l_{\max} for $E/n_0 = 12$ Td. Calculations have been performed with $U_\infty = 3$, and $N = 5000$	65
4.8	Transport coefficients for the Lucas-Saelee model, (4.13), with varying F . ‘1 = 1’ and ‘1 = 2’ refer to the moment method of Ness and Robson [34], ‘T’ to the calculations of Taniguchi et al. [41], ‘L’ to the Boltzmann calculations of Lucas and Saelee [42], and ‘MC’ the Monte Carlo results of Lucas and Saelee [42]. Calculations have been performed with $l_{\max} = 5$ and $N = 5000$	67
4.10	Convergence in l_{\max} of the bulk transport coefficients for the ionization model (4.14) for $E/n_0 = 1000$ Td and $Q = \frac{1}{2}$. Calculations have been performed with $N = 5000$, and $U_\infty = 250$	68
4.9	Comparison of average ionization rate, α^{EII}/n_0 , mean energies, ϵ , flux drift velocities, W^{flux} , and bulk drift velocities W for EII for model (6.21) for different reduced fields E/n_0 and energy sharing fractions Q . The first column lists the current kinetic theory calculations, the second column lists the results of our Monte Carlo simulations [9], and the third includes the kinetic theory calculations of Ness and Robson [34]. $Q = \text{AFE}$ corresponds to ‘all fractions equiprobable’. Note: there was an error in the AFE case in the original Ness and Robson work [34], which has been recalculated. The values enclosed in square brackets have been calculated using a similar Burnett function expansion to that of Ness and Robson.	69
5.1	Drift velocities, in units of 10^3 ms^{-1} , as a function of the reduced electric field, for electrons in neon at $T_0 = 77$ K. The stated uncertainty for the ANU experimental drift velocities [43] is 1%.	81

5.2	Drift velocity, in units of 10^3 ms^{-1} , as a function of the reduced electric field, for electrons in neon at $T_0 = 293 \text{ K}$. The stated uncertainty for the ANU drift velocities is 1%.	83
5.3	The RMS relative difference between experimental and calculated transport parameters. The $E/n_0 = 1.821$ and 2.003 Td W are not part of the error calculation for the 293 K data set.	84
5.4	The maximum relative difference between experimental and calculated transport parameters. The relative difference is given above the value of E/n_0 at which it occurs. The E/n_0 at 1.821 and 2.003 Td at 293 K were excluded from consideration.	84
5.5	The characteristic energy D_T/μ , (in eV) with electric field (in Td), for electrons in neon at $T_0 = 293 \text{ K}$. The stated uncertainty of the Rikkyo data is 3%.	85
5.6	The thermal diffusion coefficient, $n_0 D$, in units of $10^{20} \text{ mm}^{-1} \text{ s}^{-1}$, for thermal electrons in neon gas.	86
5.7	The parameters ρ_L and G_L for helium in the model potential. Note $\alpha_d = 1.383 (\text{a}_0^3)$ [44]. The particular numerical criteria (and their source) used to fix ρ_L and G_L are specified.	89
6.1	Comparison of average ionization rates, α^{ion}/n_0 , mean energies, ϵ , and flux drift velocities, W , for PII for model (6.21) for different reduced fields E/n_0 and energy sharing fractions Q . Columns ‘Current’ correspond to the current kinetic theory calculations, and columns ‘MC’ are the results of the Monte Carlo simulation. Note, $Q = \text{AFE}$ corresponds to ‘all fractions equiprobable’.	103
6.2	Convergence of transport properties with l_{max} for PII model (6.21) at 1000 Td and $Q = 1/2$	104
6.3	Comparison of average ionization rate, α^{ion}/n_0 , mean energies, ϵ , and flux drift velocities, W , for PII for model (6.27). The superscripts a and b refer to $w(U) = 0$ and $w(U) = 1$ respectively. Columns ‘Current’ correspond to the current kinetic theory calculations, and columns ‘MC’ are the results of Monte Carlo simulation.	108
8.1	Comparison of the transport quantities calculated from non-hydrodynamic (first row) and time asymptotic hydrodynamic (second row) formalisms for model (8.34) at various volume fractions Φ	139

1

Introduction

1.1 Motivation and aims

Electron and positron (lepton) impact processes in gases, liquids and soft-condensed matter underpin a diverse range of scientific fields and applications. To optimize the applications and extract new fundamental physics from experiments, it is important to have a full understanding of the space, time, and energy distribution of the primary and secondary particles. Electron-driven processes in gaseous systems were the cornerstone of the digital age through the development of low-temperature plasma processing of microelectronic devices. Programs involving complex modelling of plasma discharges and the species induced (electrons, ions, neutrals, radicals), informed by accurate microscopic scattering information (experiment and theory) together with diagnostics, permitted optimal control design [45, 46]. The next frontier is biological applications for medical diagnostics and therapy. For applications involving the human body, there is a need to be able to accurately quantify the biological consequences of radiation, including damage to DNA, with the aim of minimizing the negative effects and improving efficacy.

The path to optimizing these technologies will be similar to that of microelectronic device development, i.e., reliant on the development of accurate predictive models underpinned by accurate fundamental science and benchmarked against experiment. Predictive modelling allows a systematic investigation of a much larger variety of systems and sampling of a much wider parameter space than can be done physically. Our program focuses on understanding two key aspects:

1. Fundamental microscopic scattering information (cross sections) that describe how electrons and positrons interact with various species in the gaseous and liquid phases.
2. Transport of electrons and positrons under highly non-equilibrium conditions in the gaseous and liquid phases.

The behaviour of electrons, positrons etc. in gases and soft-condensed matter is quantified via important properties, including temporal and spatial profiles, mobilities, diffusion rates, ionization

rates and energy deposition, which can then inform and optimize the relevant technologies. We discuss some of the processes and applications in detail now.

1.1.1 Electron driven processes and applications

Studies of charged particle behaviour dates back to the birth of modern atomic physics, in the late nineteenth and early twentieth centuries. The invention of cathode ray tubes and discovery of X-rays [47] spurred interest in the conductivity of electricity through gases. British experimentalists Thomson, Townsend and Wilson [48] determined that the cathode rays were electrons, and made the first accurate estimates of the electron's mass and charge. Subsequent experiments by Thomson, Townsend, Millikan, Fletcher, Rutherford, Moseley, Frank and Hertz largely established the structure of an atom [49,50] and laid the foundations for the electron swarm experiments discussed in detail in Section 1.2.

Today, the technological consequences of these early investigations and associated electron-induced processes are ubiquitous. There are applications to an extremely diverse range of scientific fields including electron radiation therapy, nuclear imaging, astrophysics, aerospace, atmospheric physics, high energy particle detectors, welding, and biomedical and toxic waste treatment industries to name but a few [45, 46, 51]. Low-temperature, weakly ionized gas discharge plasma processing is used in the manufacture of microelectronic devices (i.e., etching, sputtering and decomposition processes) contributing billions of dollars to the world economy alone [45].

Radiation damage One of the most important limitations in diagnostic nuclear medicine, radiation therapy, radiation safety etc. is the risk of ionizing-radiation-induced cancer [52,53]. Ionizing radiation can induce chemical changes in biological matter leading to chromosome damage, cell death, oncogenic transformation, and acute radiation sickness [54]. It is thus necessary to be able to accurately assess patient and practitioner radiation doses [55].

In positron emission tomography, which is discussed in detail in Section 1.1.2, the emitted positron interacts with matter and deposits energy randomly and rapidly via collisional processes including excitation and ionization events. Approximately 70% of charged particle energy deposition occurs via ionization [54]. In an ionization event, the imparted energy is greater than the binding energy of the molecule which results in the emission of an electron from the now positively charged ion. Because water makes up such a large percentage of living systems, the interaction between radiation and water molecules is extremely important. The secondary ion species produced by the ionization of H₂O are unstable and can produce further free radicals via dissociation, which can in turn disrupt cellular mechanisms directly or via damage to genetic material [54]. There is also a cascade of ionized electrons that accompany the path of the emitted positron (approximately 10⁵ ionized electrons emitted per MeV deposited primary radiation in matter [56,57]), which makes these secondary electrons the most abundant of all secondary species produced by the interaction. The kinetic energy distribution of the secondary electrons in H₂O indicates that the vast majority are produced in the energy region below 10 eV [57,58]. Furthermore, Sanche and co-workers have showed that electrons with energy below 20 eV are largely responsible for single and double strand breaks in plasmid DNA via dissociative electron attachment [59,60]. Hence both the primary and secondary species can cause severe damage to DNA, which can lead to mutagenic, genotoxic and other potential DNA lesions.

To determine a suitable balance between image quality and patient dose (and hence the risk of radiation-induced damage) dosimetric data is required. The international Medical Internal Radiation Dosimetry (MIRD) Committee of the Society of Nuclear Medicine has developed a meth-

odology for calculating the radiation dose to selected organs and the whole body from internally administered radionuclides [61–63]. The MIRDO formalism takes into account variables associated with the deposition of ionizing radiation energy and those associated with the biologic system for which the dose is being calculated. Although some of the variables are known with relatively high degree of accuracy, others are best estimates on simplified assumptions that, taken together, provide an estimate of the dose to the average (reference) adult, adolescent, child and fetus [61].

Plasma medicine Plasma medicine is a rapidly emerging multi-disciplinary field capitalizing on concepts and techniques from physics, chemistry, medicine, hygiene, biology, material sciences, microelectronics and engineering [64–68]. The products of low-temperature plasmas (e.g. electrons, ions, excited species) can be manipulated by electric and magnetic fields to achieve a variety of goals, e.g. the sterilization of medical equipment. Advancements in the manipulation of non-equilibrium plasmas has led to the development of low-temperature plasmas which are still capable of driving plasma chemistry. Cold atmospheric plasma (CAP) devices, which exhibit electron temperatures of a few electron volts while the neutral and ion temperatures are close to room temperature, have opened the possibility to extend plasma treatments to heat-sensitive and vulnerable objects such as living tissue under ambient conditions.

A key process in applications of CAPs is the interaction of reactive oxygen and nitrogen species (RONs) with biological targets, which are well known to produce beneficial effects [69–71]. Plasma needles [68,72,73] and torches [74–81], contact-free sterilization [64,67,82], the stimulation of tissue regeneration [83,84], inducement of blood coagulation [85,86], cosmetic re-structuring of tissue, drug delivery and even cancer treatment [70] are amongst the envisaged applications. While there has been considerable effort invested in studying RONs and their impact on cells [70,87], much less attention has been given to the role of electrons, despite their importance in many of the relevant electron-induced processes both in the gas and tissue phases.

Liquid particle detectors Liquid-phase noble gases were proposed by Alvarez in 1968 as good candidates for high-energy particle detectors [88]. Ionizing radiation can excite electrons into conduction levels so that they can be transported through the liquid by an applied electric field, which is the general operating principle of time projection chambers (TPCs). Liquid-phase noble gases, particularly liquid argon (LAr) and liquid xenon (LXe), are good candidates for use in TPCs due to their commercial availability, high mobility and low diffusion of electrons, which can then provide high-quality imaging and high-resolution energy measurements from the detection of the ionization charge. LAr and LXe TPCs overcome the deficiencies of both bubble chambers (which are limited in size and sensitive only for short times) and large-size calorimetric detectors (which suffer from coarse granularity and limitations in the identification of electromagnetic showers). At present, several LAr and LXe TPCs have been built for dark matter searches [89–92], neutrino detection [92–94], and have been used in high-energy beam-line experiments [92,95]. Optimizing these liquid TPC particle detectors requires an accurate understanding of electron drift and diffusion in noble liquids subject to electric fields.

1.1.2 Positron driven processes and applications

The positron is the antimatter counterpart of the electron, and possesses the same mass and quantum spin, but has an opposing charge [96]. The prediction and subsequent discovery of the positron is one of the great successes of quantum mechanics and twentieth century physics. In 1928, Paul Dirac introduced the eponymous Dirac equation, a unification of quantum mechanics,

special relativity, and the concept of spin to explain the Zeeman effect [97]. Dirac realized that both the positive and negative solutions of his equation were equally valid, and that the latter had real physical existence [98]. Only a few years later in 1932, experimental evidence of the positron was found by Anderson [99] while investigating cosmic rays in cloud chamber experiments, and was later confirmed by Blackett and Occhialini [100].

When a particle interacts with its corresponding antiparticle, the two can annihilate [101]. Annihilation is the process by which a particle-antiparticle pair are converted into new sets of particles and energy obeying energy and momentum conservation laws. Annihilation of a positron-electron pair can proceed by a number of mechanisms [102]. When the positron and electron are both in the singlet spin state the most probable annihilation channel is the two-gamma process

$$e^+ + e^- = 2\gamma.$$

Annihilation can also occur via the emission of higher numbers of gamma rays, but become increasingly unlikely. The ratio of the cross sections for three- and two- gamma ray emission is $\approx \frac{1}{370}$ [103], and higher order processes are expected to decrease by similar fractions. Conservation of momentum would require an annihilating electron-positron pair at rest to produce collinear gamma rays. However, De Benedetti and co-workers [104, 105] discovered that the angle between the two-gamma rays emitted following positron annihilation in various solids differed from precisely 180 degrees. The small acollinearity can be attributed to the motion of the bound electrons, the positrons having essentially thermalized.

Mohorovicic [106] proposed the existence of a quasi-stable bound state of a positron and an electron in 1934, called positronium, which was discovered experimentally in 1951 by Deutsch [107]. Similar to hydrogen, the ground state of positronium has two possible configurations based on the relative spin orientations of the positron and electron. The spin state has a significant influence on its annihilation lifetime [108]. The singlet state (1^1S_0) is called para-positronium and has a lifetime of approximately 1.25×10^{-10} s, while the triplet state (1^3S_1) is called ortho-positronium and has a much longer lifetime of 1.4×10^{-7} s. The annihilation of positrons and positronium in gases has been systematically exploited to determine properties including hyperfine structure, lifetime, annihilation selection rules and photon energy spectrums [101, 109]. Many of the early experimental techniques developed are still in use today [110].

Positrons are much more difficult to produce, accumulate and control than electrons due to their scarcity in nature and propensity to annihilate. For these reasons the applications of positrons are more narrow, and specifically exploit the annihilation of free positrons and positronium. Examples include positron annihilation spectroscopy [111], which is a useful tool for probing the structure of materials, and positotherapy [112], which is a new technique which has been demonstrated to affect apoptosis and necrosis of tumours on the cellular level. A major motivation behind several investigations in this thesis is applications to the nuclear imaging technique of positron emission tomography.

Positron emission tomography Positron emission tomography (PET) has become a well established and powerful non-invasive tool for measuring the rate of biological processes in humans and animals [113]. In PET, a short-lived positron-emitting radionuclide is used to mark a biologically active substance which can then be tracked as it travels through, and is metabolized by, the body. It therefore provides a functional or metabolic, rather than structural, assessment of tissue. All biological substrates and most drugs contain an atom that can be replaced by a positron emitter [114]. Radiolabelled compounds are created by substituting a positron emitter such as ^{11}C ,

^{13}N , ^{15}O , and ^{18}F (there are many other less common ones - ^{14}O , ^{64}Cu , ^{124}I , ^{76}Br , ^{82}Rb , ^{68}Ga), for equivalent stable elements in components of biological importance, which then have essentially the same biochemical properties as the original compound [113]. The radionuclide undergoes beta-positive decay randomly and spontaneously at a rate determined by its half-life, emitting an energetic positron along with a neutrino. The emitted positron proceeds to scatter repeatedly off molecules in the medium until slowing down sufficiently and encountering a localized electron. As discussed in the previous section, the positron and electron can form the short-lived bound state called positronium which can annihilate to produce signature gamma rays. The annihilation photons that are produced have identical energies of 511 keV [102] and are emitted simultaneously in opposite directions, neglecting a slight non-collinearity, where they are measured by the detector ring of the PET apparatus [115].

The fundamental difference between PET and other medical imaging techniques, such as X-ray imaging, computed tomography and magnetic resonance imaging, is that the former assesses functional and metabolic characteristics, whereas the latter generally assess structural or morphologic features. PET can sometimes detect clinically relevant changes even when no changes or minimal ones are detected by morphologic imaging [116]. The study of physiological factors and metabolic rates through PET has found major clinical applications in oncology, neurology, cardiology and a number of other areas. The non-invasive methodology of PET also allows the investigation of metabolic functions of normal volunteers to develop experimental models for various human diseases and disorders [117]. For most applications fluorodeoxy-glucose (FDG) is the preferred tracer, and it is now widely manufactured around the globe. Regionally specific discrepancies in glucose uptake can indicate the existence of pathological disorders. PET's most widespread application has been for the detection and staging of cancer in patients, as FDG can differentiate between normal and malignant tissue based on glucose transport and glycolysis. A patient's responses to therapy and the effectiveness of treatment plans can be monitored and assessed. One of the fastest growing uses of PET imaging is in the area of drug development [118, 119], as the previously isolated imaging and pharmaceutical communities begin to coalesce [120–123].

When the detector ring of the PET apparatus registers a pair of annihilation photons near-simultaneously, their origin can be determined along a line connecting the two points of detection using coincidence logic [54]. A coincidence event is assumed to have occurred when a pair of measurements by opposing detectors is recorded within a specified timing window, which is necessary to account for a difference in distances as well as to allow for signal transit times through cables and electronics. Photons that do not both arrive within the timing window are ignored. Scintillation crystals coupled to photomultiplier tubes are used as detectors in PET. Mathematical algorithms make use of the detected photons to reconstruct images of selected planes within the object [117].

The spatial resolution of PET imaging is also dependent on a number of physical factors regarding the fundamental physics of positron emission and annihilation [124]. After emission, the positron travels away from the source some finite distance before undergoing annihilation, called the penetration range. Hence the PET apparatus can deduce the location of the annihilation event but not the location of the radioactive source of interest. Higher initial positron emission energies lead to larger penetration distances and reduced spatial image resolution. For the current generation of scanners and certain isotopes, the positron penetration range represents perhaps the most significant effect on image resolution [125]. There have been a number of attempts at combating this effect, from utilizing isotopes with small emission energies, to more sophisticated techniques involving encapsulating the positron-emitter in a material lattice to greatly reduce the penetration distance [126, 127]. The penetration distance can also be reduced by the presence of a magnetic field, which will cause the positron to travel in a helical path. Involving magnetic fields

comes with significant technological difficulties, e.g. developing PET-appropriate photon detectors that are insensitive to magnetic fields, however these are being overcome with the growing interest in combined PET-MRI scanners [124, 128].

Another limitation is due to the non-collinearity of annihilation photons whereby they are rarely emitted at exactly 180 degrees from each other. This is a direct result of conservation laws. At the end of its range the positron has a small residual momentum, and coupled with the electron's own energy and momentum, the resulting annihilation photons are generally required to have a net momentum. This has a relatively small effect on low resolution imaging, but becomes very important for higher resolutions. It should be noted that the positron range and non-collinearity do not depend on the technology and hence cannot be overcome by simply employing smaller detector elements etc.

1.1.3 Current status of modelling in soft-condensed matter

The rapid development of both equilibrium and non-equilibrium statistical mechanics since the 1950's is due to the simultaneous advancement of computing technology and numerical techniques, particularly the development of Monte Carlo methods by Metropolis et al. [129] and the molecular dynamics of Alder and Wainwright [130] in 1953 and 1956 respectively [131]. The modern landscape of transport modelling is now dominated by Monte Carlo methods, thanks to their power and flexibility when dealing with complex geometries, boundary conditions, and complex and coupled physical systems. The general operating principle of a Monte Carlo simulation is to follow a large number of individual incident particles through subsequent collisions and applying specific rules each time one of the expected interaction processes occurs. By applying statistics to a sufficiently large number of particle 'histories', macroscopic properties can be determined from microscopic cross sections, even for complex situations where deterministic approaches are infeasible. Monte Carlo codes can be divided into two classes; 1.) General purpose codes, which simulate particle transport and were developed for general high energy physics or for dosimetry (e.g. GEANT4 [132], EGS4 [133], EGSnrc [134], ITS [135], MCNP [136], PENELOPE [137], PARTRAC [138], EPOTRAN [139], and LEPTS [140, 141]). The advantages of these general purpose codes are that they are widely used, well documented, and in the public domain leading to a large international community for continued updates, bug fixing, and support, often with the most current programming tools and hardware facilities available [142]; 2.) Dedicated codes, designed for specific simulations and more narrow application (e.g. PETSIM [143], SIMSET [144], EIDOLOM [145], PET-EGS [146], and Reilhac [147] are all Monte Carlo simulation packages designed specifically for PET configurations). While general purpose codes such as GEANT4 remain quite complex with many extra capabilities which inflate the code sizes and complicate their use for specific applications, dedicated codes provide greater programming simplicity and ease of use at the cost of a decreased dedicated user-base. These codes are often developed by small research groups and have a user base much smaller than communities involved in high particle physics or dosimetry, hence maintenance and long-term existence are uncertain. Dedicated Monte Carlo codes developed also tend to suffer more from limitations in terms of validation and accuracy [142].

Whether general or dedicated, the existing numerical packages for modelling electron and positron transport have some deficiencies/issues that need to be addressed.

Benchmarking A simulation code needs to be thoroughly benchmarked and validated. Often in Monte Carlo simulations we find lepton trajectories are used as a method of differentiating

various background media [148]. While these are illustrative and important in developing nanodosimetric models, this is not a measurable that can be used for validation. Generally, thermalization simulations are performed with the range/dispersion and energy deposition sampled and measured. These measures are not strict benchmarks, since there exists degeneracy in the scattering cross sections that can generate the same range/dispersion. The only tunable parameters in such validation experiments are the initial distribution of the emitted leptons and these are insufficient to remove/test degeneracy. The application of electric fields to drive systems into highly non-equilibrium states, however, represents a stringent benchmark and test of degeneracy, through the modifications of the phase-space distribution function. One group that does appreciate the need for systematic benchmarks is Petrović and co-workers [149–151].

Low energy processes A full description of lepton transport in soft matter, particularly as medicine moves towards the realm of cellular microdosimetry, necessarily includes transport in the low-energy regime. Above 10 keV the Born-Bethe [152, 153] approximation can be used to accurately describe molecules combining the atomic species H, C, N, and O [154]. Below this energy, scattering cross sections are required to properly describe the various processes of the particles from emission down to their final thermalization. In Monte Carlo codes, the collisions are usually based on multiple scattering theories and/or energy loss distributions leading to some inaccuracies in the calculated track of the particles, which is exacerbated at low energies [155]. Furthermore, ‘effective cross sections’ which are sometimes used in simulations are not measurable quantities such that their use is both arbitrary and inaccurate - groups of processes may be lumped together to form an average cross section or be omitted entirely. For PET modelling, a complete set of differential and integral cross sections describing all elastic and inelastic processes induced by positrons and secondary electrons are required for a proper calculation of transport quantities [156].

Structure and density effects In dilute gases, the scattering centres of the medium can be considered independent and uncorrelated. During a collision, only a single medium particle is sampled at a time leading to large simplifications in the underlying theory. When considering denser media, such as dense gases, liquids and biological matter, the temporal and spatial correlations of the scattering centres becomes important. The de Broglie wavelengths of the incoming particle can then be of the order of the interparticle spacing, which leads to significant multiple scattering effects. The complexity of this more realistic scenario invalidates the assumptions and simplifications made in most current models, however, structure effects are of critical importance for accurately modelling swarm behaviour at low energies [157]. Density effects include coherent scattering [3], quantum self interference [158, 159], screening of the long range polarization potential [2], and the formation of bubbles or clusters [160–163]. A more satisfying model of charged particle transport in soft-condensed materials incorporating density effects is required. A detailed discussion of liquid and structure effects is given in Chapters 7 and 8.

1.1.4 Aims of this study

To overcome the deficiencies described in the previous section, a kinetic theory approach to modelling leptons in soft-condensed matter is chosen rather than the usual Monte Carlo approach. Instead of considering the trajectories and behaviour of individual particles, kinetic theory considers the probability distribution of the swarm as a whole, and has a good pedigree for lepton transport in gases. The aim is to bring to bear on this problem the highly accurate mathematical and computational machinery developed for the Boltzmann equation treatment of swarms and

plasmas. In this work, a kinetic theory is developed to describe highly non-equilibrium electron and positron transport, with particular attention paid to understanding the scattering mechanisms in gases and soft-condensed matter. Differences between the gas-phase and liquid-phase transport manifests themselves most strongly in the low-energy regime. While the treatment of biological matter is the final goal, this work focuses on atomic liquids for which there is a large body of literature and benchmarks for the underlying scattering mechanisms and transport. From the kinetic theory model the microscopic information can be used to generate macroscopic properties including spatio-temporal profiles, collision rates and transport coefficients. Systematic benchmarking of our numerical scheme for all collisional processes is a major theme in this work, and here swarm experiments play a major role. Swarm experiments have a long history, and have been performed for electrons and positrons in many species in gas and liquid phases, with a high degree of accuracy.

1.2 Swarm experiments

In a charged-particle swarm, the density of the constituents is so low that the charged particles do not influence the external electric field and the Coulomb interaction between the charged particles is negligible. Swarms can be considered the low lepton-density limit of gas discharges, as opposed to plasmas which operate at the high electron-density limit. A variety of configurations of swarm experiments exist [50, 101, 110, 164–167] to measure the physical properties of electron or positron swarms. The general operating principle is to apply electric fields to drive the swarm out of thermal equilibrium such that a quasi-steady state is achieved by a balance between power input from the electric field and the energy loss rate via collision of the swarm particles with a neutral background medium. Variations in the applied field allow one to selectively probe different energy regions in the cross sections. An early use of swarm experiment measurements were to ‘unfold’ and extract complete sets of cross sections from transport data.

Detailed sets of lepton-molecule interaction cross sections are now compiled through a combination of binary collision experiments (crossed beam [168], trap-based [169]) and quantum calculations. One of the key functions of modern-day swarm experiments is to assess the completeness and accuracy of the cross section sets. Swarm experiments are many-scattering experiments, where there is a balance established between the number of particles and the momentum and energy transfers occurring. If the transport coefficients calculated from a given set of cross sections fit well with swarm experiment measurements, then this set of cross sections is complete in the sense that it satisfies the various balance requirements. Hence swarm experiments provide a stringent test of cross section sets derived from combination of binary-collision experiments and theoretical calculations. Limitations of the swarm technique for determining cross sections are also well known [170, 171], and include non-uniqueness, limited resolution, and averaging over the angular distribution. Indeed the non-uniqueness problem for swarms, which is overcome by direct measurement of cross sections in binary collision experiments, has led to interest in the former waning considerably. Ideally both swarm and binary techniques are used together in a complementary, iterative fashion - cross sections are determined by binary collision/theoretical techniques, validated against swarm experiments via a transport calculation, which then informs adjustments to the cross sections, and so on.

1.2.1 Swarm measurements in dilute gases

Electron swarm experiments in the gas phase

The foundations for swarm physics were developed alongside accurate electron experiments in the 1970's and 1980's measuring transport coefficients [50, 51, 171]. Australia has a rich history in the field of experimental (and theoretical) swarm physics, ushered in through the seminal work of Huxley, Crompton and co-workers (see [50]) . The prototypical swarm experiment is the well known Time of Flight (TOF) experiment, which is based on releasing a source of electrons into a gas in the presence of an electric field between the source and the detector, and measuring the current (see e.g. the more recent work of Nakamura and co-workers [172, 173]). From the current various different transport coefficients (drift velocity, diffusion coefficient, etc) or combinations of them can be determined depending on the experimental configuration. A variation of the standard TOF experiment involves analysing the arrival time spectra of the electrons [174, 175]. Likewise, Pulsed Townsend (PT) experiments allowed the extension to higher energies, and also enabled the determination of attachment and ionization rates [176, 177]. In Steady-State Townsend (SST) experiments, a constantly emitting electron source allows a steady-state to be established with a background gas at equilibrium between two electrode plates, from which diffusion coefficients, excitation and ionization rates can be measured [178, 179]. The Cavalleri experiment uses a novel method for detecting the number of remaining electrons in the diffusion cell which allows direct measurement of the longitudinal diffusion coefficient [180, 181]. Swarm experiments in electric and magnetic fields performed by Schmidt and co-workers [182] are particularly noteworthy, since they provided additional transport coefficients (e.g. drift velocities and diffusion tensors with additional elements) as a possible method to address the well known degeneracy issue with cross sections and transport coefficients.

At present there are very few experimental centres surviving, with only the notable groups of de Urquijo and co-workers [176, 183–186], Franck and co-workers [187, 188] and more recently Satoh and co-workers [189] still active in this area.

Positron swarm experiments in the gas phase

The development of the low energy positron beam in the 1970's (see reviews by Griffith and Heyland, and Charlton [169, 190]) allowed the measurement of scattering cross sections directly, and interest in positron swarm techniques has subsequently declined. There are currently no positron swarm experiments of equivalent accuracy to their electron counterpart. Experimental techniques in the gas phase can be divided into two major categories; the measurement of annihilation lifetimes, and the Doppler broadening of the annihilation radiation. The basis of traditional lifetime experiments were formulated by Shearer and Deutsch in 1949 [191], and are based on the idea of measuring the lifetimes of a large number of positrons from their production to annihilation with background medium electrons, which are then collated into a lifetime spectrum. The initial timing signal is provided by the gamma-ray emission which accompanies the beta-decay of a radioactive source (such as ^{22}Na) while the photons accompanying eventual annihilation provide the stopping signal, both of which are detected using pairs of scintillation counters arranged appropriately on the exterior of the chamber which contains the medium and the source. During the slowing down of free positrons, a significant number form positronium, and hence the positron lifetime spectra consists of components due to both direct annihilation and the decay of positronium. The early experiments on positron diffusion in gases were mainly concerned with positronium formation, particularly the ortho-positronium state. The annihilation rate is proportional to the parameter

Z_{eff} , which is a measure of the effective number of target electrons as experienced by the positron due to polarization effects. An important landmark in the study of positron lifetime spectra of gases was the discovery of a shoulder region in the Z_{eff} profiles which can be characterised in terms of a shoulder width, τ_s , and related to the thermalization time of the positrons [110]. The shoulder region was first observed in argon by Falk and Jones [192], Tao et al. [193], and Paul [194]. Z_{eff} has been measured for field-free annihilation in noble gases [11,195], and molecular species [15,196–198], and for positrons subject to a static electric field in noble gases [11, 13, 15, 199, 200] and limited molecular species [15, 201–204].

A trap-based method of studying thermalized positron annihilation in gases was developed by Surko and co-workers [205, 206]. Essentially, the gas species is added to an accumulation of low-energy positrons, and then the effect on the number of trapped particles measured to deduce lifetimes and zero-field Z_{eff} . For thermalized positrons, the momentum of the centre of mass motion of an electron-positron pair is predominantly that of the electron [104, 105]. The centre of mass motion creates a Doppler shift in the annihilation photons as measured in the laboratory frame of reference, which can also be analysed by the positron-trap technique. The annihilation of positrons in a wide variety of molecular gases have been investigated with this technique [102].

There have also been limited attempts to directly measure positron drift velocities in gases. Two different approaches have been developed by Paul and co-workers [207–209] and Charlton and co-workers [101, 110]. According to Charlton [110], the main experimental difficulty has been in getting suitable drift lengths and times to compute the drift velocity using systems in which the positrons are derived directly from a radioactive source. The importance of the non-conservative process of positronium formation on transport coefficients has only recently been understood and re-evaluation of transport data from this viewpoint is warranted.

1.2.2 Swarm measurements in dense gaseous and liquid phases

Swarm experiments in dense gases and liquids are much more limited in number than their dilute gas counterparts, since liquid systems provide extra experimental difficulties [210]. Electron mobilities and characteristic energies have been measured for a range of noble gas liquids, including argon [28–30, 211–213], krypton [28, 212, 214], and xenon [28, 212, 213, 215], dense non-polar gases such as CO_2 [216, 217], and dense polar molecular gases including NH_3 [218–221] and H_2O [222]. The role of molecular impurities in atomic liquids has also been investigated experimentally [212], which can give rise to a number of radically new effects [223].

Field free annihilation lifetime studies have been reported for positrons in liquid helium [127, 224–227] and liquid argon [228, 229]. Annihilation lifetimes studies of positrons in liquids subject to electric fields are particularly rare, and have been limited to a handful of experiments by Pepe and co-workers in nitrogen [230, 231], helium [231, 232] and argon [231, 232]. In these works the variation of the positronium formation fraction with electric field strength is investigated along with the free positron and triplet state positronium lifetimes.

1.3 Kinetic theory of electron and positron swarms

A macroscopic volume of gas consists of a very large number of molecules (typically $\sim 10^{23}$) which, ignoring quantum effects, each obey the laws of classical mechanics. If the initial positions and momenta of all particles in the system were perfectly known in conjunction with the laws of interaction between the molecules, then the evolution of the system could, in principle (if not in practice), be calculated exactly. However, rarely is the initial state known exactly, and solving such

an initial value problem for a number of particles of realistic order is at present an impossible task. Instead, the only way to treat the system is as an ensemble of many similar systems in a probabilistic way, i.e. with statistics and probability distributions. Statistical mechanics provides the link between microscopic and macroscopic descriptions of matter, and kinetic theory is that branch of statistical mechanics which describes systems through a phase-space distribution $f(\mathbf{r}, \mathbf{v}, t)$. Study of a macroscopic system requires calculation of $f(\mathbf{r}, \mathbf{v}, t)$ from a kinetic equation.

A phase-space is a multi-dimensional space in which every degree of freedom or parameter of the system is represented as an axis. A particle in phase-space varies smoothly in position and velocity by the action of gradients and external forces, and varies abruptly in velocity due to collisions with other particles. The behaviour of a particle in phase-space thus appears as a contiguous flow of points, associated with a 6-dimensional ‘velocity’, with occasional abrupt vertical changes in the velocity co-ordinate due to collisions. Spatial variation of the distribution is ignored during scattering since the duration of a collision is assumed negligibly small compared with the mean free path, and takes place over a distance negligible in comparison to any relevant macroscopic length. The system is completely described by Liouville’s equation. Bogoliubov [233], Born and Green [234], Kirkwood [235,236] and Yvon [237] independently derived an infinite chain of equations (BBGKY) hierarchy for a reduced dimension of the Liouville. Assuming two body interactions and that any external field is small compared to the force of interaction during a collision, the kinetic equation resulting from the reversible BBGKY hierarchy is the irreversible Boltzmann equation, first derived (in a different way) by Ludwig Boltzmann in 1872 [238].

1.3.1 The Boltzmann equation

Research on the Boltzmann equation has advanced considerably beyond the classical gases Boltzmann intended, and generalizations have been successful in studying positron transport in gases, electron transport in solids and plasmas, neutron transport in nuclear reactors, phonon transport in superfluids, and radiative transfer in planetary and stellar atmospheres [131,239]. The form of the Boltzmann equation we consider in this work is

$$\left(\frac{\partial}{\partial t} + \mathbf{v} \cdot \nabla + \mathbf{a} \cdot \frac{\partial}{\partial \mathbf{v}} \right) f(\mathbf{r}, \mathbf{v}, t) = -J(f(\mathbf{r}, \mathbf{v}, t)), \quad (1.1)$$

where $f(\mathbf{r}, \mathbf{v}, t)$ is the phase-space distribution function, \mathbf{v} is the velocity relating to the incoming particle, and \mathbf{a} refers to the acceleration from external forces applied to the system. The Boltzmann equation represents the way in which the representative 7-point ‘fluid’ behaves in phase-space, and is in effect an extension of continuity to 6 dimensions. Microscopic scattering information is included in the collision operator, J , via appropriate scattering cross sections for each of the different collisional processes. In order for the Boltzmann equation to produce macroscopic irreversible behaviour from microscopic reversible information, the molecular chaos assumption or ‘Stosszahlansatz’ is required [238]. This assumption states that the distribution functions of the two particles are uncorrelated before a collision, but not so afterwards, thereby introducing an arrow of time.

1.3.2 Two-term vs. multi-term solutions

Kinetic theory was developed alongside the early investigations in swarm physics i.e. investigations of electrical conductivity of gases induced by X-rays. Experiments by Thomson, Rutherford and Townsend were crucial in the discovery of the electron, the determination of the electronic and atomic charge, and elucidating the ionization process. In 1909 Lorentz [240] undertook an analysis of electrical conductivity in metals, which marked the earliest theoretical investigation of

electron motion. Pidduck [241, 242] generalized Lorentz's work on electron motion in metals to a treatment of electron motion in gases. Pidduck's results were subsequently re-discovered by a number of other authors, and influential papers by Wannier [243], Allis [244] and Waldmann [245] in the 1950's cemented the kinetic theory of charged particles. The first rigorous solution of the Boltzmann equation with an expansion method was independently formulated by Chapman and Enskog between 1910 and 1920. In the Chapman-Enskog [246] theory, the distribution is expanded about the equilibrium solution which is only valid for near equilibrium conditions and hence not particularly useful for most situations in swarm physics. A good review of the early developments in electron transport is given by Huxley and Crompton [50]. This work prior to the 1980's relied on the so called 'two-term approximation'. The two-term approximation requires that the velocity distribution function can be written as a dominant isotropic component, f_0 , with a small anisotropic contribution, f_1 , i.e. the first two terms of a Legendre polynomial expansion in velocity-space. This assumption of quasi-isotropy in velocity space can be violated in many situations, e.g. when inelastic collisions are involved, or when strong electric and/or magnetic fields cause transverse spatial gradients [247, 248]. The consequence is clear; one must go beyond the two-term approximation, to multi-term expansions.

The modern era really began with the introduction of techniques from atomic and nuclear physics into kinetic theory by Kumar [249, 250], particularly the techniques of irreducible spherical tensor analysis and separation of centre-of-mass and relative velocity co-ordinates through the Talmi transformation. Viehland, Mason and collaborators formulated the first strong field solution of Boltzmann's equation for ions [251, 252], which in turn laid the basis for the first accurate multi-term solution of Boltzmann's equation for electrons [253]. Robson, Ness, White and co-workers have extended the standard multi-term technique to studies of conservative and non-conservative collisions in arbitrary crossed electric and magnetic field configurations [247, 254]. The numerical methods developed by these authors involve an expansion of the distribution function speed dependence in Sonine polynomials about a variety of Maxwellian-weighted functions. There have also been a number of other methods proposed for representing speed dependences of the phase-space distribution function, e.g., finite difference schemes [255–259] and splines [35, 260].

Despite the development of multi-term Boltzmann solutions and the well known limitations of the two-term approximation, use of the latter is still widespread and often of questionable validity. This can be attributed to the computational simplicity of low-order expansions, and also to the popularity of the free and user-friendly computer package BOLSIG+ [261], which is promoted by the online electron and ion information database LXCat [262], and is based *a priori* on the two-term approximation.

1.3.3 Transport in the hydrodynamic regime

A solution of the full multi-term space-time dependent Boltzmann equation is a complex and formidable challenge. Previous investigations have relied on one of a number of simplifications to make the problem more tractable, e.g. employing the two-term approximation, or considering only spatially homogeneous or steady-state systems. A common approach is to consider swarms and plasmas only in the 'hydrodynamic regime' i.e. the regime where there are no strong gradients imposed by large temperature differences, shearing flows, sources or sinks, and the explicit influence of boundaries are ignored. The spatial gradients of the swarm number density decay purely by the motion of particles, and does so at a much slower rate than the gradients of momentum, energy, and the higher velocity moments which can rapidly dissipate via collisions. In the hydrodynamic regime, the spatial dependence of the phase-space distribution functions are functionals of the

number density, $n(\mathbf{r}, t)$, and the implicit space-time dependence of the phase-space distribution and all velocity moments is adequately represented by a ‘density gradient expansion’ [263]. The swarm experiments that developed alongside the kinetic theory of gases deliberately operate in the hydrodynamic regime, such that the coefficients of the density gradient expansion, called transport coefficients, relate directly to swarm experiment measurables such as drift velocities, diffusion coefficients, etc.

The diffusion equation was originally used to unfold swarm experiments to determine the microscopic scattering cross sections. An important distinction between ‘bulk’ transport coefficients and ‘flux’ transport coefficients needs to be made, since it is the former which are generally determined in swarm literature. Physically, flux transport coefficients describe the mean velocity and diffusion of the particles in the swarm, whereas the bulk transport coefficients describe the spread about, and motion of, the swarm’s centre of mass. When non-particle-conserving processes are operative, the bulk and flux coefficients can differ by several orders of magnitude, and even exhibit entirely different quantitative behaviour [264–268]. Following the convention of [269], this phenomena is referred to as the Tagashira-Sakai-Sakamoto (TSS) effect after the researchers who first recognized and investigated the differences between the two transport coefficients [264, 265]. Informed by swarm experiments, work by Kumar, Robson, Mason, McDaniel and Viehland established a unified treatment of both electrons and ions (which had previously been developed separately) in the hydrodynamic regime, as well as establishing many useful and well-known empirical laws e.g., the Wannier energy relation, the generalized Einstein relations, Blanc’s law, Tonks’s theorem, and so on [269, 270]. Subsequent studies of electrons subject to electric fields were performed with a multi-term Boltzmann approach [34, 271]. Multi-term Boltzmann equation investigations have been performed for electrons subject to RF electric fields [248, 272–274] and electric and magnetic fields [247, 254, 275].

As discussed earlier, the latter part of the twentieth century saw the rise of crossed beam experiments, and the demise of swarm experiments, such that there are currently only a few groups remaining with operational swarm experiments despite their importance [276]. Instead, transport coefficients and hydrodynamic calculations have found an important role in informing low-temperature plasma modelling, which has influenced later investigations. In particular, transport coefficients are directly used for fluid models [46, 270] and also for the fluid parts of the hybrid models [277]. Swarm conditions are the free diffusion limit of the plasma and hence results from swarm limit analyses provide benchmarks for plasma codes in this limit.

1.3.4 Transport in the non-hydrodynamic regime

Strong gradients can be caused by boundary effects, strong electric or magnetic fields, varying fields, sources or sinks of particles etc., which introduce non-hydrodynamic conditions. In situations where the hydrodynamic regime is not applicable, the space-time dependence of the phase-space distribution function cannot be projected onto the number density. A density gradient expansion is no longer valid and transport coefficients are no longer meaningful quantities. Instead the configuration space dependence of the Boltzmann equation must be treated on an equal footing with the energy space dependence, which makes for a particularly computationally difficult problem even for simple geometries [278–280]. It is no surprise that systematic studies of such non-hydrodynamic phenomena lag behind their hydrodynamic counterparts. The Frank-Hertz experiment [281, 282], which helped lay the groundwork for quantum and atomic physics, is the prototypical example of non-hydrodynamic phenomena. A simple view of the Frank-Hertz experiment is the successive acceleration of electrons due to an electric field, which then rapidly lose energy due to an inelastic

channel, which gives rise to periodic spatial structures in the distribution function and velocity moments.

One of the first investigations of non-hydrodynamic phenomena using the Boltzmann equation was carried out by Morse et al. [283] to study the spatial variation that developed from an isotropic monoenergetic electron beam. In this pioneering work the calculations were simplified by assuming only elastic collision described by a constant cross section and assuming the two-term approximation. Thomas and Thomas [284] later also solved the two-term approximation Boltzmann equation alongside Monte Carlo simulations to calculate the time-dependent reaction rate for an electron avalanche, which showed oscillations about the asymptotic, hydrodynamic value. The method of characteristics was developed by Segur and co-workers [38, 285–287] to describe the motion of charged particles along characteristic lines in configuration and energy space. In a similar philosophy, an integral method based on flux-corrected transport was investigated by Kushner and co-workers [288, 289], but could only consider forward and backward scattering. More recently, extensive studies of non-hydrodynamic electron phenomena have been performed by the group at Griefswald, including field free spatial relaxation [290], and spatial relaxation in the presence of uniform [291–293], non-uniform [294] and periodic electric fields [295–297]. Similar kinetic studies on spatial relaxation of the electrons in uniform and spatially periodic fields have been performed by Golubovskii et al. [298–301]. The majority of these investigations have been limited to the two-term approximation in solving the space-dependent Boltzmann equation. Li and co-workers [254, 302, 303] developed a multi-term eigenvalue theory approach to investigate the spatial relaxation of electrons in arbitrary electric and magnetic field configurations.

Solution of the full kinetic equation for electrons including both the space and time dependence have also recently been performed [304–306]. These authors were restricted to a two-term approximation in Legendre polynomials to make the problem computationally feasible. As discussed in Section 1.3.2, for atomic systems a two-term analysis may provide sufficient accuracy, but in general a multi-term representation of the distribution function is required. This thesis addresses this limitation and includes the first development of a multi-term kinetic solution of the space and time dependent Boltzmann equation, as discussed in Chapter 8.

1.3.5 Kinetic modelling of lepton transport in dense gases, liquids and structured matter

In rarefied gas mediums the spacing between medium particles is much greater than the de Broglie wavelength of the swarm particle, such that only a single scattering centre is sampled during a binary collision. The surrounding medium particles can be considered to be moving randomly with no correlation between them. The behaviour of charged particles in materials with inter-particle spacing comparable or smaller than the de Broglie wavelength is very different to rarefied gases [157], and represents a complex problem. The major contributions to these differences arise from the small inter-particle spacings and their highly correlated separations. The de Broglie wavelengths of the swarm particles are often orders of magnitude larger than the interatomic spacing, which leads to significant quantum-like effects. Even within a semi-classical picture, where the swarm particles are assumed to act as point-like particles, no particular volume is ‘owned’ by a single atom. This means the typical picture for transport in a gas, i.e. a series of individual collision events separated by the mean-free path, is no longer valid, making it important to consider multiple scattering effects of the electron from many atoms simultaneously. Of particular note is the effect of ‘coherent scattering’ and the pair correlations of the liquid.

Many previous calculations for electrons in dense systems have neglected these liquid effects for simplicity, modelling dense fluids by applying a theory for dilute gases with only an appropriate increase of the density. Experimentally, this was shown to be quantitatively and qualitatively wrong [157]. However, a few alternative theories exist that have explored liquids in different ways. Borghesani et al. [307] have heuristically combined the liquid effects identified above to obtain an effective cross section. When used in the standard equations from kinetic theory for mobility in a non-zero field, their results have been shown to be remarkably accurate. Braglia and Dallacasa [308] have derived a theory that addresses both enhancements and reductions to the zero-field mobility through a Green's function approach with appropriate approximations to the self-energy, but do not go beyond linear response theory and hence do not explain non-equilibrium behaviour at high fields.

There are, in essence, two major problems to address in liquid scattering. The first is how to determine the effective atomic potential scattering of a charged particle in a liquid or dense state, from which one can derive a scattering cross section. When the neighbouring medium particles are close together, the long-range polarization force between a positron/electron and a polarizable atom is screened by the presence of other polarizable atoms. There is considerable overlap of the polarization force fields of different atoms, and to a lesser extent, of the static fields of nearest neighbours. In simple liquids, although the mutual configuration of particles moves continuously, the position and momentum of each atom should represent the configuration perfectly at any moment. Lekner in 1967 [2] outlined a process for calculating the screening of the polarization interaction from knowledge of the pair correlation function. Lekner accounted for the overlap of neighbouring atom potentials in the liquid state by defining an 'ensemble average' potential from which the appropriate cross sections can be calculated. Many of the techniques for calculating polarization, static, and exchange potentials have improved since Lekner's original paper, hence the same procedure can be followed with modern scattering methodologies. Sakai et al. [157] have been able to improve agreement with experiment by empirically modifying the resultant cross sections of the Lekner formalism and by including inelastic processes. Atrazhev et al. [309] were able to simplify the arguments of Lekner [2] to argue that, for small energies, the effective cross section becomes dependent on the density only and obtained good agreement with experiment. However the distance at which to enforce this new behaviour of the effective cross section remains a free parameter in the theory and this constant effective cross section must be found empirically. Atrazhev and co-workers went on to consider the interaction as a muffin tin potential, with each cell being a Wigner-Seitz sphere surrounding each atom in the liquid. They used a variable phase function method which could describe the absence of a Ramsauer minimum in the liquid cross section along with density fluctuations of the liquid [310-312].

The second problem is how to calculate transport properties once the potential is known. A general view of charged-particle interactions with a dense medium is as the scattering of a wave representing the charged particle by the medium as a whole. If one considers an incoming plane wave scattering off molecules in the medium into spherical waves, where the new signal is measured by a detector some distance away from the volume, then a first approximation to the scattering is the 'single scatterer approximation' in which the scattered beam is the coherent sum of contributions from many molecules which interfere to effectively produce a diffraction pattern of the medium. This is known as coherent scattering. Multiple scattering effects are taken as negligible, though are accountable through modifications to the cross sections [307, 313]. The approach to including coherent scattering effects due to structure in the framework of modern kinetic theory was proposed by Cohen and Lekner in 1967 [3], using concepts previously put forward by Van Hove in 1954. Van Hove showed that the first Born approximation scattering cross section could be

expressed in terms of a suitably generalized pair distribution function depending on a space vector and a time interval [314]. Essentially, the wave associated with the charged particle moving through the condensed material transfers energy to the collective excitations of the system, and all necessary information about the excitations in the single-scatterer approximation are contained in the Van Hove space-time pair correlation function, or more directly, its Fourier transform. The differential cross section for scattering in a dense medium is then proportional to the product of the single-atom differential cross section, which depends purely on properties of the interaction, and the structure function which encompasses properties of the medium only. The new scattering cross section, which incorporates the structure due to inter-particle correlation, can now be used to construct a governing kinetic equation, and has recently been investigated by White and Robson [1, 315].

1.3.6 Monte Carlo modelling of lepton transport in dense gases, liquids and structured matter

As discussed in Section 1.1.3, Monte Carlo simulation [149, 151, 156, 316–319] (and in a similar spirit particle-in-cell and hybrid models [277, 320–322]) is the dominant method for modelling charged particle transport. Even so, there are few authors who focus on non-equilibrium swarm transport in soft condensed matter, and even fewer who have addressed the deficiencies outlined. Sakai et al. [157] performed the first Monte Carlo simulation of electron scattering in liquid argon using a dynamic structure factor to account for coherent scattering. A similar approach was used by Kundhardt and co-workers to investigate electrons in liquid argon and xenon [323–325]. More recently, Tattersall [9] has adapted the static structure factor work of Wojcik and Tachiya [326] to develop a Monte Carlo code targeted specifically at non-equilibrium swarm transport, extending the work of Sakai [157], and applying it to a much greater variety of systems. The simulations of Tattersall have been used repeatedly throughout this thesis for benchmarking and validation purposes.

1.4 Structure of the thesis

The ultimate aim to develop predictive models of lepton transport in biological matter requires the systematic development of a benchmarked transport theory that accounts for all relevant underlying microscopic physics in the problem (see Section 1.3.5) and accounts for the full space-time evolution of the lepton phase-space distribution function. The scope of this thesis, however, is limited to:

1. The development of a time-dependent solution of the Boltzmann equation for electron and positron hydrodynamic swarm transport via a multi-term Legendre polynomial expansion of the velocity distribution function.
2. Systematic benchmarking of the Boltzmann equation solver for a range of non-equilibrium model and real systems, and its application to assess/develop various electron/positron cross section sets for atomic gases.
3. The modification of the Boltzmann collision operator and associated collision cross sections to account for density effects in simple non-polar liquids, and its benchmarking for electrons in liquid argon.

4. The extension of the multi-term solution of Boltzmann's equation to the non-hydrodynamic regime, and investigation of the spatio-temporal evolution of swarms in gaseous and liquid systems.

In Chapter 2, the kinetic theory of an electron or positron swarm moving through a background medium is detailed. The governing kinetic equation is the Boltzmann equation. The velocity dependence of the charged particle distribution function is represented in terms of Legendre polynomials, and the Boltzmann equation is decomposed into a system of coupled equations for the distribution function coefficients. In such an expansion, no limitation is placed on the number of terms in the Legendre polynomial expansion, i.e., this represents a true multi-term description. In the hydrodynamic regime, the space-dependence of the distribution function is represented by a second order density gradient expansion which accounts for non-conservative collisions. Expressions are given for the hydrodynamic components of the distribution function and transport coefficients. The collision operators are detailed for the important scattering processes in electron and positron transport, e.g., elastic, excitation, ionization, positron annihilation and positronium formation. Particular attention is given to coherent elastic scattering, which is a many-body effect important to transport in dense gases and liquids. We finish the chapter with a discussion of the initial and boundary conditions required.

Chapter 3 details the numerical techniques and considerations employed in this thesis for solving the Boltzmann equation representations and related expressions given in Chapter 2. Three different discretizations of the energy-space and collision operator are discussed; a centred Finite Difference representation and two pseudo-spectral methods, one based on Chebyshev polynomials and one on Laguerre functions. The temporal evolution of the system is achieved with an implicit-Euler method, and it is shown that the time-asymptotic solution can be found directly by solving an eigenvalue problem.

In Chapter 4, the kinetic theory and numerical schemes developed for Boltzmann's equation in the hydrodynamic regime are benchmarked for a number of model systems. Simple analytic cross section models allow us to individually and systematically validate the solution technique for each of the different collisional processes required in the full description. Particular attention is given to particle loss processes, such as positron annihilation, and particle gain processes, such as electron impact ionization. The calculations are compared with previous authors and an independent Monte Carlo simulation where possible. The inclusion of coherent scattering effects is benchmarked for a simple model liquid, and a detailed description of the phenomenology is given in Appendix A via fluid modelling.

In Chapters 5 and 6, the now-benchmarked numerical code is applied to real, dilute, gaseous systems. The Boltzmann equation provides the connection between microscopic cross sections and the macroscopic transport coefficients measured in swarm experiments. In particular, the application of an electric field to swarm experiments represents a stringent test on the validity of the cross section set, particularly above thermal energies. In Chapter 5 the electron-neon and positron-helium systems are investigated in the low-energy regime, using new sets of cross sections provided by scattering theoreticians. We then comment on the accuracy of new and existing cross section sets and make recommendations for the cross sections that are most consistent with swarm experiment measurements.

In Chapter 6 the positron-H₂ system is studied with respect to the ionization process. A positron impact ionization kinetic theory collision operator is derived for the first time. Particular attention is given to the effect of the energy-sharing between post-ionization constituents, and the

influence that different energy-partitioning models has on transport coefficients. A basic energy-partitioning model that captures, at least qualitatively, the basic physics of high energy and near-threshold positron ionization is proposed, which is fit to experimental H_2 data to investigate the transport of positrons in dilute H_2 gas.

In Chapter 7 the scattering of electrons is considered in gas-phase and liquid-phase argon. The study of excess electrons in dense gases and liquids is a complex problem, requiring the inclusion of many effects that are not present in dilute gaseous systems. The calculations we present in this chapter are based on a generalization of the Cohen and Lekner formalism, overcoming several approximations which are no longer necessary in modern day transport and scattering theory. The importance of an accurate description of static, polarization and exchange potentials is highlighted. There are two key modifications to the scattering potential necessary; one due to the screening of the long-range potential, and one due to contributions from other particles in the bulk. We perform calculations specifically for the noble gas of argon, which is an excellent test bed for new theories due to the good availability of experimental data, i.e. drift velocities and characteristic energies.

In Chapter 8, the kinetic theory developed for transport in the hydrodynamic regime is extended to the non-hydrodynamic regime. In the non-hydrodynamic regime, the full energy-space and configuration-space need to be resolved at each time. A numerical scheme is developed for the full, non-equilibrium, multi-term, spatio-temporal solution of the Boltzmann equation Green's function, from which a variety of experimental configurations and applications can be modelled. The spatio-temporal evolution of electron swarms is then investigated in a modified Percus-Yevick hard-sphere liquid system, and then real gaseous and liquid argon to elucidate the influence of liquid effects on the relaxation.

2

Kinetic theory

2.1 Introduction

In this chapter a kinetic equation for a dilute swarm of light-mass charged particles, such as positrons or electrons, moving through a dilute gaseous or structured medium is detailed. The swarm will be considered to be a non-degenerate, non-relativistic, one-component swarm of N particles each of mass m confined in a volume V . It is assumed that the swarm-particle density is so low that the Coulomb interactions between them are negligible, and furthermore, to a first approximation the overall state of equilibrium of the background medium is effectively undisturbed. It is generally a requirement that the background medium be a dilute gas [270,327,328], however, in this work we extend our investigation to include dense gases and liquids under the same conceptual framework.

Kinetic theory is the branch of statistical mechanics that describes a system through a ‘phase-space’ distribution function. A phase-space [329] is a space in which all possible states of a system are represented. Essentially, every degree of freedom or parameter of the system is represented as an axis of a multidimensional space. The succession of points traced in the phase-space is analogous to the system’s state evolving over time. For mechanical systems, the phase-space usually consists of all possible values of position and velocity variables, i.e., each of the N particles has three dimensions of configuration-space, \mathbf{r} , and three dimensions of velocity-space, \mathbf{v} . The time evolution of a state, $\mathbf{z}(\mathbf{r}, \mathbf{v})$, can be written as

$$\dot{\mathbf{z}} = \frac{d\mathbf{z}}{dt}, \quad (2.1)$$

where \mathbf{z} is then a $6N$ -dimensional vector. Given an initial state, \mathbf{z}_0 , equation (2.1) can be used to determine \mathbf{z} at subsequent times. If the initial data are not known with absolute accuracy, then one must instead introduce a probability density, $P(\mathbf{z})$, for the initial data, and then seek to compute the probability density at subsequent times, provided that the forces are known and the only

uncertainty is the initial data [239]. The system is completely described by Liouville's equation, which describes the probability of finding the $6N$ -dimensional system in a given state of position and momenta of the particle constituents. Bogoliubov [233], Born and Green [234], Kirkwood [235, 236] and Yvon [237] independently derived an infinite chain of equations (BBGKY hierarchy) for a reduced dimension of the Liouville equation. By introducing a direction of time into the system, which is synonymous with the stosszahlansatz introduced by Boltzmann in 1872 [238], the infinite chain of equations can be terminated at the first equation. Assuming two-body interactions only, the kinetic equation resulting from the BBGKY hierarchy is the irreversible Boltzmann equation (which could equivalently be derived from the complete set of Newton's equations of motion), and is the fundamental kinetic equation used in this work.

The Boltzmann equation [330] is

$$\left(\frac{\partial}{\partial t} + \mathbf{v} \cdot \nabla + \mathbf{a} \cdot \frac{\partial}{\partial \mathbf{v}} \right) f(\mathbf{r}, \mathbf{v}, t) = -J(f(\mathbf{r}, \mathbf{v}, t)), \quad (2.2)$$

where $f(\mathbf{r}, \mathbf{v}, t)$ is the phase-space distribution function and \mathbf{a} refers to the acceleration from external forces applied to the system. Equation (2.2) represents the fundamental equation from which macroscopic properties can be determined, i.e., from a knowledge of f , all relevant information about the system can be obtained. The Boltzmann equation represents the way in which the representative 7-point 'fluid' behaves in phase-space, and is in effect an extension of continuity to 6 dimensions. The left hand side of equation (2.2) describes the way f changes by the collision-less motion of the particles. The first term, $\frac{\partial}{\partial t} f$, describes the explicit time dependence of f at a fixed position \mathbf{r} and velocity \mathbf{v} , while the remaining terms, $\mathbf{v} \cdot \nabla$ and $\mathbf{a} \cdot \frac{\partial}{\partial \mathbf{v}}$, represent the convective flow in configuration and momentum space respectively. The right hand side of equation (2.2) is the eponymous Boltzmann collision integral, $J(f)$, which accounts for both conservative and non-conservative collisions between the swarm particle and a neutral molecule. The representation of the collision processes is an integral part of kinetic theory, and it is through the collisional operator that microscopic collisional information is included.

2.2 Multi-term Legendre polynomial expansion

The starting point for most modern-day solutions [330] of Boltzmann's equation, (2.2), is the representation of the velocity-space angle-dependence of the charged particle phase-space distribution function in terms of spherical harmonics, $Y_m^{[l]}$ [331], i.e.,

$$f(\mathbf{r}, \mathbf{v}, t) = \sum_{l=0}^{\infty} \sum_{m=-l}^l f_m^{(l)}(\mathbf{r}, v, t) Y_m^{[l]}(\hat{\mathbf{v}}), \quad (2.3)$$

where $\hat{\mathbf{v}}$ is the unit vector for velocity, i.e. $\mathbf{v} = v\hat{\mathbf{v}}$. Truncation of the infinite series (2.3) at some $l = l_{\max}$ designates the ' $(l_{\max} + 1)$ -term approximation'. The history of charged particle transport in gases has been dominated by the two-term approximation [50], i.e., where only the first two terms in l have been included. The assumption of quasi-isotropy is violated in many situations, particularly when inelastic collisions are included [253]. Such an assumption is not necessary in our formalism. Rather, l_{\max} is treated as a free parameter to be increased until some convergence or accuracy criterion is met.

If there is a single preferential direction, $\hat{\mathbf{a}}$, in the physical system, perhaps due to an applied electric field, then the system has a symmetry that can be exploited to reduce the scale of the

problem. In this case, the full spherical harmonic expansion reduces to a Legendre polynomial expansion, i.e.,

$$f(\mathbf{r}, \mathbf{v}, t) = \sum_{l=0}^{\infty} f_l(\mathbf{r}, v, t) P_l(\mu), \quad (2.4)$$

where $\mu = \hat{\mathbf{a}} \cdot \hat{\mathbf{v}}$ and P_l is the l th Legendre polynomial [332]. Specifically, the coefficients in equations (2.3) and (2.4) are related by $f_m^{(l)} = \frac{4\pi}{2l+1} f_l Y_m^{(l)}(\hat{\mathbf{a}})$.

2.2.1 Plane-parallel geometry

If there is a preference in the z direction (see Figure 2.1) then $f(\mathbf{r}, \mathbf{v}, t) \rightarrow f(z, v, \mu, t)$, where $\mu = \hat{\mathbf{z}} \cdot \hat{\mathbf{v}} = \cos \theta$. Equation (2.2) can then be written as,

$$\left(\frac{\partial}{\partial t} + \left[v \frac{\partial}{\partial z} + a_z \frac{\partial}{\partial v} \right] \mu + \frac{a_z}{v} (1 - \mu^2) \frac{\partial}{\partial \mu} + J \right) f(z, v, \mu, t) = 0, \quad (2.5)$$

where a_z is the acceleration which is now entirely in the z direction. Substituting the Legendre polynomial expansion (2.4) into equation (2.5) and equating the Legendre polynomial coefficients leads to an infinite chain of coupled partial differential equations:

$$\frac{\partial f_l}{\partial t} + \sum_{p=\pm 1} \Delta_l^{(p)} \left[v \frac{\partial}{\partial z} + a_z \left(\frac{\partial}{\partial v} + p \frac{l + \frac{3p+1}{2}}{v} \right) \right] f_{l+p} + J_l(f_l) = 0, \quad (2.6)$$

where

$$\Delta_l^{(+1)} = \frac{(l+1)}{(2l+3)}, \quad (2.7)$$

$$\Delta_l^{(-1)} = \frac{l}{(2l-1)}, \quad (2.8)$$

and J_l is the Legendre decomposition of the collision operator. Equation (2.6) can be re-cast in terms of energy, $U = \frac{1}{2}mv^2$, i.e.,

$$\frac{\partial f_l}{\partial t} + \left(\frac{2}{m} \right)^{\frac{1}{2}} \sum_{p=\pm 1} \Delta_l^{(p)} \left[U^{\frac{1}{2}} \frac{\partial}{\partial z} + qE \left(U^{\frac{1}{2}} \frac{\partial}{\partial U} + p \frac{l + \frac{3p+1}{2}}{2} U^{-\frac{1}{2}} \right) \right] f_{l+p} + J_l(f_l) = 0, \quad (2.9)$$

where a_z has been replaced by the electric field, E , i.e. $a_z = qE/m$. We will generally work in the energy representation, but will switch between the two when convenient. Solution of this equation is required under general operating regimes present in most experiments and applications. In the following section we consider a specific regime where the space-time dependence is projected onto the number density, i.e., the hydrodynamic regime. This allows us to make connection with traditional estimations of swarm transport coefficients obtained from swarm experiments, operating in the hydrodynamic regime. The non-hydrodynamic regime is considered in Chapter 8.

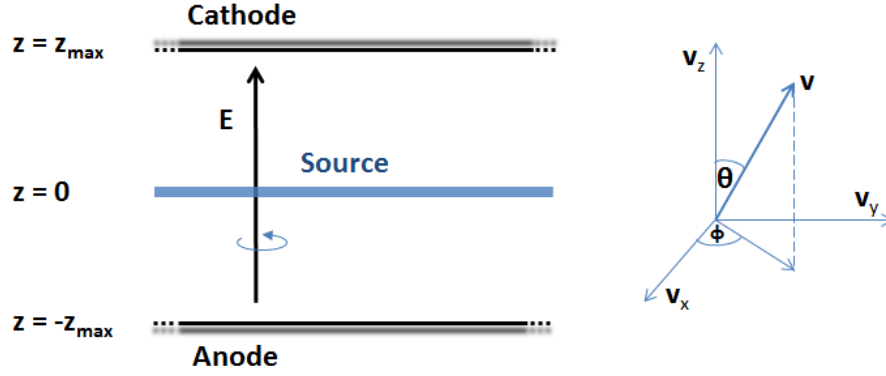


Figure 2.1: Schematic of the electric field direction and plane-parallel configuration-space geometry studied in this thesis.

2.2.2 Hydrodynamic regime

Transport coefficients, which will be detailed in Section 2.4, are defined in the ‘hydrodynamic regime’ where the spatial dependence of the phase-space distribution functions are functionals of the number density, $n(\mathbf{r}, t)$ [263]. The gradients of momentum, energy, and higher velocity moments, can be rapidly dissipated locally by virtue of collisions, whereas gradients of the swarm number density can only decay by the motion of particles and do so at a much slower rate. If there are no strong gradients imposed externally, such as large temperature differences, shearing flows, sources or sinks, and the explicit influence of boundaries are ignored, then the hydrodynamic regime is applicable. Here, the implicit space-time dependence of the phase-space distribution and all velocity moments is adequately represented by a ‘density gradient expansion’. To satisfactorily account for the effect of non-conservative processes a second order truncation of the density gradient expansion in Cartesian co-ordinates is required [263, 271], i.e.,

$$\begin{aligned}
 f(\mathbf{r}, \mathbf{v}, t) = & n(\mathbf{r}, t) F(\mathbf{v}) - F^{(L)}(\mathbf{v}) \frac{\partial}{\partial z} n(\mathbf{r}, t) - F^{(T)}(\mathbf{v}) \left[\cos \phi \frac{\partial}{\partial x} + \sin \phi \frac{\partial}{\partial y} \right] n(\mathbf{r}, t) \\
 & + \sqrt{\frac{1}{3}} F^{(2T)}(\mathbf{v}) \left[\frac{\partial^2}{\partial x^2} + \frac{\partial^2}{\partial y^2} + \frac{\partial^2}{\partial z^2} \right] n(\mathbf{r}, t) \\
 & + \sqrt{\frac{2}{3}} F^{(2L)}(\mathbf{v}) \left[\frac{1}{2} \left(\frac{\partial^2}{\partial x^2} + \frac{\partial^2}{\partial y^2} \right) - \frac{\partial^2}{\partial z^2} \right] n(\mathbf{r}, t),
 \end{aligned} \tag{2.10}$$

where ϕ is the azimuthal angle, and the superscripts L and T are quantities defined parallel and transverse to the electric field (defined to be in the z direction) respectively. The inclusion of more terms in equation (2.10) introduces coefficients representing the skewness and kurtosis of the swarm, however, these are not considered in this work and all transport properties of interest can be found by using the coefficients from the second order expansion. Our solution of the Boltzmann equation in the hydrodynamic regime, (2.2), requires the decomposition of the density gradient coefficients $F(\mathbf{v})$, $F^{(L)}(\mathbf{v})$, $F^{(2L)}(\mathbf{v})$ and $F^{(2T)}(\mathbf{v})$ in velocity space through an expansion

in Legendre polynomials, $P_l(\mu)$,

$$F(\mathbf{v}) = \sum_{l=0}^{\infty} F_l(v) P_l(\mu), \quad (2.11)$$

$$F^{(L)}(\mathbf{v}) = \sum_{l=0}^{\infty} F_l^{(L)}(v) P_l(\mu), \quad (2.12)$$

$$F^{(2T)}(\mathbf{v}) = \sum_{l=0}^{\infty} F_l^{(2T)}(v) P_l(\mu), \quad (2.13)$$

$$F^{(2L)}(\mathbf{v}) = \sum_{l=0}^{\infty} F_l^{(2L)}(v) P_l(\mu). \quad (2.14)$$

The first transverse component, $F^{(T)}(\mathbf{v})$, must be represented in terms of an expansion in associated Legendre polynomials [332], $P_l^1(\mu)$,

$$F^{(T)}(\mathbf{v}) = \sum_{l=1}^{\infty} F_l^{(T)}(v) P_l^1(\mu). \quad (2.15)$$

Exploiting the orthogonality of Legendre and associated Legendre polynomials, along with the density gradient expansion (2.10), the Boltzmann equation can be re-written as a hierarchy of equations [271]. If we first define the spatially-homogeneous energy-space Legendre polynomial Boltzmann operator, \mathcal{L} , which operates on a function $\Phi_l(U)$, i.e.,

$$\mathcal{L}\Phi_l = \left(\frac{\partial}{\partial t} + \omega_0 + J_l \right) \Phi_l + \left(\frac{2}{m} \right)^{\frac{1}{2}} \sum_{p=\pm 1} \Delta_l^{(p)} qE \left(U^{\frac{1}{2}} \frac{\partial}{\partial U} + p \frac{(l + \frac{3p+1}{2})}{2} U^{-\frac{1}{2}} \right) \Phi_{l+p}, \quad (2.16)$$

then the hierarchy of equations for $\Phi_l = \{F_l, F_l^{(L)}, F_l^{(2T)}, F_l^{(2L)}\}$ can each be written as,

$$\mathcal{L}\Phi_l = h_l^{(s)}, \quad (2.17)$$

where

$$h_l^{(0)} = 0, \quad (2.18)$$

$$h_l^{(L)} = \left(\frac{2U}{m} \right)^{\frac{1}{2}} \left(\frac{l+1}{2l+3} F_{l+1} + \frac{l}{2l-1} F_{l-1} \right) - \omega_1 F_l, \quad (2.19)$$

$$h_l^{(2T)} = \left(\frac{2U}{3m} \right)^{\frac{1}{2}} \left[\frac{l+1}{2l+3} \left(F_{l+1}^{(L)} + (l+2) F_{l+1}^{(T)} \right) + \frac{l}{2l-1} \left(F_{l-1}^{(L)} - (l-1) F_{l-1}^{(T)} \right) \right] - \omega_2 F_l - \left(\frac{1}{3} \right)^{\frac{1}{2}} \omega_1 F_l^{(L)}, \quad (2.20)$$

$$h_l^{(2L)} = - \left(\frac{U}{3m} \right)^{\frac{1}{2}} \left[\frac{l+1}{2l+3} \left(2F_{l+1}^{(L)} - (l+2) F_{l+1}^{(T)} \right) + \frac{l}{2l-1} \left(2F_{l-1}^{(L)} + (l-1) F_{l-1}^{(T)} \right) \right] - \bar{\omega}_2 F_l + \left(\frac{2}{3} \right)^{\frac{1}{2}} \omega_1 F_l^{(L)}. \quad (2.21)$$

Similarly, the first transverse component, $F_l^{(T)}$, is given by

$$\begin{aligned} & \left(\frac{\partial}{\partial t} + \omega_0 + J_l \right) F_l^{(T)} \\ & + \frac{l+2}{2l+3} \left(\frac{2}{m} \right)^{\frac{1}{2}} qE \left[U^{\frac{1}{2}} \frac{\partial}{\partial U} + \frac{(l+2)}{2} U^{-\frac{1}{2}} \right] F_{l+1}^{(T)} \\ & + \frac{l-1}{2l-1} \left(\frac{2}{m} \right)^{\frac{1}{2}} qE \left[U^{\frac{1}{2}} \frac{\partial}{\partial U} - \frac{(l-1)}{2} U^{-\frac{1}{2}} \right] F_{l-1}^{(T)} = \left(\frac{2U}{m} \right)^{\frac{1}{2}} \left(\frac{1}{2l-1} F_{l-1} - \frac{1}{2l+3} F_{l+1} \right). \end{aligned} \quad (2.22)$$

The expansion coefficients, $F_l^{(s)}$, satisfy the normalization conditions

$2\pi \left(\frac{2}{m} \right)^{\frac{3}{2}} \int_0^\infty dU U^{\frac{1}{2}} F_0^{(s)} = \delta_{s,0}$. The quantities $\omega_0, \omega_1, \omega_2$ and $\bar{\omega}_2$ [271] can be written compactly as

$$\omega_0 = -T_\alpha (F_0), \quad (2.23)$$

$$\omega_1 = T_F (F_1) - T_\alpha (F_0^{(L)}), \quad (2.24)$$

$$\omega_2 = T_F \left(\frac{1}{\sqrt{3}} [F_1^{(L)} + 2F_1^{(T)}] \right) - T_\alpha (F_0^{(2T)}), \quad (2.25)$$

$$\bar{\omega}_2 = -T_F \left(\sqrt{\frac{2}{3}} [F_1^{(L)} - F_1^{(T)}] \right) - T_\alpha (F_0^{(2L)}), \quad (2.26)$$

where T_F and T_α are general flux and particle non-conserving operators respectively, i.e.,

$$T_F (F(U)) = \frac{2\pi}{3} \left(\frac{2}{m} \right)^2 \int dU U F(U), \quad (2.27)$$

$$T_\alpha (F(U)) = 2\pi \left(\frac{2}{m} \right)^{\frac{3}{2}} \int dU U^{\frac{1}{2}} J_0^{NC} (F(U)), \quad (2.28)$$

where $J^{NC} (F_l)$ is the total non-conservative collision operator for particle non-conserving processes, i.e., $J^{NC} (F_l)$ is the sum of particle loss and particle gain processes such as electron attachment, electron ionization, positron annihilation and positronium formation etc.

The system of equations (2.16)–(2.26), represent a hierarchy of kinetic equations where an equation corresponding to a coefficient with level $s > 0$ depends upon coefficients from previous levels. For example, the distribution F_l appears in h_l when solving for $F_l^{(L)}$ and $F_l^{(T)}$ and therefore one must solve the zeroth level first. Similarly, the second level equations depend on coefficients found from the first and zeroth levels. It should also be noted that, in the presence of non-conservative collisions, the ω coefficients contained within h_l involve an integration which is dependent on the very density gradient expansion coefficient, $F^{(s)}$, that is the subject of the equation, resulting in a non-linear expression. For example, in the second level longitudinal equation, h_l includes an $\bar{\omega}_2$ term. The functional form of $\bar{\omega}_2$ has a dependence upon the distribution $F_0^{(2L)}$.

There remains the task of finding explicit expressions for the collision operator and their Legendre decompositions, for each of the relevant collisional processes.

2.3 Collision operators

The solution of equation (2.6) for the f_l , and the solution of equations (2.16)–(2.22) for the $F_l^{(s)}$ depends intimately on the collision processes included through the collision operator projections J_l .

The relevant collisional processes for the positron and electron transport considered in this work are detailed below, with a particular focus on the adjustments required for modelling transport in dense or structured media.

2.3.1 Coherent scattering

A swarm of particles moving through a dense gas, liquid, solid, or other structured system is scattered by atoms which interact with one another, and are therefore correlated both temporally and spatially. A first approximation of the scattering is the single-scattering from multiple centres approximation, in which the scattered amplitude at a point is the coherent sum of amplitudes collectively scattered from the individual atoms. This is termed ‘coherent scattering’. From the most general point of view, a particle wave moving through a liquid or solid transfers energy to collective excitations of the system. In the Born approximation, the scattering cross section is expressible in terms of a generalized pair-distribution function $G(\mathbf{r}, t)$ depending on a space vector \mathbf{r} , and time interval t [314]. The generalized pair-distribution function $G(\mathbf{r}, t)$ is a natural extension of the conventional pair-correlation function, $g(\mathbf{r})$ [333]. In the absence of quantum effects $G(\mathbf{r}, t)$ is the likelihood to find, at time $t' + t$, a particle at position $r' + r$ given that the particle was at a point r' at time t' . This definition has to be slightly modified for a quantum system. In the limit of $t \rightarrow 0$, $G(\mathbf{r}, t) \rightarrow g(\mathbf{r})$. In the single-scatterer approximation, all necessary information about the excitations is contained in the single-atom cross section and $G(\mathbf{r}, t)$, or more directly, its Fourier transform, termed the dynamic structure factor, $S(\Delta\mathbf{k}, \Delta\omega)$. The dynamic structure factor plays an important role in developing a collisional rate of change [3]. It is convenient to work with wave number, \mathbf{k} , and angular frequency, ω , instead of particle velocity and energy respectively. It is easy to switch between the two representations via

$$\hbar\mathbf{k} = m\mathbf{v}, \quad (2.29)$$

$$\hbar\omega = U = \frac{1}{2}mv^2. \quad (2.30)$$

A schematic of the coherent elastic scattering process is given in Figure 2.2. Undashed and dashed quantities refer to swarm-particle properties before and after a collision respectively. By employing the definition of the double differential cross section $\frac{d^2\sigma}{d\hat{\mathbf{k}}'d\omega'}$ [334] one can build up an expression for the change of a property of velocity, $\phi(\mathbf{v})$, due to collisions,

$$\begin{aligned} \left[\frac{\partial}{\partial t} \phi(\mathbf{v}) \right]_{\text{col}} &= \int d\mathbf{v} \phi(\mathbf{v}) J[f(\mathbf{v})], \\ &= n_0 \int d\mathbf{v} v f(\mathbf{v}) \int_0^\infty d\omega' \int_{\hat{\mathbf{k}}'} d\hat{\mathbf{k}}' [\phi(\mathbf{v}) - \phi(\mathbf{v}')] \frac{d^2\sigma}{d\hat{\mathbf{k}}'d\omega'}, \end{aligned} \quad (2.31)$$

where $\hat{\mathbf{k}}$ is the unit vector designating the wave number direction. Van Hove [314] showed that the double differential cross section can be expressed in terms of the single particle differential cross section (in the laboratory frame of reference) $\sigma_{\text{lab}}(|\Delta\mathbf{k}|, \hat{\mathbf{k}}')$ and the dynamic structure factor $S(\mathbf{k}, \Delta\omega)$, i.e.,

$$\frac{d^2\sigma}{d\hat{\mathbf{k}}'d\omega'} = \sigma_{\text{lab}}(|\Delta\mathbf{k}|, \hat{\mathbf{k}}') S(\mathbf{k}, \Delta\omega), \quad (2.32)$$

where $\Delta\mathbf{k} = \mathbf{k} - \mathbf{k}'$ is the change in the wave vector, and $\Delta\omega = \omega - \omega'$ is the change in energy due to the interaction with the medium as a whole. It is important at this point to note that the double differential scattering cross section is made up of two independent parts, i.e., the single

scattering cross section which depends purely on properties of the interaction potential, and the dynamic structure factor which depends only upon properties of the medium. The collisional rate of change of $\phi(\mathbf{v})$ is then given by,

$$\left[\frac{\partial}{\partial t} \phi(\mathbf{v}) \right]_{\text{col}} = n_0 \int d\mathbf{v}' v f(\mathbf{v}') \int_0^\infty d\omega' \times \int_{\hat{\mathbf{k}}'} d\hat{\mathbf{k}}' [\phi(\mathbf{v}) - \phi(\mathbf{v}')] \sigma_{\text{lab}}(|\Delta\mathbf{k}|, \hat{\mathbf{k}}') S(\mathbf{k}, \Delta\omega). \quad (2.33)$$

For light particles, the dynamic structure factor must satisfy the first three sum rules for a momentum exchange \mathbf{K} and energy exchange Q ,

$$\int_{-\infty}^{\infty} dQ S(\mathbf{K}, Q) = S(\mathbf{K}), \quad (2.34)$$

$$\int_{-\infty}^{\infty} dQ Q S(\mathbf{K}, Q) = \frac{K^2}{2m_0}, \quad (2.35)$$

$$\int_{-\infty}^{\infty} dQ Q^2 S(\mathbf{K}, Q) \approx 2k_b T_0 \frac{K^2}{2m_0}, \quad (2.36)$$

where $S(\mathbf{K})$ is known as the ‘static structure factor’ [3,157] and is the Fourier transform of the pair correlation function. A useful analogy can be found by viewing coherent scattering from an optics viewpoint i.e. as a multi-slit experiment. The resulting ‘pattern’ is the combination of diffraction due to each individual slit (single particle scattering) along with the interference pattern from the collection of slits as a whole (scattering centres) with Doppler shifting. In practice, the arguments \mathbf{K} and Q may be specified in some experimental arrangement set up to probe the properties of the medium.



Figure 2.2: Schematic of coherent scattering, where the incoming plane wave (with wave parameters \mathbf{k} and ω) is scattered from multiple scattering centres simultaneously into spherical outgoing waves (with wave parameters \mathbf{k}' and ω') through an angle χ .

The sum rules (2.34)–(2.36) are only true for independent \mathbf{K} and Q . Since \mathbf{k} and ω are not independent, the integral in equation (2.33) cannot be evaluated immediately. To enforce independence we expand about zero energy exchange, where the magnitude of \mathbf{k} does not change, but due to the rotation through a scattering angle χ , still has a non-zero vectorial change. The associated momentum exchange, $\Delta\mathbf{k}_0$, is related to $\Delta\mathbf{k}$ through

$$\Delta\mathbf{k} = \mathbf{k} - \mathbf{k}' = \Delta\mathbf{k}_0 + (k - k') \hat{\mathbf{k}}'. \quad (2.37)$$

When evaluating subsequent expressions arising from this expansion, we use the following identities:

$$|\Delta \mathbf{k}_0|^2 = 2k^2 (1 - \cos \chi) , \quad (2.38)$$

$$\hat{\mathbf{k}}' \cdot \Delta \mathbf{k}_0 = -k (1 - \cos \chi) . \quad (2.39)$$

In the limit of small relative energy exchanges, $\Delta\omega/\frac{1}{2}mv^2$, the following approximations can be made:

$$\sigma_{\text{lab}}(|\Delta \mathbf{k}|, \hat{\mathbf{k}}') = \sigma(v, \chi) - \frac{v}{4} \left(\frac{\Delta\omega}{\frac{1}{2}mv^2} \right) \frac{\partial}{\partial v} \sigma(v, \chi) , \quad (2.40)$$

$$S(\Delta \mathbf{k}, \Delta\omega) \approx S(\Delta \mathbf{k}_0, \Delta\omega) + \frac{1}{2}mv \left(\frac{\Delta\omega}{\frac{1}{2}mv^2} \right) \hat{\mathbf{k}}' \cdot \left[\frac{\partial}{\partial \mathbf{K}} S(\mathbf{K}, \Delta\omega) \right]_{\mathbf{K}=\Delta \mathbf{k}_0} , \quad (2.41)$$

which can now be used in the evaluation of collision integrals.

Now that the double differential scattering cross section incorporating coherent scattering has been constructed, we now need to determine the collision integrals (including their Legendre decompositions) for the various collisional processes. Only the elastic collision process is coherent, and hence influenced by the structure of the medium. For an inelastic process, energy is transferred on a localized site during scattering. Scattering is hence incoherent and interference effects do not manifest themselves. Processes such as attachment, annihilation, and positronium formation from a kinetic theory viewpoint are simple particle loss processes, and hence the collision operators representing such processes are just the direct scattering part of the original Boltzmann collision operator. Consequently, the structure of the material only plays a role in the elastic scattering processes.

2.3.2 Elastic collisional processes

Elastic scattering is a particle-conserving process in which the kinetic energy in the centre-of-mass frame is conserved. To derive the collisional operator for elastic collisions, let us first express the collisional rate of change (2.33) formally as

$$\left[\frac{\partial}{\partial t} \phi(\mathbf{v}) \right]_{\text{col}} = \int d\mathbf{v}' f(\mathbf{v}') J^\dagger(\phi) , \quad (2.42)$$

where the adjoint operator $J^\dagger(\phi)$ is defined as

$$J^\dagger(\phi) = n_0 \int_0^\infty d\omega' \int_{\hat{\mathbf{k}}'} d\hat{\mathbf{k}}' [\phi(\mathbf{v}) - \phi(\mathbf{v}')] \sigma_{\text{lab}}(|\Delta \mathbf{k}|, \hat{\mathbf{k}}') S(\mathbf{k}, \Delta\omega) , \quad (2.43)$$

which plays a key role in transport theory. This is the adjoint of the particle-medium collision operator $J(f)$, and the two are related via

$$\int d\mathbf{v} \phi(\mathbf{v}) J(f) = \int d\mathbf{v}' f(\mathbf{v}') J^\dagger(\phi) . \quad (2.44)$$

Let us now represent a property $\phi(\mathbf{v}) = \sum_l \phi_l(v) P_l(\mu)$ and consider the change due to collisions of the individual, $\phi_l(v) P_l(\mu)$. For light particles, i.e., $m/m_0 \ll 1$, we make use of the approximation

$$\phi(v') \approx \phi(v) - \frac{1}{2}v \left(\frac{\Delta\omega}{\frac{1}{2}mv^2} \right) \frac{\partial}{\partial v} \phi(v) + \mathcal{O} \left(\frac{\Delta\omega}{\frac{1}{2}mv^2} \right)^2 . \quad (2.45)$$

Rate of change of a scalar

For the scalar case of $l = 0$, equation (2.33) becomes,

$$\begin{aligned}
\left[\frac{\partial}{\partial t} \phi_0(v) \right]_{\text{col}} &= n_0 \int d\mathbf{v} v f(\mathbf{v}) \int_{\hat{\mathbf{k}}'} d\hat{\mathbf{k}}' \\
&\quad \times \int_{-\infty}^{\infty} d(\Delta\omega) [\phi_0(v) - \phi_0(v')] \sigma_{\text{lab}}(|\Delta\mathbf{k}|, \hat{\mathbf{k}}') S(\mathbf{k}, \Delta\omega), \\
&\approx n_0 \int d\mathbf{v} f(\mathbf{v}) \frac{1}{m} \frac{\partial}{\partial v} \phi(v) \int_{\hat{\mathbf{k}}'} d\hat{\mathbf{k}}' \sigma(v, \chi) \\
&\quad \times \sigma(v, \chi) \int_{-\infty}^{\infty} d(\Delta\omega) (\Delta\omega) S(\Delta\mathbf{k}_0, \Delta\omega), \tag{2.46}
\end{aligned}$$

where expansions (2.40), (2.41) and (2.45) have been substituted, with terms above second order in $\left(\frac{\Delta\omega}{\frac{1}{2}mv^2}\right)$ neglected. The integral over post-collision energies, ω' , has been replaced by an equivalent integral over $\Delta\omega$ to make connection with the expansions. It should be noted that first order terms cannot be neglected for the scalar case, lest there be no energy change due to collisions. The above is true for zero temperature. To account for temperature, the second order terms must be retained [1,157]. We can now evaluate the integral over $\Delta\omega$ using the sum rules (2.34)–(2.36), i.e.,

$$\begin{aligned}
\left[\frac{\partial}{\partial t} \phi_0(v) \right]_{\text{col}} &= n_0 \int d\mathbf{v} f(\mathbf{v}) \frac{1}{m} \frac{\partial}{\partial v} \phi(v) \int_{\hat{\mathbf{k}}'} d\hat{\mathbf{k}}' \sigma(v, \chi) \\
&\quad \times \int_{-\infty}^{\infty} d(\Delta\omega) (\Delta\omega) S(\Delta\mathbf{k}_0, \Delta\omega), \\
&\approx n_0 \int d\mathbf{v} f(\mathbf{v}) \frac{1}{m} \frac{\partial}{\partial v} \phi(v) \int_{\hat{\mathbf{k}}'} d\hat{\mathbf{k}}' \sigma(v, \chi) \frac{\Delta\mathbf{k}_0 \cdot \Delta\mathbf{k}_0}{2m_0}, \\
&= n_0 \int d\mathbf{v} f(\mathbf{v}) \frac{m}{m_0} v^2 \frac{\partial}{\partial v} \phi(v) \int_{\hat{\mathbf{k}}'} d\hat{\mathbf{k}}' \sigma(v, \chi) (1 - \cos \chi), \\
&= n_0 \int d\mathbf{v} f(\mathbf{v}) \frac{m}{m_0} v^2 \sigma_m(v) \frac{\partial}{\partial v} \phi(v), \\
&= 4\pi n_0 \int dv v^2 f_0(v) \frac{m}{m_0} v^2 \sigma_m(v) \frac{\partial}{\partial v} \phi(v), \tag{2.47}
\end{aligned}$$

where σ_m is the ‘momentum-transfer cross section’,

$$\sigma_m = \sigma_0 - \sigma_1, \tag{2.48}$$

where σ_l are the coefficients of a Legendre polynomial expansion, i.e.,

$$\sigma_l = \int_{\hat{\mathbf{k}}'} d\hat{\mathbf{k}}' \sigma(v, \chi) P_l(\cos \chi). \tag{2.49}$$

Comparing (2.42) with (2.47), it follows that

$$J_0^\dagger(\phi) = n_0 \frac{m}{m_0} v^2 \sigma_m(v) \frac{\partial}{\partial v} \phi(v), \tag{2.50}$$

and similarly from (2.44),

$$J_0(f_0) = -\frac{1}{v^2} \frac{\partial}{\partial v} \left[n_0 \frac{m}{m_0} v^4 \sigma_m(v) f_0 \right]. \tag{2.51}$$

It should be noted that these scalar operators are of exactly the same form as the corresponding operators for an unstructured dilute gas medium, derived by Pidduck [335] and Davydov [336]. The derivation including thermal motion of the background medium is more complicated, but follows along similar lines [1, 157]. For this reason, we merely quote the result,

$$J_0(f_0) = -\frac{1}{v^2} \frac{\partial}{\partial v} \left[n_0 \frac{m}{m_0} v^3 \sigma_m(v) \left(v f_0 + \frac{k_b T_0}{m} \frac{\partial}{\partial v} f_0 \right) \right]. \quad (2.52)$$

Rate of change of a vector or tensor

For the case of $l \geq 1$,

$$\begin{aligned} \left[\frac{\partial}{\partial t} \phi_l(v) P_l(\cos \chi) \right]_{\text{col}} &= n_0 \int d\mathbf{v} v f(\mathbf{v}) d\omega' \int_{\hat{\mathbf{k}}'} d\hat{\mathbf{k}}' \\ &\quad \times \int_{-\infty}^{\infty} d(\Delta\omega) [\phi_l(v) P_l(\cos \theta) - \phi_l(v') P_l(\cos \theta')] \sigma_{\text{lab}}(|\Delta\mathbf{k}|, \hat{\mathbf{k}}') S(\mathbf{k}, \Delta\omega), \\ &\simeq n_0 \int d\mathbf{v} v f(\mathbf{v}) \phi_l(v) \int_{\hat{\mathbf{k}}'} d\hat{\mathbf{k}}' [P_l(\cos \theta) - P_l(\cos \theta')] \\ &\quad \times \int_{-\infty}^{\infty} d(\Delta\omega)' \sigma(v, \chi) S(\Delta\mathbf{k}_0, \Delta\omega), \end{aligned} \quad (2.53)$$

where only the leading term in $\left(\frac{\Delta\omega}{\frac{1}{2}mv^2}\right)$ has been kept. The integral over $d(\Delta\omega)$ can be done immediately, yielding

$$\left[\frac{\partial}{\partial t} \phi_l(v) P_l(\cos \chi) \right]_{\text{col}} \approx n_0 \int d\mathbf{v} v f(\mathbf{v}) \phi_l(v) \int_{\hat{\mathbf{k}}'} d\hat{\mathbf{k}}' [P_l(\cos \theta) - P_l(\cos \theta')] \sigma(v, \chi) S(\Delta\mathbf{k}_0). \quad (2.54)$$

If we define $\Sigma(v, \chi) = \sigma(v, \chi) S(\Delta\mathbf{k}_0)$, then we can represent the angular dependence via the expansion

$$\begin{aligned} \Sigma(v, \chi) &= \sum_l \Sigma_l(v) P_l(\chi), \\ &= \sum_l \Sigma_l(v) P_l(\hat{\mathbf{k}} \cdot \hat{\mathbf{k}}'), \\ &= \sum_{l,m} \frac{4\pi}{2l+1} \Sigma_l(v) Y_m^{(l)}(\hat{\mathbf{k}}) Y_m^{[l]}(\hat{\mathbf{k}}'), \end{aligned} \quad (2.55)$$

where $Y_m^{(l)}$ is the complex conjugate of $Y_m^{[l]}$, i.e., $Y_m^{(l)} = \left(Y_m^{[l]}\right)^*$. Similarly,

$$P_l(\cos \theta') = \frac{4\pi}{2l+1} \sum_m Y_m^{(l)}(\hat{\mathbf{k}}') Y_m^{[l]}(\hat{\mathbf{a}}), \quad (2.56)$$

such that

$$\begin{aligned}
& \int_{\hat{\mathbf{k}}'} d\hat{\mathbf{k}}' [P_l(\cos\theta) - P_l(\cos\theta')] \sigma(v, \chi) S(\Delta\mathbf{k}_0) \\
&= P_l(\cos\theta) \int_{\hat{\mathbf{k}}'} d\hat{\mathbf{k}}' \sum_{l'} \Sigma_{l'}(v) P_{l'}(\chi) \\
&\quad - \int_{\hat{\mathbf{k}}'} d\hat{\mathbf{k}}' \frac{4\pi}{2l+1} \sum_m Y_m^{(l)}(\hat{\mathbf{k}}') Y_m^{[l]}(\hat{\mathbf{a}}) \sum_{l', m'} \frac{4\pi}{2l'+1} \Sigma_{l'}(v) Y_{m'}^{(l')}(\hat{\mathbf{k}}) Y_{m'}^{[l']}(\hat{\mathbf{k}}'), \\
&= P_l(\cos\theta) \Sigma_0(v) \\
&\quad - \frac{4\pi}{2l+1} \sum_m \sum_{l', m'} \Sigma_{l'}(v) Y_m^{[l]}(\hat{\mathbf{a}}) Y_{m'}^{(l')}(\hat{\mathbf{k}}) \int_{\hat{\mathbf{k}}'} d\hat{\mathbf{k}}' Y_m^{(l)}(\hat{\mathbf{k}}') Y_{m'}^{[l']}(\hat{\mathbf{k}}'), \\
&= P_l(\cos\theta) \Sigma_0(v) - \frac{4\pi}{2l+1} \sum_m \Sigma_l(v) Y_m^{[l]}(\hat{\mathbf{a}}) Y_m^{(l)}(\hat{\mathbf{k}}), \\
&= P_l(\cos\theta) \Sigma_0(v) - P_l(\cos\theta) \Sigma_l(v), \tag{2.57}
\end{aligned}$$

which leads to

$$\begin{aligned}
\left[\frac{\partial}{\partial t} \phi_l(v) P_l(\cos\theta) \right]_{\text{col}} &\approx n_0 \int d\mathbf{v} v f(\mathbf{v}) \phi_l(v) P_l(\cos\theta) (\Sigma_0(v) - \Sigma_l(v)), \\
&\simeq 4\pi n_0 \int dv v^2 v f_l(v) \phi_l(v) [\Sigma_0(v) - \Sigma_l(v)]. \tag{2.58}
\end{aligned}$$

Clearly, for $l \geq 1$,

$$J_l^\dagger(\phi) = n_0 v [\Sigma_0(v) - \Sigma_l(v)] \phi_l(v), \tag{2.59}$$

$$\begin{aligned}
J_l(f_l) &= n_0 v [\Sigma_0(v) - \Sigma_l(v)] f_l(v), \\
&= \tilde{\nu}_l(v) f_l(v), \tag{2.60}
\end{aligned}$$

where

$$\tilde{\nu}_l = n_0 v [\Sigma_0(v) - \Sigma_l(v)]. \tag{2.61}$$

For $l = 1$ we have an effective momentum-transfer collision frequency accounting for coherence effects. In summary

$$J_l^{\text{el}}(f_l(v)) = \begin{cases} -\frac{m}{m_0} \frac{1}{v^2} \frac{\partial}{\partial v} \left[v^3 \nu_m(v) \left(f_0(v) + \frac{k_b T_0}{m v} \frac{\partial f_0}{\partial v} \right) \right], & l = 0, \\ \tilde{\nu}_l^{\text{el}}(v) f_l(v), & l \geq 1, \end{cases} \tag{2.62}$$

or, equivalently in energy-space,

$$J_l^{\text{el}}(f_l(U)) = \begin{cases} -\frac{2m}{m_0} U^{-\frac{1}{2}} \frac{\partial}{\partial U} \left[U^{\frac{3}{2}} \nu_m(U) \left(f_0(U) + k_b T_0 \frac{\partial f_0}{\partial U} \right) \right], & l = 0, \\ \tilde{\nu}_l^{\text{el}}(U) f_l(U), & l \geq 1. \end{cases} \tag{2.63}$$

In the dilute gas limit, that is, when the coherent scattering is suppressed and collisions are binary, $S(\Delta\mathbf{k}_0) \rightarrow 1$, $\Sigma(v, \chi) \rightarrow \sigma(v, \chi)$, $\tilde{\nu}_l^{\text{el}} \rightarrow \nu_l^{\text{el}}$, and the usual expressions [335, 336] are recovered.

2.3.3 Collisional excitation processes

In an excitation collision, the energy of the impacting particle exceeds some threshold energy causing a state change in the medium, leading to a difference in the pre- and post-collision kinetic

energy. Like elastic collisions, it is also a particle-conserving process. For an excitation process, energy is transferred on a localized site during scattering. Scattering is hence incoherent and interference effects do not manifest themselves. Examples include electronic excitations, and rotational and vibrational excitations in molecular species. Particle-conserving ionization collisions, such as positron impact ionization are also an example of a conservative inelastic process (with respect to the positron), but will be considered in a more comprehensive manner in Chapter 6. Impact particles with an energy below the required inelastic threshold energy undergo elastic or super-elastic collisions. For media with a non-zero background temperature the medium particles may already exist in an excited state, and super-elastic collisions are possible where the de-excitation of the medium imparts energy to the swarm particle.

Excitations are an incoherent process, so it is reasonable to work in the centre-of-mass frame for binary collisions. For a swarm particle velocity, \mathbf{v} , and neutral velocity \mathbf{v}_0 , the relative velocity is given by $\mathbf{g} = \mathbf{v} - \mathbf{v}_0$. For binary particle-conservative collisions in a background medium, we assume the Wang-Chang et al. collision operator [337],

$$J^{\text{exc}}(f) = \sum_{\substack{j,k \\ j \neq k}} \int d\mathbf{v}_0 d\hat{\mathbf{g}}' [f(\mathbf{r}, \mathbf{v}, t) F_j(\mathbf{v}_0) - f(\mathbf{r}, \mathbf{v}', t) F_k(\mathbf{v}_0')] g \sigma(jk; g, \chi), \quad (2.64)$$

where F is the velocity distribution of the neutral molecules (not to be confused with the density gradient expansion coefficients). The indices j and k represent the initial and final internal states respectively, of the molecular gas. Inelastic and super-elastic collisions correspond to $j > k$ and $j < k$ respectively. The differential cross section $\sigma(jk; g, \chi)$ describes the possibility of scattering a swarm particle of velocity \mathbf{v} from a neutral molecule in the j th state with velocity \mathbf{v}_0 to the k th state of the neutral molecule. According to energy conservation we have,

$$\frac{1}{2}\mu g^2 + U_j = \frac{1}{2}\mu g'^2 + U_k, \quad (2.65)$$

where the reduced mass of the system is given by

$$\mu = \frac{mm_0}{m + m_0}. \quad (2.66)$$

This simplifies for light particles to $\mu \approx m$.

When deriving the Legendre polynomial decomposition form of the elastic collision operator, a first-order approximation in the mass ratio m/m_0 is required to obtain a non-zero expression. If the background gas has internal degrees of freedom then, to zeroth order in the mass ratio, energy exchange can still occur through excitation and de-excitation of those internal states. Hence unlike the isotropic part of the elastic collision integral, the scalar part of the inelastic collision integral does not vanish under a zeroth order mass assumption. The Legendre decomposed form of the collision operator was derived by Frost and Phelps [338], as extension of the work of Holstein [339], and is given in energy-space by,

$$J_l^{\text{exc}}(f_l) = \left(\frac{2}{mU}\right)^{\frac{1}{2}} \sum_{j < k} \begin{cases} n_{0j} [U\sigma^{\text{exc}}(jk; U) f_0 - \Delta U_{kj}^+ \sigma^{\text{exc}}(jk; \Delta U_{kj}^+) f_0 (\Delta U_{kj}^+)] \\ + n_{0k} [U\sigma^{\text{exc}}(kj; U) f_0 - \Delta U_{kj}^- \sigma^{\text{exc}}(kj; \Delta U_{kj}^-) f_0 (\Delta U_{kj}^-)] , & l = 0, \\ n_{0j} U \sigma^{\text{exc}}(jk; U) f_l(U) + n_{0k} U \sigma^{\text{exc}}(kj; U) f_l(U) , & l \geq 1, \end{cases} \quad (2.67)$$

where $\sigma^{\text{exc}}(jk; U)$ and $\sigma^{\text{exc}}(kj; U)$ represent excitation and de-excitation integral cross sections with an associated threshold energy of $U_{kj} = U_k - U_j$, and n_{0j} and n_{0k} is the density of the

background particles in the state j and k respectively. We use the shorthand $\Delta U_{kj}^{\pm} = U_k \pm U_j$. We assume that the background neutrals are in equilibrium such that they have a Maxwell-Boltzmann distribution in velocity space,

$$F_j(v_0) = n_{0j} \left(\frac{m}{2\pi k_b T_0} \right)^{\frac{3}{2}} \exp \left[-\frac{m}{2k_b T_0} v_0^2 \right], \quad (2.68)$$

which is associated with a number density of neutrals in the j th quantum state, n_{0j} , given by [340]

$$n_{0j} = \left(\frac{n_0}{Z_1} \right) g_j \exp \left(\frac{-U_j}{k_b T_0} \right), \quad (2.69)$$

where n_0 is the total neutral number density, g_j is the degeneracy of j th state, and Z_1 is the single particle partition function,

$$Z_1 = \sum_j g_j \exp \left(\frac{-U_j}{k_b T_0} \right). \quad (2.70)$$

It is clear that, provided the degeneracy does not increase substantially, for larger threshold energies U_j the associated n_{0j} are small, and hence super-elastic processes can be ignored for these processes. For processes that have smaller threshold energy levels, such as rotations and vibrations, the excited states may be populated and super-elastic processes can be crucial, particularly for low energy studies.

From the principle of microscopic reversibility and detailed balancing [341], the excitation and de-excitation collisions are related via

$$g_k (U - U_{kj}) \sigma^{\text{exc}}(kj; U - U_{kj}) = g_j U \sigma^{\text{exc}}(jk; U), \quad (2.71)$$

$$g_k U \sigma^{\text{exc}}(kj; U) = g_j (U + U_{kj}) \sigma^{\text{exc}}(jk; U + U_{kj}). \quad (2.72)$$

2.3.4 Attachment, annihilation and positronium formation

Electron attachment, positron annihilation and positronium formation occur through distinctly different physical mechanisms. However, from a transport theory perspective they each represent a unidirectional particle loss process, and hence the form of their collision operators are identical. Since there is no post-collision scattering the collision operator is simply [34],

$$J^{\text{loss}}(f) = \sum_k f(\mathbf{r}, \mathbf{v}, t) \int d\mathbf{v}_0 f_{0k}(\mathbf{v}_0) g \sigma^{\text{loss}}(k; g), \quad (2.73)$$

where k are the available loss process channels, and $\sigma^{\text{loss}}(k; g)$ is the cross section for the k th loss process. This is equivalent to introducing a loss-process collision frequency $\nu_k^{\text{loss}}(g)$ given by

$$\nu_k^{\text{loss}}(g) = \int d\mathbf{v}_0 f_{0k}(\mathbf{v}_0) g \sigma^{\text{loss}}(k; g), \quad (2.74)$$

which allows (2.73) to be written as

$$J^{\text{loss}}(f) = \sum_k \nu_k^{\text{loss}}(g) f(\mathbf{r}, \mathbf{v}, t), \quad (2.75)$$

and then,

$$J_l^{\text{loss}}(f_l) = \sum_k \nu_k^{\text{loss}}(U) f_l(U). \quad (2.76)$$

Reversible reactions, possibly characterizing chemical equilibrium are not considered here.

2.3.5 Ionization processes

Ionization by electron impact is fundamentally different from ionization by positron impact. Since the ejected electron is of the same species as the impacting particle, electron impact ionization (EII) is a non-particle-conserving process. Since the scattered positron is a different particle type than the ejected electron, positron impact ionization (PII) is a particle-conserving-process with respect to the positron swarm. A different collision operator needs to be used for each case. Although ionization is a three-body process, if we restrict our analysis to light swarm particles and heavy neutrals, we can assume the neutrals remain at rest during a collision to zeroth order in the mass ratio, m/m_0 . In effect, we assume that both the energy and momentum post-ionization are shared between the scattered and ejected particles.

The EII collision operator, J^{EII} , is given by [342]

$$J^{\text{EII}}(f) = n_0 v \sigma^{\text{EII}}(v) f(\mathbf{r}, \mathbf{v}, t) - 2n_0 \int d\mathbf{v}' v' \sigma^{\text{EII}}(v') B(\mathbf{v}, \mathbf{v}') f(\mathbf{r}, \mathbf{v}', t), \quad (2.77)$$

where σ^{EII} is the total EII cross section, and $B(\mathbf{v}, \mathbf{v}')$ is a probability density that partitions the available momentum after ionization between the two electrons. Specifically, $B(\mathbf{v}, \mathbf{v}')$ represents the probability of one of the two electrons after ionization having a velocity in the range \mathbf{v} to $\mathbf{v} + d\mathbf{v}$, provided that the incident electron has a velocity \mathbf{v}' . The first term on the right hand side of (2.77) represents the direct loss due to scattering from an element of phase-space, while the second term represents a source resulting from the scattering and ejection of electrons from other elements of phase-space. The factor of two on the right hand side of (2.77) is a consequence of the indistinguishability of the post-collision electrons.

The Legendre decomposition of (2.77) yields [342]

$$J_l^{\text{EII}}(f) = \begin{cases} n_0 v \sigma^{\text{EII}}(v) f_0(v) - 2n_0 \int_0^\infty dv' v'^3 \sigma^{\text{EII}}(v') B_0(v, v') f_0(v'), & l = 0, \\ n_0 v \sigma^{\text{EII}}(v) f_l(v), & l \geq 1, \end{cases} \quad (2.78)$$

where $B_0(v, v')$ is the zeroth-order Legendre decomposition of the momentum partition density, $B(\mathbf{v}, \mathbf{v}')$, which can be found from,

$$B_l(v, v') = 2\pi \int_{-1}^1 d(\cos \chi) B(\mathbf{v}, \mathbf{v}') P_l(\cos \chi). \quad (2.79)$$

It should be highlighted that for central scattering forces the partition function has the form $B(\mathbf{v}, \mathbf{v}') = B(v, v'; \hat{\mathbf{v}} \cdot \hat{\mathbf{v}}')$.

To our knowledge, a full kinetic theory collision operator for conservative PII has never been developed. Instead it has been treated as a standard excitation process in the existing literature [1, 31, 315, 343–345]. In this work the complete PII ionization operator is considered, a derivation of which is given in Chapter 6. To zero order in the mass ratio, m/m_0 , the collision operator for PII is given by,

$$J^{\text{PII}}(f) = n_0 v \sigma^{\text{PII}}(v) f(\mathbf{r}, \mathbf{v}, t) - n_0 \int d\mathbf{v}' v' \sigma^{\text{PII}}(v') B(\mathbf{v}, \mathbf{v}') f(\mathbf{r}, \mathbf{v}', t), \quad (2.80)$$

where σ^{PII} is the total conservative ionization cross section. The momentum partition density, $B(\mathbf{v}, \mathbf{v}')$, now has a slightly different definition, i.e. it represents probability of the (single) positron after ionization having a velocity in the range \mathbf{v} to $\mathbf{v} + d\mathbf{v}$, provided that the incident positron has

a velocity \mathbf{v}' . The differences between (2.77) and (2.80) is the factor of two in front of the integral term, which is a consequence of indistinguishability vs distinguishability for the two different processes, along with the definition of B . The specific form of the sharing of momentum between post-ionization particles, dictated by $B(\mathbf{v}, \mathbf{v}')$, has a significant influence on the swarm transport properties, especially for positron swarms.

The Legendre projections for the PII operator (derived in Chapter 6) are given by

$$J_l^{\text{PII}}(f_l) = \begin{cases} n_0 v \sigma^{\text{PII}}(v) f_0(v) - n_0 \int_0^\infty dv' v'^3 \sigma^{\text{PII}}(v') B_0(v, v') f_0(v'), & l = 0, \\ n_0 v \sigma^{\text{PII}}(v) f_l(v), & l \geq 1. \end{cases} \quad (2.81)$$

Re-writing (2.78) and (2.81) in terms of energy and ionization collision frequency,

$$J_l^{\text{EII}}(f_l) = \begin{cases} \nu^{\text{EII}}(U) f_0(U) - 2U^{-\frac{1}{2}} \int_0^\infty dU' U'^{\frac{1}{2}} \nu^{\text{EII}}(U') P(U, U') f_0(U'), & l = 0, \\ \nu^{\text{EII}}(U) f_l(U), & l \geq 1, \end{cases} \quad (2.82)$$

and

$$J_l^{\text{PII}}(f_l) = \begin{cases} \nu^{\text{PII}}(U) f_0(U) - U^{-\frac{1}{2}} \int_0^\infty dU' U'^{\frac{1}{2}} \nu^{\text{PII}}(U') P(U, U') f_0(U'), & l = 0, \\ \nu^{\text{PII}}(U) f_l(U), & l \geq 1, \end{cases} \quad (2.83)$$

where $P(U, U')$ is the energy-partitioning function, defined such that $P(U, U')dU$ represents the probability of the positron (or one of the two electrons in the case of EII) having an energy in the range $U + dU$ after ionization for an incident positron of energy U' . The energy-partitioning function has the following properties:

$$P(U, U') = 0 \quad \text{for } U' < U + U_1, \quad (2.84)$$

$$\int_0^{U' - U_1} P(U, U') dU = 1 \quad \text{for } U' \geq U + U_1, \quad (2.85)$$

where U_1 is the ionization threshold energy. The energy-sharing, which is determined by the energy-partitioning function P , is a major theme in the present work and the impact of different energy-partition models is highlighted in Chapter 6.

2.4 Transport properties and transport coefficients

2.4.1 Transport properties

In swarm experiments only a few macroscopic variables can be controlled and/or measured [50]. The particular experimental configurations are specified numerically purely through boundary conditions and initial conditions. Examples include the Time of Flight, Pulsed Townsend (PT) [50], Steady-State Townsend (SST) [346, 347], Cavalleri [348] and Annihilation Lifetime [101] experiments. The distribution function, f , contains all relevant information about the system, but is not an experimentally measurable quantity. Instead, the connection between kinetic theory and experiment is made via the continuity equation,

$$\frac{\partial}{\partial t} n(\mathbf{r}, t) + \nabla \cdot \Gamma(\mathbf{r}, t) = S(\mathbf{r}, t), \quad (2.86)$$

where n is the number density, Γ is the particle flux, and S represents a source or sink of particles. In the full non-hydrodynamic situation, the important measurable quantities, such as number density, flux and mean energy, are space-time dependent, and can be calculated via

$$n(\mathbf{r}, t) = \int d\mathbf{v} f(\mathbf{r}, \mathbf{v}, t), \quad (2.87)$$

$$\Gamma(\mathbf{r}, t) = \int d\mathbf{v} \mathbf{v} f(\mathbf{r}, \mathbf{v}, t), \quad (2.88)$$

$$\epsilon(\mathbf{r}, t) = \frac{1}{n(\mathbf{r}, t)} \int d\mathbf{v} \frac{1}{2} m v^2 f(\mathbf{r}, \mathbf{v}, t). \quad (2.89)$$

More discussion of the non-hydrodynamic transport properties is given in Chapter 8.

2.4.2 Transport coefficients

The continuity equation is not particularly useful in its exact form, equation (2.86). If the hydrodynamic regime applies, i.e., spatial gradients are weak and boundary conditions are negligible such that the space-time dependence of the distribution function can be projected onto the number density, then ‘transport coefficients’ can be identified as the coefficients of a density gradient expansion [263]. The bridge between theory and experiment is then the diffusion equation [349], which also identifies two types of transport coefficients, known as flux and bulk coefficients. Physically, the flux transport coefficients detail mean velocity and diffusion of the particles in the swarm, whereas the bulk transport coefficients are concerned with the spread about, and motion of, the swarm’s centre of mass. It is important to recognize the difference, as it is the bulk and not the flux transport coefficients which are generally measured and tabulated in the vast majority of swarm experiment literature [349]. When there are no non-conservative processes, the two sets of coefficients are identical, however in the presence of non-conservative processes the flux properties and bulk transport coefficients can differ by up to several orders of magnitude, and sometimes even exhibit completely different qualitative behaviour e.g. negative absolute mobility [350, 351] and negative differential conductivity [31, 352]. Following the convention of [269], this phenomena is referred to as the Tagashira-Sakai-Sakamoto (TSS) effect after the researchers who first recognized and investigated the differences between the two transport coefficients.

The transport coefficients [263, 271] that will be used extensively in this work, including mean energy, ϵ , bulk drift velocity, W , and the bulk transverse and longitudinal diffusion coefficients, D_T and D_L respectively, can be written using the operators defined in equations (2.27)–(2.28), i.e.,

$$\epsilon(t) = 2\pi \left(\frac{2}{m}\right)^{\frac{3}{2}} \int dU U^{\frac{3}{2}} F_0(U, t), \quad (2.90)$$

$$\begin{aligned} W(t) &= T_F(F_1(U, t)) - T_\alpha(F_0^{(L)}(U, t)), \\ &= W^{\text{flux}}(t) - T_\alpha(F_0^{(L)}(U, t)), \end{aligned} \quad (2.91)$$

$$\begin{aligned} D_T(t) &= T_F(F_1^{(T)}(U, t)) - T_\alpha\left(\frac{1}{\sqrt{3}}\left[F_0^{(2T)}(U, t) + \frac{1}{\sqrt{2}}F_0^{(2L)}(U, t)\right]\right), \\ &= D_T^{\text{flux}}(t) - T_\alpha\left(\frac{1}{\sqrt{3}}\left[F_0^{(2T)}(U, t) + \frac{1}{\sqrt{2}}F_0^{(2L)}(U, t)\right]\right), \end{aligned} \quad (2.92)$$

$$\begin{aligned} D_L(t) &= T_F(F_1^{(L)}(U, t)) - T_\alpha\left(\frac{1}{\sqrt{3}}\left[F_0^{(2T)}(U, t) - \sqrt{2}F_0^{(2L)}(U, t)\right]\right), \\ &= D_L^{\text{flux}}(t) - T_\alpha\left(\frac{1}{\sqrt{3}}\left[F_0^{(2T)}(U, t) - \sqrt{2}F_0^{(2L)}(U, t)\right]\right). \end{aligned} \quad (2.93)$$

The superscript ‘flux’ designates flux transport quantities, which differ from the bulk transport quantities on the left hand side of equations (2.91)–(2.93) when non-conservative processes are operative. Another useful quantity is the average collision rate, α , for a process with collision frequency ν , i.e.,

$$\alpha(t) = 2\pi \left(\frac{2}{m}\right)^{\frac{3}{2}} \int dU U^{\frac{1}{2}} \nu(U) F_0(U, t). \quad (2.94)$$

When ν describes non-conservative processes, α represents the rate of loss or gain of particles to the system. When ν is due purely to annihilation collisions ($\nu = \nu^{\text{ann}}$), then a connection can be made to the Z_{eff} parameter commonly reported in positron investigations [101],

$$Z_{\text{eff}}(t) = \frac{1}{\pi r_0^2 c n_0} \alpha^{\text{ann}}(t). \quad (2.95)$$

If the hydrodynamic regime is not applicable, then the space-time dependence of the distribution function cannot be projected onto the number density, and transport coefficients are not meaningful quantities. Instead, the kinetic properties of the swarm particles are space-time dependent, and must be calculated as such, as in (2.87)–(2.89).

2.5 Initial and boundary conditions

2.5.1 Initial energy distribution

To solve the time-dependent set of coupled equations (2.6), or the hierarchy (2.16)–(2.22), requires an initial condition, $f_l(r, v, 0)$, for all l . The Legendre polynomial coefficients can be determined from the source distribution function, $f(\mathbf{r}, \mathbf{v}, 0) = f^s(\mathbf{r}, \mathbf{v})$, by exploiting the orthogonality of Legendre polynomials [332],

$$f_l^s(r, v) = \left(\frac{2l+1}{2}\right) \int f^s(\mathbf{r}, \mathbf{v}) P_l(\mu) d\mu. \quad (2.96)$$

In positron experiments un-moderated positrons have a peak in their emission energy spectrum of around half an MeV, which then lose energy rapidly via collisions [101]. There is usually little information known about the initial source distribution in thermalization experiments. Three common initial distributions are:

1. An isotropic distribution constant in speed-space up to some cut-off value, $v_\infty = \sqrt{2U_\infty/m}$, i.e. $f_0(v) = \Theta(v_\infty - v) C$, where $\Theta(x)$ is the Heaviside step function and C is a normalization constant. The mean energy of this distribution function is given by the identity, $\epsilon = \frac{3}{5}U_\infty$.
2. An isotropic distribution constant in energy-space up to a cut-off value, U_∞ , i.e., $f_0(U) = \Theta(U_\infty - U) U^{-\frac{1}{2}} C$, where $\Theta(x)$ is the Heaviside step function and C is a normalization constant. The mean energy of this distribution function is given by the identity, $\epsilon = \frac{1}{2}U_\infty$.
3. A drifted Maxwellian distribution,

$$f_{\text{DM}}(\mathbf{v}) = n \left(\frac{m}{2\pi k_b T_i}\right)^{\frac{3}{2}} \exp\left[-\frac{m}{2k_b T_i} (\mathbf{v} - \mathbf{W}_i)^2\right], \quad (2.97)$$

with prescribed temperature and drift velocity parameters T_i and \mathbf{W}_i , respectively. The drifted Maxwellian is well known in equilibrium statistical mechanics, and is non-isotropic if \mathbf{W}_i is non-zero.

The first two source distributions were used by Campeanu and Humberston [12] in their investigations of helium, whereas the third is commonly employed by Li and co-workers when analysing spatial relaxation [278, 303]. We will utilize all three source distribution types throughout this thesis.

2.5.2 Boundary conditions

Appropriate boundary conditions in both configuration and energy space must be applied to uniquely specify the solution to Boltzmann's equation. Considering the Legendre-decomposed system (2.6), clearly there are $l_{\max} + 1$ configuration space conditions and also $l_{\max} + 1$ energy space conditions that need to be specified.

Winkler and collaborators [257, 353, 354] have analysed the multi-term, even-order approximation, and discovered that the general solution of the steady-state, spatially-homogeneous, hierarchy contains $\frac{1}{2}(l_{\max} + 1)$ non-singular and $\frac{1}{2}(l_{\max} + 1)$ singular fundamental solutions when U approaches infinity, and the physically relevant solution has to be sought within the non-singular space of solutions. They give the boundary conditions necessary for the determination of the non-singular physically relevant solution as

$$\begin{aligned} f_l(U = 0) &= 0 \quad \text{for odd } l, \\ f_l(U = U_\infty) &= 0 \quad \text{for even } l, \\ f_l(U > U_\infty) &= 0 \quad \text{for all } l, \end{aligned} \tag{2.98}$$

where U_∞ represents a sufficiently large energy. The configuration-space boundary conditions depend on the exact experimental setup being modelled, and a variety of setups exist [50, 101, 110, 164–167]. A detailed discussion is postponed until Chapter 8.

3

Numerical techniques

3.1 Introduction

In Chapter 2, a semi-analytic representation of Boltzmann's equation, (2.2), was derived via a Legendre polynomial expansion of the angular component of the velocity-space. Further progress can now be achieved computationally. In this chapter, the numerical methods and techniques employed to find solutions of the systems of equations we outline in (2.9) or (2.16)–(2.22) are detailed.

3.2 Operator splitting

The full Boltzmann equation, (2.2), is a very challenging numerical problem involving transport and collision contributions in energy, configuration and time dimensions. It has been noted [355] that the collision part of the Boltzmann equation is generally stiff, while the advection part is non-stiff, and that, ideally, one would like to be able to solve the two with tools specifically designed for the individual components. Operator splitting allows one to do just that. The basic idea behind operator splitting methods is to separate a complex problem into a series of simpler tasks, called split sub-problems. The sub-problems can be chosen to represent separate physical processes, to separate and reduce dimensions, to isolate more interesting regions of the domain, to deal with physical processes on different time scales, or simply for algebraic reasons. The splitting leads to a splitting error, which can be estimated theoretically. More detail on the splitting methods used is given in Chapter 8, and a good discussion on the basic studies can be found in [356].

It is convenient to employ operator splitting to separate the configuration-space dependence of the Boltzmann equation, i.e., the advection part, from the remaining spatially-homogeneous part:

$$\frac{\partial}{\partial t} f(\mathbf{r}, \mathbf{v}, t) + S_U(f(\mathbf{r}, \mathbf{v}, t)) + S_Z(f(\mathbf{r}, \mathbf{v}, t)) = 0, \quad (3.1)$$

where S_U and S_Z are the spatially-homogeneous and configuration-space advection operators respectively,

$$S_U(f(\mathbf{r}, \mathbf{v}, t)) = \mathbf{a} \cdot \frac{\partial}{\partial \mathbf{v}} f(\mathbf{r}, \mathbf{v}, t) + J(f(\mathbf{r}, \mathbf{v}, t)), \quad (3.2)$$

$$S_Z(f(\mathbf{r}, \mathbf{v}, t)) = \mathbf{v} \cdot \nabla f(\mathbf{r}, \mathbf{v}, t). \quad (3.3)$$

The remainder of this chapter (and Chapters 4–7) will focus specifically on the spatially-homogeneous or hydrodynamic parts of the Boltzmann equation. Chapter 8 will focus on the numerical techniques required for including the configuration-space dependence, which can be combined directly with the spatially homogeneous solution developed here via operator splitting.

3.3 Energy-space representation

To demonstrate the energy-space discretizations employed in subsequent chapters, the steady-state, spatially homogeneous Legendre decomposed Boltzmann equation, i.e.,

$$\mathcal{L}(f_l) = 0, \quad (3.4)$$

where

$$\mathcal{L}(f_l) = \left(\frac{2}{m}\right)^{\frac{1}{2}} \sum_{p=\pm 1} \Delta_l^{(p)} qE \left(U^{\frac{1}{2}} \frac{\partial}{\partial U} + p \frac{(l + \frac{3p+1}{2})}{2} U^{-\frac{1}{2}} \right) f_{l+p} + J_l(f_l), \quad (3.5)$$

is chosen as the prototypical example. In this section, a very flexible and general framework for the energy-space discretization is developed, with a focus on three particular numerical schemes: pseudo-spectral methods based on Chebyshev polynomials and Laguerre functions, and a finite difference scheme. Although many of the comments here also apply to the configuration-space discretization, a detailed discussion of configuration space is delayed until Chapter 8.

3.3.1 Local vs. global approximations

The simplest numerical schemes, such as finite difference (FD) schemes, are based on low-order, local approximations, i.e., using information from a small number of neighbouring points from where the solution is sought [357]. These are flexible methods that can be applied to irregular domains [358, 359], complicated boundary conditions [360], shock fronts and discontinuous regions [361, 362], especially when only low or moderate accuracy is desired. However, local methods offer limited accuracy and slow convergence, such that a very fine and computationally expensive grid may be required in order to accurately resolve a function. Most energy-space discretizations of the Boltzmann equation use local approximation methods.

Alternatively, instead of only using a few nearby points, one can use information from the entire computational domain. These are called global approximation methods and include spectral and pseudo-spectral schemes [363–365]. Global approximations are usually very high-order, and have excellent error convergence properties which, depending on the smoothness of the solution, demonstrate ‘exponential’ or ‘spectral’ convergence (as opposed to the algebraic convergence achievable by FD) [365]. Global algorithms suffer much greater losses in accuracy and efficiency than local alternatives when considering irregular domains or sharp variations, and are more costly per degree of freedom. However, in situations where global methods work well, savings up to several orders of magnitude in computational memory and time can be realized [365].

3.3.2 Pseudo-spectral method

There is some ambiguity of nomenclature in the literature; terms such as spectral, pseudo-spectral, collocation, discrete ordinate etc. are used and defined differently by various authors [195,366–370]. All methods that directly use information from the solution at discrete points, or ‘nodes’, are termed collocation schemes, and collocation schemes that employ global basis functions extending over the entire computational domain are termed pseudo-spectral. The pseudo-spectral approach appears to have been first used by Slater [371] and Kantorovic [372] in 1934 in specific applications, and was subsequently developed by many workers [363,373–375]. An excellent summary of the theory and applications of spectral methods, and the first to give a unifying mathematical assessment is presented by Gottlieb and Orszag [363]. Modern applications of the pseudo-spectral method to charged-particle transport belong almost entirely to Shizgal and co-workers [376–378], who employ the Discrete Ordinate (DO) method, which can be considered a pseudo-spectral method [370] based on Lagrange interpolation.

The different types of spectral methods, including pseudo-spectral methods, may be viewed as a class of discretization schemes known generically as the Method of Weighted Residuals (MWR) [379]. The key elements of the MWR are ‘trial functions’ and ‘test functions’. The trial functions are used as the basis functions for a truncated series expansion of the solution, while the test functions are used to ensure that the differential equation is satisfied as closely as possible by the truncated series expansion [364]. This is achieved by minimizing the residual, i.e., the error in the differential equation produced by using the truncated expansion instead of an exact solution, with respect to a suitable norm. The choices of test function, trial function, and method of minimizing the residual lead to the many different numerical methods e.g. finite volume [380], finite element [381], finite difference [382], Galerkin, Tau and pseudo-spectral [383].

In the pseudo-spectral approach, the test functions are translated Dirac delta functions centred at ‘collocation nodes’, and require that the system of equations be exactly satisfied at those points. To formalize this, let H be a differential or integral operator such that

$$Hf(x) = g(x), \quad (3.6)$$

then, in following the MWR, the desired function $f(x)$ is approximated by a finite sum of $N + 1$ trial functions, $T_n(x)$, i.e.,

$$f(x) \simeq f_N(x) = \sum_{n=0}^N a_n T_n(x), \quad (3.7)$$

where $f_N(x)$ represents the N^{th} -order approximation of $f(x)$, and a_n are the expansion coefficients. The residual, R , is defined by

$$R(x; a_0, a_1, \dots, a_N) \equiv Hf_N(x) - g(x). \quad (3.8)$$

If the T_n are global functions extending over the entire domain, then the pseudo-spectral solution is distinguished as the solution to a_n which forces R to zero at $N + 1$ specified collocation nodes.

Different choices of trial functions can fit interchangeably under the one framework. Applying the general pseudo-spectral method to (3.5) yields

$$\begin{aligned}
& \mathcal{L} \left(\sum_{n=0}^N a_n^l T_n(U) \right) \\
&= \left(\frac{2}{m} \right)^{\frac{1}{2}} \sum_{p=\pm 1} \Delta_l^{(p)} qE \left(U^{\frac{1}{2}} \frac{\partial}{\partial U} + p \frac{(l + \frac{3p+1}{2})}{2} U^{-\frac{1}{2}} \right) \sum_{n=0}^N a_n^{l+p} T_n(U) + J_l \left(\sum_{n=0}^N a_n^l T_n(U) \right), \\
&= \left(\frac{2}{m} \right)^{\frac{1}{2}} \sum_{n=0}^N \left[\sum_{p=\pm 1} \Delta_l^{(p)} qE \left(U^{\frac{1}{2}} \frac{\partial}{\partial U} T_n(U) + p \frac{(l + \frac{3p+1}{2})}{2} U^{-\frac{1}{2}} T_n(U) \right) a_n^{l+p} + J_l(T_n(U)) a_n^l \right],
\end{aligned} \tag{3.9}$$

where we have taken

$$f_l(U) \simeq \sum_{n=0}^N a_n^l T_n(U). \tag{3.10}$$

No assumption on the specific form of the trial function has yet been introduced, and any choice can now be inserted into equations (3.9)–(3.10). An appropriate choice of trial function has three general properties [383]: they are easy to compute; they are complete, i.e. the trial functions are sufficient to represent all functions in the class of solutions with arbitrarily high accuracy; and they are orthogonal with respect to some weight function. The relation (3.7) suggests that there is still a further choice to be made: whether to work with the collocation-point function values directly, or with the series coefficients. It has been found that the latter approach is more robust and flexible [384], easily allowing natural interpolation and extrapolation, node-manipulation, over- and under-collocation, etc.

Chebyshev polynomials

One of the most popular choices of trial functions for pseudo-spectral schemes are the Chebyshev polynomials [366]. Chebyshev polynomials are important in approximation theory because the roots of the Chebyshev polynomials of the first kind are useful in minimizing the problem of Runge’s phenomenon in polynomial interpolation [385]. Boyd [383] is particularly vocal about the virtues of a Chebyshev polynomial basis.

The Chebyshev polynomials of the first and second kind, $T(x)$ and $U(x)$, are the set of polynomials defined on the interval $[-1,1]$, by

$$T_n(x) = \cos(n \arccos(x)), \tag{3.11}$$

$$U_n(x) = \begin{cases} \frac{\sin((n+1) \arccos(x))}{\sin(\arccos(x))}, & -1 < x < 1, \\ (n+1)x^n, & x = \pm 1, \end{cases} \tag{3.12}$$

respectively [332]. The first few Chebyshev polynomials of the first kind are shown in Figure 3.1. The derivative of $T_n(x)$ can easily be computed from the relation

$$\frac{d}{dx} T_n(x) = n U_{n-1}(x), \tag{3.13}$$

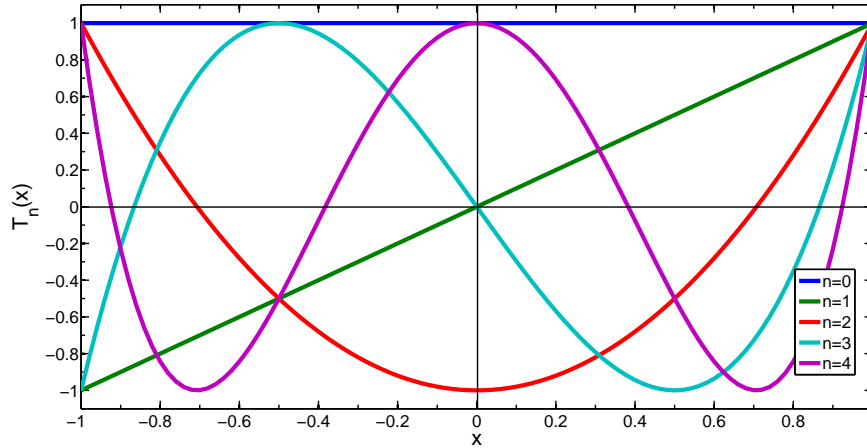


Figure 3.1: The first five Chebyshev polynomials of the first kind, (3.11), on the interval $-1 < x < 1$.

or by exploiting recurrence relations [332], such that

$$\frac{d}{dx}T_n(x) = n \begin{cases} 2 \sum_{\text{odd } j}^{n-1} T_j(x), & \text{when } n \text{ is even,} \\ \left(2 \sum_{\text{even } j}^{n-1} T_j(x) \right) - T_0(x), & \text{when } n \text{ is odd.} \end{cases} \quad (3.14)$$

It should be noted that the differentiation matrix resulting from either (3.13) or (3.14) is applied to the series coefficients, and is hence different from the more common differentiation matrices which are applied to the function values directly [366].

The roots of $T_n(x)$, x_k , are easy to compute,

$$x_k = \cos\left(\frac{\pi}{2n}(2k-1)\right), \quad k = 1, \dots, n. \quad (3.15)$$

The x_k in (3.15) are often simply called the ‘Chebyshev nodes’. It has long been known that to deal with Runge’s phenomenon, i.e., the problem of large, unwanted oscillations at the edges of an interval when using high-order polynomial interpolation, one must use sets of nodes that are clustered at the endpoints of the interval, with an asymptotic density proportional to $(1-x^2)^{-\frac{1}{2}}$ as $n \rightarrow \infty$ [386]. Chebyshev nodes represent the simplest such family of clustered point sets, obtained by projecting equally spaced points on the unit circle down to the unit interval $[-1, 1]$. It should be noted that, although the Chebyshev polynomials are naturally defined on $[-1, 1]$, transformations can be applied to map them onto a general interval $[a, b]$ including the infinite and semi-infinite intervals [383].

The energy-space boundary conditions (2.98) can be represented in term of the Chebyshev polynomials, i.e.,

$$\begin{aligned}
f_{l\text{ odd}}(U = 0) = 0 &\approx \sum_{n=0}^N a_n^l T_n(U = 0), \\
&= \sum_{n=0}^N a_n^l T_n(x = -1), \\
&= \sum_{n=0}^N a_n^l (-1)^n, \\
&= a_0^l - a_1^l + a_2^l - a_3^l + \cdots + (-1)^N a_N^l,
\end{aligned} \tag{3.16}$$

and

$$\begin{aligned}
f_{l\text{ even}}(U = U_\infty) = 0 &\approx \sum_{n=0}^N a_n^l T_n(U = U_\infty), \\
&= \sum_{n=0}^N a_n^l T_n(x = 1), \\
&= \sum_{n=0}^N a_n^l, \\
&= a_0^l + a_1^l + a_2^l + a_3^l + \cdots + a_N^l.
\end{aligned} \tag{3.17}$$

Laguerre functions

When the trial functions used in a pseudo-spectral method exhibit advantageous behaviour, such as satisfying homogeneous boundary conditions, the solution also exhibits this behaviour [383]. The Laguerre functions (not to be confused with Laguerre polynomials) are a natural choice of trial function for problems defined on the semi-infinite interval, $[0, \infty)$, since they exhibit behaviour desired in the solution of the velocity distribution, i.e., exponential decay of the functions and derivatives to zero asymptotically. Although Laguerre functions and polynomials are well known and often discussed [332, 387], they have a poor reputation and are seldom used in numerical approximation [384]. Shen [388] has attributed the previous disappointing results to the use of Laguerre polynomials rather than Laguerre functions, which are not suitable for practical computations due to the extremely ill-conditioned behaviour of Laguerre polynomials and associated quadrature.

The Laguerre polynomials, $L_n(x)$, are the set of polynomials defined on $[0, \infty)$ which can be computed from the recurrence relations [332],

$$L_0(x) = 1, \tag{3.18}$$

$$L_1(x) = -x + 1, \tag{3.19}$$

$$(n + 1) L_{n+1}(x) = (-x + (2n + 1)) L_n(x) - n L_{n-1}(x). \tag{3.20}$$

The Laguerre polynomials are orthogonal with respect to the weight $\exp(-x)$, such that one can then construct the Laguerre functions, $T_n(x)$, which are simply the Laguerre polynomials rescaled by $\exp(-x/2)$, i.e.,

$$T_n(x) = e^{-x/2} L_n(x), \tag{3.21}$$

and are thus orthonormal. The first few Laguerre polynomials and Laguerre functions are shown in Figures 3.2 and 3.3.

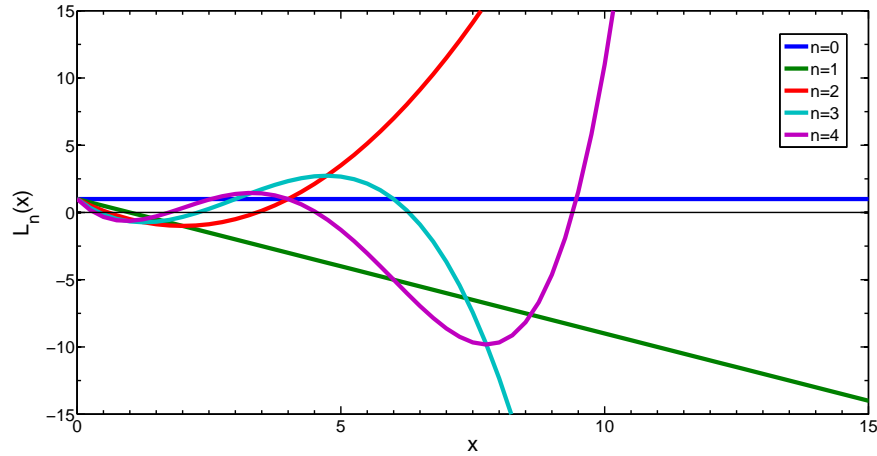


Figure 3.2: The first five Laguerre polynomials, (3.18)-(3.20), on the interval $0 < x < 15$.

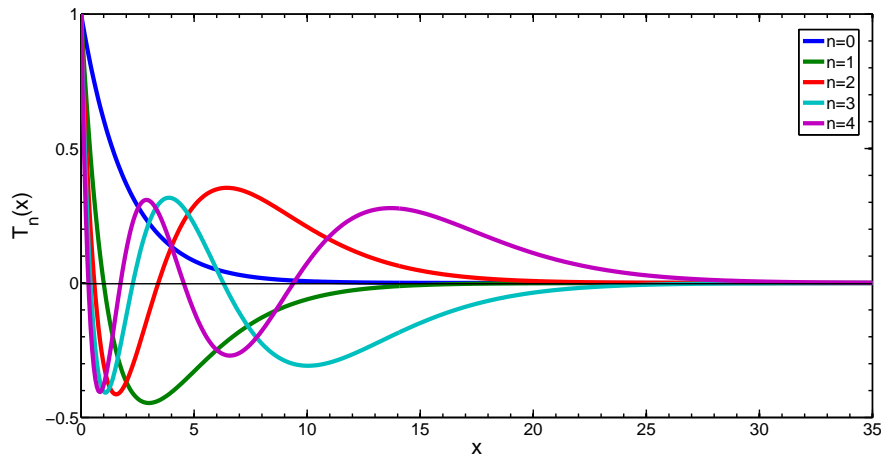


Figure 3.3: The first five Laguerre functions, (3.21), on the interval $0 < x < 35$.

The derivative of the Laguerre functions can easily be computed from [384],

$$\frac{d}{dx}T_n(x) = - \begin{cases} \frac{1}{2}T_0(x), & n = 0, \\ \sum_{j=0}^{n-1} T_j(x) + \frac{1}{2}T_n(x), & n \geq 1. \end{cases} \quad (3.22)$$

The semi-infinite interval can be mapped onto itself, leading to a free scaling parameter k which can be varied to optimize computations. Scaled Laguerre functions, $\tilde{T}_n(x)$, can be defined by

$$\tilde{T}_n(x) \equiv \tilde{T}_n(x; k) = T_n(kx), \quad (3.23)$$

which are orthogonal but not orthonormal. Usually asymptotic boundary conditions need to be enforced explicitly, however by choosing Laguerre functions they are enforced implicitly.

The collocation points for an n th-order Laguerre function series expansion are the same as the standard choice for a Laguerre polynomial series expansion [384], i.e.,

$$\begin{aligned} x_0 &= 0, \\ \left. \frac{d}{dx} L_{n+1}(x) \right|_{x_i} &= 0, \quad 1 < i < n. \end{aligned} \quad (3.24)$$

The collocation points are clustered quadratically near $x = 0$. This is the same quadratic clustering that occurs in Chebyshev and Legendre pseudo-spectral schemes, which provides numerical stability by suppressing Runge's phenomenon [389].

The energy-space boundary conditions (2.98) can be represented in term of the Laguerre functions, i.e.,

$$f_{l \text{ odd}}(U = 0) = 0 \approx \sum_{n=0}^N a_n^l T_n(U = 0), \quad (3.25)$$

$$= \sum_{n=0}^N a_n^l T_n(x = 0), \quad (3.26)$$

$$= \sum_{n=0}^N a_n^l, \quad (3.27)$$

$$= a_0^l + a_1^l + a_2^l + a_3^l + \cdots + a_N^l, \quad (3.28)$$

and

$$f_{l \text{ even}}(U = U_\infty) = 0 \approx \sum_{n=0}^N a_n^l T_n(U = U_\infty). \quad (3.29)$$

Collocation nodes

The pseudo-spectral and finite difference methods are examples of collocation methods, which require information from a set of collocation nodes to discretize a system of differential and integral equations. Collocation of a single term of equations (3.9)–(3.10) at the point U_m , leads to the following:

$$\mathcal{L}(T_{mn}) a_n^l = \left(\frac{2}{m}\right)^{\frac{1}{2}} \left[\sum_{p=\pm 1} \Delta_l^{(p)} qE \left(U_m^{\frac{1}{2}} D_{mn} + p \frac{(l + \frac{3p+1}{2})}{2} U^{-\frac{1}{2}} T_{mn} \right) a_n^{l+p} + J_l(T_{mn}) a_n^l \right], \quad (3.30)$$

where

$$T_{mn} = T_n(U_m), \quad (3.31)$$

$$D_{mn} = \left. \frac{\partial}{\partial U} T_n(U) \right|_{U_m}. \quad (3.32)$$

The system (3.30) can easily be represented numerically as a matrix.

For an N th-order approximation, $N + 1$ pieces of information are required from the collocation nodes in conjunction with the boundary conditions or constraints. At first glance it would appear that the choice of collocation points is arbitrary, however there is a close relation between the best choice of collocation nodes and the trial functions employed. In effect, the collocation nodes are

tied to quadrature rules for the orthogonality of the trial functions. Boyd [383] suggests that as a rule of thumb, the collocation nodes should be the roots of the first discarded basis function. However, there is some flexibility, e.g., sometimes we wish to include the location of boundary conditions.

A summary of the two pseudo-spectral schemes investigated in this work is as follows:

Chebyshev polynomials The Chebyshev polynomials basis functions and derivatives, (3.11)–(3.14), are collocated at standard Chebyshev nodes, (3.15), supplemented with the boundary conditions (3.16)–(3.17).

Laguerre functions The Laguerre function basis functions and derivatives, (3.18)–(3.22), are collocated at standard Laguerre polynomial nodes, (3.24), supplemented with the boundary conditions (3.25)–(3.29).

3.3.3 Finite difference method

The finite difference (FD) method [390] is a local approximation method in contrast to the pseudo-spectral methods described in the previous subsection. However, FD can be written in a way consistent with the pseudo-spectral schemes, and hence all three methods are treated interchangeably within the same framework. FD approximates derivatives by combining nearby function values using a set of weights. They are widely used, simple to program, and lead to sparse matrices with band structures approximating derivatives [357].

Following the work of Winkler and collaborators [257, 353, 354], the system of ODEs (3.5) is discretized at centred points using Centred Difference, i.e.,

$$\left. \frac{df(U, t)}{dx} \right|_{U_{i+1/2}} = \frac{f(U_{i+1}, t) - f(U_i, t)}{U_{i+1} - U_i}, \quad (3.33)$$

$$f(U_{i+1/2}, t) = \frac{f(U_{i+1}) + f(U_i)}{2}, \quad (3.34)$$

so that equation (3.5) evaluated at $i + 1/2$ becomes,

$$\begin{aligned} \mathcal{L}f|_{i+1/2} = J_l(f)|_{i+1/2} + \left(\frac{2}{m}\right)^{\frac{1}{2}} \sum_{p=\pm 1} \Delta_l^{(p)} qE \left[U_{i+1/2}^{\frac{1}{2}} \left(\frac{f_{l+p}(U_{i+1}) - f_{l+p}(U_i)}{U_{i+1} - U_i} \right) \right. \\ \left. + p \frac{\left(l + \frac{3p+1}{2}\right)}{2} U_{i+1/2}^{-\frac{1}{2}} \left(\frac{f_{l+p}(U_{i+1}) + f_{l+p}(U_i)}{2} \right) \right], \quad (3.35) \end{aligned}$$

for $i = 0, 1, \dots, N-1$. Although a general form can be constructed for an arbitrary grid, the simplest case is for evenly spaced points, i.e.,

$$U_i = i\Delta U \quad \text{for} \quad 0 \leq i \leq N, \quad (3.36)$$

where ΔU is a constant. The centred difference scheme is not biased in either direction as is the case for the forward and backward first-order FD schemes.

Equations (3.33) and (3.34) can be written in matrix form,

$$\begin{bmatrix} f_{1/2} \\ f_{1+1/2} \\ \vdots \\ f_{N-1/2} \end{bmatrix} = \frac{1}{2} \begin{bmatrix} 1 & 1 & & & \\ & 1 & 1 & & \\ & & \ddots & \ddots & \\ & & & 1 & 1 \end{bmatrix} \begin{bmatrix} f_0 \\ f_1 \\ \vdots \\ f_{N-1} \\ f_N \end{bmatrix}, \quad (3.37)$$

$$\mathbf{f}^c = \mathbf{T}\mathbf{f}^s, \quad (3.38)$$

and

$$\frac{d}{dU} \begin{bmatrix} f_{1/2} \\ f_{1+1/2} \\ \vdots \\ f_{N-1/2} \end{bmatrix} = \frac{1}{\Delta U} \begin{bmatrix} -1 & 1 & & & \\ & 1 & -1 & & \\ & & \ddots & \ddots & \\ & & & 1 & -1 \end{bmatrix} \begin{bmatrix} f_0 \\ f_1 \\ \vdots \\ f_{N-1} \\ f_N \end{bmatrix}, \quad (3.39)$$

$$\frac{d}{dU}\mathbf{f}^c = \mathbf{D}\mathbf{f}^s, \quad (3.40)$$

where $[f]_i = f(U_i)$, the superscripts c and s refer to the interval midpoint and endpoint nodes respectively, ΔU is the constant interval spacing, and

$$\mathbf{T} = \frac{1}{2} \begin{bmatrix} 1 & 1 & & & \\ & 1 & 1 & & \\ & & \ddots & \ddots & \\ & & & 1 & 1 \end{bmatrix}, \quad (3.41)$$

$$\mathbf{D} = \frac{1}{\Delta U} \begin{bmatrix} -1 & 1 & & & \\ & 1 & -1 & & \\ & & \ddots & \ddots & \\ & & & 1 & -1 \end{bmatrix}. \quad (3.42)$$

Discretising at the centre between two solution nodes results in a system of linear equations that is under-determined, however the extra information is naturally provided by boundary conditions which are appended. The boundary conditions (2.98) here are simply,

$$\begin{aligned} f_{l\text{odd}}(U = 0) &= 0, \\ &= f_{l\text{odd}}(U_0), \end{aligned} \quad (3.43)$$

and

$$\begin{aligned} f_{l\text{even}}(U = U_\infty) &= 0, \\ &= f_{l\text{even}}(U_N). \end{aligned} \quad (3.44)$$

It is important to note that the system (3.35) is not collocated explicitly at $U = 0$, and thereby avoids problems that can arise regarding the cross sections and collision frequencies in this limit. For example, in the two-term approximation with only elastic processes operative, (3.4) yields a

relation between $\frac{\partial}{\partial U} f_0$ and f_1 , i.e.,

$$f_1 = -\frac{qE}{m} \frac{U^{\frac{1}{2}}}{\nu_m} \frac{\partial}{\partial U} f_0, \quad (3.45)$$

which is divergent if $\nu_m \rightarrow 0$ faster than $U^{\frac{1}{2}}$. Even in situations where $U^{\frac{1}{2}} \rightarrow 0$ faster than ν_m , equation (3.45) is difficult to properly represent numerically in its current form. Thankfully these problems are sidestepped by the centred collocation scheme, and direct implementation of the boundary conditions at $U = 0$ for odd l .

3.3.4 Representation of cross sections

The cross section sets which serve as inputs into the Boltzmann equation solver are often tabulated from experimental or theoretical investigations. To get a representation of inputs on the computational mesh, interpolation is required. Different methods of interpolation include linear interpolation, cubic splines, Chebyshev polynomials, Laguerre functions etc., and can be applied to either the cross sections directly or collision frequencies with respect to energy or speed. This choice of interpolation method can lead to significant differences in the calculated distributions and velocity moments when the input mesh is too sparse, particularly in situations where there is limited available data in a given energy regime (see Section 5.2.2). We have chosen to work with the collision frequency as a function of energy, which is a natural input for the collision operators, rather than the cross sections directly. Of course, when the input cross sections or collision frequencies have an analytic form, the problem of interpolation is avoided.

3.3.5 Representation of collision operators and h_l

Here we detail special considerations which must be made to the representation of the collision operators and non-zero h_l elements of the higher order hydrodynamic equations.

Elastic

The form of the elastic collision operator we consider is given in equation (2.63). For a cold gas ($T_0 = 0$ K), applying the pseudo-spectral representation, the elastic operator becomes,

$$J_l^{\text{el}}(T_{mn}) a_n^l = \begin{cases} -\frac{2m}{m_0} U_m^{\frac{1}{2}} \left(\sum_{k=0}^N D_{mk} b_k \right) a_n^l, & l = 0, \\ \tilde{\nu}_l^{\text{el}}(U_m) T_{mn} a_n^l, & l \geq 1, \end{cases} \quad (3.46)$$

where $T_{mn} = T_n(U_m)$, and

$$\sum_{k=0}^N T_k(U_m) b_k = U_m^{\frac{3}{2}} \nu_1^{\text{el}}(U_m) T_n(U_m), \quad (3.47)$$

$$D_{mk} = \left. \frac{d}{dU} T_k(U) \right|_{U_m}. \quad (3.48)$$

To apply the pseudo-spectral differentiation operator, it is necessary to have a representation of the full target for differentiation (i.e., $U^{\frac{3}{2}} \nu_1^{\text{el}} T_n$) in terms of the basis functions, which is described by equations (3.47)–(3.48).

Similarly, employing the finite difference representation (3.33)–(3.34), yields,

$$J_l^{\text{el}}(f_l)|_{i+1/2} = \begin{cases} -\frac{2m}{m_0} U_{i+1/2}^{-\frac{1}{2}} \frac{\left(U_{i+1}^{\frac{3}{2}} \nu_1^{\text{el}}(U_{i+1}) f_0(U_{i+1}) - U_i^{\frac{3}{2}} \nu_1^{\text{el}}(U_i) f_0(U_i) \right)}{(U_{i+1} - U_i)}, & l = 0, \\ \tilde{\nu}_l^{\text{el}}(U_{i+1/2}) \frac{f_l(U_{i+1}) + f_l(U_i)}{2}, & l \geq 1, \end{cases} \quad (3.49)$$

for $i = 0, 1, \dots, N - 1$. An extra difficulty arises when considering the extension to non-zero temperatures, equation (2.63), which now involves a second derivative term. In this work, only the finite difference operator is used for these types of problems, though the extension for pseudo-spectral is straightforward. A 4-point stencil (3-point on the edges) is required to construct a symmetric second order derivative, i.e.,

$$\frac{d^2 f(U)}{dU^2} \Big|_{U_{i+1/2}} = \frac{1}{(\Delta U)^2} \begin{cases} f(U_0) - 2f(U_1) - f(U_2), & i = 0, \\ \frac{1}{2} [f(U_{i+2}) - f(U_{i+1}) - f(U_i) + f(U_{i-1})], & 0 < i < N - 1, \\ f(U_{N-2}) - 2f(U_{N-1}) - f(U_N), & i = N - 1, \end{cases} \quad (3.50)$$

where for this form it has been assumed that the energy grid is evenly spaced with $\Delta U = U_{i+1} - U_i$.

Attachment, annihilation and positronium formation

The representation of the collision operator for simple loss processes, equation (2.76), is straightforward for both pseudo-spectral and finite difference schemes, i.e.,

$$J_l^{\text{loss}}(T_{nm}) a_n^l = \nu^{\text{loss}}(U_m) T_{mn} a_n^l, \quad (3.51)$$

and

$$J_l^{\text{loss}}(f_l)|_{U_{i+1/2}} = \nu^{\text{loss}}(U_{i+1/2}) \frac{f_l(U_{i+1}) + f_l(U_i)}{2}, \quad (3.52)$$

respectively.

Excitation

The Frost-Phelps form of the excitation collision operator is given in equation (2.67). The unique aspect of this operator is the discrete energy shifts corresponding to excitation and de-excitation terms. The cross sections are not a problem, as they can be interpolated in the usual way on the input mesh. The difficulty is in treating the shift of the f_0 , which needs to be represented in terms of the solution nodes. To stay consistent with the overall scheme, a linear interpolation with respect to the two nearest solution nodes is performed. For example, the excitation operator for a cold gas (so that no de-excitation processes are available) with a single excitation channel with threshold energy of U_1 can be represented (in a slightly different form from equation (2.67)) as

$$J_l^{\text{exc}}(U_{i+1/2}) = \nu^{\text{exc}}(U_{i+1/2}) \frac{f_l(U_{i+1}) + f_l(U_i)}{2} - \begin{cases} \left(\frac{U_{i+1/2} + U_1}{U_{i+1/2}} \right)^{1/2} \nu^{\text{exc}}(U_{i+1/2} + U_1) f_0(U_{i+1/2} + U_1), & l = 0, \\ 0, & l \geq 1, \end{cases} \quad (3.53)$$

where

$$f_0(U_{i+1/2} + U_I) = \begin{cases} wf_0(U_m) + (1-w)f_0(U_{m+1}), & U_{i+1/2} + U_I \leq U_\infty, \\ 0, & U_{i+1/2} + U_I > U_\infty, \end{cases} \quad (3.54)$$

where m and $m+1$ are the indices of the energy mesh nodes straddling $U_{i+1/2} + U_I$, and $w = (U_{i+1/2} + U_I - U_m) / (U_{m+1} - U_m)$. Since $f_0(U > U_\infty) = 0$, no extrapolation is required.

Ionization

The ionization operator for EII is given in equation (2.82). The comments here apply equally to PII collision operator. The integral term of equation (2.82) includes the distribution function, which then makes the Boltzmann equation non-linear. However, if we choose to represent the integral numerically with a linear quadrature method, i.e., as a weighted sum, then solving for the distribution function again becomes a linear problem. For evenly spaced nodes, Simpson's rule is chosen for the numerical integration. The integral term in equation (2.82) is represented as,

$$\int_0^\infty dU' U'^{\frac{1}{2}} \nu^{\text{EII}}(U') P(U_{i+1/2}, U') f_0(U') = \sum_{m=0}^N w_m U_m^{\frac{1}{2}} \nu^{\text{EII}}(U_m) P(U_{i+1/2}, U_m) f_0(U_m), \quad (3.55)$$

where according to Simpson's rule [390]

$$w_m = \frac{\Delta U}{3} \begin{cases} 1, & m = 0, \\ 4, & m \text{ odd}, \\ 2, & m \text{ even}, \\ 1, & m = N, \end{cases} \quad (3.56)$$

So that finally,

$$J_l^{\text{EII}}(f(U_{i+1/2})) = \nu^{\text{EII}}(U_{i+1/2}) \frac{f_l(U_{i+1}) + f_l(U_i)}{2} - \begin{cases} 2U_{i+1/2}^{-\frac{1}{2}} \sum_{m=0}^N w_m U_m^{\frac{1}{2}} \nu^{\text{ion}}(U_m) P(U_{i+1/2}, U_m) f_0(U_m), & l = 0, \\ 0, & l \geq 1. \end{cases} \quad (3.57)$$

Higher order hydrodynamic terms

The higher order hydrodynamic equations, (2.16)–(2.26), involve non-zero h_l terms. When non-conservative processes are included such that $J_0^{\text{NC}} \neq 0$, then the ω terms given in (2.23)–(2.26) involve the target distribution function coefficient encased in an integral with respect to energy. Similar to the case of the ionization operator considered above, this non-linear problem becomes linear when the integral is represented as a weighted sum with Simpson's rule. For example,

consider ω_0 from equations (2.23) and (2.28):

$$\begin{aligned}\omega_0 &= -2\pi \left(\frac{2}{m}\right)^{\frac{3}{2}} \int_0^\infty dU U^{\frac{1}{2}} J_0^{\text{NC}}(F_0(U_m)) , \\ &\approx -2\pi \left(\frac{2}{m}\right)^{\frac{3}{2}} \sum_{m=0}^N w_m U_m^{\frac{1}{2}} J_0^{\text{NC}}(F_0(U_m)) , \\ &= -2\pi \left(\frac{2}{m}\right)^{\frac{3}{2}} \sum_{m=0}^N w_m U_m^{\frac{1}{2}} \nu^{\text{NC}}(U_m) F_0(U_m) ,\end{aligned}\tag{3.58}$$

where the w_m are again given by Simpson's rule (3.56). In the same way, the quantities ω_1 , ω_2 and ω_3 can be linearized with respect to $F_0^{(\text{L})}$, $F_0^{(2\text{T})}$ and $F_0^{(2\text{L})}$.

Energy-space truncation

For the numerical simulations, an appropriate energy-space truncation must be chosen, which is not known *a priori*. In general practice, a truncation energy, U_∞ , is chosen such that the ratio $f_0(U_\infty)/\max[f_0(U)]$ is at least 10^{-10} [259].

3.4 Temporal representation

We now turn our discussion to the temporal dependence of the Boltzmann equation. To do so, we consider the prototypical example,

$$\frac{\partial}{\partial t} f_l + \mathcal{L}(f_l) = 0 ,\tag{3.59}$$

where \mathcal{L} is still defined as in (3.4).

3.4.1 Asymptotic time behaviour

We are often interested in the asymptotic time behaviour of the phase-space distribution and the macroscopic transport coefficients, hence a method of solving for this state directly rather than following a full, computationally expensive, temporal relaxation is advantageous. When non-particle-conserving processes are operative, such as annihilation, a steady-state can exist in the sense that the macroscopic transport averages (but not the phase-space distribution function), such as mean energy, drift velocity, Z_{eff} etc., remain unchanged in time [34, 303]. Both the conservative and non-conservative situations can be treated using the same formalism, which extracts the asymptotic time-dependence of the distribution function through an eigenvalue expansion. The usual approach is to represent the time-dependence as a sum of exponentials [16, 391], i.e.,

$$f_l(U, t) = F_l(U)\tau(t) ,\tag{3.60}$$

where $\tau(t)$ is an eigenfunction satisfying the eigenvalue equation,

$$\frac{d}{dt}\tau(t) = \alpha\tau(t) ,\tag{3.61}$$

and hence the prototypical problem (3.59) becomes,

$$\alpha F_l(U) + \mathcal{L}(F_l(U)) = 0 .\tag{3.62}$$

The α are assumed to form a discrete set [16, 391], i.e., $\alpha \rightarrow \alpha_n$, $n = 1, 2, \dots$, and that only exponentially decaying solutions are physically realistic, such that in the asymptotic limit only the eigenfunction corresponding to $\alpha_* = \min(|\Re(\alpha_n)| \leq 0)$ survives. When only conservative processes are operative, a steady-state exists for both the distribution function and transport coefficients, and α_* will be 0 (or numerically close to 0). When non-conservative processes are operative the asymptotic solution yields an $\alpha_* \neq 0$, and only the transport coefficients have steady-state values. It can be demonstrated that the surviving eigenvalue, α_* , is equivalent to the average total non-conservative collision frequency;

$$\begin{aligned} \int [\alpha_* F + \mathcal{L}F] d\mathbf{v} &= 0, \\ &= 2\pi \left(\frac{2}{m}\right)^{\frac{3}{2}} \left[\alpha_* \int dU U^{\frac{1}{2}} F_0 + \int dU U^{\frac{1}{2}} J^{\text{NC}}(F_0) \right], \\ &= 2\pi \left(\frac{2}{m}\right)^{\frac{3}{2}} \left[\alpha_* + \int dU U^{\frac{1}{2}} \nu^{\text{NC}}(U) F_0 \right], \end{aligned} \quad (3.63)$$

where the normalization of F_0 and particle-conserving nature of the other collision and convective components of equation (2.9) have been invoked. It follows from equations (2.23), (2.28) and (3.63) that $\alpha_* = - \int dU U^{\frac{1}{2}} \nu^{\text{NC}}(U) F_0 = \frac{1}{2\pi} \left(\frac{2}{m}\right)^{-\frac{3}{2}} \omega_0$.

There are numerous numerical techniques for solving generalized eigenvalue problems [392–394]. Two different types of ‘spurious’ eigenvalues can arise from generalized eigenproblems, numerically spurious and physically spurious [365]. A numerically spurious eigenvalue is a poor approximation to an exact eigenvalue, i.e., an eigenvalue belonging to a mode that is under-resolved by N degrees of freedom. A given numerically spurious eigenvalue can be computed accurately by using sufficiently large N . Physically spurious eigenvalues arise from the inappropriate application of boundary conditions or other misrepresentation of the physics. One common cause is the use of algebraic constraints to analytically reduce a system of equations before being approximated numerically [365]. Physically spurious eigenvalues cannot be overcome by simply increasing the degrees of freedom. The question remaining is how to include boundary conditions consistently in equation (3.62). Rather than using special spectral methods to avoid or filter problematic eigenmodes [363, 395], we can avoid physically spurious eigenvalues by using the ‘descriptor’ framework [396, 397] for including boundary conditions. The descriptor framework is posed as a generalized eigenvalue problem that explicitly retains algebraic constraints in the computation of the eigenvalues. Once discretized in energy-space, as described in Section 3.3, equation (3.62) becomes a generalized eigenvalue matrix equation of the form,

$$\alpha \mathbf{f} + \mathbf{L} \mathbf{f} = 0, \quad (3.64)$$

where \mathbf{L} is the matrix representing the discretization of the \mathcal{L} operator. Boundary conditions can also be represented in matrix form, i.e.,

$$\mathbf{G} \mathbf{f} = \mathbf{0}. \quad (3.65)$$

The descriptor framework invokes the construction of the new generalized eigenvalue problem,

$$\alpha \overline{\mathbf{M}} \mathbf{f} + \overline{\mathbf{L}} \mathbf{f} = \mathbf{0}, \quad (3.66)$$

where

$$\bar{\mathbf{M}} = \begin{bmatrix} \mathbf{G} \\ \mathbf{I} \end{bmatrix}, \quad \bar{\mathbf{L}} = \begin{bmatrix} \mathbf{0} \\ \mathbf{L} \end{bmatrix}, \quad (3.67)$$

and \mathbf{I} is the identity matrix. This is a natural way to include boundary conditions with the added benefit of avoiding physically spurious eigenvalues.

3.4.2 Temporal discretization

The discretization of the energy-space (and later, configuration-space) of equation (2.9) leads to a coupled system of ODEs. This is the philosophy behind the widely used and well established Method of Lines (MOL) [398–402]. The system of ODE's corresponding to the prototypical problem (3.59) can be written in matrix form as

$$\mathbf{M} \frac{d}{dt} \mathbf{f} + \mathbf{L} \mathbf{f} = \mathbf{0}, \quad (3.68)$$

where \mathbf{L} and \mathbf{M} are matrices resulting from the discretization process, commonly known as the ‘stiffness matrix’ and ‘mass matrix’ respectively [402]. Clearly, equation (3.66) is the equivalent of equation (3.68) in the time-asymptotic limit. The MOL formalism allows easy implementation of linear boundary conditions or constraints via the mass matrix. If the discretized boundary conditions and constraints of (3.68) are represented by $\mathbf{G} \mathbf{f} = \mathbf{0}$, where \mathbf{G} is a coefficient matrix and $\mathbf{0}$ is a vector of zeros, then $\frac{d}{dt} \mathbf{G} \mathbf{f} = \mathbf{G} \frac{d}{dt} \mathbf{f} = \mathbf{0}$. Provided the initial solution satisfies the constraints then,

$$\bar{\mathbf{M}} \frac{d}{dt} \mathbf{f} = \bar{\mathbf{L}} \mathbf{f}, \quad (3.69)$$

where $\bar{\mathbf{M}}$ and $\bar{\mathbf{L}}$ are the modified mass and stiffness matrices,

$$\bar{\mathbf{M}} = \begin{bmatrix} \mathbf{G} \\ \mathbf{M} \end{bmatrix}, \quad \bar{\mathbf{L}} = \begin{bmatrix} \mathbf{0} \\ \mathbf{L} \end{bmatrix}. \quad (3.70)$$

The system (3.69) is too large and, in general, complicated to solve analytically, and so one is eventually forced to discretize the time variable as well. The temporal evolution is achieved using a first-order implicit Euler method [403], i.e.,

$$\bar{\mathbf{M}} \frac{\mathbf{f}(t_{n+1}) - \mathbf{f}(t_n)}{t_{n+1} - t_n} + \bar{\mathbf{L}} \mathbf{f}(t_{n+1}) = \mathbf{0}, \quad (3.71)$$

or equivalently

$$\left(\frac{\bar{\mathbf{M}}}{t_{n+1} - t_n} + \bar{\mathbf{L}} \right) \mathbf{f}(t_{n+1}) = \frac{\bar{\mathbf{M}}}{t_{n+1} - t_n} \mathbf{f}(t_n), \quad (3.72)$$

where t^n and t^{n+1} are successive times. The first-order implicit Euler method has been chosen for its good stability properties.

When considering the spatially-inhomogeneous situation, the time discretization is coupled with the configuration space discretization to satisfy conditions for numerical stability and conservation (see Chapter 8).

3.4.3 Temporally-adaptive energy mesh

In many applications, a high-energy source of charged particles must be followed as they relax, often through many orders of magnitude of energy, to eventual thermalization. In order to provide appropriate energy-space resolution of the distribution function over the full relaxation, a simple ‘adaptive’ energy-space mesh has been developed. Assuming that the source distribution requires a higher energy truncation than the thermalized distribution, then the distribution at time t is interpolated onto a new energy mesh with a maximum value of U_* whenever

$$U_*/U_\infty \leq 3/4, \quad (3.73)$$

where U_∞ is the current truncation value and U_* is determined from

$$f_0(U = U_*) / \max[f_0(U)] = 10^{-10}. \quad (3.74)$$

It has been found that these parameter choices provide a good balance between accurately representing the distribution function components and minimizing the accumulation of interpolating errors.

4

Hydrodynamic benchmark systems

This chapter contains material that has been published in the following journal articles:

[7] G. J. Boyle, W. J. Tattersall, D. G. Cocks, S. Dujko and R. D. White. Kinetic theory of positron-impact ionization in gases. *Physical Review A*, **91**, 052710 (2015).

doi:10.1103/PhysRevA.91.052710.

[9] W. J. Tattersall, D. G. Cocks, G. J. Boyle, S. J. Buckman and R. D. White. Monte Carlo study of coherent scattering effects of low-energy charged particle transport in Percus-Yevick liquids. *Physical Review E*, **91**, 043304 (2015). doi:10.1103/PhysRevE.91.043304

This chapter includes Monte Carlo calculations performed by W. J. Tattersall for the model hard-sphere system. All other work described in this chapter is my own.

4.1 Introduction

The theory developed in Chapter 2 and numerical techniques described in Chapter 3 for the solution of the Boltzmann equation in the hydrodynamic regime, (2.16)–(2.22), is applied to a series of model systems. The purpose of this chapter is to systematically benchmark the theory and associated computational code for each of the collisional processes required in a full description of positron/electron transport, and to compare against previous kinetic theory calculations and independent Monte Carlo simulations where possible. The validation of space-dependent non-hydrodynamic transport is postponed until Chapter 8. It is to be emphasized that more realistic cross section sets can (and will in later chapters) be employed for real world systems using the same code. The simple and analytic form of the model cross sections employed here are particularly useful for isolating the individual processes and physical phenomena which may be obscured in real systems by the presence of multiple interaction processes. In Section 4.6 a benchmark model for a system of hard spheres with a structure described by the Percus-Yevick model is considered. The Percus-Yevick structure factor is analytic and has free parameters which can be adjusted to emulate specific real liquids. Also presented in this chapter are convergence testing results for

computational parameters including energy-space truncation, U_∞ , number of collocation nodes, N , and the Legendre polynomial series expansion truncation, l_{\max} .

4.2 Elastic collisions

4.2.1 Constant elastic collision frequency

The first interaction model considered is of the form

$$\begin{aligned}\sigma_m &= 5U^{-\frac{1}{2}} \text{ \AA}^2, \\ m_0 &= 4 \text{ amu}, \\ E/n_0 &= 1 \text{ Td},\end{aligned}\tag{4.1}$$

where U is in units of eV. For this particular power law, known as the ‘Maxwell model’, the momentum transfer collision frequency, $\nu_m = n_0 \sqrt{\frac{2U}{m}} \sigma_m(U)$, is a constant. As such, the Boltzmann equation is solvable analytically for both cold gases and gases with a non-zero temperature. The transport coefficients for a constant collision frequency are given exactly for light particles ($m \ll m_0$) by [404]

$$W = \frac{qE}{m\nu_m},\tag{4.2}$$

$$\epsilon = \frac{1}{2} \frac{m_0}{q} W^2 + \frac{3}{2} \frac{k_b T_0}{q},\tag{4.3}$$

$$n_0 D_T = n_0 D_L = \frac{2q\epsilon}{3m\nu_m}.\tag{4.4}$$

Transport properties for the solution of Boltzmann’s equation under model (4.1) calculated using the finite difference numerical scheme (Section 3.3.3) are given in Table 4.1 for increasing l_{\max} . Results obtained using the Chebyshev polynomial and Laguerre pseudo-spectral methods (Section 3.3.2) differ from the finite difference method calculations by less than 0.01% and have hence been omitted. The calculated transport properties agree up to at least the fourth significant figure with the analytical values for all properties investigated. There are differences of less than 0.05% between the quantities calculated using $l_{\max} = 1$ and $l_{\max} = 5$ expansions, which validates the use of a two-term approximation when only elastic collisions are operative.

Table 4.1: Transport coefficients for model (4.1) with varying l_{\max} and T_0 . ‘An.’ refers to the analytic value to 5 significant figures found from equations (4.2)–(4.4). Calculations have been performed with $U_\infty = 12$ and $N = 5000$.

T_0 [K]	l_{\max}	ϵ [eV]	W [10^4 ms^{-1}]	$n_0 D_T$ [$10^{24} \text{ m}^{-1} \text{ s}^{-1}$]	$n_0 D_L$ [$10^{24} \text{ m}^{-1} \text{ s}^{-1}$]
0	An.	0.72916	0.59310	2.8831	2.8831
	1	0.7292	0.5931	2.883	2.882
	3	0.7292	0.5931	2.883	2.883
	5	0.7292	0.5931	2.883	2.883
	293	An.	0.76703	0.59310	3.0328
293	1	0.7670	0.5931	3.033	3.032
	3	0.7670	0.5931	3.033	3.033
	5	0.7670	0.5931	3.033	3.033

4.2.2 Constant elastic cross section

The second elastic-only interaction model considered is of the form

$$\begin{aligned}\sigma_m &= 5 \text{ \AA}^2, \\ m_0 &= 4 \text{ amu}, \\ E/n_0 &= 1 \text{ Td}.\end{aligned}\tag{4.5}$$

All scattering is assumed elastic and isotropic. This model is known as the ‘hard-sphere model’ and unlike the Maxwell model, (4.1), the momentum-transfer collision frequency is now a function of energy. In the two-term approximation, analytic solutions of Boltzmann’s equation exist for cross sections of the form $\sigma_m = \beta U^{\frac{p}{2}} \text{ \AA}^2$ and $T_0 = 0 \text{ K}$, such that

$$\epsilon = \frac{1}{2} m \frac{\Gamma\left(\frac{5}{2p+4}\right)}{\Gamma\left(\frac{3}{2p+4}\right)} \eta^2,\tag{4.6}$$

$$W = \frac{1}{3} \left(\frac{0.1E_{\text{Td}}}{\beta}\right) \left(\frac{q}{m}\right) \frac{2p+4}{\eta^{p+1}} \frac{\Gamma\left(\frac{p+6}{2p+4}\right)}{\Gamma\left(\frac{3}{2p+4}\right)},\tag{4.7}$$

where Γ is the incomplete gamma function (not to be confused with the transport property, flux), and

$$\eta = \left[\frac{1}{3} \frac{m_0}{m} (2p+4) \left(\frac{q}{m}\right)^2 \left(\frac{0.1E_{\text{Td}}}{\beta}\right)^2 \right]^{\frac{1}{2p+4}}.\tag{4.8}$$

For model (4.5), $\beta = 5$ and $p = 0$. It should be noted that the above expressions are only true in the two-term approximation, and do not give an analytic solution to the full Boltzmann equation. For the non-zero temperature case considered, our calculations are compared against those of White [32]. Transport properties for the solution of Boltzmann’s equation for model (4.5) calculated using the finite difference numerical scheme described in Section 3.3.3 are given in Table 4.2. Once again, the calculated transport values do not change significantly for $l_{\text{max}} > 1$, and agree with the analytical values for $T_0 = 0 \text{ K}$, and the results of White [32] for $T_0 = 293 \text{ K}$ to less than 0.05%.

Table 4.2: Transport coefficients for model (4.5) with varying l_{max} and T_0 . ‘Two-term.’ refers to the two-term approximation analytic value to 5 significant figures found from equations (4.6)–(4.7). ‘White’ refers to the value quoted in [32]. Calculations have been performed with $U_{\infty} = 6$ and $N = 5000$.

T_0 [K]	l_{max}	ϵ [eV]	W [10^4 ms^{-1}]	$n_0 D_{\text{T}}$ [$10^{24} \text{ m}^{-1} \text{ s}^{-1}$]	$n_0 D_{\text{L}}$ [$10^{24} \text{ m}^{-1} \text{ s}^{-1}$]
0	Two-term	0.72932	0.57595	-	-
	1	0.7293	0.5760	3.204	1.572
	3	0.7293	0.5759	3.202	1.573
	5	0.7293	0.5759	3.202	1.573
293	White	0.75057	0.56896	-	-
	1	0.7507	0.5689	3.248	1.639
	3	0.7507	0.5689	3.247	1.640
	5	0.7507	0.5689	3.247	1.640

4.2.3 Alternating electric field

The application of a time-varying AC electric field to the constant cross section model (4.5), can be used to validate the time-stepping numerics. In contrast to the uniform DC field of model (4.5), we consider an oscillating field of the form

$$\begin{aligned} E/n_0 &= 1 \cos(\omega t) \text{ Td}, \\ T_0 &= 0 \text{ K}, \end{aligned} \quad (4.9)$$

where ω is the angular frequency. A ‘steady-state’ can be achieved in that a repetitious behaviour with respect to the cycling of the electric field is eventually achieved, independent of the initial distribution. The initial distribution affects the transient behaviour of the system as it relaxes to this periodic steady-state. To reach the steady-state quickly and efficiently, a constant $1/\sqrt{2}$ Td DC electric field was initially applied for a small number of large time-steps to allow the source distribution to relax, after which the oscillatory field in model (4.9) was switched on and a much finer time-step size relative to the angular frequency applied. A minimum of ten cycles were used to ensure that any transient motion had dissipated. The temporal profiles of transport coefficients (ϵ , W , $n_0 D_L$ and $n_0 D_T$) for model (4.9) for varying angular frequencies is shown in Figures 4.1–4.3, along with the digitized data of White [33]. There are small differences that could be attributed to digitizing error as much as differences in the solution approaches, but it is clear that the appropriate temporal behaviour is being satisfactorily reproduced. A detailed discussion and physical justification of the phenomena is given in [33].

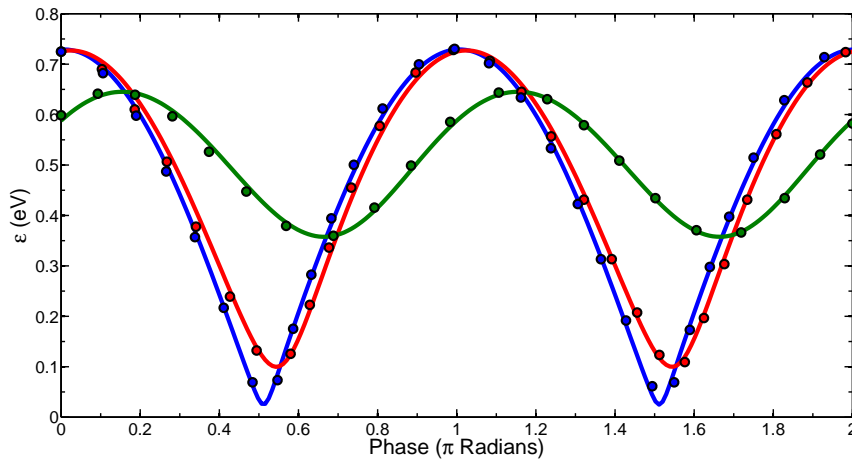


Figure 4.1: Variation of mean energy, ϵ , for model (4.9) over a range of reduced angular frequencies, ω/n_0 . Calculations have been performed with $U_\infty = 10$, $l_{\max} = 1$, and $N = 5000$.

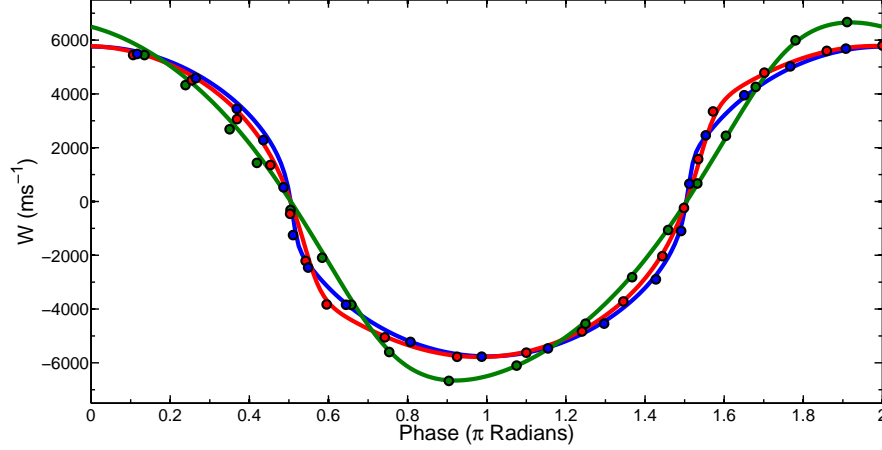


Figure 4.2: Variation of drift velocity, W , for model (4.9) over a range of reduced angular frequencies, ω/n_0 . Calculations have been performed with $U_\infty = 10$, $l_{\max} = 1$, and $N = 5000$.

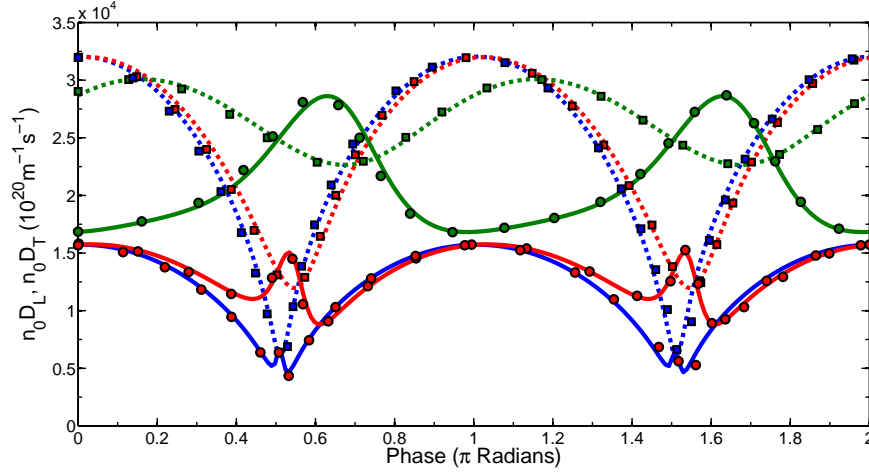


Figure 4.3: Variation of diffusion coefficients, $n_0 D_L$ and $n_0 D_T$, for model (4.9) over a range of reduced angular frequencies, ω/n_0 . Calculations have been performed with $U_\infty = 10$, $l_{\max} = 1$, and $N = 5000$.

Cycle-averaged and root mean square (RMS) transport coefficients are given in Table 4.3, and compared to the calculations of White [33]. The two sets of values agree to within 0.1% for all transport coefficients across all angular frequencies.

Table 4.3: Cycle-averaged ($\bar{\epsilon}$, $n_0 \overline{D_T}$, and $n_0 \overline{D_L}$) and RMS (W_{RMS}) values of the transport coefficients for model (4.9) at various applied reduced angular frequencies. ‘White’ refers to the value quoted in [33]. Calculations have been performed with $U_\infty = 10$, $N = 5000$ and $l_{\max} = 1$.

ω/n_0 [rad m ⁻³ s ⁻¹]	Method	$\bar{\epsilon}$ [eV]	W_{RMS} [10 ⁴ ms ⁻¹]	$n_0 \overline{D_T}$ [10 ²⁴ m ⁻¹ s ⁻¹]	$n_0 \overline{D_L}$ [10 ²⁴ m ⁻¹ s ⁻¹]
10 ⁻¹⁹	Current	0.4647	4.597	2.450	1.214
	White	0.4647	4.597	2.448	1.215
10 ⁻¹⁸	Current	0.4704	4.623	2.491	1.335
	White	0.4703	4.623	2.490	1.335
10 ⁻¹⁷	Current	0.5068	4.796	2.662	2.097
	White	0.5070	4.797	2.662	2.099

4.3 Power-law loss processes

Benchmarking for simple particle loss processes such as attachment, annihilation and positronium formation is performed by considering the following model:

$$\begin{aligned}
 \sigma_{\text{in}} &= 10U^{-\frac{1}{2}} \text{ \AA}^2, \\
 \sigma^{\text{loss}} &= aU^p \text{ \AA}^2, \\
 E/n_0 &= 0.4 \text{ Td}, \\
 m_0 &= 16 \text{ amu}, \\
 T_0 &= 293 \text{ K}.
 \end{aligned} \tag{4.10}$$

As the name suggests, the consequence of a loss process is the non-conservation of particle number density. Despite the changing number density, a steady-state can still exist for the transport coefficients, which are essentially normalized with respect to the number density. Non-conservative processes highlight the differences between flux and bulk transport coefficients, as defined in Section 2.4.2.

Transport properties for model (4.10) with various values for the a and p parameters are detailed in Table 4.4. The values $p = \frac{1}{2}$, $-\frac{1}{2}$ and -1 correspond to collision frequencies that increase, are constant, and decrease with energy respectively. Our results generally agree with those given in [34] to within 0.5%. It should be noted that there are errors in the results listed in [34] for some bulk properties, and these cases have been re-calculated using a similar Burnett function expansion to that used by Ness and Robson (which are included in Table 4.4 enclosed within square brackets), which now agree closely with our calculations.

Energy-dependent loss collisional processes can have a large effect on the flux and bulk transport coefficients. When $p = \frac{1}{2}$, the loss process collision frequency increases with energy which means that high-energy particles are preferentially lost from the swarm, leading to an overall attachment cooling. The amount of cooling is directly proportional to the magnitude of the loss process, hence as a and α^{loss} increase in Table 4.4 the mean energy, drift velocities and diffusion coefficients decrease for the swarm. The opposite effect, attachment heating, is shown when the loss process collision frequency decreases with energy, i.e., $p = -1$. Now low-energy swarm particles are preferentially removed from the swarm, leading to an increase in mean energy, drift and diffusion coefficients with increasing a and α^{loss} . When $p = -\frac{1}{2}$, the loss process collision frequency is constant with respect to energy, and particles are lost uniformly along the energy spectrum. Hence no attachment heating or cooling is observed, and bulk and flux values are identical.

In Table 4.5 the convergence in l_{max} is tested for a single value of $a = 10^{-5}$, with $N = 5000$. No difference is observed in the transport coefficients for $l_{\text{max}} > 1$, which implies that a two-term approximation is adequate to describe the transport coefficients to four figure accuracy. Anisotropy in the velocity distribution arises from the change in momentum of the scattered particle. Since simple loss processes do not involve a scattered component, only the speed distribution is modified.

Table 4.4: Transport coefficients for model (4.10) with varying a and p . Note the values in square brackets are the corrected values for those given by Ness and Robson [34]. Calculations have been performed with $l_{\max} = 1$, and $N = 5000$.

p	a [$\text{\AA}^2 (\text{eV})^{-p}$]	α^{loss}/n_0 [$10^{-20} \text{ m}^3 \text{ s}^{-1}$]	ϵ [eV]	W [10^3 ms^{-1}]	$n_0 D_T$ [$10^{23} \text{ m}^{-1} \text{ s}^{-1}$]	$n_0 D_L$ [$10^{23} \text{ m}^{-1} \text{ s}^{-1}$]	W^{flux} [10^3 ms^{-1}]	$n_0 D_T^{\text{flux}}$ [$10^{23} \text{ m}^{-1} \text{ s}^{-1}$]	$n_0 D_L^{\text{flux}}$ [$10^{23} \text{ m}^{-1} \text{ s}^{-1}$]
$\frac{1}{2}$	0	0	0.1545	1.186	3.055	3.055	1.186	3.055	3.055
	10^{-5}	9.152×10^{-1}	0.1543	1.183	3.046 [3.046]	3.032 [3.032]	1.186	3.051	3.050
	10^{-4}	9.032×10^0	0.1523	1.152	2.967 [2.968]	2.840 [2.840]	1.186	3.011	3.011
	10^{-3}	8.092×10^1	0.1364	0.9375	2.414 [2.414]	1.730 [1.730]	1.186	2.697	2.698
	10^{-2}	5.026×10^2	0.0847	0.4480	1.154 [1.154]	0.4072 [0.4071]	1.186	1.675	1.675
	10^{-1}	2.079×10^3	0.03506	0.1518	0.3910 [0.3910]	0.1007 [0.1007]	1.186	0.6929	0.6926
	1	7.179×10^3	0.01210	0.04841	0.1247 [0.1247]	0.03071 [0.03071]	1.185	0.2390	0.2390
	10	2.335×10^4	0.003931	0.01525	0.03955 [0.03957]	0.00977 [0.00978]	1.183	0.0776	0.0772
$-\frac{1}{2}$	0	0	0.1545	1.186	3.055	3.055	1.186	3.055	3.055
	10^{-5}	5.931×10^0	0.1545	1.186	3.055	3.055	1.186	3.055	3.055
	10^{-2}	5.931×10^3	0.1545	1.186	3.055	3.055	1.186	3.055	3.055
	1	5.931×10^5	0.1545	1.186	3.055	3.055	1.186	3.055	3.055
-1	0	0	0.1545	1.186	3.055	3.055	1.186	3.055	3.055
	10^{-6}	2.080×10^0	0.1548	1.190	3.066 [3.066]	3.070 [3.070]	1.186	3.060	3.061
	10^{-5}	2.054×10^{-1}	0.1572	1.227	3.159 [3.159]	3.199 [3.199]	1.186	3.107	3.107
	10^{-4}	1.865×10^{-2}	0.1795	1.583	4.079 [4.082]	4.438 [4.457]	1.186	3.548	3.540
	3×10^{-4}	4.782×10^{-2}	0.2217	2.288	5.899 [5.909]	6.790 [6.853]	1.186	4.384	4.372
	5×10^{-4}	7.158×10^{-2}	0.2571	2.890	7.452 [7.463]	8.757 [8.835]	1.186	5.084	5.086
	7×10^{-4}	9.240×10^{-2}	0.2884	3.425	8.831 [8.843]	10.51 [10.58]	1.186	5.701	5.700
	9×10^{-4}	1.114×10^{-3}	0.3169	3.920	10.09 [10.11]	12.12 [12.17]	1.186	6.265	6.262
	10^{-3}	1.204×10^{-3}	0.3303	4.148	10.69 [10.70]	12.88 [12.92]	1.186	6.531	6.529
	2×10^{-3}	1.982×10^{-3}	0.4472	6.163	15.88	19.40	1.186	8.842	8.841
	5×10^{-3}	3.757×10^{-3}	0.7132	10.75	27.63	34.26	1.186	14.1	14.1

Table 4.5: Transport coefficients for model (4.10) with varying p and l_{\max} . Calculations have been performed with $N = 5000$.

p	l_{\max}	α^{loss}/n_0 [$10^{-20} \text{ m}^3 \text{ s}^{-1}$]	ϵ [eV]	W [10^3 ms^{-1}]	$n_0 D_T$ [$10^{23} \text{ m}^{-1} \text{ s}^{-1}$]	$n_0 D_L$ [$10^{23} \text{ m}^{-1} \text{ s}^{-1}$]	W^{flux} [10^3 ms^{-1}]	$n_0 D_T^{\text{flux}}$ [$10^{23} \text{ m}^{-1} \text{ s}^{-1}$]	$n_0 D_L^{\text{flux}}$ [$10^{23} \text{ m}^{-1} \text{ s}^{-1}$]
$\frac{1}{2}$	1	0.9152	0.1543	1.183	3.046	3.032	1.186	3.051	3.050
	3	0.9152	0.1543	1.183	3.046	3.032	1.186	3.051	3.050
	5	0.9152	0.1543	1.183	3.046	3.032	1.186	3.051	3.050
$-\frac{1}{2}$	1	5.931	0.1545	1.186	3.055	3.058	1.186	3.055	3.058
	3	5.931	0.1545	1.186	3.055	3.058	1.186	3.055	3.058
	5	5.931	0.1545	1.186	3.055	3.058	1.186	3.055	3.058
-1	1	20.54	0.1572	1.227	3.159	3.199	1.186	3.107	3.107
	3	20.54	0.1572	1.227	3.159	3.199	1.186	3.107	3.107
	5	20.54	0.1572	1.227	3.159	3.199	1.186	3.107	3.107

4.3.1 Convergence properties of finite difference and pseudo-spectral schemes

In Section 3.3 three different energy-space discretizations were described; a centred finite difference method, a pseudo-spectral method based on Chebyshev polynomials and a pseudo-spectral method based on Laguerre functions. In the results tabulated thus far, there have been insignificant differences in the converged results that arise from the three methods, and so only the finite difference method results have been included. The major difference between the three schemes is in the convergence rates of the solutions with respect to the number of energy-space nodes. The finite difference scheme is a low-order, local approximation, while the pseudo-spectral schemes are high-order, global approximations. The pseudo-spectral schemes have excellent error convergence properties that depend on the smoothness of the solution, and hence for certain situations can boast savings up to several orders of magnitude in computational memory and time over low-order schemes [383].

The convergence rates of the finite difference scheme, Chebyshev pseudo-spectral scheme, and Laguerre function pseudo-spectral scheme are compared for the following power law attachment model:

$$\begin{aligned}
 \sigma_m &= 10 \text{ \AA}^2, \\
 \sigma^{\text{loss}} &= 10^{-3} U^{-\frac{1}{2}} \text{ \AA}^2, \\
 m_0 &= 16 \text{ amu}, \\
 T_0 &= 0 \text{ K}, \\
 E/n_0 &= 0.4 \text{ Td}.
 \end{aligned} \tag{4.11}$$

The attachment collision frequency for model (4.11) is independent of energy, and hence the distribution function components in the hydrodynamic regime, F_l , are unaffected by the attachment process. Under the two-term approximation, an analytic solution of model (4.11) for F_0 and F_1 can be found, and compared to the numerical results. The distribution function components are smooth and do not demonstrate discontinuities or singularities, so it is expected that they should be well approximated by pseudo-spectral methods.

The variation of the root mean square (RMS) error between the analytic and numerical solution for F_0 with the number of terms in the series, N , is shown in Figure 4.4 for the three energy-space discretization schemes. The RMS error profiles for both the Chebyshev polynomials and Laguerre functions demonstrate exponential convergence, with the latter reaching machine precision first. The error profile of the finite difference method however exhibits much slower, algebraic convergence of $\sim \mathcal{O}(N^{-1.6})$. For model (4.11), machine precision is reached in ~ 40 terms by the pseudo-spectral schemes, whereas the finite difference scheme has only reached an RMS error of $\sim 10^{-4}$ in 1000 terms. This example highlights the computational time and memory advantages that can be achieved by pseudo-spectral methods.

Unfortunately, the performance of the pseudo-spectral schemes is intimately linked to the smoothness of the solution and its derivatives. The model (4.11) is a particularly advantageous system for the pseudo-spectral schemes, since the collision frequencies for both elastic and attachment processes are smoothly-varying, operate at all energies (i.e., they do not ‘turn on’ or ‘turn off’), and do not introduce singularities at $U = 0$. When these conditions are not met, the spectral convergence properties of the pseudo-spectral schemes can be destroyed. For the inelastic processes considered in the following sections, the cross sections turn on at non-zero threshold energies, often abruptly, which introduces discontinuities that are not handled well by global approximation methods [383, 405]. It can be concluded that pseudo-spectral schemes are particularly

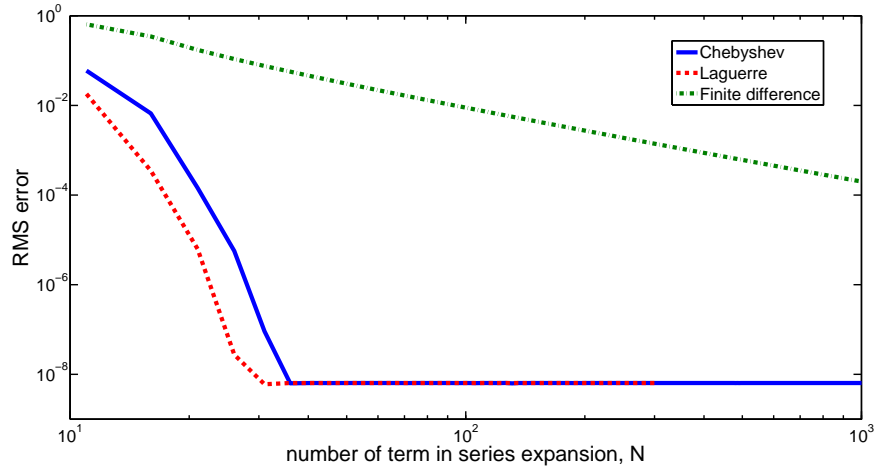


Figure 4.4: Convergence of RMS error with number of terms for finite difference, Chebyshev and Laguerre pseudo-spectral solutions for model (4.11).

useful and efficient when only elastic and simple attachment processes are operative, which is often true in low-energy transport studies, but for the general case (and henceforth in this work) the finite difference scheme is employed.

4.4 Excitations

In an excitation collision, the energy of the impacting particle exceeds some threshold energy causing a state change in the internal states of the medium, leading to a difference in the pre- and post-collision energy. Like elastic collisions, it is also a particle-conserving process. The excitation process benchmarks in this section assume a cold gas, such that there are no excited states occupied and no super-elastic processes. Scattering is assumed to be isotropic.

4.4.1 Reid's ramp model

The following model, initially developed by Reid [39], is used to benchmark particle conserving excitation processes:

$$\begin{aligned}
 \sigma_m &= 6.0 \text{ \AA}^2, \\
 \sigma^{\text{exc}} &= \begin{cases} 10(U - 0.2) \text{ \AA}^2, & U \geq 0.2 \text{ eV}, \\ 0, & U < 0.2 \text{ eV}, \end{cases} \\
 m_0 &= 4 \text{ amu}, \\
 T_0 &= 0 \text{ K}.
 \end{aligned} \tag{4.12}$$

This model is now a standard benchmark in the field, due to its known failure of the two-term approximation. Transport coefficients for model (4.12) are given in Table 4.6. Ness and Robson [34] have collated results from a number of different authors using a variety of approaches, which are also included in Table 4.6 for comparison. The accuracy of the various methods are included in brackets when known. Our calculations agree with those of Ness and Robson to within 0.05% for each of the reduced fields considered, which also agree closely with the other methods tabulated.

Table 4.6: Transport coefficients for Reid’s ramp model, (4.10), with varying E/n_0 . ‘M’ refers to the moment method of Ness and Robson [34], ‘POR’ the cubic spline method of Pitchford et al. [35, 36], ‘McM’ the relaxation method method of MacMahon [37], ‘FEM’ the finite element method of Segur et al. [38], ‘PDM’ the path differential method of Segur et al. [38], ‘Reid’, ‘Brag’, ‘Skull’ and ‘Penet’ the Monte Carlo results of Reid [39], Braglia et al. [40], Skullerud [38] and Penetrante [36] respectively. The accuracy of the various methods are included in brackets when known. Calculations have been performed with $l_{\max} = 5$ and $N = 5000$.

E/n_0 [Td]	Method	ϵ [eV]	W [10^4ms^{-1}]	$n_0 D_T$ [$10^{24} \text{m}^{-1} \text{s}^{-1}$]	$n_0 D_L$ [$10^{24} \text{m}^{-1} \text{s}^{-1}$]
1	Current	0.1015	1.272	0.9750	0.7591
	M (6 term)	0.1015	1.272	0.9751	0.7591
	POR (6 term)		1.272	0.9749	
	McM (6 term)	0.1015	1.272		
	FEM	0.1015	1.271	0.9749	0.7594
	PDM	0.1018	1.270	0.9735	0.7623
	Reid (MC)	0.1013(10)	1.255(13)		
	Brag (MC)	0.1014(5)	1.272(6)	0.975(10)	
12	Current	0.2689	6.838	1.135	0.5688
	M (6 term)	0.2689	6.839	1.135	0.5688
	POR (6 term)	0.269	6.838	1.134	0.57
	McM (6 term)	0.269	6.84		
	FEM	0.2689	6.832	1.135	0.569
	PDM	0.269	6.832	1.131	0.569
	Reid (MC)		6.87(7)		
	Brag (MC)	0.269(1)	6.84(3)	1.136(10)	
24	Penet (MC)	0.270(1)	6.86(2)	1.16(4)	0.58(3)
	Current	0.4080	8.882	1.1337	0.4606
	M (6 term)	0.4079	8.886	1.134	0.4609
	POR (6 term)	0.408	8.885	1.132	0.46
	McM (6 term)	0.408	8.89	1.133	0.460
	FEM	0.4074	8.881	1.134	0.463
	PDM	0.4083	8.874	1.131	0.4613
	Reid (MC)	0.408(2)	8.89(9)	1.145(23)	
Brag (MC)	0.408(2)	8.88(4)	1.134(10)	0.473(5)	
	Skul (MC)	0.4074	8.869	1.130	0.465
	Penet (MC)	0.409(1)	8.89(2)	1.16(4)	0.48(2)

In Table 4.7 the variation of the transport coefficients with l_{\max} is shown for $E/n_0 = 12$ Td. It is evident that the two-term approximation is inadequate and significantly overestimates the mean energy and drift velocity, while underestimating the diffusion coefficients. An $l_{\max} = 5$ expansion is required to get transport coefficient convergence to four significant figures. The $l_{\max} = 1$ calculations give errors as large as 20% with respect to the converged values. The $l_{\max} = 3$ are accurate to within 0.2%, which are sufficient for most practical purposes.

Table 4.7: Transport coefficients for Reids ramp model, (4.12), with varying l_{\max} for $E/n_0 = 12$ Td. Calculations have been performed with $U_\infty = 3$, and $N = 5000$.

l_{\max}	ϵ [eV]	W [10^4ms^{-1}]	$n_0 D_T$ [$10^{24} \text{m}^{-1} \text{s}^{-1}$]	$n_0 D_L$ [$10^{24} \text{m}^{-1} \text{s}^{-1}$]
1	0.2736	7.029	1.369	0.5065
3	0.2689	6.840	1.137	0.5684
5	0.2689	6.838	1.135	0.5688
7	0.2689	6.838	1.135	0.5688

4.5 Electron impact ionization

In this section the electron impact ionization (EII) collision operator is benchmarked. EII is a fundamentally different process than ionization by positron impact (PII), due to the ejected electrons contributing to the electron swarm in the former case. A different collision operator needs to be used for each case. EII benchmarks have been investigated by a number of authors, and the Lucas-Saelee [42] and Ness-Robson [34] models are considered here. PII is investigated in detail in Chapter 6.

4.5.1 Model of Lucas and Saelee

To understand the fundamental effects of EII on the transport properties we consider the Lucas-Saelee model [34, 42],

$$\begin{aligned}
 \sigma_{\text{m}} &= 4U^{-\frac{1}{2}} \text{Å}^2, \\
 \sigma^{\text{exc}} &= \begin{cases} 0.1(1-F)(U-15.6) \text{Å}^2, & U \geq 15.6 \text{ eV}, \\ 0, & U < 15.6 \text{ eV}, \end{cases} \\
 \sigma^{\text{EII}} &= \begin{cases} 0.1F(U-15.6) \text{Å}^2, & U \geq 15.6 \text{ eV}, \\ 0, & U < 15.6 \text{ eV}, \end{cases} \\
 E/n_0 &= 10 \text{ Td}, \\
 m/m_0 &= 10^{-3}, \\
 T_0 &= 0 \text{ K}.
 \end{aligned} \tag{4.13}$$

The energy-partition function, $P(U, U')$, for this model is such that all energy-sharing fractions are equiprobable. It should be noted that, in this model, the total cross section for inelastic and ionization collisions is independent of the parameter F , and the threshold energies are the same for both processes. Thus, it can be used to isolate the separate effects of inelastic and ionization collisions, respectively. In the literature, it is not unusual to ignore the distinction, and to treat ionization as merely another conservative inelastic excitation (see, e.g. [257, 259, 292, 406–408] and others), completely ignoring the effect of particle generation in collisions. If this approximation were to hold for the present model, there would be no variation in the calculated properties with respect to F . The transport properties for model (4.13) are tabulated in Table 4.8, along with the results from various methods quoted in [34]. There is some significant variation in the results from the different calculation methods. The ionization rates, mean energies and bulk drift velocities calculated in this work agree with the values of [34] to less than 0.3%, 0.5% and 1% respectively. There are larger differences of 1% and 5% between the transverse and longitudinal diffusion coefficients respectively. Slightly better agreement is found with the Monte Carlo results of Taniguchi et al. [41], where our results are consistent to within 1% for all transport coefficients across all F .

4.5.2 Model of Ness and Robson

The energy-partitioning function, P , which was described in Section 2.3.5, controls the partitioning of the post-ionization energy between the scattered and ejected constituents, and is a major theme

Table 4.8: Transport coefficients for the Lucas-Saelee model, (4.13), with varying F . ‘1 = 1’ and ‘1 = 2’ refer to the moment method of Ness and Robson [34], ‘T’ to the calculations of Taniguchi et al. [41], ‘L’ to the Boltzmann calculations of Lucas and Saelee [42], and ‘MC’ the Monte Carlo results of Lucas and Saelee [42]. Calculations have been performed with $l_{\max} = 5$ and $N = 5000$.

F	Method	α^{EII} [$10^{-15} \text{ m}^3\text{s}^{-1}$]	ϵ [eV]	W [10^4 ms^{-1}]	$n_0 D_{\text{T}}$ [$10^{24} \text{ m}^{-1}\text{s}^{-1}$]	$n_0 D_{\text{L}}$ [$10^{24} \text{ m}^{-1}\text{s}^{-1}$]
0	Current	0	5.565	7.319	27.26	26.54
	1 = 1	0	5.55	7.33	27.3	26.3
	1 = 2	0	5.55	7.32	27.2	26.5
	T	0	5.56	7.32	27.4	26.5
	L	0	5.58	7.4	27	26.5
	MC	0	5.60	7.4	27	26.5
	0.5	Current	1.333	5.224	8.593	27.26
1 = 1		1.34	5.21	8.59	27.6	27.6
1 = 2		1.34	5.21	8.60	27.5	28.0
T		1.3	5.23	8.6	27.5	29
L		1.50	5.49	8.3	27	27.5
MC		1.32	5.30	8.6	28.5	31
1.0		Current	2.420	4.969	9.474	27.23
	1 = 1	2.43	4.96	9.47	27.7	27.9
	1 = 2	2.43	4.96	9.48	27.6	28.4
	T	2.4	4.95	9.5	27.5	29.5
	L	2.93	5.40	9.2	26.5	28.5
	MC	2.45	5.10	9.6	26.5	28.5

in the present work (see Chapter 6). To investigate the effect of the energy partitioning function on EII transport properties Ness and Robson [34] proposed the following model:

$$\begin{aligned}
 \sigma_{\text{m}} &= 10 \text{ \AA}^2, \\
 \sigma^{\text{exc}} &= \begin{cases} 1 \text{ \AA}^2, & U \geq 10 \text{ eV}, \\ 0, & U < 10 \text{ eV}, \end{cases} \\
 \sigma^{\text{EII}} &= \begin{cases} 1 \text{ \AA}^2, & U \geq 15 \text{ eV}, \\ 0, & U < 15 \text{ eV}, \end{cases} \\
 m_0 &= 25 \text{ amu}, \\
 T_0 &= 0 \text{ K}.
 \end{aligned} \tag{4.14}$$

The energy-partition function, $P(U, U')$, for this model is such that one of the post-ionization electrons receives a fraction, Q , of the available energy. Due to the indistinguishability of post-collision particles, the results for Q and $1 - Q$ with respect to EII are identical, and so we consider only $Q \geq 0.5$. As detailed in Section 6.2.3, the modified Frost-Phelps form of the collision operator (6.20) breaks down when $Q = 0$, hence there is no value given in Table 4.9 corresponding to $Q = 0$ and $Q = 1$ (if one of the electrons gets the fraction $Q = 1$ of the available energy, then the other receives $Q = 0$ and the same problem is encountered). The EII calculations using our kinetic theory model agree closely with both our Monte Carlo simulations and the kinetic theory approach in [34]. There are generally differences of less than 0.6% and 0.3% in the ionization rate and mean energy respectively, between the present kinetic theory results and both the Monte Carlo simulation and [342] over the whole range of reduced fields and energy sharing fractions, except for the AFE case. An error is present in the AFE calculations of [342]. Values for the AFE case have been re-calculated using a similar Burnett function expansion to that of Ness and Robson

(which are included in Table 4.9 enclosed within square brackets) which agree closely with our calculations. Both the flux and bulk drift velocities generally agree to within 0.3% between the three calculation methods over the range of fields and energy-sharing fractions considered.

In Table 4.10 the variation of the transport coefficients with l_{\max} is shown for $E/n_0 = 1000$ Td. An $l_{\max} = 5$ expansion is required to get transport coefficient convergence to four significant figures. The $l_{\max} = 1$ calculations give errors as large as 20% with respect to the converged values. The $l_{\max} = 3$ are accurate within 0.8%.

Table 4.10: Convergence in l_{\max} of the bulk transport coefficients for the ionization model (4.14) for $E/n_0 = 1000$ Td and $Q = \frac{1}{2}$. Calculations have been performed with $N = 5000$, and $U_\infty = 250$.

l_{\max}	α^{EII}/n_0 [$10^{-15} \text{ m}^3 \text{ s}^{-1}$]	ϵ [eV]	W [10^5 ms^{-1}]	$n_0 D_T$ [$10^{24} \text{ m}^{-1} \text{ s}^{-1}$]	$n_0 D_L$ [$10^{24} \text{ m}^{-1} \text{ s}^{-1}$]
1	1.278	16.03	6.749	6.376	3.385
3	1.250	15.91	6.821	5.776	4.248
5	1.249	15.88	6.822	5.735	4.256
7	1.249	15.88	6.822	5.735	4.256

4.6 Percus-Yevick hard-sphere model

A major focus of the present work is extending the kinetic theory formalism beyond dilute gases to dense gases, liquids and soft-condensed matter such as biological matter. In order to investigate the effects of structure on charged particle transport, a model for the structure function is required. One such model, frequently employed in the literature, is that for a system of hard-sphere potentials obtained by applying the Percus-Yevick approximation as a closure to the Ornstein-Zernike equation, which yields a pair-correlation function [409,410]. The static structure factor, S_{PY} , is found via the Fourier transform of the pair-correlation function, the angle-integration of which is used directly in the numerical simulations. In particular, we use the model of Percus and Yevick with the Verlet-Weiss correction [411,412] to better emulate the structure of a real liquid:

$$S_{\text{PY}}(\Delta k) = \left[1 + \frac{24\eta(S_1 + S_2 + S_3)}{(\Delta k)^2} \right]^{-1}, \quad (4.15)$$

$$S_1 = \frac{2}{(\Delta k)^2} \left(\frac{12\gamma}{(\Delta k)^2} - \beta \right), \quad (4.16)$$

$$S_2 = \frac{\sin(\Delta k)}{\Delta k} \left(\alpha + 2\beta + 4\gamma - \frac{24\gamma}{(\Delta k)^2} \right), \quad (4.17)$$

$$S_3 = \frac{2 \cos(\Delta k)}{(\Delta k)^2} \left(\beta + 6\gamma - \frac{12\gamma}{(\Delta k)^2} \right) - \cos(\Delta k) (\alpha + \beta + \gamma), \quad (4.18)$$

where Δk is the momentum exchange, $\eta = \Phi - \frac{\Phi^2}{16}$, $\alpha = \frac{(1+2\eta)^2}{(1-\eta)^4}$, $\beta = -\frac{6\eta(1+\frac{\eta}{2})^2}{(1-\eta)^4}$, $\gamma = \frac{\eta\alpha}{2}$. The volume fraction parameter, Φ , specifies how tightly packed the hard spheres in the medium are. It can be written in terms of the hard-sphere radius r and the neutral number density, n_0 , as $\Phi = \frac{4}{3}\pi r^3 n_0$. Low volume fractions indicate a larger inter-particle spacing, whereas higher volume fractions indicate a smaller inter-particle spacing. Figure 4.5 shows the static structure value, $S(\Delta k)$, for different values of Φ . We have modelled systems with a range of densities, from $\Phi = 0$, which emulates a dilute gas, to $\Phi = 0.4$, which states that 40% of the volume is excluded by the hard-sphere potentials of the neutral molecules. The oscillatory nature exhibited in the structure

Table 4.9: Comparison of average ionization rate, α^{EII}/n_0 , mean energies, ϵ , flux drift velocities, W^{flux} , and bulk drift velocities W for EII for model (6.21) for different reduced fields E/n_0 and energy sharing fractions Q . The first column lists the current kinetic theory calculations, the second column lists the results of our Monte Carlo simulations [9], and the third includes the kinetic theory calculations of Ness and Robson [34]. $Q = \text{AFE}$ corresponds to ‘all fractions equiprobable’. Note: there was an error in the AFE case in the original Ness and Robson work [34], which has been recalculated. The values enclosed in square brackets have been calculated using a similar Burnett function expansion to that of Ness and Robson.

E/n_0 [Td]	Q	α^{EII}/n_0 [$10^{-15} \text{ m}^3 \text{ s}^{-1}$]		ϵ [eV]		W^{flux} [10^5 ms^{-1}]		W [10^5 ms^{-1}]	
		Current	MC	Current	MC	Current	MC	Current	MC
300	0		1.620	1.61	6.739	6.73	2.780	3.236	3.23
	$\frac{1}{4}$	1.598	1.611	6.737	6.741	6.73	2.752	3.200	3.204
	$\frac{1}{2}$	1.595	1.596	6.739	6.741	6.73	2.748	3.194	3.196
	$\frac{3}{4}$	1.591	1.589	6.742	6.744	6.74	2.744	3.189	3.192
	$\frac{1}{2}$	1.600	1.606	6.733	6.746	6.75	2.756	3.198	3.206
	AFE					[6.73]			[3.21]
500	0		4.643	4.68	9.009	8.99	3.920	4.752	4.74
	$\frac{1}{4}$	4.504	4.515	9.007	9.007	9.01	3.835	4.632	4.644
	$\frac{1}{2}$	4.482	4.492	9.013	9.023	9.01	3.823	4.617	4.62
	$\frac{3}{4}$	4.464	4.452	9.017	9.028	9.02	3.814	4.604	4.61
	$\frac{1}{2}$	4.511	4.525	9.000	9.007	9.04	3.846	4.635	4.647
	AFE					[9.00]			[4.64]
800	0		9.736	9.62	13.17	13.21	5.112	6.284	6.25
	$\frac{1}{4}$	9.413	9.422	13.01	13.02	13.01	4.953	6.108	6.118
	$\frac{1}{2}$	9.357	9.372	12.99	12.99	12.99	4.933	6.090	6.092
	$\frac{3}{4}$	9.320	9.339	12.97	12.98	12.97	4.919	6.079	6.08
	$\frac{1}{2}$	9.461	9.445	13.03	13.02	13.09	4.968	6.137	6.12
	AFE					[13.02]			[6.13]

factor is echoed in the behaviour of the transport coefficients. In the limit $\Delta k \rightarrow \infty$, $S \rightarrow 1$, and the dilute gas case is regained.

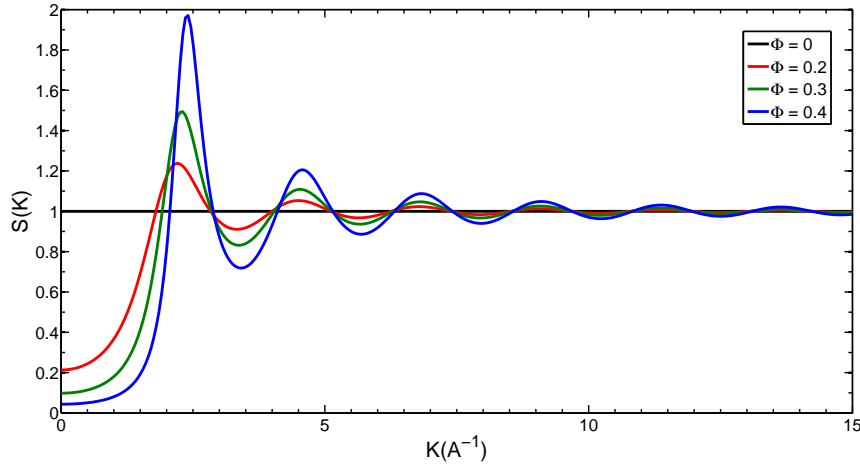


Figure 4.5: The variation of the static structure factor with momentum exchange Δk for the Percus-Yevick model (with Verlet-Weiss correction) for various volume fractions, Φ .

In the hard-sphere model, the elastic collision cross section is constant and isotropic. For isotropic scattering $\sigma(v, \chi)$ is independent of angle χ , and the structure-modified momentum-transfer cross section, $\Sigma_m(v) = \Sigma_0(v) - \Sigma_1(v)$, accounting for coherent structure effects can be found from

$$\Sigma_m(v) = \sigma_m(v) s(v), \quad (4.19)$$

where $\sigma_m(v)$ is the momentum-transfer cross section for single particle scattering and $s(v)$ is the angle-integrated structure factor, given by,

$$s(v) = \frac{1}{2} \int_{-1}^1 S\left(\frac{2mv}{\hbar} \sin\left(\frac{\chi}{2}\right)\right) (1 - \cos \chi) d(\cos \chi). \quad (4.20)$$

It should be noted that the assumption of isotropy is for simplicity in illustrating the technique, and by no means a necessity.

The details of the hard-sphere model implemented are

$$\begin{aligned} \sigma_m &= 6 \text{ \AA}^2, \\ \Phi &= 0, 0.2, 0.3, 0.4, \\ m_0 &= 4 \text{ amu}, \\ T_0 &= 0 \text{ K}. \end{aligned} \quad (4.21)$$

The effective momentum-transfer collision frequencies for this model as a function of the volume fraction are shown in Figure 4.6. Physically, one expects that as the energy increases, and hence de Broglie wavelength decreases, the effects of coherent scattering are reduced and the structure-modified profiles of the transport coefficients converge on the dilute gas phase profile. This behaviour is consistent with Figure 4.6, and it is to be expected that the oscillatory nature of the structure factor and high energy convergence with the dilute gas profiles will be reflected in the transport coefficients.

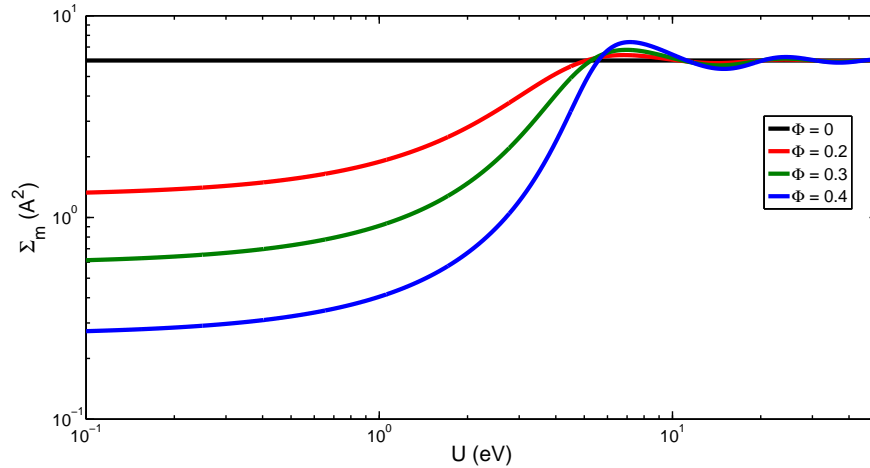


Figure 4.6: The energy variation of the structure-modified momentum-transfer cross section, Σ_m , for various volume fractions Φ , for a dense gas of hard spheres.

4.6.1 Transport coefficients

The same Percus-Yevick hard-sphere system was studied in [9], and a comparison with the Monte Carlo simulation results act as a benchmark for the Boltzmann code solution. The variation of the mean energy (ϵ), drift velocity (W), and the transverse and longitudinal diffusion coefficients (D_T and D_L respectively) with reduced electric field are presented in Figures 4.7–4.10 for various volume fractions. The independent Monte Carlo simulation results agree to within 1% each of the transport coefficients at all reduced electric fields considered. It should be noted that, in general, the Monte Carlo statistical error [413] is not visible at these scales, being less than 1% in all cases.

It is evident that the presence of coherent scattering causes significant differences between the volume fraction profiles. A thorough discussion of the phenomenology of the Percus-Yevick hard-sphere system is given in Appendix A, where fluid modelling furnishes semi-analytic expressions which will greatly aid the discussion. Equations (A.24) and (A.25), in the appendix are restated here for clarity, i.e.,

$$W = \frac{qE}{m\tilde{\nu}_m}, \quad (4.22)$$

$$\epsilon = \frac{1}{2}m_0W^2\frac{\tilde{\nu}_m}{\nu_m}, \quad (4.23)$$

where $\tilde{\nu}_m$ is the momentum-transfer collision frequency including coherent scattering effects. At low field strengths, and hence low energies, increasing the volume fraction decreases the collision frequency, leading to an increase in W as per equation (4.22). The effect on mean energy is a little more complex due to the non-linear nature of equation (4.23), but generally in the low field strength and low energy region the same behaviour is observed as for the drift velocity. Physically, coherent scattering generally acts to reduce the momentum transfer, thus enhancing the electric field's ability to pump energy and momentum into the system. The enhancements in the mean energy, drift velocity and diffusion coefficients due to enhanced coherent scattering effects then follows. At higher field strengths, the volume fraction profiles converge to the dilute gas phase profile, a reflection of the increase in mean particle energy and decrease in the associated de Broglie wavelength and subsequent suppression of coherent scattering effects. It should also be noted that for the larger volume fractions in Figure 4.8 there exists a small window of electric field strengths

for which the drift velocity decreases despite an increase in the applied electric field strength. This is the phenomena known as ‘negative differential conductivity’ (NDC), conditions for which have been investigated by a number of authors [31, 266, 267, 414]. The NDC observed in Figure 4.8 is purely a consequence of medium structure. A condition for the occurrence of structure-induced NDC, derived in Appendix A, is given by

$$\frac{d \ln \left(\frac{\bar{\nu}_m}{\nu_m} \right)}{d \ln \epsilon} > 1, \quad (4.24)$$

which is only satisfied in this model for the $\Phi = 0.3$ and $\Phi = 0.4$ cases. The excellent agreement between the Boltzmann solution and Monte Carlo simulation results observed in Figures 4.7–4.10 with respect to the transport coefficients (ϵ , W , D_T and D_L), and successful demonstration of structure-induced NDC for the model system validates our numerical scheme when including coherent scattering effects.

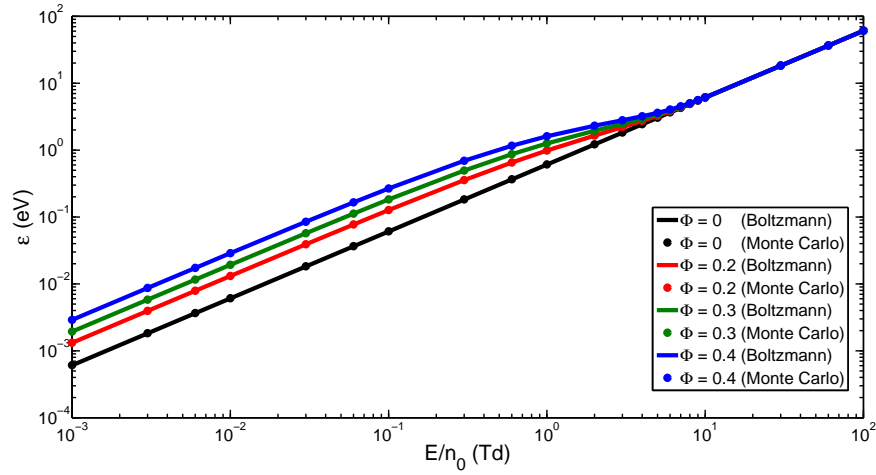


Figure 4.7: Mean energy, ϵ , for Percus-Yevick model (4.21) as a function of reduced electric field, E/n_0 , for a range of volume fractions, Φ .

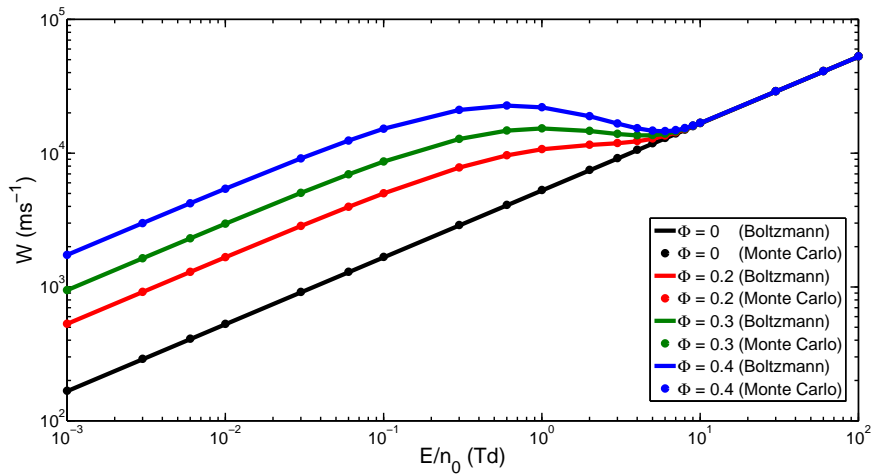


Figure 4.8: Drift velocity, W , for Percus-Yevick model (4.21) as a function of reduced electric field, E/n_0 , for a range of volume fractions, Φ .

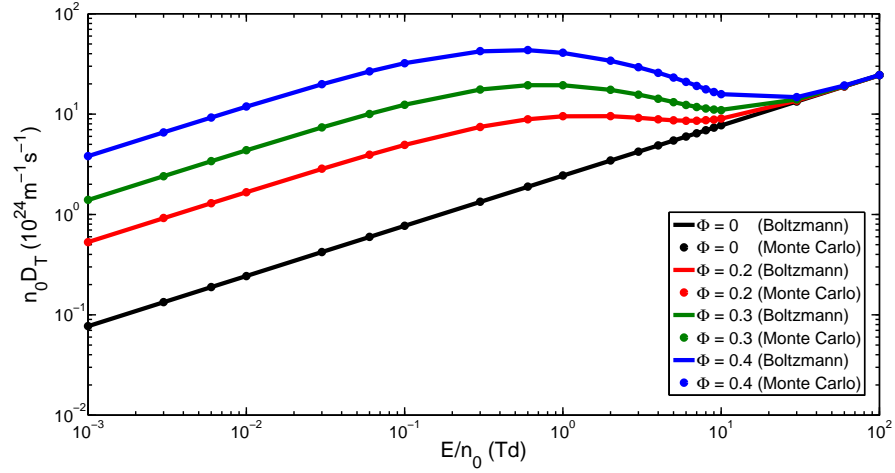


Figure 4.9: Transverse diffusion coefficient, $n_0 D_T$, for Percus-Yevick model (4.21) as a function of reduced electric field, E/n_0 , for a range of volume fractions, Φ .

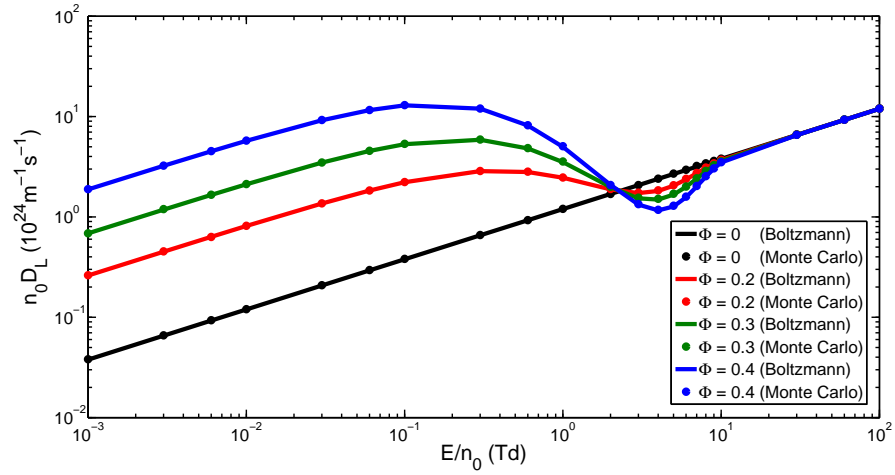


Figure 4.10: Longitudinal diffusion coefficient, $n_0 D_L$, for Percus-Yevick model (4.21) as a function of reduced electric field, E/n_0 , for a range of volume fractions, Φ .

4.7 Conclusion

In this chapter, a variety of benchmark systems for conservative and non-conservative collisional processes have been considered in order to thoroughly validate the computational code and theory developed. The transport coefficients calculated agree closely with previous investigations for each of the model systems investigated. The validation having been completed, the transport of electrons and positrons in real gases and liquids are considered in the proceeding chapters.

5

Low-energy electron and positron transport in atomic gases

This chapter contains material that has been published in the following journal articles:

[5] G. J. Boyle, M. J. Casey, R. D. White, Y. Cheng and J. Mitroy. Transport properties of electron swarms in gaseous neon at low values of E/N . *Journal of Physics D: Applied Physics*, **47**, 345203 (2014). doi:10.1088/0022-3727/47/34/345203.

[6] G. J. Boyle, M. J. Casey, R. D. White, and J. Mitroy. Transport theory for low-energy positron thermalization and annihilation in helium. *Physical Review A*, **89**, 022712 (2014). doi:10.1103/PhysRevA.89.022712.

This chapter includes cross section calculations and theory performed by J. Mitroy and Y. Cheng. The cross section theory has been summarized here, and full details are to be found in the cited publications. The transport property calculations and analysis were performed by the author. All other work described in this chapter is my own.

5.1 Introduction

In Chapter 4, the Boltzmann equation solution scheme developed was systematically benchmarked for a number of simple model systems. In this chapter, the solution scheme is applied to real gases for both electron and positron systems, in the low-energy regime. The systems investigated are simple atomic systems, the cross sections for which are reaching benchmark status [414, 415]. The Boltzmann equation is a useful tool for evaluating the accuracy and completeness of cross section sets, serving as the connection between theoretical investigations on the microscopic scale, and the swarm experiments on the macroscopic scale [276]. In particular, the application of an electric field to thermalization experiments represents a stringent test on the validity of the cross section set, particularly above thermal energies. This allows us to work closely with scattering theoreticians

to comment on the accuracy and completeness of currently used cross sections sets and to make recommendations.

We first consider electron swarms in atomic neon in Section 5.2. The electron-helium system has already been heavily investigated, such that it can essentially be considered a solved problem with regards to practical applications [416–419]. The electron-neon system however, has yet to reach the same benchmark status as electron-helium. Accordingly, a stringent analysis of the low-energy cross section with particular emphasis on a detailed comparison with swarm experiments at low values of E/n_0 is required. An investigation of transport parameters calculated from a recent all-order many-body perturbation theory treatment of the cross section [420] is compared with experimental drift velocities measurements [43], and characteristic energy measurements [10] at applied reduced electric fields of $E/n_0 < 2$ Td. We also comment on the accuracy of various theoretical and empirical electron-neon cross section sets in the low-energy regime. A recommended elastic momentum-transfer cross section is then constructed.

Positron swarms in atomic helium are considered in Section 5.3. When considering positron swarms, there is always the possibility of in-flight annihilation of the positron with the atomic electrons, and experiments typically exploit this to determine a number of annihilation parameters. Previous simulations [12, 16] determine Z_{eff} , as defined in equation (2.95), to compare with experiment. Mitroy [6] has calculated collision cross sections for helium which give a more complete description of the positron-helium annihilation cross section. The improved momentum-transfer and annihilation cross sections are employed in our kinetic theory calculations to give improved descriptions of the time dependence of Z_{eff} for positrons injected into helium, as well as the variation of Z_{eff} versus E/n_0 for experiments where the annihilation region is immersed in an electric field.

It is customary in discussions on cross sections, particularly in the low-energy regime, to speak of the speed and energy in terms of wavelength, k . Transformations between the representations are straightforward, i.e.

$$\hbar k = mv, \quad (5.1)$$

$$U = \frac{\hbar^2 k^2}{2m}. \quad (5.2)$$

5.2 Electron swarms in gaseous neon

The electron-helium system is the most thoroughly investigated electron-atom collision system. There have been numerous experiments and calculations that have studied practically every important reaction channel for this system [416–419]. The quality of agreement between theory and experiment is now very good and for many practical applications the calculation of the electron-helium collision properties can be regarded as a solved problem. Indeed, electron-helium cross sections computed with the Kohn variational method at energies below the first excitation threshold are often adopted as a benchmark cross section [415, 421].

This section is focused on the electron-neon system. A study by Alves et al. [416] of electron-neon cross section sets concluded that they were adequate for the purposes of plasma modelling where an overall accuracy of 10% is needed. Furthermore, it was noted that theoretical cross section sets from B-spline R-matrix calculations [416, 422, 423] could reproduce swarm parameters in good agreement with the cross sections over a range of E/n_0 varying from 10^{-2} to 10^3 Td [416]. Coincident with this work, a state of the art method for atomic structure, the relativistic all-order many body perturbation theory with single and double excitations (SDpT) [424, 425], was adapted

by Mitroy and co-workers to describe low-energy electron-neon scattering [420]. The derived cross sections were able to reproduce most existing elastic and momentum-transfer cross section data to an accuracy of better than 5%.

Accordingly, it is now appropriate to perform a stringent analysis of the low-energy cross section with particular emphasis on a detailed comparison with swarm experiments at low values of E/n_0 . There have been measurements of the drift velocity, W , [43, 177, 426–428] and the characteristic energy (the ratio of the transverse diffusion coefficient D_T to the mobility $\mu = W/E$, D_T/μ) [10]. These measurements have been used to generate estimates of the momentum-transfer cross section [10, 43, 429–432]. Other transport parameters that have been measured include the transverse diffusion coefficient at thermal energies [180, 181, 433–435] and the longitudinal diffusion coefficient [436]. Expressions for the transport coefficients are given in Section 2.4.

5.2.1 Cross sections

In the low-energy regime, the electron transport is reliant on three types of low-energy cross section. These are the elastic cross section, σ_T , the momentum-transfer cross section, σ_m , and the viscosity cross section, σ_v . The viscosity cross section is needed for solutions of the Boltzmann equation that go beyond the two-term approximation. All can be defined in terms of angular integrals of the differential cross section $\sigma(k, \chi)$ where χ is the scattering angle. Furthermore, expressions in terms of phase shifts are also known. These cross sections are defined

$$\begin{aligned}\sigma_T(k) &= 2\pi \int \sigma(k, \chi) \sin(\chi) \, d\chi, \\ &= \frac{4\pi}{k^2} \sum_{\ell=0} ((\ell+1) \sin^2(\delta_\ell^+) + \ell \sin^2(\delta_\ell^-)),\end{aligned}\tag{5.3}$$

$$\begin{aligned}\sigma_m(k) &= 2\pi \int (1 - \cos \chi) \sigma(k, \chi) \sin(\chi) \, d\chi, \\ &= \frac{4\pi}{k^2} \sum_{\ell=0} \left(\frac{(\ell+1)(\ell+2)}{(2\ell+3)} \sin^2(\delta_\ell^+ - \delta_{\ell+1}^+) \right. \\ &\quad + \frac{\ell(\ell+1)}{(2\ell+1)} \sin^2(\delta_\ell^- - \delta_{\ell+1}^-) \\ &\quad \left. + \frac{(\ell+1)}{(2\ell+1)(2\ell+3)} \sin^2(\delta_\ell^+ - \delta_{\ell+1}^-) \right),\end{aligned}\tag{5.4}$$

$$\begin{aligned}\sigma_v(k) &= 2\pi \int (1 - \cos^2 \chi) \sigma(k, \chi) \sin(\chi) \, d\chi, \\ &= \frac{4\pi}{k^2} \sum_{\ell=0} \left(\frac{2\ell(\ell+1)}{(2\ell-1)(2\ell+1)(2\ell+3)} \sin^2(\delta_\ell^+ - \delta_\ell^-) \right. \\ &\quad + \frac{(\ell+1)(\ell+2)(\ell+3)}{(2\ell+3)(2\ell+5)} \sin^2(\delta_\ell^+ - \delta_{\ell+2}^+) \\ &\quad + \frac{\ell(\ell+1)(\ell+2)}{(2\ell+1)(2\ell+3)} \sin^2(\delta_\ell^- - \delta_{\ell+2}^-) \\ &\quad \left. + \frac{2(\ell+1)(\ell+2)}{(2\ell+1)(2\ell+3)(2\ell+5)} \sin^2(\delta_\ell^+ - \delta_{\ell+2}^-) \right).\end{aligned}\tag{5.5}$$

In these equations, δ_ℓ^+ refers to the phase shift with $j = \ell + \frac{1}{2}$ and δ_ℓ^- refers to the phase shift with $j = \ell - \frac{1}{2}$. The expression for the momentum-transfer cross section is compatible with that

previously given by McEachran [437].

The $\ell = 0, 1$ and 2 phase shifts were obtained from a recent calculation using relativistic many-body perturbation theory [420]. This SDpT calculation iterates many-body perturbation theory for an excitation space allowing for all possible single and double excitations until convergence is reached. The effects of triple excitations are included perturbatively [425].

The SDpT phase shifts cover an energy range from $k = 0$ to $k = 0.80 a_0^{-1}$. These phase shifts are extended to higher energies using a central field model. The effective Hamiltonian (in atomic units) for the electron with co-ordinate \mathbf{r}_0 moving in the field of the atom is written

$$H = -\frac{1}{2}\nabla_0^2 + V_{\text{dir}}(\mathbf{r}_0) + V_{\text{exc}}(\mathbf{r}_0) + V_{\text{pol}}^L(\mathbf{r}_0). \quad (5.6)$$

In equation (5.6), $V_{\text{dir}}(\mathbf{r}_0)$ and $V_{\text{exc}}(\mathbf{r}_0)$ are the direct and exchange interactions of the scattering electron with the neon target which is represented by a Hartree-Fock wavefunction. The angular momentum dependent polarization potential is given the form

$$V_{\text{pol}}^L(\mathbf{r}_0) = -\frac{\alpha_d(1 - \exp(-r_0^6/\rho_L^6))}{2r_0^4}, \quad (5.7)$$

where α_d is the static dipole polarizability which is set to $2.669 a_0^3$ [420]. The adjustable parameters, ρ_L are fixed by reference to the value of the phase shifts near $k \approx 0.80 a_0^{-1}$.

Higher ℓ phase shifts are given by the modified effective range theory (MERT) formula [438–440],

$$\tan(\delta_\ell) = \frac{\pi\alpha_d k^2}{(2\ell - 1)(2\ell + 1)(2\ell + 3)}. \quad (5.8)$$

The SDpT cross sections are tabulated on a dense momentum grid, with spacings of $\Delta k = 0.001 a_0^{-1}$ at the lowest momenta and a spacing of $\Delta k = 0.01 a_0^{-1}$ at the higher momenta. The net number of points in the tabulation is 139. A momentum grid provides a better representation of the variations in the cross section at low energies than a similarly sized energy grid.

One characteristic of the e^- -neon σ_m is its abnormally small size of $\approx 0.17 \times 10^{-20} \text{ m}^2$ at zero-energy ($U = 0$). The cross section increases rapidly as the energy increases and is about three times larger at thermal energies.

Besides the SDpT cross section set, two other theoretical cross section sets have been considered. One set is the momentum-transfer cross section from the *ab initio* B-spline R-matrix (BSR) calculations [422, 423]. The basis used in this calculation was large. The BSR calculation does not report the viscosity cross section (or phase shifts) that would allow a solution of the Boltzmann equation to go beyond the two-term approximation. However, the BSR calculation gave elastic, excitation and ionization cross sections that extend to high-energy and therefore can be used in simulations of electron transport at high E/n_0 .

Another theoretical cross section is that from the multi-configuration Hartree-Fock (MCHF) calculations [441]. One limitation with the MCHF data is that the data is restricted to energies with $U \leq 7 \text{ eV}$ and further only the elastic and momentum-transfer cross sections are given. The MCHF σ_m was set to its 7 eV value for all energies greater than 7 eV when solving the Boltzmann equation.

Other momentum-transfer cross sections are essentially derived from experiment. The cross section of Robertson [43] was determined by solving the two-term Boltzmann equation and iteratively adjusting the momentum-transfer cross section. The same approach was used by the Rikkyo group [10], except in this case the momentum-transfer cross section was tuned by fitting to the characteristic energy D_T/μ . Another approach by O'Malley and Crompton used modified effective

range theory (MERT) to help derive expressions of the scattering phase shifts at low-energy [432] by fitting the ANU drift velocity measurements. The scattering length derived from the O'Malley fit was $0.214 \pm 0.005 a_0$. Most of the electron-Ne momentum-transfer cross sections in the LXCat database [416, 442] incorporate elements of the Robertson [43] or O'Malley [432] σ_m .

The recommended cross section published by Buckman and Elford [18, 443] is an amalgam of the Robertson and O'Malley cross sections for $U < 4$ eV. The zero-energy cross section of $0.163 \times 10^{-20} \text{ m}^2$ is slightly larger than that of O'Malley. At higher energies this cross section was derived from crossbeam measurements [444, 445] and the MCHF calculations [441, 446].

The cross section of Morgan [416, 447] is essentially the Buckman cross section up to 4 eV, but has omitted many energies from the Buckman tabulation below 0.03 eV. The Morgan cross section starts to deviate from the Buckman cross section for $U > 4$ eV.

The SIGLO database [416, 448, 449] uses the Robertson σ_m [43] data from 0.03 to 6.0 eV. The zero-energy cross section of $0.161 \times 10^{-20} \text{ m}^2$ was computed using the O'Malley scattering length [432]. The cross section at energies greater than 6 eV is different from the Robertson cross section and is taken from Shimamura [450].

The Biagi σ_m is stated to be taken from version 8.9 of the Magboltz Monte Carlo program [416, 451–453]. At low energies, the momentum-transfer cross section is based on the MERT fitting formulae of O'Malley [432]. Examination of the source code of the Magboltz program indicates no values below 1 eV, but values below 1 eV are tabulated in the LXcat database. The $U = 0$ cross section was fixed to the value at 0.0001 eV, but this is about 8% larger than expected from the O'Malley scattering length.

The Puech data for neon was initially described in [454, 455]. It is stated that this cross section was taken from Robertson [43] for $U < 7$ eV while the cross section of Hayashi is used at higher energies. Examination of the tabulation reveals differences of a few percent with the Robertson σ_m across the energy range for which Robertson tabulate the cross section.

A new empirical cross section was constructed from the SDpT by multiplying it by a simple energy dependent scaling factor of the form, $A = 1/(1 + \alpha \exp(-U/\beta))$. The choice of $\alpha = 0.08$ and $\beta = 0.089$ eV gave a σ_m that gave a superior fit to the ANU W data for $E/n_0 < 0.01$ Td. This cross section is identified in all subsequent text as the SDpTv2 cross section. The scattering length of the SDpTv2 cross section is $0.2158 a_0$.

In the following subsections, detailed comparisons of transport parameters computed with the SDpT, BSR, SDpTv2 and Buckman cross sections are given as a function of the applied reduced electric field, E/n_0 . The Buckman cross section was chosen as a representative example of the empirically derived cross sections. Some summary assessments, e.g. the root mean square differences from experiment, where all cross sections are tested against available transport data are also made.

5.2.2 Comparisons with transport data

Comparisons are made with four sets of experimental data. First there are the drift velocities of the ANU group [43]. Drift velocities at applied electric fields ranging from 0.001594 Td to 2.003 Td have been made at 77 K and 293 K. The stated uncertainty for this set of drift velocities is $\pm 1\%$. In addition, there are the characteristic energies from the University of Rikkyo group [10]. They were obtained at 293 K using values of E/n_0 ranging from 0.014 Td to 0.40 Td and are reported with a stated uncertainty of $\pm 3\%$. Finally, the diffusion coefficient at thermal energies has been measured [181, 433–435].

The mass of the neon atom in the solution of the Boltzmann equation was taken as 20.1797 amu [456].

Validity of the two-term approximation

Two different solutions of the Boltzmann equation were made using the SDpT cross section. One of the solutions was made using the two-term approximation. The other solution was a four-term solution which included the viscosity cross section, σ_v . The differences in the drift velocity and diffusion coefficients due to the two-term and four-term solutions was always less than 0.01% at all values of $E/n_0 < 2$ Td. This is a reflection of the isotropic nature of the velocity distribution function at these reduced electric fields. This is a consequence of the dominance of elastic scattering which is essentially isotropic nature, and as such collisions act to randomize the velocities with minimal changes in the speeds. This level of precision justifies the use of the two-term approximation in this reduced electric field regime, and all transport parameters quoted in this section, unless stated otherwise, were computed with the two-term approximation.

Numerical representation of the cross section

As the present work is focused on the comparisons with swarm parameters at a level of accuracy approaching 1% it is desirable to test the accuracy of the numerical representation of the cross sections. The cross sections used in the solution of the Boltzmann equation are typically given as a set of discrete points tabulated on a numerical grid [10, 43]. The density of grid points, and the approach used to interpolate between those points will have an impact upon the calculated transport parameters. This is evidenced by the fact that the improved numerical representations of vibrational cross sections did go some way towards reducing the discrepancies between vibrational cross sections derived from swarm and beam experiments [182].

The importance of the numerical representation of the cross section was tested by solving the Boltzmann equation with different tabulations of the same SDpT cross section. The SDpT cross sections use a high density tabulation with velocity increments of $0.001 a_0^{-1}$ near the $U = 0$ threshold. The SIGLO cross section has no cross section values below 0.030 eV. Removing all points below 0.03 eV from the SDpT tabulated cross section results in the 77 K W at $E/n_0 = 0.001594$ Td decreasing by 0.2% and the 77 K D_T/μ characteristic energy increasing by 8%. The characteristic energy is potentially much more sensitive to the numerical representation of the cross section than the drift velocity.

Comparison with drift velocities

Drift velocities at $T_0 = 77$ K computed with the SDpT, SDpTv2, BSR and Buckman cross sections are compared with the measured ANU drift velocities in Table 5.1. The SDpT W utilized a multi-term solution of the Boltzmann equation and natural cubic spline interpolation was used to convert the tabulated values into a continuous function. All other calculations were done using the two-term approximation and linear interpolation. Table 5.2 compares the ANU $T_0 = 293$ K W [43] with those computed with the SDpT, SDpTv2, BSR and Buckman cross sections. The mean energy of the swarm at 77 K and 293 K is depicted in Figure 5.1 for applied reduced electric fields ranging from approximately 0.001 Td to 2.0 Td. The mean energies and swarm parameters for the two different temperatures are almost the same for $E/n_0 > 0.03$ Td. The lowest mean energy for the 77 K data set occurs at 0.001594 Td and was 0.031 eV.

The SDpT W tend to be slightly smaller (about 0.5 – 2%) than the 77 K ANU drift velocities for $E/n_0 < 0.010$ Td. For larger values of E/n_0 there are no instances of differences exceeding

Table 5.1: Drift velocities, in units of 10^3 ms^{-1} , as a function of the reduced electric field, for electrons in neon at $T_0 = 77 \text{ K}$. The stated uncertainty for the ANU experimental drift velocities [43] is 1%.

E/n_0 [Td]	SDpT [420]	SDpTv2	BSR [416, 422, 423]	Buckman [443]	ANU [43]
0.001594	0.4177	0.4258	0.3998	0.4245	0.424
0.002390	0.4994	0.5070	0.4884	0.5055	0.508
0.003187	0.5639	0.5700	0.5563	0.5693	0.572
0.003984	0.6180	0.6245	0.6117	0.6227	0.625
0.004781	0.6651	0.6711	0.6590	0.6691	0.671
0.005578	0.7072	0.7127	0.7007	0.7106	0.712
0.006374	0.7454	0.7504	0.7381	0.7481	0.751
0.007171	0.7805	0.7851	0.7724	0.7827	0.785
0.007968	0.8131	0.8173	0.8041	0.8148	0.817
0.01195	0.9499	0.9525	0.9354	0.9497	0.953
0.01594	1.060	1.061	1.040	1.058	1.062
0.01992	1.153	1.154	1.129	1.150	1.154
0.02390	1.235	1.236	1.208	1.232	1.235
0.03187	1.378	1.378	1.347	1.374	1.378
0.03984	1.501	1.501	1.468	1.496	1.500
0.04781	1.611	1.611	1.576	1.605	1.609
0.05578	1.711	1.711	1.674	1.704	1.707
0.06374	1.803	1.803	1.765	1.795	1.800
0.07171	1.889	1.889	1.850	1.881	1.885
0.07968	1.970	1.970	1.931	1.962	1.965
0.1195	2.325	2.324	2.281	2.315	2.320
0.1594	2.624	2.624	2.577	2.616	2.618
0.1992	2.888	2.888	2.839	2.883	2.883
0.2104	2.957	2.957	2.907	2.953	2.953
0.2390	3.126	3.126	3.075	3.125	3.125
0.3187	3.550	3.550	3.492	3.555	3.55
0.3984	3.921	3.921	3.856	3.932	3.92
0.4781	4.250	4.250	4.182	4.269	4.25
0.5259	4.432	4.432	4.362	4.455	4.44
0.5578	4.548	4.548	4.477	4.574	4.55
0.6374	4.819	4.819	4.746	4.853	4.82

1%. The SDpTv2 cross section, which has a smaller cross section below $U < 0.15 \text{ eV}$, gives drift velocities that reproduce the ANU data with higher accuracy. Table 5.3 reports the root mean square (RMS) of the relative difference between calculated and experimental transport parameters for a number of momentum-transfer cross sections. The RMS relative difference of the SDpTv2 cross section is four times smaller than the RMS relative difference for the SDpT cross section. Another useful estimate of the accuracy is the largest relative difference between the calculated and measured transport parameters. These are listed in Table 5.4. This is 1.70% for the SDpT cross section, and 0.42% for the SDpTv2 cross section. The SDpTv2 cross section is in perfect agreement with the 77 K ANU transport data given that the stated experimental uncertainty is 1% [43].

Both the SDpT and SDpTv2 cross sections give almost the same drift velocities for the 293 K data set. The lowest value of E/n_0 for the 293 K data set was 0.01518 Td. The lowest mean energy for this data set is about 0.05 eV, and at this energy the differences between the SDpT and SDpTv2 σ_m are insignificant. The transport coefficients computed with these cross sections agree with the ANU W to better than 0.5% for all $E/n_0 < 1.5 \text{ Td}$.

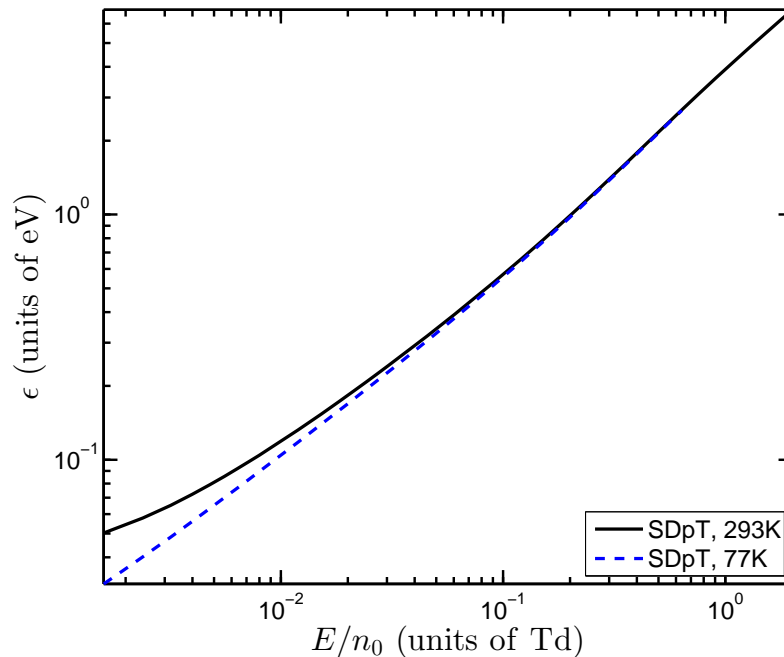


Figure 5.1: The mean energy (in eV) as a function of E/n_0 (in Td) for electron swarms in neon. The mean energy was computed using the SDpT cross section.

The SDpT and SDpTv2 transport parameters show substantial differences with the ANU data at $E/n_0 = 1.821$ and 2.003 Td. The mean energy exceeds 5 eV when $E/n_0 > 1.6$ Td and it is likely that excitations to the lowest energy excited states near 16.6 eV are starting to influence W at the two largest values of E/n_0 .

The discrepancies between the BSR W and experiment are much larger, with a 5.7% discrepancy with the 77 K ANU drift velocity at $E/n_0 = 0.001594$ Td and an RMS difference of 2.2%. The BSR drift velocity is smaller than the ANU (and SDpT) drift velocities at all values of E/n_0 which is indicative of a cross section which is too large. The BSR momentum-transfer cross section is larger than the SDpT cross section for all energies below the first excitation threshold. The difference is especially significant at $U = 0$ eV where the BSR cross section is set to 0.500×10^{-20} m² (equivalent to a scattering length of $0.377 a_0$), about 3 times larger than the SDpT cross section. The BSR σ_m is roughly constant for $U < 0.01$ eV, a functional dependence that is not compatible with MERT. The very large differences in the zero-energy cross section do not lead to a commensurate change in the drift velocity because the cross section is so small at $U = 0$. The tendency for the BSR drift velocities to be smaller than experiment is also apparent in the 293 K data set.

The Buckman cross section is based on the original momentum-transfer cross section of Robertson [43]. As expected, this cross section does a uniformly good job of reproducing the measured drift velocities at almost all values of E/n_0 . The RMS difference of this momentum-transfer cross section with the 77 K and 293 K drift velocity data is less than 1%. The Buckman cross section does tend to be about 1% larger than the ANU drift velocity for $E/n_0 > 0.6$ Td.

The *ab initio* MCHF σ_m gives larger RMS differences with the ANU drift velocities than the SDpT or SDpTv2 cross sections. The larger RMS difference is partly due to incomplete information about its behaviour at higher energies.

The SIGLO, Morgan and Biagi cross sections accurately reproduce the ANU drift velocity to a high degree of accuracy, and the largest RMS difference resulting from any of these cross sections is less than 0.4%. This is not surprising since all three cross section sets are based on the

Table 5.2: Drift velocity, in units of 10^3 ms^{-1} , as a function of the reduced electric field, for electrons in neon at $T_0 = 293 \text{ K}$. The stated uncertainty for the ANU drift velocities is 1%.

E/n_0 [Td]	SDpT [420]	SDpTv2	BSR [416, 422, 423]	Buckman [443]	ANU [43]
0.01518	0.9738	0.9756	0.9530	0.9721	0.976
0.01821	1.052	1.053	1.028	1.050	1.052
0.02125	1.122	1.123	1.096	1.119	1.122
0.02428	1.186	1.187	1.158	1.183	1.185
0.02732	1.246	1.246	1.216	1.242	1.243
0.03035	1.301	1.301	1.270	1.296	1.300
0.04553	1.536	1.536	1.501	1.530	1.532
0.06071	1.729	1.729	1.691	1.722	1.723
0.09106	2.046	2.046	2.005	2.038	2.040
0.1214	2.311	2.311	2.267	2.302	2.300
0.1518	2.544	2.544	2.498	2.536	2.532
0.1821	2.754	2.754	2.706	2.748	2.741
0.2125	2.948	2.948	2.897	2.944	2.935
0.2428	3.127	3.127	3.075	3.126	3.115
0.2732	3.297	3.297	3.241	3.298	3.284
0.3036	3.456	3.456	3.398	3.460	3.445
0.3643	3.750	3.750	3.688	3.759	3.738
0.4250	4.018	4.018	3.952	4.033	4.004
0.4553	4.144	4.144	4.076	4.161	4.130
0.4857	4.264	4.264	4.195	4.284	4.255
0.5464	4.492	4.492	4.421	4.518	4.478
0.6071	4.704	4.704	4.632	4.736	4.699
0.7589	5.178	5.178	5.105	5.226	5.170
0.9106	5.589	5.589	5.517	5.654	5.576
1.062	5.954	5.954	5.883	6.033	5.945
1.214	6.284	6.284	6.216	6.377	6.280
1.336	6.529	6.529	6.462	6.631	6.542
1.821	7.377	7.377	7.317	7.509	7.813
2.003	7.659	7.659	7.601	7.799	8.491

Robertson [43] or O'Malley [432] cross sections at low energies with some fine tuning occurring at energies greater than 4 eV.

Comparison with the characteristic energy

Table 5.5 gives the characteristic energy, D_T/μ , for a swarm travelling through neon gas at $T_0 = 293 \text{ K}$. Experimental data comes from the Rikkyo group [10]. The key conclusion to be drawn from the Table 5.5 is that there is a 3% discrepancy at the level of the transport coefficients between cross sections that reproduce drift velocity measurements and cross sections that reproduce the Rikkyo data for the transverse diffusion coefficients.

The SDpT D_T/μ tend to be larger than the Rikkyo data. The RMS difference is 2.5% with the largest difference being 3.5%. The largest differences tend to occur at the smallest values of E/n_0 . This is clearly visible in Figure 5.2 where the relative difference is given. The SDpT cross section would need to be increased in order to be compatible with the Rikkyo experiment. However, the SDpTv2 σ_m is actually smaller than the SDpT σ_m . Hence the RMS difference of the SDpTv2 transport parameters with the Rikkyo data has increased to 3.3%. Figure 5.2 shows that the increase in the difference with the Rikkyo data is most prominent at the lowest E/n_0 .

Four of the empirical cross sections, the Buckman, SIGLO, Morgan and Biagi cross sections have RMS differences that range from 2.8% to 3.7%. These cross sections give a D_T/μ that exceeds

Table 5.3: The RMS relative difference between experimental and calculated transport parameters. The $E/n_0 = 1.821$ and 2.003 Td W are not part of the error calculation for the 293 K data set.

Set	W 77 K [43]	W 293 K [43]	D_T/μ [10]
SDpT [420]	0.00618	0.00295	0.0253
BSR [416, 422, 423]	0.0221	0.0163	0.0132
MCHF [441]	0.00542	0.00819	0.0239
SDpTv2	0.00146	0.00296	0.0333
SIGLO [416, 448]	0.00143	0.00209	0.0318
Buckman [443]	0.00324	0.00718	0.0278
Morgan [416, 447]	0.00369	0.00154	0.0366
Biagi v8.9 [416, 452, 453]	0.00299	0.00285	0.0303
Puech [416, 454, 455]	0.0143	0.0104	0.0157

Table 5.4: The maximum relative difference between experimental and calculated transport parameters. The relative difference is given above the value of E/n_0 at which it occurs. The E/n_0 at 1.821 and 2.003 Td at 293 K were excluded from consideration.

Set	W 77 K [43]	W 293 K [43]	D_T/μ [10]
SDpT	0.0170	0.00477	0.0346
	0.002390	0.1214	0.014
BSR [416, 422, 423]	0.0571	0.0236	0.0237
	0.001594	0.01518	0.35
MCHF [441]	0.0101	0.0180	0.0391
	0.002390	1.214	0.014
SDpTv2	0.00417	0.00475	0.0553
	0.001594	0.1214	0.014
SIGLO [416, 448, 449]	0.00301	0.00380	0.0530
	0.5259	0.2732	0.014
Buckman [443]	0.00694	0.0154	0.0507
	0.6374	1.214	0.014
Morgan [416, 447]	0.00817	0.00310	0.0639
	0.007968	0.01518	0.014
Biagi v8.9 [416, 452, 453]	0.00502	0.00523	0.0591
	0.003187	1.336	0.014
Puech [416, 454, 455]	0.0380	0.0171	0.0267
	0.001594	0.2732	0.30

experiment in all cases. The inherent discrepancy between the drift velocity and diffusion data are clearly seen in Table 5.3. The cross section sets that have less than 0.5% RMS discrepancy with the drift velocity data all have greater than 3% RMS relative differences with the diffusion data.

The BSR cross section gives a smaller RMS difference with the Rikkyo data than the other two *ab initio* cross sections. The BSR cross section is larger than these other cross sections and this results in smaller values of D_T/μ . The BSR D_T/μ are mostly 1 – 2% too small over the entire range of E/n_0 . However, the relative difference of all values of BSR D_T/μ lie within the stated uncertainty of 3%. One feature of the graph is the 1.6% jump that occurs between 0.30 and 0.35 Td.

The Puech cross section has RMS differences with the W and D_T/μ data of 1.0 to 1.5%. This suggests that this cross section has been constructed to give equally good fits to both the W and D_T/μ transport data.

The cross sections that give the better than 0.5% accuracy fits to the ANU drift velocities give RMS differences of 3% with the D_T/μ data. This does not constitute an irreconcilable conflict since the stated uncertainty in the Rikkyo measurements was 3%. However, one aim of this

Table 5.5: The characteristic energy D_T/μ , (in eV) with electric field (in Td), for electrons in neon at $T_0 = 293$ K. The stated uncertainty of the Rikkyo data is 3%.

E/n_0 [Td]	SDpT [420]	SDpTv2	BSR [416, 422, 423]	Buckman [443]	Rikkyo [10]
0.014	0.1314	0.1340	0.1268	0.1334	0.127
0.017	0.1491	0.1518	0.1442	0.1511	0.146
0.020	0.1660	0.1687	0.1606	0.1679	0.162
0.025	0.1926	0.1953	0.1864	0.1943	0.187
0.030	0.2177	0.2204	0.2105	0.2193	0.213
0.035	0.2418	0.2444	0.2336	0.2431	0.236
0.040	0.2649	0.2674	0.2557	0.2660	0.260
0.050	0.3091	0.3115	0.2978	0.3098	0.300
0.060	0.3511	0.3533	0.3379	0.3513	0.341
0.070	0.3914	0.3935	0.3764	0.3911	0.382
0.080	0.4304	0.4324	0.4137	0.4297	0.420
0.10	0.5054	0.5072	0.4856	0.5038	0.491
0.12	0.5774	0.5791	0.5549	0.5750	0.562
0.14	0.6473	0.6488	0.6221	0.6440	0.630
0.17	0.7492	0.7506	0.7204	0.7449	0.730
0.20	0.8486	0.8499	0.8165	0.8435	0.828
0.25	1.011	1.012	0.9733	1.005	0.987
0.30	1.169	1.170	1.127	1.163	1.14
0.35	1.326	1.327	1.279	1.320	1.31
0.40	1.480	1.481	1.429	1.476	1.46

section is to test the quality of various momentum-transfer cross sections at a 1% level of precision. Consequently, precedence should be given to fitting ANU W data ahead of Rikkyo D_T/μ data.

Comparison with the thermal diffusion coefficient

The thermal diffusion coefficient for electrons diffusing in neon has been measured on a number of occasions [181, 433–435]. Discounting some earlier measurements, estimates have been made at Oak Ridge National Laboratory (ORNL) [433], the Laboratori C. I. S. E [180, 181] and the ANU [434, 435]. The C.I.S.E. value of n_0D is converted from the stated diffusion constant of $D_0 = (2860 \pm 100) \text{ cm}^2 \text{ s}^{-1}$ [181] by assuming that measurements were taken at a gas temperature of 273 K.

The three experimental diffusion constants are not compatible within their mutual experimental uncertainties when temperature dependent effects are taken into consideration. Preference is given to the ANU value of n_0D .

Comparisons of experimental diffusion coefficients, n_0D with calculations using the SDpT and BSR cross section sets can be found in Table 5.6. The mean energy of a thermal electron cloud at 295 K is 0.0381 eV. The n_0D diffusion coefficient varies slowly with temperature. For example, using the SDpTv2 cross section and decreasing the temperature results in n_0D decreasing from $75.04 \times 10^{20} \text{ mm}^{-1} \text{ s}^{-1}$ to $74.14 \times 10^{20} \text{ mm}^{-1} \text{ s}^{-1}$, a change of only 1.2%.

The good agreement between the MCHF and ANU n_0D coefficients suggests that the ANU diffusion experiment would be consistent with a scattering length that is close to the MCHF calculation, namely $0.2218 a_0$ [441]. The SDpTv2 value of n_0D of $75.04 \times 10^{20} \text{ mm}^{-1} \text{ s}^{-1}$ lies just outside the error bounds for the ANU measurement.

One of the issues affecting comparisons with the empirically derived cross sections such as the SIGLO, Morgan and Biagi is their numerical representation. These cross sections all have relatively few tabulated points below 0.1 eV where the cross section changes by a factor of 4. This had an

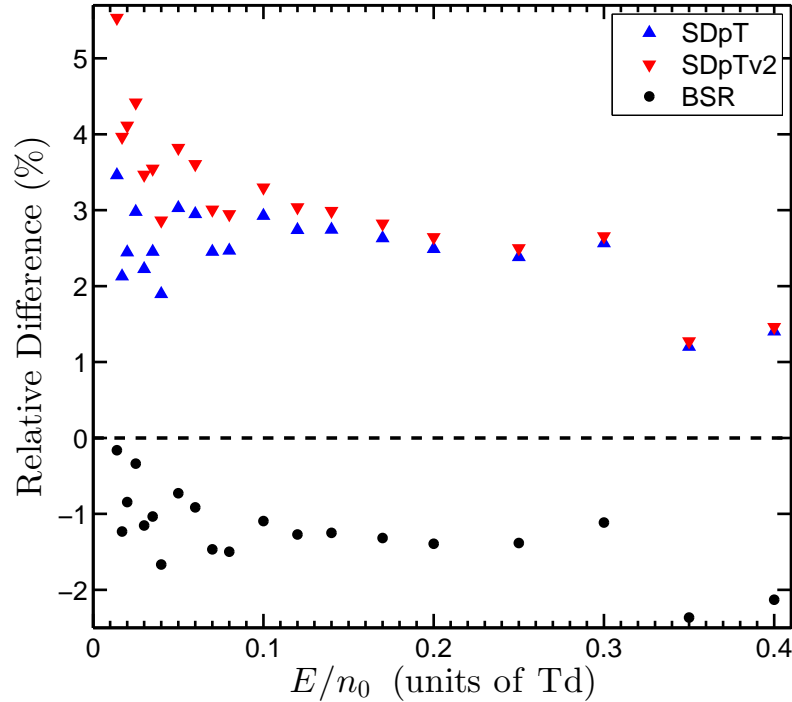


Figure 5.2: The relative difference, between calculated characteristic energies and the experimental data of the University of Rikkyo [10] group.

Table 5.6: The thermal diffusion coefficient, n_0D , in units of $10^{20} \text{ mm}^{-1} \text{ s}^{-1}$, for thermal electrons in neon gas.

Source	n_0D	
	$T_0 = 295 \text{ K}$	$T_0 = 273 \text{ K}$
ORNL [433] ($T_0 = 300 \text{ K}$)	64.7	
Laboratori C.I.S.E [181, 434, 435]		76.9 ± 2.4
ANU [434]	$72.7^{+2.0}_{-0.9}$	
SDpT [420]	71.28	70.36
BSR [416, 422, 423]	59.51	58.05
MCHF [441]	72.73	71.81
SDpTv2	75.04	74.14
SIGLO [416, 448, 449]	77.61	77.01
Buckman [443]	74.68	73.81
Morgan [416, 447]	75.93	75.13
Biagi v8.9 [416, 452, 453]	79.97	79.48
Puech [416, 454, 455]	66.47	65.41

impact of 1-4% on the calculated diffusion constant. A significant part of the differences between the n_0D values of the Buckman, SIGLO, Morgan and Biagi values of n_0D arises from the energies at which the cross sections are tabulated.

The BSR cross section gives a diffusion coefficient of $59.5 \times 10^{20} \text{ mm}^{-1} \text{ s}^{-1}$, about 20% lower than the ANU value. This underestimate further illustrates the problems with the BSR cross section at energies below 0.15 eV.

One of the salient conclusions drawn from Table 5.6 is the overall degree of consistency between the Buckman, SDpTv2, MCHF and ANU values of n_0D . The Buckman and SDpTv2 cross section give very similar drift velocities that are close to ANU values [43]. These are effectively compatible with the ANU n_0D within the experimental uncertainty.

There is one other electron transport parameter that has been measured for neon, the longitudinal diffusion coefficient on mobility, D_L/μ [428]. However, the lowest value of E/n_0 for which measurements have been made is 1.4 Td and the effects of inelastic collisions could make a contribution here. Consequently, no calculations of the longitudinal diffusion parameter were made.

5.2.3 Recommended low-energy momentum-transfer cross section

Two measures have been given as metrics to test the performance of the different cross sections against the drift velocity and transverse diffusion data. These are the root mean square of the relative difference between the calculated and measured transport parameters and secondly the largest relative difference between the calculated and measured transport parameters.

The SIGLO momentum-transfer cross section gives drift velocities with very small RMS difference from the ANU experiment of 0.14% at 77 K and 0.21% at 293 K, which are slightly smaller than those using the SDpTv2 cross section. Despite these very low differences from ANU drift velocity data, in many aspects the SDpTv2 cross section has one significant advantage over the SIGLO cross section. For example, the SDpTv2 diffusion constant, n_0D , is closer to the ANU experimental value than the SIGLO value of n_0D . The smaller RMS difference of the SIGLO values of W is of minor importance since all of the SIGLO and SDpTv2 values of the drift velocity lie within the stated 1% uncertainty. However, the SDpTv2 cross section, being derived from a large *ab initio* calculation, has a functional dependence based on a properly founded dynamical description of the electron-neon interaction as opposed to the SIGLO cross section which like other purely empirical cross sections is a table of numerical values constructed to fit experimental values of the drift velocity. In effect, the SDpTv2 σ_m varies smoothly as a function of energy in a manner that can be expected to be consistent with the actual momentum-transfer cross section.

5.3 Positron swarms in gaseous helium

In the classic positron gas annihilation experiment [11, 169, 457], positrons are emitted into a gas, undergo thousands of inelastic collisions while thermalizing and eventually a mixture of low-energy positrons and ortho-positronium is left in the gas. The free positrons and ortho-positronium then experience elastic collisions until they are in thermal equilibrium with the gas. When positrons collide with atoms, there is always the possibility of in-flight annihilation of the positron with the atomic electrons, and experiments typically result in the determination of a number of annihilation parameters. One parameter is the positronium fraction, i.e. the number of positrons surviving in the form of free positronium. Another parameter is the annihilation parameter, $z_{\text{eff}}(k)$, which can be defined in terms of the spin-averaged annihilation cross section, $\sigma^{\text{ann}}(k)$ by the identity [458]

$$z_{\text{eff}}(k) = \frac{k \sigma^{\text{ann}}(k)}{\pi c r_0^2}, \quad (5.9)$$

where r_0 is the classical electron radius and c is the speed of light. The annihilation parameter is determined by measuring the intensity of 2γ annihilation as a function of time. Finally, there is the pick-off annihilation rate which is a consequence of annihilating collisions between the positron in long-lived triplet positronium and the electrons in the target atom.

In addition, the time dependence of the Z_{eff} during thermalization contains information about the momentum-transfer cross section, the initial energy distribution of the positrons, and the energy dependence of Z_{eff} . The time dependent behaviour of Z_{eff} for positrons annihilating in the rare gases

has been extracted from the annihilation signal [11–13, 459, 460]. Experimental information about the energy dependence of the positron-atom momentum-transfer and annihilation cross sections can also be obtained by performing experiments in a static electric field [15]. The presence of the electric field leads to the drifting and diffusing positrons having a different energy distribution at equilibrium.

In this section the spatially-homogeneous Boltzmann equation is solved to determine the behaviour of $Z_{\text{eff}}(t)$ for positrons thermalizing in helium. The simulations are restricted to positrons with an energy below the positronium formation threshold where the only possible processes are elastic scattering and positron annihilation with the atomic electrons. The present solutions gave a fit to the experimental data [11, 12] that was significantly improved over previous simulations [12, 16]. The variation of the equilibrium z_{eff} versus electric field strength has also been determined and again the agreement with experimental data was a significant improvement over previous calculations [15, 16].

5.3.1 Cross sections

The collision model is based upon an earlier semi-empirical model of positron scattering and annihilation [461]. In this model, the interaction between the positron and the atoms was written as the sum of two terms. The first term is the repulsive direct interaction as computed from the Hartree-Fock wave function of the target atom. The second term is a semi-empirical polarization potential. In the earlier work [461], a single polarization potential was used for all partial waves. In the present work, the polarization potential depends on the orbital angular momentum, L , of the colliding positron. The effective Hamiltonian given in equation (5.6) is simplified by the lack of the exchange process in positron scattering, i.e.,

$$H = -\frac{1}{2}\nabla_0^2 + V_{\text{dir}}(\mathbf{r}_0) + V_{\text{pol}}^L(\mathbf{r}_0). \quad (5.10)$$

The adjustable parameter, ρ_L in the polarization potential (5.7) is fixed by reference to some external factor, e.g. the value of the scattering length as deduced from a high precision *ab initio* calculation. All the complicated many-body interactions between the positron and atomic electrons can be absorbed into the polarization potential. There have been many investigations of positron-atom interactions in the past that have used conceptually similar Hamiltonians [462–469].

The underlying philosophy of the collision model is semi-empirical, no attempt at determining the specific form of the polarization potential by *ab initio* calculation is made. Phase shifts and cross sections produced by this approach have been shown to reproduce *ab initio* calculations over an energy range up to 10 eV provided the adjustable parameter in the polarization potential, namely ρ_L is tuned to reproduce the *ab initio* phase shift at some energy [461]. In low-energy scattering, the speed of the incident particle is negligible compared to the speed of light, and instead the relativistic effects are due to the speed of the electrons in the inner most shells of the target atom. In perturbation theory, relativistic effects are proportional to the fourth power of the atomic number, and become more important as the nuclear charge increases. The helium atom spectrum however, is simple enough that the fine-structure splitting is extremely small, and a non-relativistic treatment is justified. The total elastic, σ_{T} , and momentum-transfer, σ_{m} , cross sections are calculated using a simplified, non-relativistic form of equations (5.3) and (5.4), namely

$$\sigma_{\text{T}}(k) = \frac{4\pi}{k^2} \sum_{\ell=0} (2\ell + 1) \sin^2(\delta_{\ell}) \quad (5.11)$$

Table 5.7: The parameters ρ_L and G_L for helium in the model potential. Note $\alpha_d = 1.383$ (a_0^3) [44]. The particular numerical criteria (and their source) used to fix ρ_L and G_L are specified.

L	ρ_L (a_0)	Source	G_L	Source
0	1.510	$\delta_0(k = 0.2) = 0.041$ [482]	2.979	$z_{\text{eff}}(k = 0.0) = 3.99$ [483]
1	1.440	$\delta_1(k = 0.3) = 0.019$ [482]	3.96	$z_{\text{eff}}(k = 0.4) = 0.497$ [484]
2	1.00	$\delta_2(k = 0.8) = 0.025$ [485]	4.65	$\text{He}^+ (G_2 - 1)/(G_1 - 1) = 1.233$ [481]

$$\sigma_m(k) = \frac{4\pi}{k^2} \sum_{\ell=0} (\ell + 1) \sin^2(\delta_{\ell+1} - \delta_\ell) \quad (5.12)$$

where δ_ℓ are the phase shifts.

Besides reproducing the low-energy elastic cross section, this model potential approach also does a reasonable job of reproducing $z_{\text{eff}}(k)$. The annihilation parameter is computed from the scattering wavefunction using [458, 470, 471]

$$z_{\text{eff}}(k) = N_e \int d^3\tau |\Psi(\mathbf{r}_1, \dots, \mathbf{r}_N)\Phi(\mathbf{v}, \mathbf{r}_N)|^2, \quad (5.13)$$

where $\Psi(\mathbf{r}_1, \dots, \mathbf{r}_N)$ is the anti-symmetrized wave function of the target atom, $\Phi(\mathbf{v}, \mathbf{r}_N)$ is the positron scattering function and $d^3\tau$ represents an integration over all electron co-ordinates. Equation (5.13) is not completely general as the total system wave function is assumed to have the product form $\Psi(\mathbf{r}_1, \dots, \mathbf{r}_N)\Phi(\mathbf{v}, \mathbf{r}_0)$. The expression for $z_{\text{eff}}(k)$ given by equation (5.13) is *spin-averaged*. In the plane wave Born approximation, where the positron wave function is written as a plane wave, the annihilation parameter is equal to the number of atomic electrons, i.e. $z_{\text{eff}}(k) = N_e$.

The $z_{\text{eff}}(k)$ predicted by equation (5.13) is likely to be an underestimate. The attractive nature of the electron-positron interaction leads to strong electron-positron correlations that increase the electron density at the position of the positron, and consequently enhances the annihilation rate [472–475]. Therefore, an L -dependent enhancement factor, G_L , is used to rescale the calculated $z_{\text{eff}}(k)$ for a given partial wave i.e. values for $z_{\text{eff}}^G(k)$ would be computed by

$$z_{\text{eff}}^G(k) = \sum_L z_{L,\text{eff}}^G(k) = \sum_L G_L z_{L,\text{eff}}(k), \quad (5.14)$$

where $z_{L,\text{eff}}(k)$ is the partial annihilation rate for a positron with angular momentum L scattering from the model potential. The values of G_L are fixed by reference to a high quality *ab initio* calculation or to experimental data. This work is concerned with low-energy scattering and under these circumstances the relative collision momentum distribution of the annihilating electron-positron pair is not expected to change much as the positron energy changes slightly. This means that the errors in using an energy independent enhancement factor should not be too large [476, 477]. There have been a number of investigations that have shown that a single multiplicative factor (for each L) can adequately represent the magnitude and energy dependence over the energy range below the first excitation threshold [461, 478–481].

The ability of the model potential calculations to realistically describe the low-energy elastic and annihilation cross sections depends crucially upon the choice of ρ_L and G_L . A number of sources have been used to provide the reference data which was used to fix ρ_L and G_L which are tabulated in Table 5.7.

The cross section computed by Mitroy [6] with the values in Table 5.7 is termed the model potential (MP) cross section set, and is depicted in Figure 5.3 and compared with other calculations and experiment. Cross sections from a polarized orbital (PO) calculation [471, 486] are shown in

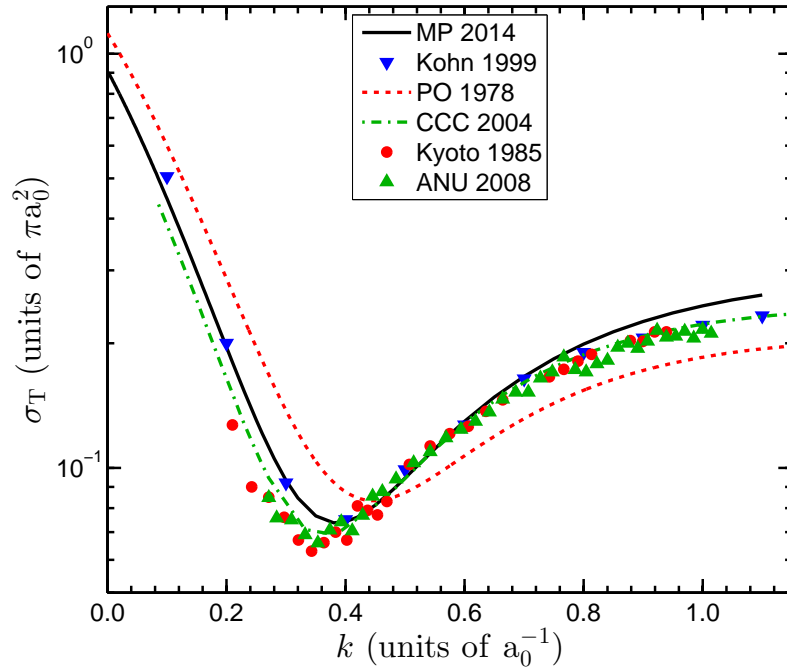


Figure 5.3: The elastic cross section, σ_T (in units of πa_0^2) for positron scattering for helium.

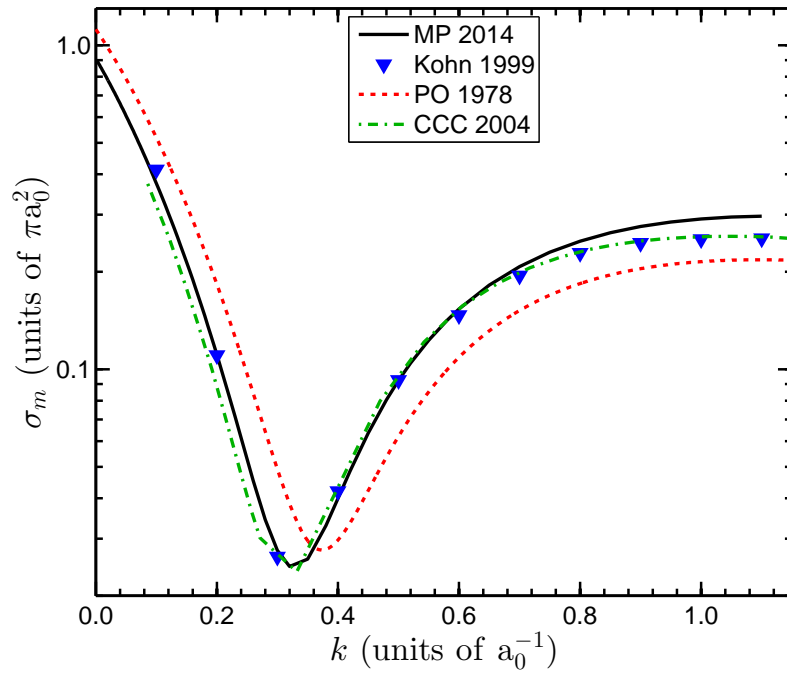


Figure 5.4: The momentum-transfer cross section, σ_m (in units of πa_0^2) for positron scattering for helium.

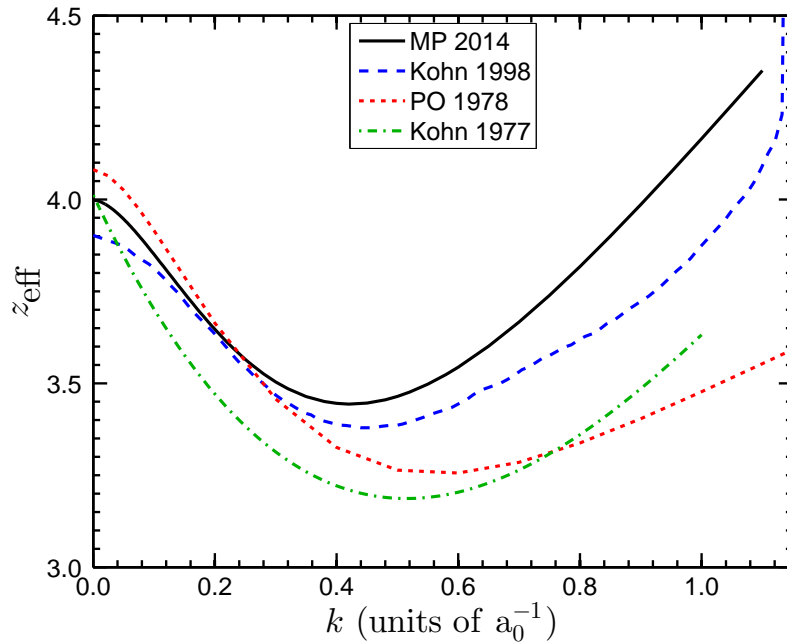


Figure 5.5: The annihilation parameter, z_{eff} for positron scattering for helium.

addition to the calculations mentioned previously. The MP cross section lies very close to the most recent elastic cross section of the University College London (UCL) group [482]. This was expected since the UCL cross section was used to set the cutoff parameters. The PO calculation gives a scattering length which is larger in magnitude and with a Ramsauer minimum occurring at a higher velocity. The convergent close coupling (CCC) calculation [485] has a scattering length that is slightly smaller in magnitude resulting in a smaller cross section below the Ramsauer minimum. There are two sets of experimental data that are included, those by the ANU [487] and Kyoto [488]. Cross sections from some older experiments [489, 490] are not included to reduce clutter in the figure.

The ANU and Kyoto group elastic cross sections do lie closer to the CCC cross sections at the lowest energies. However, the cross sections based on Kohn variational calculations should be preferred. The Kohn variational phase shifts have been validated by new calculations based on the confined variational method (CVM) [483, 491] which reproduce the experimental $Z_{\text{eff}} = \langle z_{\text{eff}} \rangle$ (see Section 2.4). The impact of systematic errors in the experiments can become more severe at the lower energies.

Figure 5.4 plots the momentum-transfer cross section as a function of k for energies below the Ps-formation threshold. It is compared with the Kohn variational momentum-transfer cross section from the UCL group [482] and the CCC momentum-transfer cross section of the Curtin group [485]. The MP cross section lies very close to the momentum-transfer cross sections from the UCL and Curtin groups.

The annihilation parameter as a function of k is depicted in Figure 5.5. The original $z_{\text{eff}}(k)$ of Campeanu and Humberston [12] is characterised by the small size of $z_{\text{eff}}(k)$ near $k = 0.5 a_0^{-1}$. However, there are some obvious problems with the Campeanu and Humberston z_{eff} . This curve shows a variation of $z_{\text{eff}}(k)$ near $k = 0$ that is linear in k . However, an application of effective range theory to annihilating collisions has shown that $z_{\text{eff}}(k) \approx Z_0 + k^2 Z_2$ where Z_0 and Z_2 are constants [492]. Another limitation of this earlier calculation is the omission of contributions from partial waves with $L > 1$. For these reasons the Campeanu and Humberston $z_{\text{eff}}(k)$ should be regarded as being superseded by the later Kohn variational calculations [484, 493].

The later variational calculation [493] did include contributions from the d -wave, and the functional form of $z_{\text{eff}}(k)$ near $k = 0$ is more compatible with the expectations of effective range theory. This later calculation had larger values of $z_{\text{eff}}(k)$ at the minimum despite not including contributions from partial waves with $L > 2$. The MP calculations do include terms from these higher partial waves, with the contribution to z_{eff} at $k = 1.1 a_0^{-1}$ being 0.101. This partly explains why the MP $z_{\text{eff}}(k)$ is larger than the Kohn variational (KV) $z_{\text{eff}}(k)$.

5.3.2 Positron diffusion and thermalization calculations

In positron annihilation studies, positrons are released from a source with an unknown distribution of energies well above thermal energies. The positrons then thermalize through energy and momentum exchanging collisions with the background gas, before eventually annihilating. The process is necessarily nonequilibrium and the positron velocity distribution is non-Maxwellian during the thermalization process. For positron annihilation studies conducted in the presence of an applied electric field, the field drives the electrons out of thermal equilibrium, and the steady-state distribution is no longer Maxwellian in nature. The connection between microscopic scattering processes and macroscopic properties, including the measured annihilation rates, is made under nonequilibrium conditions through Boltzmann's equation [238]. Under spatially homogeneous conditions, the motion of a dilute ensemble of positrons (charge q) moving through a dense background gas of neutral atoms (density n_0) in the presence of an applied electric field E can be described by the Boltzmann equation, (2.2). For the regime of interest, the interaction processes determining the macroscopic properties are elastic scattering and annihilation, characterized respectively by a differential elastic cross section $\sigma(g, \chi)$ (where g and χ are the speed and scattering angle in the centre of mass frame), and the annihilation cross section $\sigma^{\text{ann}}(g)$. First, it must be emphasized that we do not assume that annihilation can be treated perturbatively [12] (i.e., setting $J^{\text{loss}} \approx 0$). The explicit modification of the distribution function due to the annihilation processes is strictly accounted for in a self-consistent manner. Secondly, this is a true multiterm theory, with none of the limitations of the two-term approximation used in previous treatments [12, 16]. There are no *a priori* assumptions on the quasi-isotropy of the velocity distribution function. Angular dependence beyond the momentum-transfer cross sections are accurately included in this multiterm theory.

Positron annihilation in helium under field-free conditions

Initially we consider positron annihilation experiments where positrons are released into a gas of known pressure and the annihilation spectra is measured and interpreted in terms of the transient $Z_{\text{eff}}(t)$ and the steady-state value, Z_{eff} . For helium, the experimental results of the UCL group for $Z_{\text{eff}}(t)$ are displayed in Figure 5.6 as a function of the reduced time, $n_0 t$. Comparison with the calculated transient $Z_{\text{eff}}(t)$ provides some assessment of the positron-helium elastic and annihilation cross sections.

There is limited information regarding the appropriate initial conditions for the speed distribution of the positrons at the start of the $Z_{\text{eff}}(t)$ measurements. Accordingly, there is little point in experimenting with a variety of initial velocity distributions. The initial distributions will have positrons with energies up to the positronium formation threshold. This choice was also made by Campeanu and Humberston [12]. With this choice, there are two obvious distribution functions that can be adopted.

The first of these would be a constant speed distribution, i.e. $f_0^{(0)}(k) = C$ where C is a constant up to some cutoff velocity, $k_\infty = \sqrt{2U_\infty/m}$. The mean energy of this distribution function is

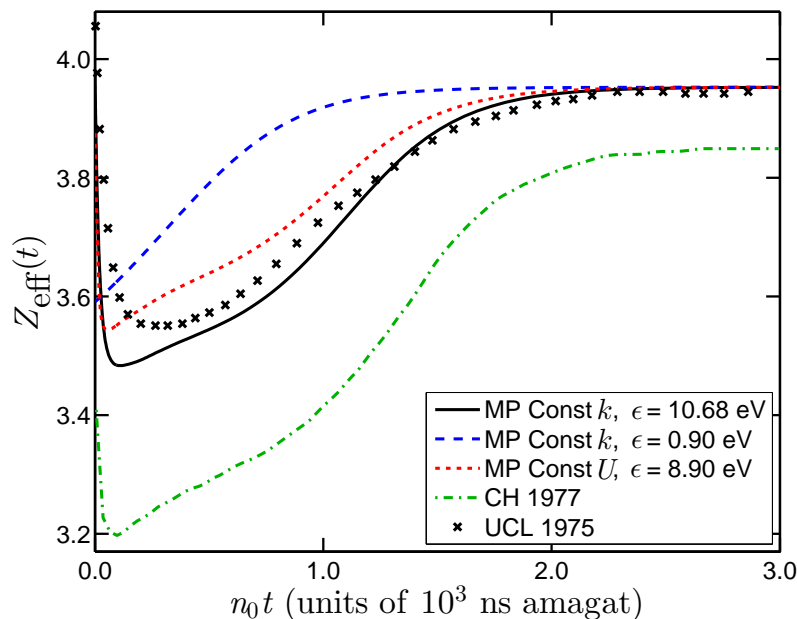


Figure 5.6: Temporal variation of $Z_{\text{eff}}(t)$ for positrons thermalizing in gaseous helium at a temperature of 293 K. The simulations are compared with the UCL experimental data [11] and the CH simulation [12]. The different initial distributions are characterised by varying distributions and average energies; Const v is a constant distribution in v space below the Ps-threshold; Const ϵ is a constant distribution in energy space below the Ps-threshold. See text for details.

given by the identity, $\epsilon = (3/5)(mk_{\infty}^2/2)$. For helium, with $k_{\infty} = 1.1438$ a.u., this leads to $\epsilon = 0.39249$ a.u. = 10.68 eV.

The second initial distribution would be one that was constant in energy space, i.e. $f_0^{(0)}(U)U^{\frac{1}{2}} = C$ where C is a constant up to some cutoff velocity, k_{∞} . The mean energy of this distribution would be $\epsilon = (1/2)(mk_{\infty}^2/2)$, which for helium gives $\epsilon = 0.32707$ a.u. = 8.90 eV.

In Figures 5.6 and 5.7 the calculated temporal variation of $Z_{\text{eff}}(t)$ and the mean energy $\epsilon(t)$ are plotted. Besides the two distributions specified above, we also show an additional $f_0^{(0)}(k) = C$ distribution with $k_{\infty} = 0.3320$ a.u. ($\epsilon = 0.90$ eV). Also shown in Figure 5.6 is the UCL experimental $Z_{\text{eff}}(t)$ and the previous simulation by Campeanu and Humberston (CH) [12]. The UCL $Z_{\text{eff}}(t)$ initially has $Z_{\text{eff}}(t = 0)$ higher than its equilibrium value, it decreases as t increases, until it stabilises before increasing to its equilibrium (thermal) value. This indicates that the initial velocity distribution should have a mean energy that is larger than the energy where $z_{\text{eff}}(k)$ is smallest. The CH profile, which used a constant speed initial distribution, shows these qualitative features. But, the minimum $Z_{\text{eff}}(t)$ during thermalization is 0.3 smaller than the minimum $Z_{\text{eff}}(t)$ seen for the UCL data and the value after thermalization is achieved is too small by 2.3%.

The $Z_{\text{eff}}(t)$ computed with the MP cross sections are in better agreement with the UCL $Z_{\text{eff}}(t)$. The minimum value of $Z_{\text{eff}}(t)$ is much closer to the minimum observed in the UCL experiment. This is a consequence of the larger value of $z_{\text{eff}}(k)$ at the minimum. The asymptotic value of the MP $Z_{\text{eff}}(t)$ is only 0.01 to 0.03 smaller than the UCL data for values of the reduced time greater than 2×10^3 ns amagat. The thermalization times are also compatible with the thermalization time for the UCL experiment. The initial constant speed distribution has a slightly longer thermalization time than the initial constant energy distribution.

Both the MP and CH simulations start with $z_{\text{eff}}(k)$ closer to 4.0 at the $k = 0$ threshold. However, the asymptotic value for the CH simulation as $t \rightarrow \infty$ is more than 0.1 smaller than experiment and the MP asymptotic values. This is due to the incorrect functional dependence of

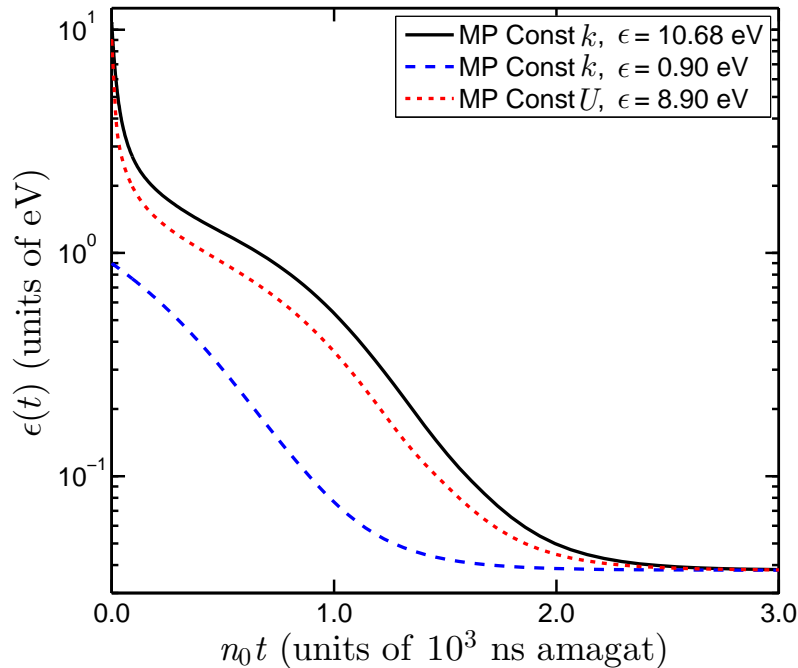


Figure 5.7: Variation of $\epsilon(t)$ for positrons thermalizing in helium for different initial conditions. The temperature of the helium gas was taken as 293 K.

the CH $z_{\text{eff}}(k)$ with k near $k = 0$. As mentioned earlier, the linear dependence of the CH $z_{\text{eff}}(k)$ with k is incompatible with effective range theory [492].

Figure 5.6 also depicts $Z_{\text{eff}}(t)$ for a positron distribution with the mean energy located at an energy lower than the minimum in the $z_{\text{eff}}(k)$ profile. The distribution does not show any sign of the minimum in the $Z_{\text{eff}}(t)$ profiles seen in the UCL experiment and other simulations.

The transient profiles, including the depth of the minimum, are determined by an interplay between the $\sigma_m(k)$, the annihilation cross section and the initial average energy of the positrons. An initial distribution with positron energies up to the Ps-formation threshold is crucial to a giving a correct prediction of the overall thermalization time. While there are small uncertainties in the MP $\sigma_m(k)$, these uncertainties have minimal impacts on the thermalization time and can be effectively neglected as a source of error. The size of the dip in $Z_{\text{eff}}(t)$ is primarily driven by the dip in $z_{\text{eff}}(k)$. The $z_{\text{eff}}(k = 0.42)/Z_{\text{eff},T}$ ratio, where $Z_{\text{eff},T}$ is the zero field value, is 0.872 for the MP calculation with the $f_0^{(0)}(k) = C$ distribution. The ratio of the dip in $Z_{\text{eff}}(t)$ measured with respect to the $Z_{\text{eff},T}$ for the UCL data is 0.90. The ratio can be expected to show some sensitivity to the initial positron distribution used to start the simulations.

One characteristic of all the calculated $Z_{\text{eff}}(t)$ in Figure 5.6 is shape of the minima which are sharper than the experimental curve. However, the experimental $Z_{\text{eff}}(t)$ was taken with a finite time resolution of 1.92 ns, and subjected to smoothing. A more precise investigation of the effects of time resolution is not possible since Figure 5.5 [12] is given in terms of reduced time and the density of the gas was not specified.

5.3.3 Positron annihilation in helium in an electric field

The application of an electric field in thermalization experiments drives the positrons out of thermal equilibrium with the background helium gas. The steady-state is achieved when the energy gain of the positrons in the electric field is balanced by the energy loss from collisions with helium

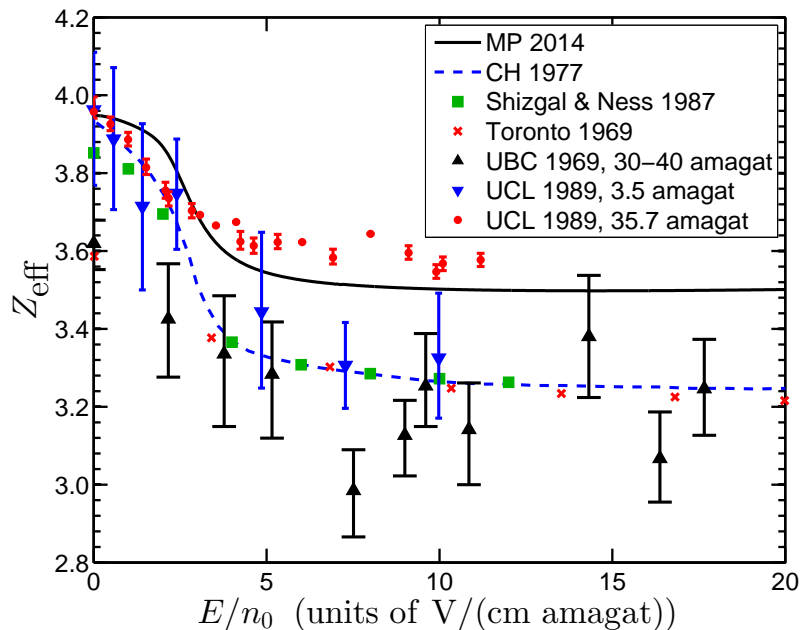


Figure 5.8: Comparison of steady-state $Z_{\text{eff}}(E/n_0)$ for thermalized positrons in helium at $T_0 = 293$ K. The curve labelled MP 2014 uses the MP cross section set. Also shown are experiments from the Toronto [13], UBC [14] and UCL [15] laboratories. Previous transport calculations are also depicted [12, 16]).

atoms. The velocity distribution of the positrons in the steady-state will no longer be a Maxwellian distribution. As the field strength is increased in magnitude, the cross sections and z_{eff} are sampled over an increasingly larger energy range. Further, the electric field modifies the steady-state velocity distribution function, and hence Z_{eff} , and necessarily modifies the transient response $Z_{\text{eff}}(t)$. The application of an electric field to the thermalization experiments represents a test on the validity of the cross section set at energies higher than thermal energies.

The variation of the steady-state Z_{eff} with an applied electric field is displayed in Figure 5.8. The MP cross section set is shown, as are results from two previous transport calculations [12, 16]. Experimental data from the University of Toronto [13], University of British Columbia (UBC) [14] and the University College London (UCL) [15] are presented. All calculated and experimental data show the same trend, there is a tendency for $Z_{\text{eff}}(E/n_0)$ to decrease as the reduced electric field, E/n_0 is increased. The reason for the decrease is easily explained by reference to the functional dependence of $z_{\text{eff}}(k)$ and the mean energy of the positron cloud at increasing E/n_0 . The increase in mean positron energy with E/n_0 is shown in Figure 5.9. The rapid increase in ϵ beginning at 2 V/(cm amagat) is a consequence of the Ramsauer-Townsend minimum in the momentum-transfer cross section at around 1.0 eV. For values of $E/n_0 > 5$ V/(cm amagat), the mean energy ranges from $1 - 3$ eV where $z_{\text{eff}}(k)$ has a broad minimum with $z_{\text{eff}}(k) \approx 3.5$.

There are effectively four sets of experimental data: the data of the Toronto [13] and UBC [14] experiments, and the two UCL datasets [15] which were taken at densities of 3.5 and 35.7 amagat. The present MP $Z_{\text{eff}}(E/n_0)$ tends to lie higher than three of the experimental datasets. However, two of these data sets (Toronto and UBC) should be given less weight since they do not reproduce the accepted value for the zero-field $Z_{\text{eff},T}$. The 3.5 amagat data from the UCL experiment has large error bars since the free positron annihilation signal was barely resolvable from the signal due to pick-off annihilation and ortho-Ps decay [15]. The most reliable experimental dataset would be the 35.7 amagat set from the UCL experiment.

The two previous transport calculations of $Z_{\text{eff}}(E/n_0)$ [12, 16] both use roughly the same $z_{\text{eff}}(k)$

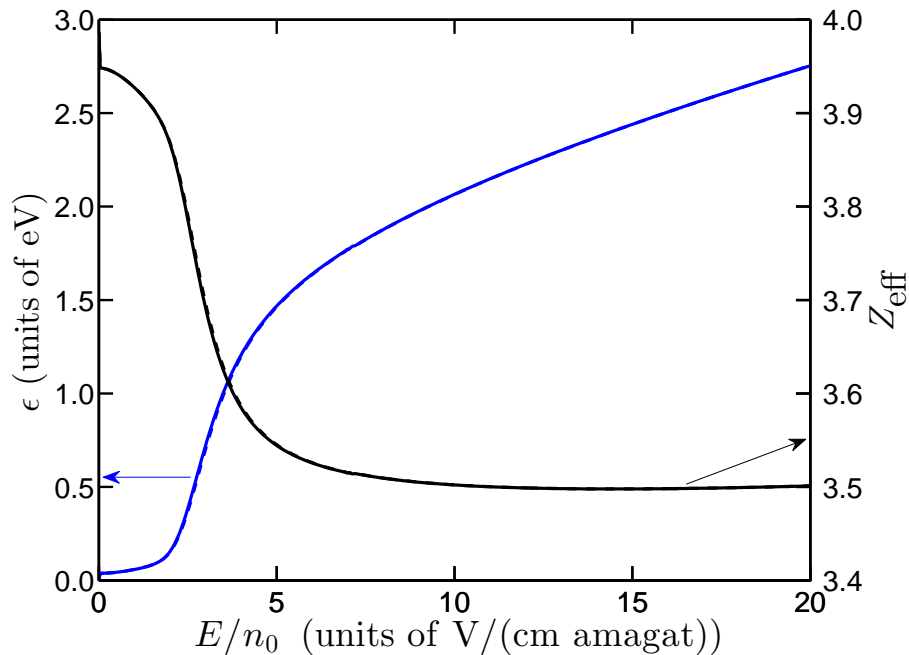


Figure 5.9: The steady-state Z_{eff} and mean energy ϵ , for positrons thermalizing in helium at $T_0 = 293$ K under the action of a reduced electric field E/n_0 using the new cross section set.

and both calculations give $Z_{\text{eff}}(E/n_0) < 3.3$ for $E/n_0 > 5$ V/(cm amagat). The present MP calculations have $Z_{\text{eff}}(E/n_0) \approx 3.5$ for $E/n_0 > 5$ V/(cm amagat). The present MP calculations have a larger $Z_{\text{eff}}(E/n_0)$ simply because the MP $z_{\text{eff}}(k)$ is larger than the CH $z_{\text{eff}}(k)$ for the relevant values of k .

The most significant comparison in Figure 5.8 is between the present transport calculation with the MP cross sections and the 35.7 amagat data from the UCL experiment [15]. The UCL data tend to be about 2 – 3% smaller than the MP curve for $E/n_0 < 3$ V/(cm amagat). However, this is a low-energy region where the MP calculation should be most reliable. At these energies, the functional dependence of $z_{\text{eff}}(k)$ is largely governed by effective range theory [492].

At higher electric fields, the MP $Z_{\text{eff}}(E/n_0)$ are larger than the Toronto and UBC data, although generally consistent when the scatter in the data is considered. The MP $Z_{\text{eff}}(E/n_0)$ are however slightly below the higher density experimental data of the UCL group [15]. While the higher pressure UCL results [15] are more accurate than their lower pressure results, at 35.7 amagat, these results may include other multiple scattering [157] and density effects [163] which have not been included in our calculations. It is also worth noting that the discrepancy is only 2 – 3%.

On the accuracy of a perturbation treatment of annihilation and the two-term approximation used in positron transport theory

If the annihilation collision frequency $\nu^{\text{ann}}(k)$, or equivalently $z_{\text{eff}}(k)$, increases/decreases monotonically with energy in the region sampled by the distribution function, there exists a preferential loss of positrons within the higher/lower energy part of the distribution. The annihilation cross section is usually many orders of magnitude smaller than the momentum-transfer cross section and so it is often assumed that annihilation can be treated as a perturbation. The loss of flux due to annihilation is typically omitted during the calculation of the distribution function (i.e. neglect the explicit ν^{ann} in the Boltzmann equation).

Calculations of positron transport in helium have also been done with the flux loss due to annihilation excluded in the calculation of the distribution function (i.e., setting $J^{\text{loss}} \approx 0$), which are compared with the non-perturbative treatment. At zero field, this non-perturbative treatment will cause the distribution function to deviate slightly from the expected Maxwellian distribution (at the helium temperature) and therefore result in a small change in the $Z_{\text{eff},T}$. For helium, the differences between the actual temperature of the thermalized distribution and gas temperature are less than 0.13%, resulting in a change to $Z_{\text{eff},T}$ of 0.0015%.

The perturbative and non-perturbative treatments can also be compared for the steady-state diffusion of positrons in an electric field. Figure 5.9 shows the thermalized Z_{eff} and ϵ for positrons diffusing in electric fields. The differences between the perturbative and non-perturbative treatments are less than 4% for the mean energy and 0.14% for Z_{eff} over the range $E/n_0 \in [0, 20]$ V/(cm amagat). These differences are essentially not visible in Figure 5.9.

The validity of the two-term approximation used in earlier transport calculations [12, 16] has been checked with an investigation of the impact of the computational parameter l_{max} in the Legendre polynomial expansion in equation (2.4). This parameter accounts for the anisotropic nature of the velocity distribution function, and also enables greater account for the anisotropy in the differential cross sections to be included. The parameter l_{max} is incremented until some convergence criteria is met, generally on the macroscopic parameters such as Z_{eff} . It was found that the two-term approximation was sufficient to guarantee accuracy to within 0.01% or better for all transport properties over the range of reduced fields considered. This is expected since low-energy positron helium elastic scattering is dominated by the s -wave. Consequently, collisional processes result in large momentum exchanges with small energy exchanges and the quasi-isotropy of the velocity distribution then follows.

5.3.4 Recommended low-energy elastic and annihilation cross sections

Transport theory calculations of the thermalization and annihilation of positrons diffusing in helium have been completed. The collision cross sections for helium were calculated from model potential values that were tuned to the best available calculations and experiments. These values are given in Table 5.7. The present calculations of the positron diffusion are largely compatible with the available experimental information. Lack of detailed knowledge in the energy distributions of the positrons at the start of the simulation does mean that some uncertainty must be attached to any conclusions. The present transport calculations, however, provide a greater degree of consistency with experiment than earlier calculations [16, 494]. The closer agreement with the experimental data has largely arisen from a more complete description of the positron-helium annihilation cross section. The use of a two-term distribution function and a perturbative treatment of positron annihilation used in previous studies are found to have a very small effect on the transient and steady-state behaviour of the positron cloud.

6

Positron impact ionization in gases

This chapter contains material that has been published in the following journal article:

[7] G. J. Boyle, W. J. Tattersall, D. G. Cocks, S. Dujko and R. D. White. Kinetic theory of positron-impact ionization in gases. *Physical Review A*, **91**, 052710 (2015).

doi:10.1103/PhysRevA.91.052710.

This chapter includes Monte Carlo simulation results performed by W. J. Tattersall. The transport property calculations and analysis were performed by me. All other work described in this chapter is my own.

6.1 Introduction

One of the major focuses of this work is eventual applications to PET [495]. To optimize PET technologies and quantify the associated radiation damage requires a thorough understanding of the processes by which an energetic positron (and the secondary species) thermalize. It has been shown recently by Sanche [496–499] that the secondary electrons created via ionization can cause significant DNA damage. The number of secondary electrons ejected along the positron track is on the order of 10^4 per MeV of primary radiation produced in water [56, 57], so it is clear that particular attention needs to be paid to the ionization process.

Although the impact from either a sufficiently energetic positron or electron can ionize a gas molecule, the ionization process differs in a crucial way: ionization by a positron is a particle-conserving process with respect to positrons, while ionization by an electron is non-particle-conserving with respect to electrons [151, 257, 407, 500, 501]. The two types of ionization will be referred to as ‘positron impact ionization’ (PII) and ‘electron impact ionization’ (EII) respectively. In the framework of kinetic theory, Ness [342] developed a collision operator for EII, however, no positron equivalent has yet been developed. Instead, previous investigations [1, 31, 315, 343–345] have generally treated positron ionization as a simple excitation process, which effectively assumes that the scattered positron receives all of the available post-ionization energy.

In this chapter, a PII equivalent of the EII collision operator of Ness is derived. Macroscopic transport coefficients, such as mean energy and flux drift velocity, are compared for a simple benchmark model using both a kinetic theory approach based on the Boltzmann equation, and an independent Monte Carlo simulation [9]. Particular attention is paid to the effect of energy-sharing between post-ionization constituents, and the influence that different energy-partitioning models have on transport. A basic energy-partitioning model that captures, at least qualitatively, the basic physics of high energy and near-threshold positron ionization is proposed, which can then be fitted to the rather limited experimental data that is available. The new kinetic theory model is used to investigate the transport of positrons in dilute H₂ gas using a recently-compiled, complete set of cross sections [156], and the proposed energy-partitioning model fit to the experimental data of Kover and Laricchia [17].

6.2 Positron impact ionization collision operator

Ionization by electron impact is fundamentally different from ionization by positron impact. Since the ejected electron is the same species as the impacting particle, EII is a non-particle-conserving process. The indistinguishability of electrons leads to a gain in the number of electrons in the swarm. Since the scattered positron can be distinguished from the ejected electron, PII is a particle-conserving-process. A different collision operator needs to be used for each case. In previous studies, PII was treated as a simple excitation process, which ignores the possible exchanges of energy between the scattered positron and ejected electron.

6.2.1 Derivation

The case of EII has been treated by Ness [342], and we follow this work closely to derive the PII collision operator. For simplicity, we consider one ionization process with a neutral in the ground state, but the generalization is straightforward. To derive the collision operator we will consider the scattering of positrons into and out of an element of phase-space, $d\mathbf{r}d\mathbf{v}$.

Let us consider a beam of positrons incident upon the background neutrals which are at rest. The flux of incident positrons, \mathbf{I} , in $d\mathbf{r}d\mathbf{v}$ is

$$\mathbf{I} = \mathbf{v}f(\mathbf{r}, \mathbf{v}, t) d\mathbf{v}. \quad (6.1)$$

If $\sigma^{\text{ion}}(v)$ is the total ionization cross section for an incoming positron of speed v , then the number of ionization collisions in $d\mathbf{r}d\mathbf{v}$ per unit time per neutral is,

$$I\sigma^{\text{ion}}(v) = v f(\mathbf{r}, \mathbf{v}, t) \sigma^{\text{ion}}(v) d\mathbf{v}, \quad (6.2)$$

and hence the total rate of positrons scattered out of the element $d\mathbf{r}d\mathbf{v}$ for n_0 neutral particles due to ionization is

$$J_{\text{out}}^{\text{ion}}(f)d\mathbf{r}d\mathbf{v} = n_0 v \sigma^{\text{ion}}(v) f(\mathbf{r}, \mathbf{v}, t) d\mathbf{r}d\mathbf{v}. \quad (6.3)$$

In EII, either the primary or ejected electrons (which are indistinguishable) from an ionization event somewhere else in phase-space may be scattered into the element $d\mathbf{r}d\mathbf{v}$. Since one can distinguish between electrons and positrons, the PII equivalent is simpler. Let us consider a new

element of phase-space with the same configuration space location but new velocity space location, i.e., $d\mathbf{r}d\mathbf{v}'$. Similar to (6.3), the total number of PII in $d\mathbf{r}d\mathbf{v}'$ per unit time is

$$n_0 v' \sigma^{\text{ion}}(v') f(\mathbf{r}, \mathbf{v}', t) d\mathbf{r}d\mathbf{v}'. \quad (6.4)$$

The momentum post-ionization is shared between the scattered positron and the ejected electron. We define a quantity $B(\mathbf{v}, \mathbf{v}')$, such that $B(\mathbf{v}, \mathbf{v}')d\mathbf{v}$ is the probability of the positron having a velocity between \mathbf{v} and $\mathbf{v} + d\mathbf{v}$ after ionization, given that the incident positron has velocity \mathbf{v}' . Assuming the neutral particle remains a bystander at rest during the process (to zeroth order in the mass ratio, m/m_0), then by conservation of momentum,

$$\mathbf{v}' = \mathbf{v} + \mathbf{v}, \quad (6.5)$$

where \mathbf{v} is the velocity of the ejected electron. It follows from equation (6.4) and the definition of $B(\mathbf{v}, \mathbf{v}')$ that the number of positrons that enter $d\mathbf{r}d\mathbf{v}$ per unit time due to an ionization event in $d\mathbf{r}d\mathbf{v}'$ is

$$n_0 v' \sigma^{\text{ion}}(v') f(\mathbf{r}, \mathbf{v}', t) B(\mathbf{v}, \mathbf{v}') d\mathbf{v}d\mathbf{r}d\mathbf{v}'. \quad (6.6)$$

Integrating over all possible incident velocities thus yields the total rate of positrons scattered into $d\mathbf{r}d\mathbf{v}$ due to PII, i.e.,

$$J_{\text{into}}^{\text{ion}}(f) d\mathbf{r}d\mathbf{v} = n_0 d\mathbf{r}d\mathbf{v} \int v' \sigma^{\text{ion}}(v') f(\mathbf{r}, \mathbf{v}', t) B(\mathbf{v}, \mathbf{v}') d\mathbf{v}'. \quad (6.7)$$

The total PII collision operator is then the difference in the rates of positrons scattered into and out of the element $d\mathbf{r}d\mathbf{v}$, i.e., $J^{\text{ion}} = J_{\text{out}}^{\text{ion}} - J_{\text{into}}^{\text{ion}}$,

$$J^{\text{ion}}(f) = n_0 v \sigma^{\text{ion}}(v) f(\mathbf{r}, \mathbf{v}, t) - n_0 \int v' \sigma^{\text{ion}}(v') B(\mathbf{v}, \mathbf{v}') f(\mathbf{r}, \mathbf{v}', t) d\mathbf{v}'. \quad (6.8)$$

If we assume central forces, then the scattering cross section and partition function are dependent only on the magnitudes of the pre- and post-collision velocities, and the angle between them, i.e., v, v' and $\hat{\mathbf{v}} \cdot \hat{\mathbf{v}}'$. We may then further define a differential scattering cross section for ionization, $\sigma^{\text{ion}}(v, v'; \hat{\mathbf{v}} \cdot \hat{\mathbf{v}}')$, such that $\sigma^{\text{ion}}(v, v'; \hat{\mathbf{v}} \cdot \hat{\mathbf{v}}') d\mathbf{v}$ is the number of positrons scattered into the range $d\mathbf{v}$ about \mathbf{v} due to incident electrons of velocity \mathbf{v}' divided by incident flux,

$$\sigma^{\text{ion}}(v, v'; \hat{\mathbf{v}} \cdot \hat{\mathbf{v}}') d\mathbf{v} = \sigma^{\text{ion}}(v') B(v, v'; \hat{\mathbf{v}} \cdot \hat{\mathbf{v}}') d\mathbf{v}. \quad (6.9)$$

The partition function satisfies a normalization condition so that

$$\sigma^{\text{ion}}(v') = \int \sigma^{\text{ion}}(v, v'; \hat{\mathbf{v}} \cdot \hat{\mathbf{v}}') d\mathbf{v}. \quad (6.10)$$

Substituting equation (6.9) into equation (6.8) gives the PII collision operator

$$J^{\text{ion}}(f) = n_0 v \sigma^{\text{ion}}(v) f(\mathbf{v}) - n_0 \int v' \sigma^{\text{ion}}(v, v'; \hat{\mathbf{v}} \cdot \hat{\mathbf{v}}') f(\mathbf{v}') d\mathbf{v}'. \quad (6.11)$$

This operator is particle-number-conserving, i.e.

$$\begin{aligned}
\int J^{\text{ion}}(f) d\mathbf{v} &= \int n_0 v \sigma^{\text{ion}}(v) f(\mathbf{v}) d\mathbf{v} - n_0 \iint v' \sigma^{\text{ion}}(v, v'; \hat{\mathbf{v}} \cdot \hat{\mathbf{v}}') f(\mathbf{v}') d\mathbf{v}' d\mathbf{v}, \\
&= n_0 \int v \sigma^{\text{ion}}(v) f(\mathbf{v}) d\mathbf{v} - n_0 \int v' f(\mathbf{v}') d\mathbf{v}' \int \sigma^{\text{ion}}(v, v'; \hat{\mathbf{v}} \cdot \hat{\mathbf{v}}') d\mathbf{v}, \\
&= n_0 \int v \sigma^{\text{ion}}(v) f(\mathbf{v}) d\mathbf{v} - n_0 \int v' \sigma^{\text{ion}}(v') f(\mathbf{v}') d\mathbf{v}', \\
&= 0,
\end{aligned} \tag{6.12}$$

as required.

6.2.2 Legendre decomposition

For central scattering forces the partition function can be decomposed in terms of Legendre polynomials, i.e.,

$$B_l(v, v') = 2\pi \int_{-1}^1 B(\mathbf{v}, \mathbf{v}') P_l(\mu) d\mu, \tag{6.13}$$

where $\mu = \hat{\mathbf{v}} \cdot \hat{\mathbf{v}}'$. For isotropic scattering, $B_l(v, v') = 0$ for $l \geq 1$. Multiplying equation (6.8) by $P_l(\cos \chi)$, and integrating over all angles leads to

$$J_l^{\text{ion}}(f_l) = n_0 v \sigma^{\text{ion}}(v) f_l(v) - \begin{cases} n_0 \int_0^\infty v' \sigma^{\text{ion}}(v') B_0(v, v') f_0(v') v'^2 dv', & l = 0, \\ 0, & l \geq 1. \end{cases} \tag{6.14}$$

We now seek to represent equation (6.14) in terms of energy rather than speed, i.e., $U = \frac{1}{2}mv^2$. The probability of a positron having a speed in the range $v + dv$ after ionization, for an incident positron of speed v' is

$$\begin{aligned}
v^2 dv \int B(v, v'; \hat{\mathbf{v}} \cdot \hat{\mathbf{v}}') d\hat{\mathbf{v}} &= B(v, v') v^2 dv, \\
&\equiv P(U, U') dU,
\end{aligned} \tag{6.15}$$

where U and U' are the post- and pre-collision positron energies respectively, and now the right-hand-side term of equation (6.15) represents the probability of a positron having an energy in the range $U + dU$ after ionization for an incident positron of U' . The energy partitioning function, $P(U, U')$, has the following properties:

$$P(U, U') = 0 \quad U' < U + U_1, \tag{6.16}$$

$$\int_0^{U' - U_1} P(U, U') dU = 1 \quad U' \geq U + U_1. \tag{6.17}$$

Finally, we can represent equation (6.14) in terms of energy and the energy-partition function, $P(U, U')$,

$$J_l^{\text{ion}}(f_l) = \nu^{\text{ion}}(U) f_l(U) - \begin{cases} U^{-\frac{1}{2}} \int_0^\infty dU' U'^{\frac{1}{2}} \nu^{\text{ion}}(U') P(U, U') f_0(U'), & l = 0, \\ 0, & l \geq 1. \end{cases} \tag{6.18}$$

6.2.3 Modified Frost-Phelps operator

If the scattered positron leaves the collision with an exact fraction, Q , of the available energy, $U' - U_I$, where U_I is the threshold energy, then the energy-partition function has the form,

$$\begin{aligned} P(U, U') &= \delta(U - Q(U' - U_I)), \\ &= \frac{1}{Q} \delta\left(U' - \left(\frac{U}{Q} + U_I\right)\right), \end{aligned} \quad (6.19)$$

and the integral in equation (6.18) reduces to,

$$J_l^{\text{ion}}(f_l) = \nu^{\text{ion}}(U) f_l(U) - \begin{cases} \frac{1}{Q} \frac{(U/Q + U_I)^{\frac{1}{2}}}{U^{\frac{1}{2}}} \nu^{\text{ion}}\left(\frac{U}{Q} + U_I\right) f_0\left(\frac{U}{Q} + U_I\right), & l = 0, \\ 0, & l \geq 1, \end{cases} \quad (6.20)$$

where $\nu^{\text{ion}}(U) = n_0 \sqrt{\frac{2U}{m}} \sigma^{\text{ion}}(U)$ is the ionization collision frequency. Equation (6.20) can be considered a ‘modified Frost-Phelps’ operator. A similar result for EII was given in [292]. In the case where the positron gets all of the available energy, i.e., $Q = 1$, equation (6.20) reduces to the standard Frost-Phelps operator as required. Clearly, equation (6.20) breaks down when $Q = 0$.

6.3 Positron ionization benchmarking

We first discuss several benchmark models which can act as a test bed for our numerical techniques and solution model. An independent Monte Carlo simulator [9] has been used to compare with the Boltzmann equation solver results. The Lucas-Saelee [42] model is a popular benchmark for EII, but focuses on the differences between excitation and ionization rather than energy-partitioning specifically. Taniguchi et al. [41] modified the partition function of the Lucas-Saelee model, which assumes a distribution with all energy-sharing fractions equiprobable, to instead share energy equally between the two electrons, but found that it did not alter the transport coefficients significantly. Instead, Ness and Robson [34] proposed a step model for testing energy-sharing for EII, which was shown to have some variation for the partitionings they investigated. The details of the model are:

$$\begin{aligned} \sigma_m &= 10 \text{ \AA}^2, \\ \sigma^{\text{exc}} &= \begin{cases} 1 \text{ \AA}^2, & U \geq 10 \text{ eV}, \\ 0, & U < 10 \text{ eV}, \end{cases} \\ \sigma^{\text{ion}} &= \begin{cases} 1 \text{ \AA}^2, & U \geq 15 \text{ eV}, \\ 0, & U < 15 \text{ eV}, \end{cases} \\ m_0 &= 25 \text{ amu}, \\ T_0 &= 0 \text{ K}. \end{aligned} \quad (6.21)$$

Transport coefficients for EII calculated using kinetic theory were compared against the results of Ness and Robson, and the Monte Carlo simulations in Table 4.9 of Chapter 4. The results support the integrity of our methods and solutions. Transport coefficients for PII under this model are given in Table 6.1 for varying energy sharing fractions, Q , where $Q = \frac{U}{U' - U_I}$. As described in Subsection 6.2.3, the collision operator (6.20) breaks down when $Q = 0$, hence there is no value

given in Table 6.1 corresponding to the kinetic model for positrons with $Q = 0$. No previous positron impact calculations exist for model (6.21), so the transport properties from our kinetic theory model are compared solely against an independent Monte Carlo simulation in Table 6.1. The uncertainty in the Monte Carlo simulations has been estimated to be less than 1% for the ionization collision rates, and less than 0.5% (generally less than 0.3%) for the drift velocity and mean energy. The two approaches give α^{ion}/n_0 , ϵ and W values which differ by less than 0.6%, 0.3% and 0.3% respectively, over the range of reduced electric fields and available energy fractions, all of which are within the corresponding Monte Carlo uncertainty. As the reduced field, E/n_0 , is increased, the velocity distribution function samples more of the ionization process leading to a greater ionization rate and a stronger dependence of the transport coefficients on the post-collision energy partitioning.

Table 6.1: Comparison of average ionization rates, α^{ion}/n_0 , mean energies, ϵ , and flux drift velocities, W , for PII for model (6.21) for different reduced fields E/n_0 and energy sharing fractions Q . Columns ‘Current’ correspond to the current kinetic theory calculations, and columns ‘MC’ are the results of the Monte Carlo simulation. Note, $Q = \text{AFE}$ corresponds to ‘all fractions equiprobable’.

E/n_0 [Td]	Q	α^{ion}/n_0 [$10^{-15}\text{m}^3\text{s}^{-1}$]		ϵ [eV]		W [10^5ms^{-1}]	
		Current	MC	Current	MC	Current	MC
300	0		1.711		6.869		2.767
	1/4	1.720	1.718	6.919	6.931	2.722	2.730
	1/3	1.725	1.719	6.940	6.942	2.711	2.706
	1/2	1.740	1.739	6.983	6.979	2.693	2.689
	2/3	1.757	1.761	7.021	7.023	2.677	2.676
	3/4	1.767	1.774	7.041	7.040	2.671	2.664
	1	1.807	1.804	7.098	7.087	2.654	2.648
	AFE	1.745	1.739	6.979	6.981	2.699	2.701
500	0		4.856		9.210		3.951
	1/4	4.915	4.917	9.379	9.375	3.819	3.822
	1/3	4.955	4.949	9.446	9.450	3.789	3.780
	1/2	5.060	5.055	9.579	9.588	3.738	3.739
	2/3	5.211	5.208	9.716	9.714	3.697	3.697
	3/4	5.288	5.293	9.788	9.789	3.678	3.678
	1	5.565	5.599	10.03	10.05	3.627	3.628
	AFE	5.119	5.107	9.589	9.577	3.754	3.755
800	0		9.903		13.30		5.260
	1/4	10.21	10.23	13.75	13.76	4.986	4.992
	1/3	10.39	10.40	13.93	13.93	4.922	4.925
	1/2	10.84	10.83	14.32	14.33	4.816	4.818
	2/3	11.40	11.41	14.79	14.81	4.719	4.725
	3/4	11.68	11.70	15.07	15.09	4.672	4.678
	1	12.92	12.95	16.27	16.31	4.518	4.527
	AFE	10.92	10.94	14.38	14.36	4.850	4.857

The convergence of transport coefficients for 1000 Td with increasing l_{max} is shown in Table 6.2. Since an even-order approximation is required for the appropriate boundary conditions, the l_{max} are odd in our calculations. Clearly the two-term approximation ($l_{\text{max}} = 1$) leads to an over-estimation of the ionization rate, mean energy and flux drift velocity by approximately 2%. Indeed six terms are required to achieve convergence to four significant figures.

The variation of mean energy with Q for PII at a reduced electric field of 800 Td is shown in Figure 6.1. For PII, the mean energy of the positron swarm increases monotonically with the energy-sharing fraction, Q . This behaviour is to be expected, as the ejected electron directly

Table 6.2: Convergence of transport properties with l_{\max} for PII model (6.21) at 1000 Td and $Q = 1/2$.

l_{\max}	α^{ion}/n_0 [$10^{-15}\text{m}^3\text{s}^{-1}$]	ϵ [eV]	W [10^5ms^{-1}]
1	12.77	18.23	5.460
3	12.47	17.96	5.350
5	12.48	17.95	5.349
7	12.48	17.95	5.349

removes energy from the positron swarm. The ionization collision frequency increases with energy in model (6.21), so that the greater the energy of the swarm, the higher the rate of ionization collisions. Hence α^{ion}/n_0 also increases monotonically with Q . The flux drift velocity, W in contrast, decreases with increasing Q . The effect of collisions is to randomize the directions of the swarm particles, such that an increase in the ionization rate decreases the average velocity of the swarm. The transport properties for the ‘all fractions equiprobable’ (AFE) distribution are very similar to that of the equal-energy sharing case.

The variation of mean energy with Q for EII at 800 Td is shown in Figure 6.2. The mean energy profile is symmetrical about $Q = 0.5$ due to the indistinguishability of post-collision electrons, and for 800 Td has a concave shape with a minimum value corresponding to equal energy-sharing. It should be noted that, in contrast to PII where the mean energy always increases with Q , the exact nature of the EII mean energy profile depends on how the distribution function samples the elastic, inelastic and ionization cross sections. The variation in the transport properties for EII with respect to Q for the fields considered is small, suggesting that EII is relatively insensitive to the exact nature of the energy-partitioning for the model (6.21). Ness and Makabe [502] have shown that for EII in argon the choice of energy-sharing fraction can in fact cause differences of $\sim 25\%$, so that care must still be taken when choosing the energy-partitioning function.

The qualitative shape of the Q -dependence of the mean energy for PII is insensitive to the reduced electric field, and the range of values for a particular reduced field is considerably larger than that for EII. In previous positron studies [257,259,315,407], PII has been treated as a standard excitation process. The current results suggest that PII is particularly sensitive to the form of the energy-partitioning and, if real-world PII differs significantly from the model of pure scattering with excitation, large errors can result. To comment on this, we need to develop a realistic model of PII energy-partitioning.

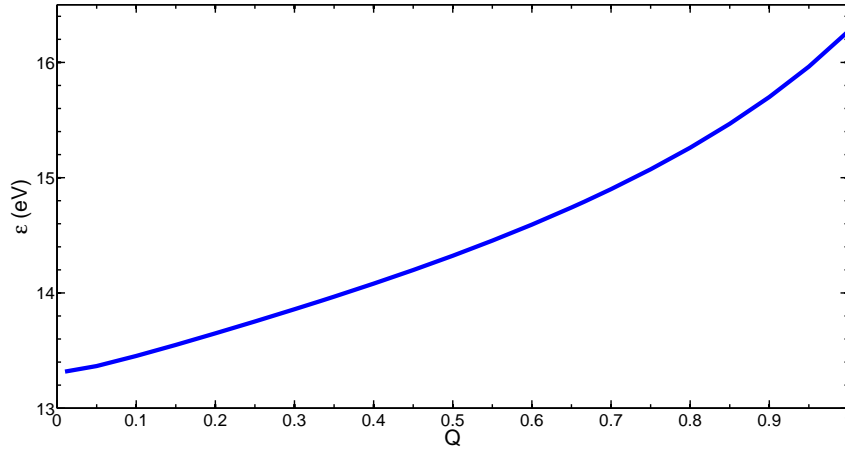


Figure 6.1: Variation of mean energy, ϵ , with energy sharing fraction, Q , for PII model (6.21) at a reduced field of 800 Td.

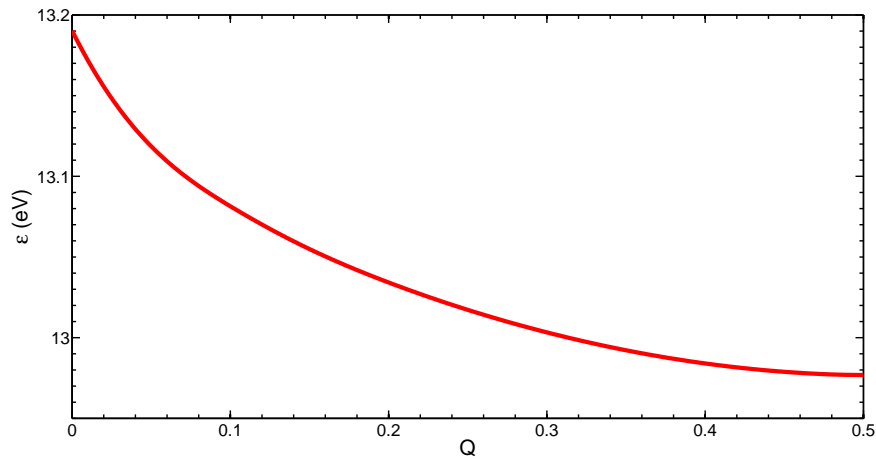


Figure 6.2: Variation of mean energy, ϵ , with energy sharing fraction, Q , for EII model (6.21) at a reduced field of 800 Td.

6.4 Positron ionization energy-partitioning model

We now wish to develop a model for post-ionization energy-partitioning that captures the following basic physical behaviours:

1. For high impact energies, the positron ionization scattering cross section approaches the electron ionization scattering cross section. The first Born approximation [503] is valid for high impact energies and shows a heavy bias towards the case where the scattered positron leaves the collision with almost all of the energy which is available post-collision.
2. For impact energies near the ionization threshold, there is significant correlation between the scattered positron and ejected electron. In the Wannier theory [243], originally developed for near-threshold EII, the repulsion between the two electrons causes them to emerge with similar energies but in opposite directions. In terms of the interaction potential between the two electrons, one may talk about a Wannier ‘ridge’ upon which the system is in an unstable equilibrium. Klar [504] was the first to adapt Wannier’s classical idea to PII. As

in Wannier's theory, the energy is predicted to be shared equally, however now the positron and electron emerge in similar directions due to the Coulomb attraction. Ashley et al. [505] measured the positron ionization cross section in helium which they were able to accurately represent by a power law, albeit different to that derived by Klar. Ihra et al. [506] extended the Wannier theory to be consistent with both Klar and experiment. The success of these power law models justifies the assumption of equal energy-sharing at near-threshold impact energies, although recent experiments [507] suggest a slight asymmetry. It should be noted that the positron and electron escape in similar directions with similar energies and are highly correlated, so no clear distinction between ionization and continuum state positronium can be made [101].

3. Ionization at intermediate energies appears to be a combination of the above two effects, i.e. a strong peak in the energy-sharing distribution corresponding to the scattered positron leaving with all the available energy, and a second peak occurring when the positron and electron emerge with similar energy and direction and in a highly correlated state. This feature has been shown in the studies of atomic hydrogen by Brauner et al. [508] and measured experimentally in H₂ by Laricchia and co-workers [17, 507].

To capture simply the above three characteristics we propose a model consisting of an exponentially decaying function, $g_{\text{high}}(Q)$, to represent the high impact energy ionization, and a rational polynomial (sometimes called the Cauchy or Lorentz distribution), $g_{\text{low}}(Q)$, centred around equal energy-sharing to represent the near-threshold ionization i.e.,

$$g_{\text{high}}(Q) = A_{\text{high}} \exp(\beta_{\text{high}} Q), \quad (6.22)$$

$$g_{\text{low}}(Q) = A_{\text{low}} \left[\beta_{\text{low}}^2 + (Q - 0.5)^2 \right]^{-1}, \quad (6.23)$$

where Q is the fraction of the available energy, A_{high} and A_{low} are normalization constants, and β_{high} and β_{low} are free parameters to be fitted. An energy-fraction-partitioning function which depends only on the impact energy and Q can then be constructed as

$$g(U', Q) = w(U') g_{\text{high}}(Q) + (1 - w(U')) g_{\text{low}}(Q), \quad (6.24)$$

where $w(U')$ is chosen as a hyperbolic tangent function to transition smoothly between g_{high} and g_{low} , i.e.,

$$w(U') = \frac{1}{2} \left[1 + \tanh \left(\gamma \frac{U' - U_{\text{I}}}{q} - \delta \right) \right], \quad (6.25)$$

where q is the elementary charge, and γ and δ are free parameters that control where and how sharp the transition is. The relationship between the energy-fraction-partitioning function, $g(U', Q)$, and the energy-partitioning function, $P(U, U')$, used in equation (6.18) is given simply by

$$g(U', Q)Q = P(U, U')U. \quad (6.26)$$

In the following subsections we shall investigate a test model with reasonable values for the free parameters which can serve as a future benchmark model, and then fit the energy-partitioning model to real experimental H₂ data.

6.4.1 Test model

In this subsection we investigate the effect that the energy-partitioning model (6.22)–(6.25) has on positron transport for a range of reduced electric field strengths. The parameters for the energy-partitioning function are

$$\begin{aligned}\beta_{\text{high}} &= 10, \\ \beta_{\text{low}} &= 0.05, \\ \gamma &= 0.05, \\ \delta &= 3.5,\end{aligned}\tag{6.27}$$

with the same cross sections, neutral temperature and mass as the model (6.21). The energy-partition function for model (6.27) is displayed in Figure 6.3.

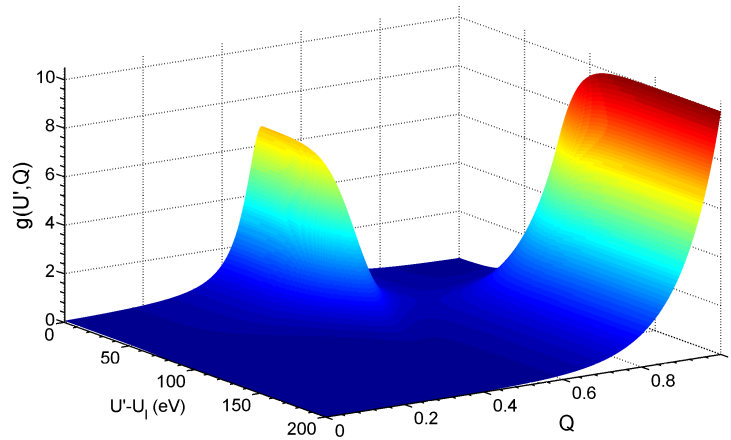


Figure 6.3: Variation of the energy-fraction-partition function with impact energy, relative to the ionization threshold, and energy sharing fraction, Q , for parameters. (6.27)

Transport properties calculated via kinetic theory and Monte Carlo are shown in Table 6.3. The kinetic theory and Monte Carlo results agree to within 0.4%. Also included in the table for 800 Td and 5000 Td are the swarm properties assuming the energy-partitioning was replaced by only g_{low} or g_{high} respectively. At 800 Td, the swarm properties for the full energy-partitioning model are close to that which results from the inclusion of only g_{low} , which indicates that the distribution is generally sampling the even energy-sharing part of the full energy-partitioning distribution. At the higher field of 4000 Td the swarm properties are now close to those that come from allowing only g_{high} to have an effect. As the field has increased, the distribution has shifted from sampling mostly the even sharing region, to the region that is heavily biased towards the positron getting large amounts of available energy.

6.4.2 Model for positron impact ionization in H_2

Laricchia and co-workers [17,507] have measured experimentally the energy-sharing of post-ionization species for PII for a specific impact energy and angle. Their results for ionization by a 1000-eV positron, where both the positron and electron emerge at the same angle of 0° , are included in Figure 6.4. It is evident that there is a bias towards the positron getting all or large amounts of the available energy, with a secondary peak close to equal energy-sharing due to electron-positron

Table 6.3: Comparison of average ionization rate, α^{ion}/n_0 , mean energies, ϵ , and flux drift velocities, W , for PII for model (6.27). The superscripts a and b refer to $w(U) = 0$ and $w(U) = 1$ respectively. Columns ‘Current’ correspond to the current kinetic theory calculations, and columns ‘MC’ are the results of Monte Carlo simulation.

E/n_0 [Td]	α^{ion}/n_0 [$10^{-15}\text{m}^3\text{s}^{-1}$]		ϵ [eV]		W [10^5ms^{-1}]	
	Current	MC	Current	MC	Current	MC
800	10.92	10.90	14.40	14.37	4.810	4.814
800 ^a	10.86	10.85	14.35	14.32	4.816	4.820
800 ^b	12.48	12.37	15.82	15.70	4.555	4.585
1600	26.29	26.26	34.12	34.04	6.331	6.348
2400	40.97	40.88	65.56	65.42	6.910	6.932
3200	53.97	53.85	104.1	103.9	7.201	7.229
4000	64.95	64.90	144.8	145.0	7.491	7.517
4000 ^a	49.18	49.11	86.49	86.52	9.509	9.527
4000 ^b	66.96	66.64	149.5	149.2	7.150	7.178

correlation effects. Our model predicts that this peak should occur at exactly $Q = 0.5$, but experiments show that there is a slight energy-sharing asymmetry in positron ionization, such that the peak actually occurs at $Q > 0.5$ [507]. A more sophisticated energy-partitioning model will need to take this effect into account. We have performed a non-linear least squares calculation to fit the free parameters of model (6.22)–(6.25) to the experimental data, which were determined to be,

$$\begin{aligned}
 \beta_{\text{high}} &= 5.88, \\
 \beta_{\text{low}} &= 0.0468, \\
 \gamma &= 0.0584, \\
 \delta &= 3.45.
 \end{aligned}
 \tag{6.28}$$

The fitted profile is shown in Figure 6.4 and qualitatively reproduces the main features of the experiment. It should be noted that at the 0 degree scattering angle the secondary peak is particularly dominant, and if one were to average the triple differential cross section over all angles, a similar form with a reduced secondary peak would result. Due to the lack of experimental data at a variety of angles, we will assume that the angle-integrated cross section has the exact same shape as the 0° angle cross section for the purpose of this work, which will have the effect of exaggerating the equal energy-sharing part of the full energy-sharing distribution. The parameters in equation (6.28) have been chosen to ensure a smooth transition between g_{low} and g_{high} while ensuring that the relative weights give the fit to experiment for an impact energy of 100 eV. The full, three dimensional energy-sharing distribution is qualitatively similar to Figure 6.3.

6.5 Positrons in H_2

In the previous subsection, a model for the post-ionization energy-sharing for PII from H_2 was proposed. In this section, the effect of the energy sharing on transport properties is investigated for PII in rarefied H_2 . The set of H_2 cross sections employed are those compiled in [156, 345] and using an elastic cross section¹ calculated with a convergent-close-coupling formalism [509] up to 1000 eV, extrapolating where necessary. It is clear that the ionization process, which turns on at 15.4 eV, is particularly important, and dominates at energies above 50 eV .

¹M. Zammit in private communication

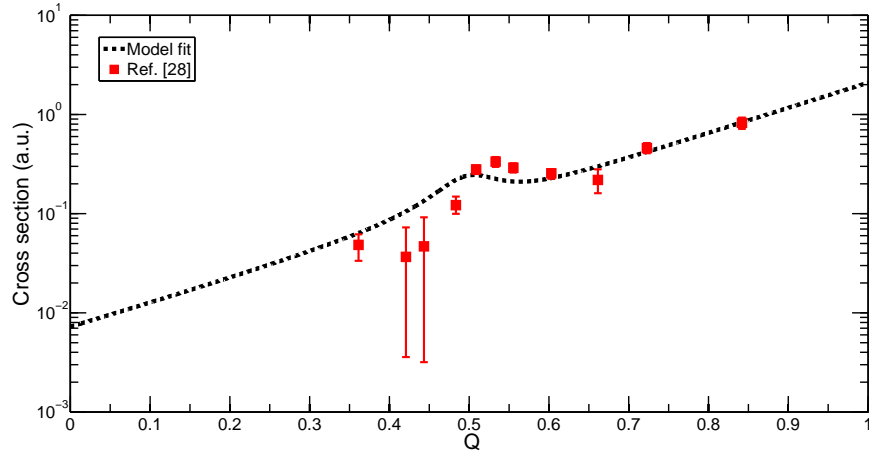


Figure 6.4: Differential PII cross section for an impact energy of 100 eV, as a function of the energy sharing fraction, Q . KL 1998 is the experimental data of Kover and Laricchia [17] for the triply differential cross section for an impact energy of 100 eV and ejection angle of 0° . The model fit has been calculated with the parameters (6.28) and by assuming that the triply differential cross section is the same at all ejection angles.

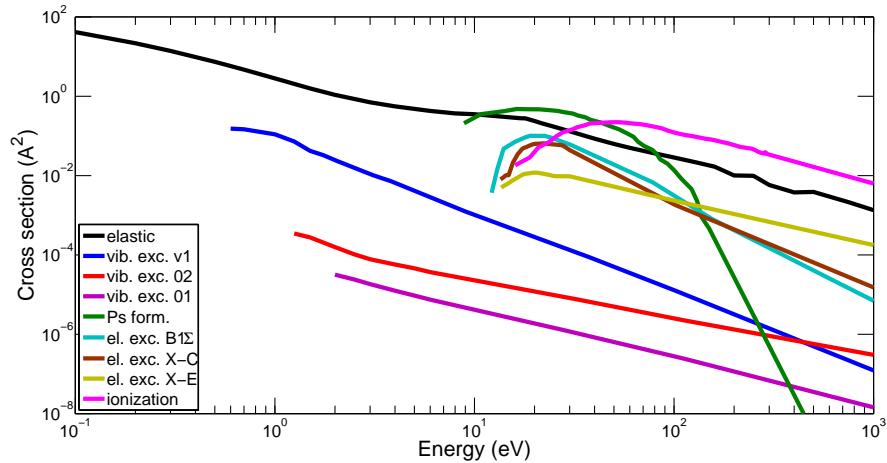


Figure 6.5: Cross section set for positron scattering in H_2 . References are given in text.

In order to assess the importance of energy-partitioning on ionization we investigated the time-dependence of the mean energy for a source of positrons in H_2 gas at 293 K as they relax to thermal equilibrium in the absence of an electric field. In positron experiments [101], unmoderated positrons have a peak in their emission energy spectrum of around half a MeV, which then lose energy rapidly via collisions. There is little information about the initial source distribution in thermalization experiments [12]. For our purposes, we wish to probe the influence of PII collisions, and accordingly choose an initial distribution with a mean energy far above the ionization threshold so that a large range of the ionization cross section can be sampled during relaxation. The source distribution is chosen to be uniform in velocity space up to the 1000 eV cutoff, which is equivalent to an initial mean energy of 600 eV as discussed in Section 2.5.1. The thermalization profiles for the energy-partitioning model (6.28), and using the PII collision operator with $Q = 0.5$ (equal energy-sharing), and $Q = 1$ (standard excitation form) are shown in Figure 6.6. There are two distinct regions of rapid relaxation: one due to ionization at high energies; and one due to the vibrational modes at lower energies. The first occurs on time scales of between 0.1 and 2 ns amagat, while the

second at about 5 ns amagat, which shows that the relaxation due to inelastic collisions is very rapid. While in the ionization-dominated region, the three profiles show significant differences in mean energy of up to an order of magnitude. The profile corresponding to $Q = 1.0$ has the highest mean energy since the positron loses the least amount of energy during an ionization collision in that limit. It takes significantly longer to relax until the positron energies fall below the ionization region, and thus they will experience more ionization collisions. The $Q = 0.5$ profile shows the lowest mean energy since the ejected electron removes large amounts of energy from the swarm, and exits the ionization region quickest. The ‘real’ H_2 model profile sits between the even energy-sharing and standard excitation profiles as expected, since it is essentially a mixture of the two. At lower energies, once ionization collisions become insignificant, all three energy partitioning profiles coalesce, resulting in essentially the same total thermalization times.

Although the total thermalization time is essentially insensitive to the form of the ionization energy-partitioning, the large differences in mean energies in the ionization-dominated region can have other important effects. In a space-dependent situation, the higher mean energies can allow the positron to travel larger distances during thermalization. This is important to PET simulations since the resolution of PET images is dependent on the distances traveled between positron emission and annihilation [495]. Similarly, the higher the mean energy, the longer the positron swarm can significantly sample the ionization cross section, and hence the more secondary electrons that are created via PII. It is the secondary electrons created in the human body during PET scans that can cause DNA damage [496–499]. Furthermore, the exact energy profile of the secondary electrons will be dependent on the form of the PII energy-partitioning.

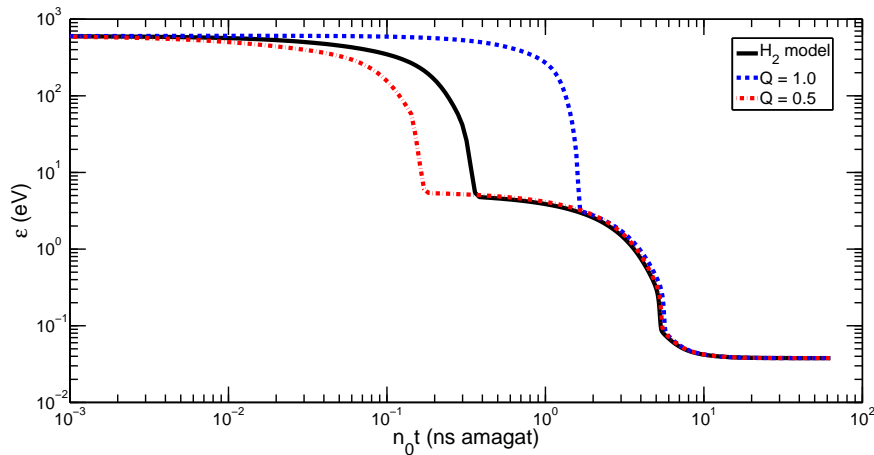


Figure 6.6: Mean energy temporal relaxation of a positron swarm in H_2 at 293 K. The initial source distribution is uniform in speed space up to 1000 eV. The H_2 model ionization parameters are given in equation (6.28) and are compared with constant energy sharing fractions of $Q = 0.5$ and $Q = 1.0$.

6.6 Conclusion

Ionization by positron impact is a fundamentally different process than ionization by electron impact. Applications such as PET demand increasingly accurate models for positron transport, so it is important to be able to describe the ionization process in detail. To this end, a kinetic theory model with a general PII collision operator has been developed for the first time. The key feature of the ionization collision operator is the energy-partition function, which controls how the available energy is shared between the post-collision constituents.

The kinetic theory results were compared against a Monte Carlo simulation for a simple test model (6.21), which may serve as a new benchmark for PII. The transport properties calculated differed between the two approaches by less than 0.6% over a range of reduced electric fields and available energy fractions, which is within their respective uncertainties. The sensitivity of the transport properties to the energy-sharing fraction Q for PII was shown to be significant, and much greater than that of EII. Thus large errors can result in real-world applications if PII is not treated carefully.

A simple energy-partition function was developed to capture qualitatively the underlying physics of PII. At high impact energies, the scattered positron leaves the collision with almost all of the available energy, while at near-threshold impact energies the Wannier theory [243] suggests that both the scattered positron and ejected electron share approximately half of the available energy. In reality, there is a slight energy-sharing asymmetry in near-threshold positron ionization [507] and a more sophisticated energy-partitioning model will need to take this asymmetry into account. The model parameters were fit to the experimental results of Kover and Laricchia [17] for positrons in H_2 with good qualitative agreement.

Using the newly constructed H_2 energy-partitioning function, we investigated the temporal relaxation of a positron swarm from a high energy source (600 eV) to thermalization at room temperature, and compared the equal-energy sharing model with the common approach of treating the PII as a standard excitation process. In the ionization-dominated region there can be more than an order of magnitude difference in the mean energy profiles, and hence the choice of energy-partition function has a significant effect on the number of ionization collisions and the energy distribution of the secondary electrons created, which is particularly important for radiation damage modelling [498].

7

Electron scattering and transport in atomic liquids

This chapter contains material that has been published in the following journal article:

[8] G. J. Boyle, R. P. McEachran, D. G. Cocks and R. D. White. Electron scattering and transport in liquid argon. *The Journal of Chemical Physics*, **142**, 154507 (2015). doi:10.1063/1.4917258.

This chapter includes scattering cross section theory and calculations for the electron-argon system (in particular, Section 7.2.1) performed by R. P. McEachran. All other work described in this chapter is my own.

The coherent scattering modifications discussed in this chapter have been benchmarked for the Percus-Yevick model in Section 4.6.

7.1 Introduction

The study of electron transport in non-polar liquids is of fundamental interest for understanding the dynamics of electronic processes in liquids and disordered systems, including dynamic and scattering processes. More recently, attention has focussed on applications including liquid state electronics, driven by use in high-energy particle detectors such as the liquid argon time projection chamber (LArTPC). Advances in the fields of plasma discharges in liquids and associated electrical breakdowns (see e.g. the review of Bruggmen [510]) are dependent on a fundamental knowledge of charged particle transport in liquids. Furthermore, the rapidly developing interdisciplinary field of plasma medicine [64–67] requires a detailed knowledge of electron transport through liquid water and other biostructures, typically under non-equilibrium conditions.

The study of excess electrons in dense gases and fluids is a complex problem, requiring the inclusion of many effects that are not present in dilute gaseous systems. The major contributions to these effects arise from the small interparticle spacings and their highly correlated separations. For thermal energies, the de Broglie wavelengths of the excess electrons are often orders of magnitude

larger than the interatomic spacing, which leads to significant quantum-like effects. Even within a semi-classical picture, where the excess electrons are assumed to act as point-like particles, no particular volume is ‘owned’ by a single atom. This means the typical picture for transport in a gas, i.e. a series of individual collision events separated by the mean-free path, is no longer valid, making it important to consider multiple scattering effects of the electron from many atoms simultaneously. Of particular note is the effect of ‘coherent scattering’ and the pair correlations of the liquid, which play very important roles.

Many previous calculations for electrons in dense systems have neglected these liquid effects for simplicity, modelling dense fluids by applying a theory for dilute gases with only an appropriate increase of the density. However, a few alternative theories exist that have explored liquids in different ways. Borghesani et al. [307] have heuristically combined the liquid effects identified above to obtain an effective cross section. When used in the standard equations from kinetic theory for mobility in a non-zero field, their results have been shown to be remarkably accurate. Braglia and Dallacasa [308] have derived a theory that addresses both enhancements and reductions to the zero-field mobility through a Green’s function approach with appropriate approximations to the self-energy but do not go beyond linear response theory and hence do not explain non-equilibrium behaviour at high fields.

In contrast to the above approaches, the seminal articles by Lekner and Cohen [2, 3] outline a method to address effects of a dense fluid from an *ab initio* approach by appropriate modifications of the microscopic processes. The article by Lekner [2] describes how an effective potential for a single collision event can be built up from knowledge of only the single-atom/electron potential and the pair correlator of the fluid as well as prescribing a method for obtaining effective cross sections from this potential. The article by Cohen and Lekner [3] then describes how the effects of coherent scattering can be included with these effective cross sections in a Boltzmann equation solution for the calculation of transport properties. Sakai et al. [157] have been able to improve agreement with experiment by empirically modifying the resultant cross sections of the Cohen and Lekner formalism and by including inelastic processes. Atrazhev et al. [309] were able to simplify the arguments of Lekner [2] to argue that, for small energies, the effective cross section becomes dependent on the density only and obtained good agreement with experiment. However the distance at which to enforce this new behaviour of the effective cross section remains a free parameter in the theory and this constant effective cross section must be found empirically. Atrazhev and co-workers went on to consider the interaction as a muffin tin potential, with each cell being a Wigner-Seitz sphere surrounding each atom in the liquid. They used a variable phase function method which could describe the absence of a Ramsauer minimum in the liquid cross section along with density fluctuations of the liquid [310–312].

The calculations presented here are based on a generalization of the Cohen and Lekner formalism, overcoming several approximations which are no longer necessary in modern day transport and scattering theory. With regard to the scattering potential, Lekner [2] used the Buckingham potential [511] as input, which we will show is completely inadequate due to its omission of the exchange interaction. This is not noticeable for gas phase measurements, due to the fitting parameter of the Buckingham potential, but shows significant differences after the liquid modifications are applied. By performing a detailed analysis of the partial phase shifts, Atrazhev and co-workers [311] were able to isolate the important properties of the potential which are required for accurate determination of the transport properties. Our calculations instead avoid these difficulties by using accurate forms for the electron-atom interaction.

With regard to the transport theory itself, we employ a previously derived extension of the Cohen and Lekner formalism for the Boltzmann equation from a two-term to a full multiterm

treatment of the velocity distribution function [1]. This theory utilises the full anisotropic detail of the cross sections that is available in our calculations. For dilute gaseous systems, the two-term approximation can be in serious error [512], and in this chapter we consider contributions to the error arising from the neglect of the full anisotropy in both the velocity distribution function and the differential scattering cross section for liquid systems.

In Section 7.2, calculations are performed specifically for the noble gas of argon, which is an excellent test bed for new theories due to the good availability of experimental data and the high degree of accuracy to which *ab initio* calculations can model the gaseous phase. Available experimental data include drift velocities and characteristic energies in both the gas and liquid phases, as well as precise single-atom cross sections. It is emphasized that we are interested in the full non-equilibrium description of the transport properties and not only that of zero-field mobilities, and so we must consider the full range of the static structure factor $S(K)$ instead of $S(0)$ which is fixed by the isothermal compressibility. The calculation of the macroscopic swarm transport properties is considered in the gaseous and liquid environments from the microscopic cross sections, modified by the screening and coherent scattering effects. The gas phase cross sections are calculated using accurate potentials in the Dirac-Fock scattering equations, and we demonstrate the importance of an accurate treatment of exchange and polarization.

7.2 Electron scattering and transport in liquid argon

In this section, we perform calculations for the electron-argon system. We first detail the calculation of the gas phase cross sections in Section 7.2.1, using accurate potentials in the Dirac-Fock scattering equations and then address, in Section 7.2.2, effects of screening in the liquid. The transition from a gas to liquid requires a modification of the scattering to include an effective scattering potential and an effective non-local exchange term which we describe in Section 7.2.3. We present the results of our transport calculations in Section 7.2.4. Initially in Section 7.2.4 we consider only the gas phase, understanding the importance of an accurate treatment of exchange and polarization and thereby establishing the credibility of the initial gas-phase potential subsequently used as input for the calculation of cross sections for the liquid phase environment. Transport coefficients calculated using the screened cross sections and associated coherent scattering effects are considered in Section 7.2.4, where they are compared with the available measured transport data. Throughout this section, we will make use of atomic units ($m = e = a_0 = \hbar = 1$) unless otherwise specified.

7.2.1 Scattering of electrons by argon gas

The core of a transport calculation is based on an accurate description of the scattering of the electron off a particle in the bulk. Effective interaction potentials are often used to determine various measurable properties, such as scattering lengths or polarizabilities. These effective potentials are successful so long as they correctly reproduce these quantities for input in other simulations. However, as mentioned above, there are many additional effects due to a dense gas or liquid which can modify the details of the scattering processes. Hence, a potential is required that does not only produce the correct scattering properties in the dilute limit but also well describes the scattering properties under a perturbation of the potential.

In the pure elastic energy region, there are only two interactions which need to be taken into account in electron-atom collisions, namely polarization and exchange. The polarization can be accounted for by means of long-range multipole polarization potentials while the exchange interaction

is represented most accurately by a short-range non-local potential formed by antisymmetrizing the total scattering wavefunction.

In the present work the scattering of the incident electrons, with wave number k , by argon atoms is described in the gaseous phase by the integral formulation of the partial wave Dirac-Fock scattering equations (see [513] for details). In matrix form, these equations can be written as

$$\begin{pmatrix} f_\kappa(r) \\ g_\kappa(r) \end{pmatrix} = \begin{pmatrix} v_1(kr) \\ v_2(kr) \end{pmatrix} + \frac{1}{k} \int_0^r dx G(r, x) \left[V(x) \begin{pmatrix} f_\kappa(x) \\ g_\kappa(x) \end{pmatrix} - \begin{pmatrix} \overline{W}_Q(\kappa; x) \\ \overline{W}_P(\kappa; x) \end{pmatrix} \right], \quad (7.1)$$

where the local potential $V(r)$ is given by the sum of the static and local polarization potentials i.e.,

$$V(r) = V_s(r) + V_p(r), \quad (7.2)$$

and $\overline{W}_P(\kappa; r)$ and $\overline{W}_Q(\kappa; r)$ represent the large and small components of the exchange interaction. In equation (7.1), $f_\kappa(r)$ and $g_\kappa(r)$ are the large and small components of the scattering wavefunction where the quantum number κ can be expressed in terms of the total and orbital angular momentum quantum numbers j and l according to

$$j = |\kappa| - \frac{1}{2} \quad \text{with} \quad l = \begin{cases} \kappa, & \text{if } \kappa > 0, \\ -\kappa - 1, & \text{if } \kappa < 0. \end{cases} \quad (7.3)$$

The free particle Green's function $G(r, x)$ in equation (7.1) is defined in terms of Riccati-Bessel and Riccati-Neumann functions (see equations (23) and (24a,b) of Ref. [513]). The kinetic energy ϵ of the incident electron and its wave number k are related by

$$k^2 = \frac{1}{\hbar^2 c^2} U (U + 2mc^2). \quad (7.4)$$

We note that if we ignore U with respect to $2mc^2$, we obtain the usual non-relativistic relationship between the wave number and the energy of the incident electron.

The static potential $V(r)$ in equation (7.2) is determined in the usual manner from the Dirac-Fock orbitals of the atom [513]. The polarization potential $V_p(r)$ was determined using the polarized orbital method [471] and contained several static multipole terms as well as the corresponding dynamic polarization terms [514, 515]. In total, the potential $V_p(r)$ contained all terms up to and including those that behave as r^{-14} asymptotically.

Finally, the exchange terms $\overline{W}_P(\kappa; r)$ and $\overline{W}_Q(\kappa; r)$ in equation (7.1) are given by

$$\begin{aligned} \overline{W}_{P \text{ or } Q}(\kappa_2; r) &= (1 + \gamma) \sum_{n'\kappa'} \{ P_{n'\kappa'}(r) \text{ or } Q_{n'\kappa'}(r) \} \\ &\times \{ -[U_{n'\kappa'} + U] \Delta_{n'\kappa'} \delta(\kappa, \kappa') + e^2 \sum_{\nu} q_{n'\kappa'} \frac{1}{2\nu + 1} C^2 \left(jj'\nu; -\frac{1}{2} \frac{1}{2} \right) \frac{1}{r} y_{\nu}(n'\kappa', \kappa; r) \}. \end{aligned} \quad (7.5)$$

Here, $C(jj'\nu; -\frac{1}{2} \frac{1}{2})$ is the usual Clebsch-Gordan coefficient and the sum over $n'\kappa'$ in equation (7.5) is over the radial part of the atomic orbitals ($P_{n'\kappa'}(r)$ and $Q_{n'\kappa'}(r)$) of the ground state, while $q_{n'\kappa'} = 2j' + 1$ is the occupation number of these closed sub-shells where the $U_{n',\kappa'}$ are the eigenvalues of these sub-shells. The exact form of the definite integral $\Delta_{n'\kappa'}$ and the indefinite integral $r^{-1} y_{\nu}(n'\kappa', \kappa; r)$ is given in equations (11) and (12) of [516]. We note that the dependence of the exchange terms (7.5) on the wavefunction requires an iterative solution for equation (7.1).

In the integral equation formulation, the scattering phase shifts can be determined from the asymptotic form of the large component of the scattering wavefunction i.e.,

$$f_{\kappa}(r) \xrightarrow{r \rightarrow \infty} A_{\kappa} \hat{j}_l(kr) - B_{\kappa} \hat{n}_l(kr), \quad (7.6)$$

where

$$A_{\kappa} = 1 - \frac{1}{k} \int_0^{\infty} dr \left\{ \bar{v}_1(kr) [V(r) f_{\kappa}(r) - \bar{W}_P(\kappa; r)] + \bar{v}_2(kr) [V(r) g_{\kappa}(r) - \bar{W}_Q(\kappa; r)] \right\}, \quad (7.7)$$

and

$$B_{\kappa} = -\frac{1}{k} \int_0^{\infty} dr \left\{ v_1(kr) [V(r) f_{\kappa}(r) - \bar{W}_P(\kappa; r)] + v_2(kr) [V(r) g_{\kappa}(r) - \bar{W}_Q(\kappa; r)] \right\}. \quad (7.8)$$

The partial wave phase shifts are then given by

$$\tan \delta_l^{\pm}(k) = \frac{B_{\kappa}}{A_{\kappa}}, \quad (7.9)$$

where the δ_l^{\pm} are the spin-up (+) and spin-down (-) phase shifts. The total elastic and momentum-transfer cross sections are given by the same relations as in (5.3)–(5.4), which can be shown to reduce to the non-relativistic results if we set $\delta_l^+(k) = \delta_l^-(k) = \delta_l(k)$.

As can be seen in Figure 7.1, neither the polarization nor the exchange interaction alone is capable of reproducing the true Ramsauer minimum in the argon momentum transfer cross section; it is only when we combine these two interactions that there is agreement with experiment. This is also true for the Ramsauer minimum in the elastic cross section.

In the original work of [2], Lekner described the elastic scattering of electrons by argon atoms by just the local dipole polarization potential of Buckingham [511] which is given by

$$V_p(r) = -\frac{\alpha_d}{2(r^2 + r_a^2)^2}, \quad (7.10)$$

where α_d is the static dipole polarizability of argon and r_a is an adjustable parameter. Lekner chose this parameter so as to obtain the experimental scattering length $a_0 = -1.5$ a.u. of [429]. This value is very close to the current recommended value of $a_0 = -1.45$ a.u. of [18]. The value obtained in the current work is $a_0 = -1.46$ a.u.

As a consequence of Lekner's choice for the adjustable parameter r_a , his simple polarization potential in equation (7.10) was able to mimic the effects of both the polarization and exchange interactions at low energies of the incident electron and his calculation was able to produce a low-energy Ramsauer minimum in the momentum transfer cross section. At higher energies his momentum transfer cross section deviates from the experimental cross section.

The calculated cross sections are shown in Figure 7.1. We obtain very good agreement with the recommended set of cross sections of [18] which combine many different experimental measurements and theoretical calculations. In order to demonstrate the importance of including the non-local exchange interaction, we have also repeated the calculation using two different model potentials that replace the non-local exchange with an effective local term in the potential [19, 20]. One of these local approximations [19] is qualitatively wrong, showing the same behaviour as that without exchange. The other approximation [20] is qualitatively similar but differs in the scattering length and position of the Ramsauer minimum by an order of magnitude. It is clear to see that there is a significant difference between the results. When we compare our results to those of the Buckingham potential, where we set $r_{\alpha} = 1.087$ a.u. such that the scattering length is $a_0 = -1.50$ a.u., we find

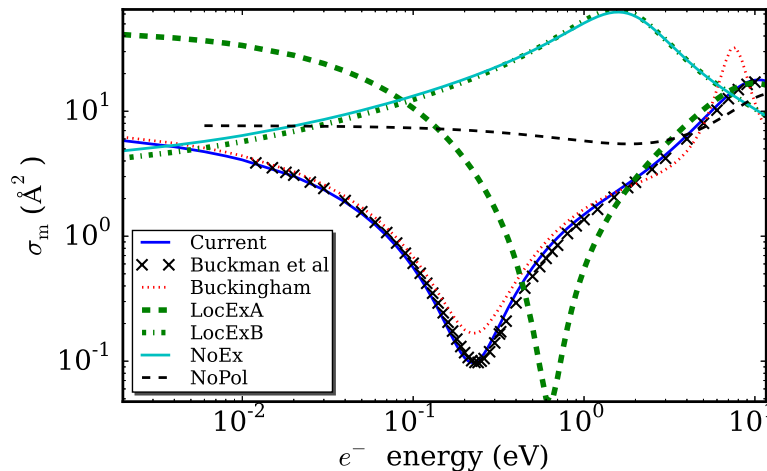


Figure 7.1: Cross sections for electron scattering from argon. The calculations described in this section, which use the non-local exchange interaction (solid line) are in good agreement with the recommended set of Buckman et al. [18]. A comparison with a calculation similar to that of Lekner [2] using a Buckingham potential (dotted line) shows loose qualitative agreement at the Ramsauer minimum, but quantitatively is incorrect. Also shown are the results from using two different effective models of a local exchange potential (thick dashed [19] and dash-dotted lines [20]) which do not agree with experimental measurement at all, as well as the cross section when exchange is included but polarization is neglected (thin dashed line).

that it does follow the general shape of the Ramsauer minimum. However, we emphasize that this is a result of the fitting parameter r_α and this potential does not accurately describe the details of the scattering.

7.2.2 Screening of the polarization interaction

The effects of the high density of the liquid are included in our calculations by several modifications of the gas scattering properties. The first of these is to account for the screening of a single induced atomic dipole by the induced dipoles of all other atoms. The procedure outlined in this section closely follows that of Lekner [2].

In the dilute gas limit, the mobile electron undergoes a collision with a single atom of the gas effectively in isolation from all other atoms in the gas. During this collision the electron induces a set of multipole moments in the atom, which in turn interact with the electron through a charge-multipole potential, resulting in the polarization potential, $V_p(r)$, of Section 7.2.1 above. For a dilute gas, the range of the potential produced by these induced multipole moments is relatively small compared with the large interatomic spacing and so it is a good approximation to neglect their effect on other atoms. However, with higher densities of the gas or liquid, many atoms can have a non-negligible induced set of multipole moments originating from both the mobile electron and from all other atoms in the bulk. The effective charge-multipole polarization potential felt by the electron at any particular location \mathbf{r}_e is then the sum of the polarization potentials from all atoms.

We consider effects originating from the induced dipoles of the atoms only and determine the effective polarization of an individual atom self-consistently. We first assume that the induced dipole strength for every atom in the bulk can be written as $f(r)\alpha_d(r)e/r^2$ where r is the distance of the electron from the atom, $\alpha_d(r)$ is the exterior dipole polarizability (see [517], equation (1)) for a single atom that results from the interaction with the electron, and $f(r)$ accounts for polarization

screening which must be determined. This simple multiplicative factor is valid, so long as we average over the atomic distribution. In the dilute-gas limit, we can safely approximate $f(r) = 1$, and in the dense case we must obtain a self-consistent expression for $f(r)$. By choosing a particular ‘focus atom’ i at location \mathbf{r}_i such that $\mathbf{r} = \mathbf{r}_e - \mathbf{r}_i$, and assuming that the coefficient $f(r)$ is known for all other atoms, which we denote by $f_{\text{bulk}}(r)$, we can calculate [2] the dipole strength for atom i from:

$$f_i(r) = 1 - \pi n_0 \int_0^\infty ds \frac{g(s)}{s^2} \int_{|r-s|}^{r+s} dt \Theta(r, s, t) \frac{\alpha_d(t) f_{\text{bulk}}(t)}{t^2} \quad (7.11)$$

which has been obtained using bipolar co-ordinates, s and t , where n_0 is the density of the bulk, $g(s)$ is the isotropic pair correlator of the bulk and the factor

$$\Theta(r, s, t) = \frac{3}{2} \frac{(s^2 + t^2 - r^2)(s^2 + r^2 - t^2)}{s^2} + (r^2 + t^2 - s^2), \quad (7.12)$$

arises due to the form of the electric field of a dipole. The integrations over s and t represent the contribution from an atom located at a distance s from atom i and a distance t from the electron. The likelihood of finding an atom is determined by $g(s)$ and so it can be seen that equation (7.11) approximates the exact polarization by that resulting from the ensemble average of all atomic configurations, given that one atom is located at \mathbf{r}_i . In this approximation, the polarization itself is always aligned along the vector $\hat{\mathbf{r}}$ between the focus atom and the electron.

The self-consistent solution to equation (7.11) is obtained by setting $f_i(r) = f_{\text{bulk}}(r)$ and solving for $f_i(r)$, which we do by iteration. The most important quantity in equation (7.11) is the pair correlator, which represents the next order in the particle distribution in the bulk beyond the average density. In the calculation of Lekner, the pair correlator was taken to be the analytical solution of the Percus-Yevick model for ease of calculation. In our calculation, we go beyond this by using the experimental measurements of Yarnell [21] to more accurately describe the correlations. The data we use, which was obtained for a bulk density of $n_0 = 0.0213 \text{ \AA}^{-3}$, is shown in Figure 7.2 and compared with the Percus-Yevick model at the same density.

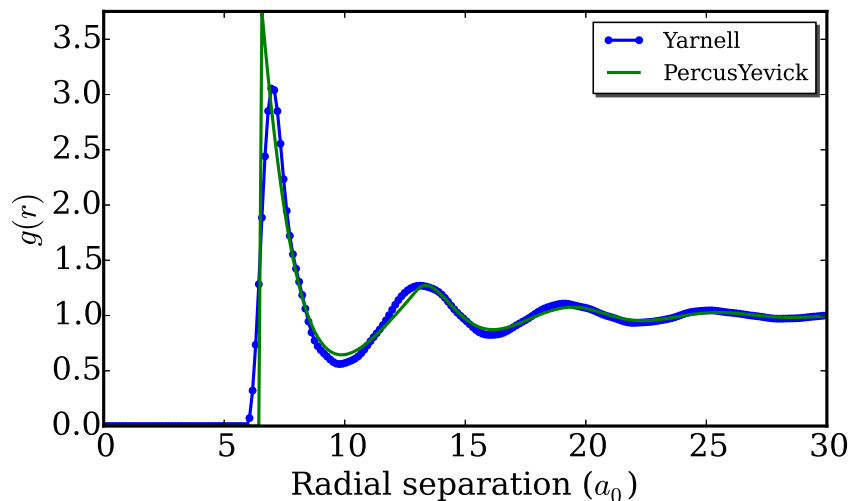


Figure 7.2: Pair correlator for argon, as reported in Yarnell [21], measured in neutron scattering experiments. Also plotted, is the pair correlator calculated in the analytical Percus-Yevick approximation as used by Lekner [2].

Using the pair correlator of argon, the screening function $f(r)$ has been self-consistently calculated, and the result is shown in Figure 7.3. Although this screening factor technically applies to the dipole term only, we work with a rather more complicated form of the polarization term than Lekner had originally considered. However, as the largest contribution to the polarization does indeed come from the dipole term, we have decided to apply the screening factor $f(r)$ to the entire polarization potential. Hence, with the screening of the polarization taken into account, the screened polarization potential, $\tilde{V}_p(r)$, of an electron with one atom in a dense fluid is given by:

$$\tilde{V}_p(r) = f(r)V_p(r). \quad (7.13)$$

We note that, in contrast to Lekner, who used only the static dipole polarizability α_d , the more accurate representation of the atom-electron interaction as described in Section 7.2.1 has already led to a radial dependence of the polarization potential $V_p(r)$ beyond that of a potential whose asymptotic behaviour is r^{-4} . The effect of the screening has hence lead to a further modification of $V_p(r)$ which is density dependent.

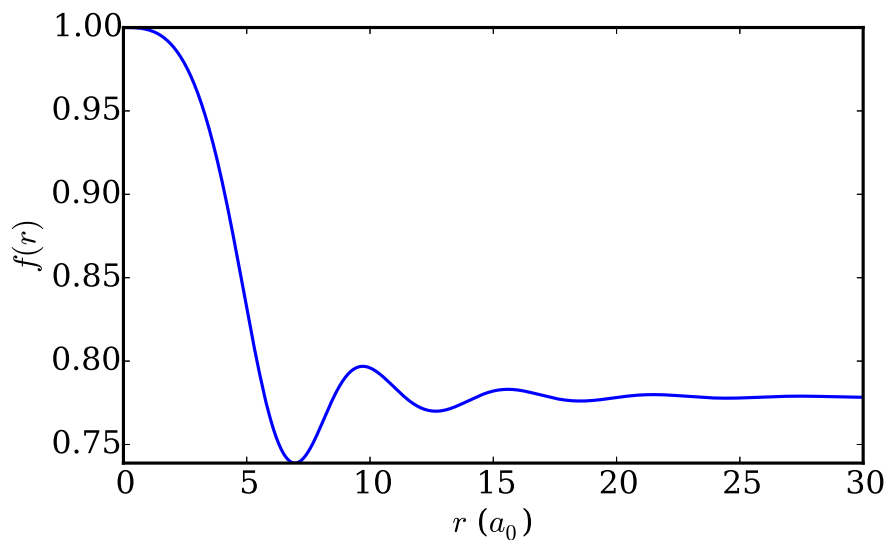


Figure 7.3: The screening function $f(r)$ of the polarization interaction potential for scattering of an electron from a single argon atom in a bulk of density $n_0 = 0.0213 \text{ \AA}^{-3}$.

7.2.3 Effective potential in a liquid

For input into the kinetic theory, we require appropriate cross sections for the scattering of the electron from a single ‘focus atom’ in the bulk. As discussed above, the presence of the other atoms screens the polarization interaction between the electron and the focus atom. However, there is another more obvious effect resulting from the other atoms in the bulk: their interaction with the electron itself remains significant even when the electron is very close to the focus atom. Hence, as outlined in Lekner [2], we build up an effective potential that is experienced by the electron throughout a single scattering event, as well as define what is meant by ‘a single scattering event’. Although we follow the general principles of [2], we calculate the cross sections in a distinctly different fashion.

The effective potential that we consider $V_{\text{eff}} = V_1 + V_2$ is made of two parts: $V_1(r)$ which corresponds to the direct interactions with the focus atom, and $V_2(r)$, which corresponds to the interaction of the electron with the rest of the bulk. As it is prohibitively expensive to treat exact

configurations of atoms in the bulk, we build the external potential V_2 by again taking the ensemble average:

$$V_2(r) = \frac{2\pi n_0}{r} \int_0^\infty dt V_1(t) \int_{|r-t|}^{r+t} ds sg(s), \quad (7.14)$$

where the order of integration has been reversed in comparison to (7.11) for numerical convenience¹. We note that taking the ensemble average has the advantage of enforcing spherical symmetry of the total effective potential V_{eff} . In calculating (7.11) and (7.14), we make use of the quantity σ_{core} , which corresponds to the hard-core exclusion diameter for the distribution of atoms in the bulk, i.e. the probability for two atoms to approach within a distance σ_{core} is vanishingly small. For argon $\sigma_{\text{core}} \approx 6a_0$ and we take advantage of this by explicitly setting $g(s) = 0$ for $s < \sigma_{\text{core}}$ and adjusting the limits of equations (7.11) and (7.14) accordingly.

In addition we go beyond Lekner's calculation by including the effects of the exchange terms in the bulk. We do this by performing the same ensemble average as in (7.14) but over the quantities \bar{W}_P and \bar{W}_Q instead of V_1 , obtaining bulk averages $\bar{W}_{P,2}$ and $\bar{W}_{Q,2}$. These are then included as effective exchange terms, $\bar{W}_{(P \text{ or } Q),\text{eff}} = \bar{W}_{P \text{ or } Q} + \bar{W}_{(P \text{ or } Q),2}$ in the Dirac-Fock scattering equations (7.1). In contrast to V_2 , these exchange terms are dependent on the wave function itself, so the ensemble averages must be recalculated at every iteration in the solution of (7.1).

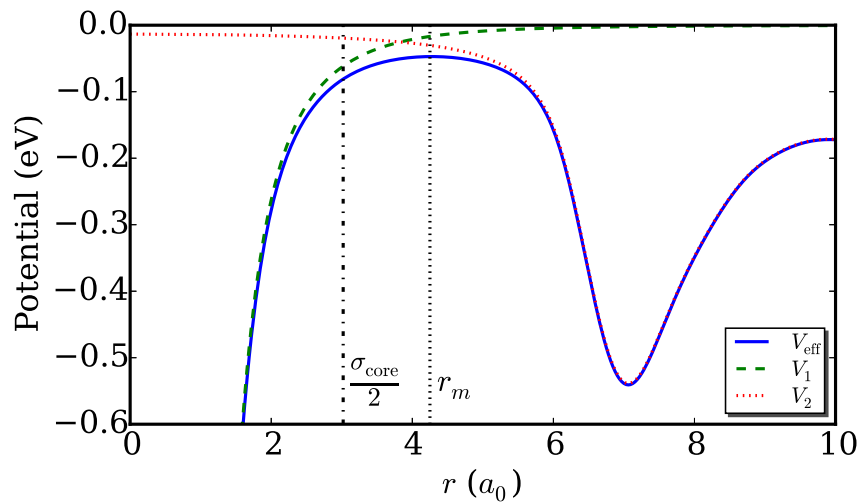


Figure 7.4: Plots of the total effective potential V_{eff} felt by an electron when colliding with one atom in the liquid. Also shown are the components, V_1 and V_2 , which represent the direct potential of the atom and the contribution of the remaining atoms in the bulk respectively. The dashed vertical lines at $\sigma_{\text{core}}/2$ and r_m indicate the hard-core exclusion radius and the proposed collisional sphere respectively. Note that effects of exchange are not represented in this figure.

A plot of the functions V_{eff} , V_1 and V_2 is shown in Figure 7.4. It can be seen that there is a turning point that occurs at a distance we denote by r_m . In the dense gas limit that we are investigating, this value is $r_m \approx 4.3a_0$. The turning point at r_m provides a natural distinction between the volume that is under the influence of the focus atom, i.e. the sphere of radius r_m , and that of the rest of the bulk. Hence, we can say that a single collision event takes place when an electron enters and leaves the radius r_m of a single atom. We note that $r_m \approx \frac{2}{3}\sigma_{\text{core}} > \sigma_{\text{core}}/2$, i.e. r_m is larger than half of the minimal interatomic separation, which could be considered to define the volume ‘owned by’ the focus atom and hence a logical choice for the ‘collision event radius’.

¹In the arrangement of (7.14), it is possible to precompute the innermost integral cumulatively once and use its values in a look-up table.

r_m is also different from the Wigner-Seitz diameter $d_{\text{WS}} = 2(4\pi n_0/3)^{-1/3} \approx 4.2 a_0$ [312], although it is very similar.

We would now like to solve for the scattering properties, in particular the cross sections, from such a collision process. We assume that it remains reasonable to extract the cross sections through the phase shifts in a partial wave equation. In order to determine these, Lekner chose to shift the effective potential by an amount V_0 such that $V_{\text{eff}}(r_m) + V_0 = 0$, and to set the potential $V_{\text{eff}}(r > r_m) = 0$, and finally matched to the asymptotic form of each partial wave in the usual fashion. In contrast, we choose to leave the potential unaltered, but calculate the phase shift at the point r_m instead, effectively setting the upper limits of equations (7.7) and (7.8) to be r_m instead of infinity. We note that this is also known as calculating the ‘phase function’ [311] at the point r_m , which is equivalent to setting $V_{\text{eff}}(r > r_m) = 0$ and matching to the asymptotic form of the wave function. We believe that this more accurately represents the available energy states in the bulk.

As we may assume $g(s) = 0$ for $s < \sigma_{\text{core}}$ and because we calculate the potential only up to a distance of $r_m \approx \frac{2}{3}\sigma_{\text{core}}$, we can see that the integral over t in (7.14) is non-zero only for $t \gtrsim \frac{1}{3}\sigma_{\text{core}} \approx 2a_0$. At these ranges, the dominant contribution to the potential comes from the polarization component. We also note that the values of $\overline{W}_{P,2}$ and $\overline{W}_{Q,2}$ are not well behaved for larger distances and so we set them to be zero for $r > \sigma_{\text{core}}/2$. We have performed calculations that neglect the contribution of $\overline{W}_{P,2}$ and $\overline{W}_{Q,2}$ to the bulk and compared these to the full calculations, which showed very little difference in the high energy regime of the resultant cross sections and a small difference of up to 5% otherwise. The effect of this change on the transport properties was a small but non-negligible deviation.

Cross sections and variation of r_m

The choice of the value for r_m is a crucial part of our calculation. It is worth mentioning that the choice we make above is consistent in the limit of $n_0 \rightarrow 0$; in this case V_2 is so weak that it is only after V_1 has significantly decayed for very large values of r that $d(V_1 + V_2)/dr = 0$. Hence, $r_m \rightarrow \infty$ as $n_0 \rightarrow 0$ and our calculation reduces to the usual scattering calculation from a single atom. However, in the dense case, it is not known whether $d(V_1 + V_2)/dr|_{r_m} = 0$ is the best choice to model the scattering in the liquid. Hence, we have also performed a sensitivity analysis on the parameter r_m . We denote the distance at which we calculate the phase shifts by r^* and allow it to vary from our initial choice of $r^* = r_m$. The resultant cross sections from a variation of $\pm \frac{1}{16}a_0$ are shown in Figure 7.5 as well as the more straightforward choice of $r^* = \sigma_{\text{core}}/2$. We note that Atrazhev et al. [312] have implicitly investigated this variation previously, in order to describe the effect of density fluctuations on the effective cross sections. In their case, the value of r^* was set to be the Wigner-Seitz cell radius, which itself depends on the density of the liquid. In contrast, we keep the density fixed while varying r^* .

It can easily be seen that the largest modification to the cross sections due to the variation in r_m occurs at low energies. Importantly, the more obvious choice of $r^* = \sigma_{\text{core}}/2$ yields a dramatically different behaviour. As will be shown later, the effect that these variations have on the transport measurements is significant and shifts the peak observed in various transport properties.

We note that we neglect the effect of density fluctuations, which would modify the effective cross section for the liquid. This was investigated by Atrazhev et al. [312], and shown to have a significant contribution to the cross sections. However, their article focused on a density for which the effective liquid cross section vanishes, causing the density fluctuations to be the largest

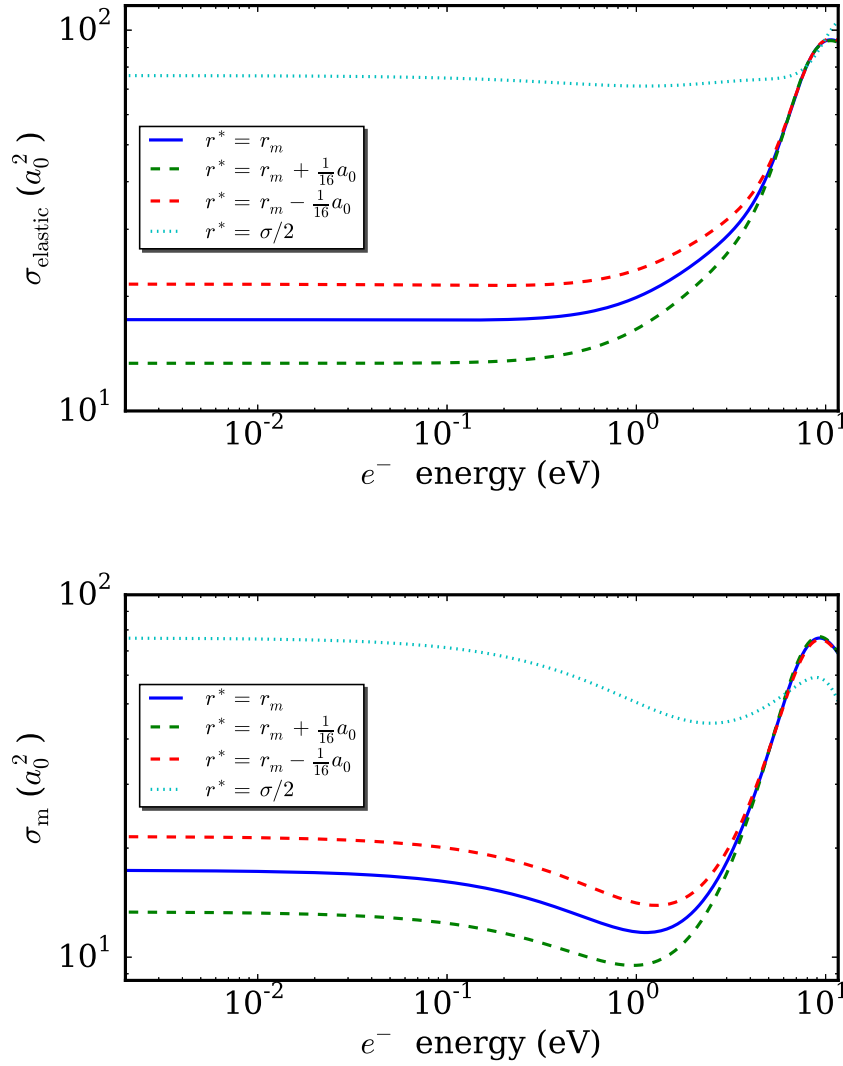


Figure 7.5: Elastic total and momentum-transfer cross sections for argon calculated from the phase shifts determined at a distance r^* . Our preferred choice for transport calculations in this work, $r^* = r_m$, corresponds to the solid line, the dashed lines are those corresponding to a variations $r^* = r_m \pm \frac{1}{16}a_0$ and the dotted line corresponds to a variation of $r^* = \sigma_{\text{core}}/2$.

contribution for small electron energies. In our case, we can expect density fluctuations to cause both enhancements and reductions of the cross sections, which would cancel out on average.

7.2.4 Results

Swarm experiments are a test of the particle, momentum and energy balance in the cross section set and the associated transport theory or simulation. In the low-field regime considered in this chapter, only conservative quasi-elastic processes are operative, and hence the ability of the calculated values of drift and characteristic energy to match the measured coefficients provides this test on momentum and energy balance.

In the following sections we consider the calculation of the macroscopic swarm transport properties in the gaseous and liquid environments from the microscopic cross sections, including screening and coherent scattering effects as discussed above. Initially in Section 7.2.4 we consider only the gas phase, focussing on understanding the importance of an accurate treatment of exchange and

polarization and establishing the credibility of the initial gas-phase potential subsequently used as input for the calculation of cross sections for the liquid phase environment. Transport coefficients calculated using the screened cross sections and associated coherent scattering effects are considered in Section 7.2.4, where they are compared with the available measured transport data in the liquid phase.

Electrons in gaseous argon – benchmarking the potential and exchange treatment

The calculated drift velocity and characteristic energy transport properties using the gas-phase cross sections detailed in Section 7.2.1 are presented in Figure 7.6. They are compared against various experimental data for this gas [22,24]. We restrict ourselves to the reduced electric fields of less than 3 Td, to ensure we are in the regime where only elastic scattering is operative.

Our current potential, with a non-local treatment of exchange, we observe agreement to within 3% or better for drift velocity and 10% or better for the characteristic energy over the majority of the reduced fields considered (fields where the transport properties are rapidly increasing have a higher percentage difference). If the exchange interaction is neglected in the calculation of the cross section, we observe that the calculated values of the transport properties depart from the measured by an order of magnitude or more, reflecting the qualitative disagreement in the form of the cross sections predicted in Figure 7.1. Given the similarities in the cross sections calculated using the local exchange potential B [20] to those neglecting exchange, the calculated transport coefficients are quite similar between the two techniques. Using the local treatment of exchange A [19], which reproduces the Ramsauer minimum in the cross section (although its depth, location and width disagree quantitatively), the transport coefficients have a similar qualitative form, however they are displaced to significantly higher fields relative to the measured values. As expected, implementation of the Buckingham potential as in Lekner [2], which was tuned to reproduce the zero-energy gas-phase cross section, produces drift velocities that are accurate to within 10%, however the characteristic energies are significantly worse than those using the current potential. The small disagreement for the characteristic energy over a small range of E/n_0 may reflect some minor limitations in the cross section database.

Electrons in liquid argon

In Figure 7.7, we compare the drift velocity and characteristic energies in both the gaseous and liquid phases. The transport coefficients are presented as a function of the reduced electric fields, so that the explicit density dependence has been scaled out and we have a true comparison of the gaseous and liquid phases. For a given reduced field, we observe that the drift velocity in the liquid phase is enhanced by as much as an order of magnitude over the gaseous phase in the reduced field range considered. Contrarily, the characteristic energy in the liquid phase is reduced relative to the gaseous phase by as much as 500% over the range of fields for which the data exists. Importantly, the measured data emphasizes that transport of electrons in liquids cannot be treated by using only the gas phase cross sections and scaling of the density to those of liquids.

We now assess the importance of including various physical processes present in liquids in reproducing the measured transport coefficients. Firstly, we assess the importance of coherent scattering effects, by implementing the gas-phase interaction potential and associated cross sections into the coherent scattering framework detailed in Section 2.3.1. The resulting cross sections are displayed in Figure 7.8. We observe in Figure 7.7 that the inclusion of only coherent scattering effects acts to enhance both the drift velocity and the characteristic energy. This is a reflection of the reduced momentum transfer cross section in Figure 7.8 in the regime where coherent scattering effects are

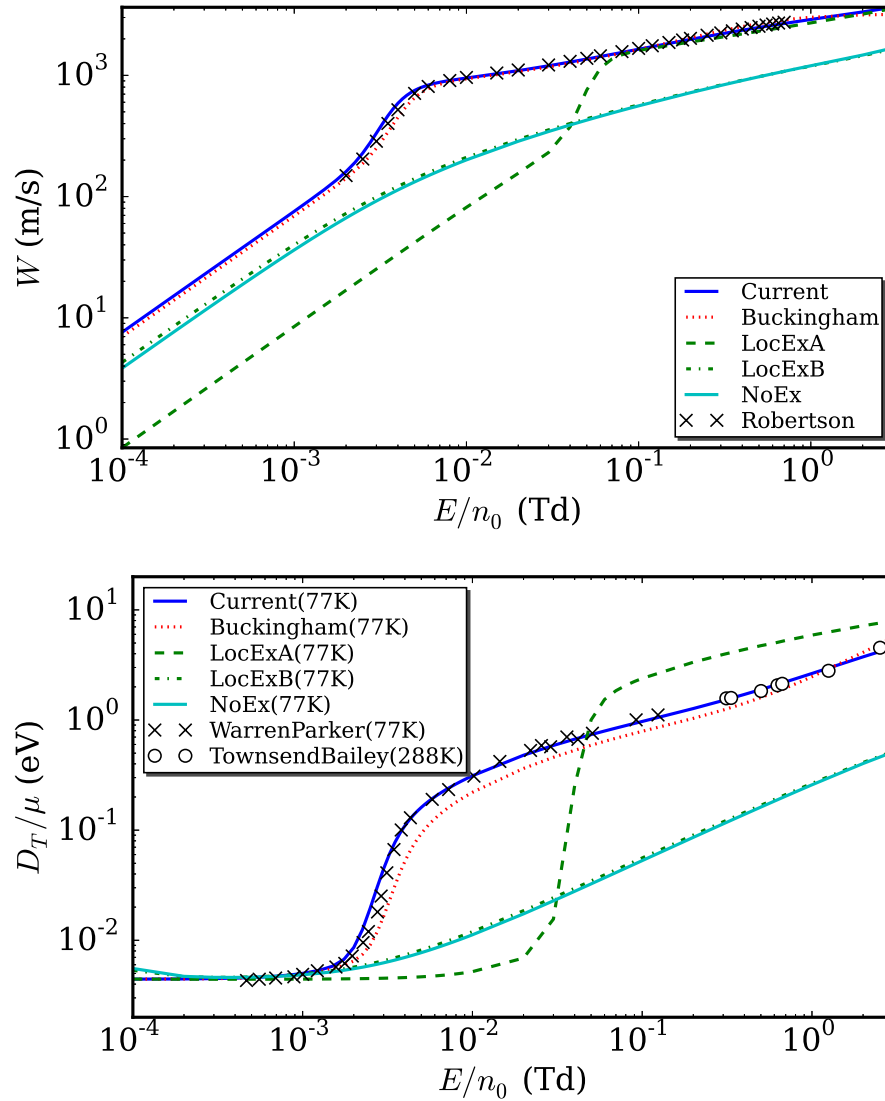


Figure 7.6: The drift velocity (top) and characteristic energy (bottom) of electrons in gaseous argon, calculated using the potentials and associated cross sections detailed in Section 7.2.1, and compared with available experimental data (Robertson [22,23] at 90 K; Warren and Parker [24,25] at 77 K; Townsend and Bailey [26,27] at 288 K). The full non-local treatment of exchange considered here is compared to two forms of local exchange potentials (LocExA [19]; LocExB [20]) and to the case when the exchange interaction is neglected altogether. The background argon gas for the calculations was fixed at 90 K for determination of the drift velocity and 77 K for the characteristic energy.

operative [1]. Interestingly, coherent scattering produces the physical process of negative differential conductivity (i.e. the fall of the drift velocity with increasing electric field) which is absent from the gas-phase calculations, as discussed elsewhere [1]. While the inclusion of coherent scattering effects results in a calculated drift velocity of the same order of magnitude as the experimental data, it does not reproduce the correct shape in the profiles, with errors as large as 250%. Further, the calculated characteristic energy produced by including coherent scattering enhances the characteristic energies relative to the gas phase which is inconsistent with the experimental data.

Second, in addition to the coherent scattering, we now include the full liquid induced effects on the potential as detailed in Sections 7.2.2 and 7.2.3. The resulting cross sections are displayed in Figure 7.8, where we emphasize that such effects act to essentially remove the Ramsauer minimum

in the cross section. This produces an enhanced and relatively constant cross section in that energy regime. This is very similar to that predicted by Atrazhev and Iakubov [309], in their reduction of the Cohen and Lekner theory, which suggested that a cross section that is only density dependent would occur for low impact energies. In Figure 7.7 we demonstrate that the inclusion of both scattering potential modification and coherent scattering produces drift velocities and characteristic energies that are both qualitatively and quantitatively in agreement with the experimental data. Errors in the drift velocities and characteristic energies are significantly reduced.

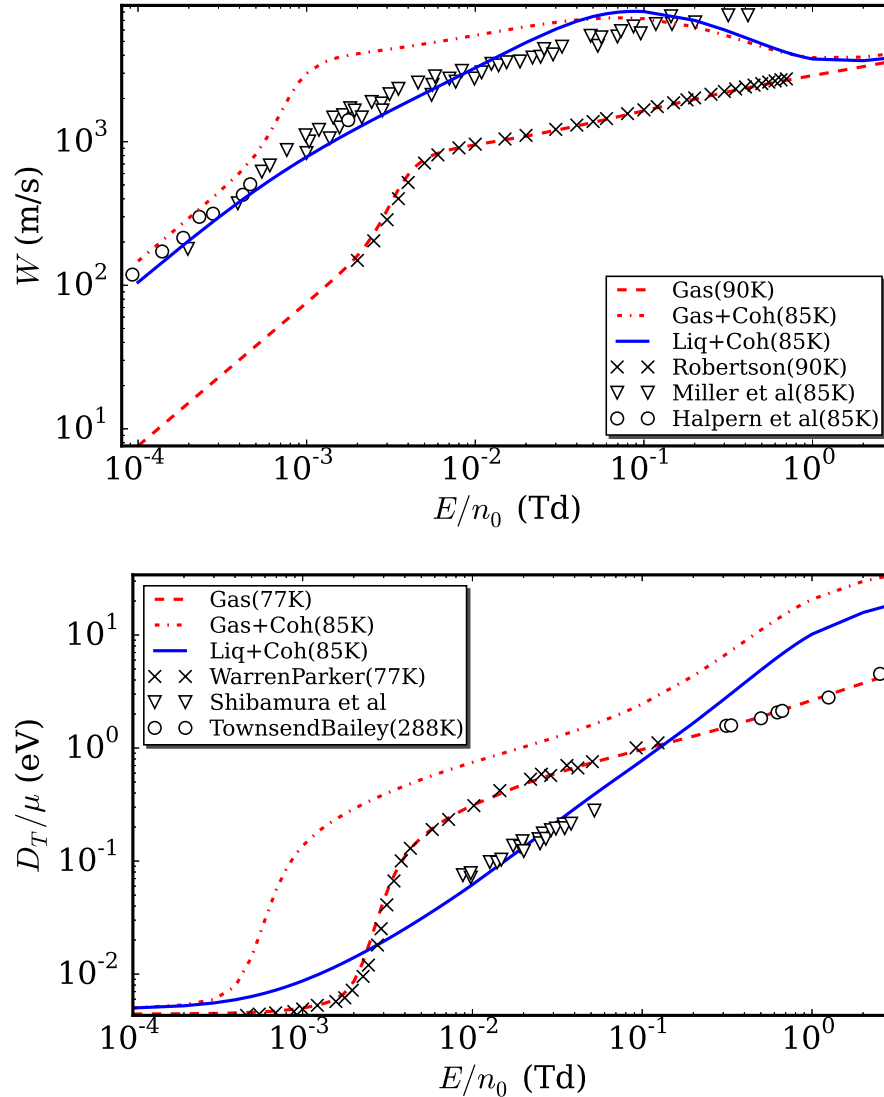


Figure 7.7: Comparison of the measured drift velocities W and characteristic energies D_T/μ in gaseous and liquid argon, with those calculated from the various approximations to the cross sections. Experimental data (Robertson [22,23] at 90 K; Miller et al. [28] at 85 K; Halpern et al. [29] at 85 K; Warren and Parker [24,25] at 77 K; Townsend and Bailey [26,27] at 288 K; Shibamura et al. [30] at an unmeasured liquid temperature). The various approximations used are: gas-phase only cross sections (Gas), gas-phase cross sections with coherent scattering (Gas+Coh), and liquid phase cross sections with coherent scattering effects (Liq+Coh). The results have been calculated using the full differential cross section and results are converged multi-term values. Experimental uncertainties are estimated at 2% for Robertson and less than 15% for Shibamura et al.

In Figure 7.5, we highlighted the sensitivity of the calculated cross sections in the liquid phase to the value of r^* at which the phase shifts are determined. The macroscopic manifestations of this

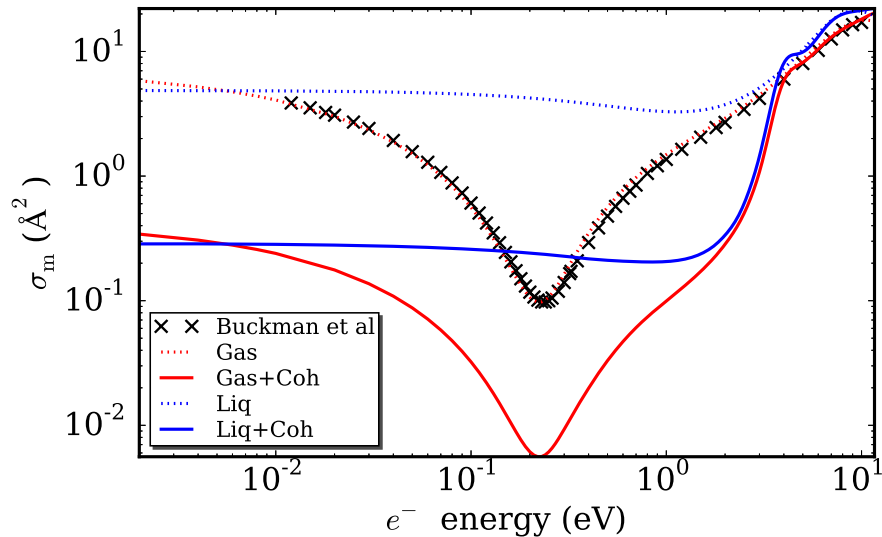


Figure 7.8: The momentum transfer cross sections in the gas-phase (Gas), liquid-phase (Liq) and their modifications when coherent scattering effects are included (+Coh). The recommended transfer cross section of reference [18] for a dilute gas is a combination of experimental measurements and theoretical calculations.

sensitivity on both the drift velocity and characteristic energy is presented in Figure 7.9. Slight modifications of r^* by $a_0/16$ from the preferred value of $r^* = r_m$ emphasize the sensitivity of the transport coefficients to this value. The choice of $r^* = \sigma_{\text{core}}/2$ produces results that are essentially translated to higher reduced electric fields. Importantly, these results indicate that the value of r_m may be energy dependent. One could possibly tune the value of r_m to match the experimental data, however we have strived to eliminate adjustable parameters in our formalism. One may also look at using an alternative scheme that is energy-dependent for choosing the value of r_m , e.g. including contributions from the exchange terms $\overline{W}_{P,\text{eff}}$ and $\overline{W}_{Q,\text{eff}}$.

7.2.5 Impact of scattering anisotropy and the two-term approximation

We conclude this section by considering the impact of the anisotropy in both the scattering cross sections and the velocity distribution function on the calculated transport properties.

In Figure 7.10 we display the differential cross sections for the gas phase and for the liquid modified differential cross sections, highlighting the impact of coherent scattering effects. For the dilute gas phase, we observe at low energies that the differential cross sections are small and essentially isotropic. As we move to higher energies, the differential cross section begins to demonstrate an increased magnitude and also enhanced anisotropy, with peaks in the forward and back-scattering directions. When we account for liquid effects in the scattering potential, we observe that similar qualitative structures are present in the resulting differential cross section, with slightly more structure than for the dilute gas phase. When the liquid phase differential cross section is combined with the structure factor accounting for coherent scattering effects, the resulting differential cross section $\Sigma(U, \chi)$ takes on a completely different qualitative structure. The forward peak in the differential cross section is removed, with suppression of the cross section at low energies and low scattering angles. The backscattering peak in the differential cross section at high energies remains unaffected, while subpeaks in the differential cross section are enhanced by the coherent scattering effects.

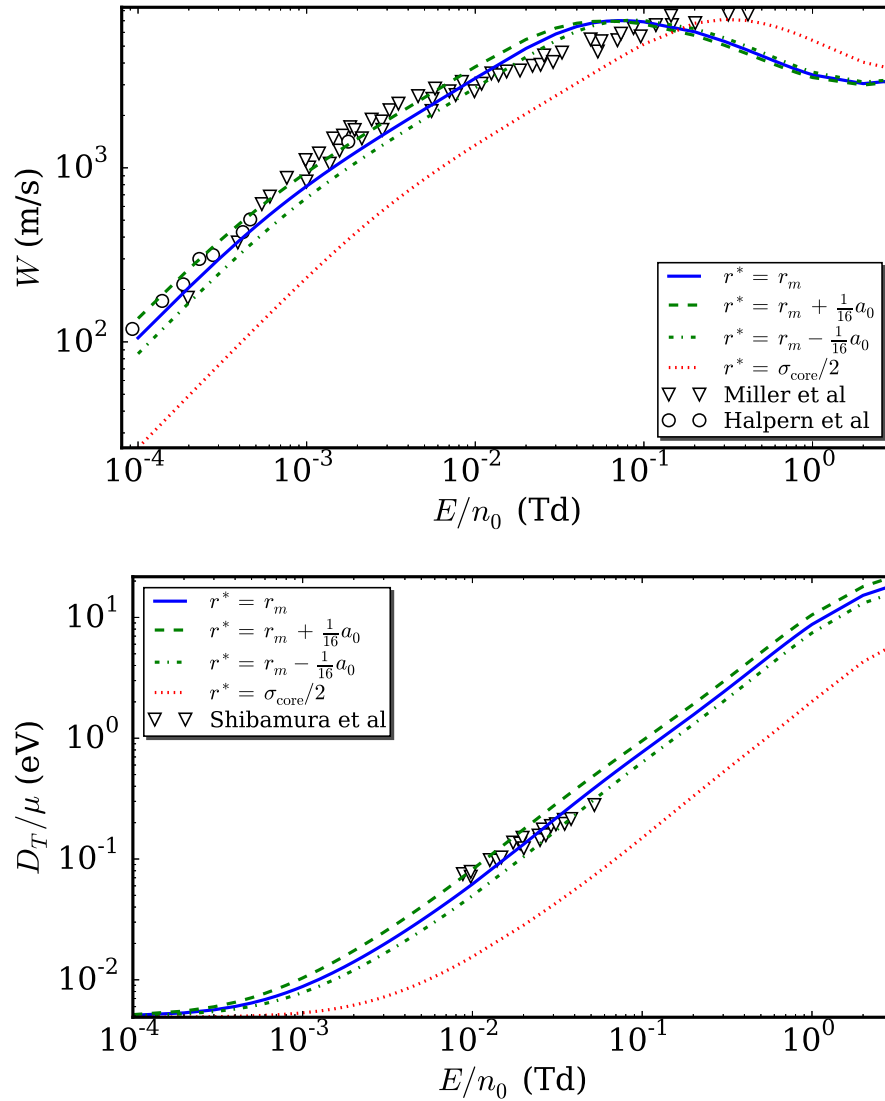


Figure 7.9: Comparison of the calculated drift and characteristic energy with variation in the distance r^* at which the phase shifts are determined. Experimental data is as detailed in Figure 7.7.

The degree of anisotropy in the distribution function is evidenced by an enhanced value of l_{max} required in the spherical harmonic expansions (2.3), and (2.4) to achieve convergence in the velocity distribution or transport properties. In Figure 7.11, we display the error in the two-term approximation ($l_{\text{max}} = 1$) and the converged multi-term result. In the gas and liquid phases we see that the two-term approximation is sufficient to ensure accuracy to within 0.5% in the drift velocity, however errors as large as 10% are present in the characteristic energy. This indicates a failure of the two-term approximation for the evaluation of the characteristic energy. Similar findings in the gas-phase were found by Brennan and Ness [518]. Theories that have used the two-term approximation to iteratively adjust cross sections may produce cross sections that are inconsistent with a multi-term framework.

In Figure 7.11 we also consider the impact of anisotropic scattering on the validity of the two-term approximation. The two-term approximation can only sample the momentum transfer cross section. Higher-order spherical harmonic components of the distribution function in expansions (2.3), and (2.4) are coupled to, and hence sample, higher-order coefficients in the expansion of the differential cross section. In Figure 7.11 we highlight the differences, using dashed lines, between

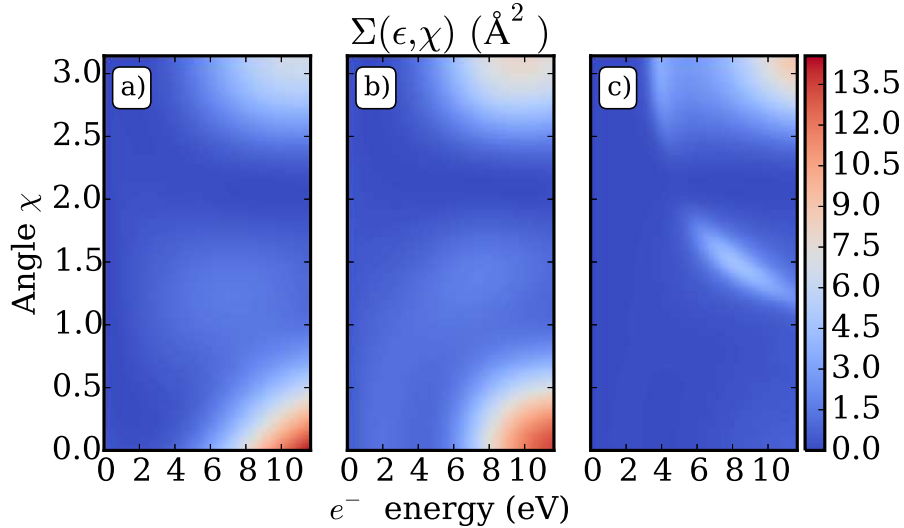


Figure 7.10: Differential cross sections in square angstroms for electrons in Ar for a) dilute gas phase, b) effective liquid phase including screening effects, and c) liquid phase cross section including coherent scattering effects $\Sigma(U, \chi)$.

the multi-term approximation using only the momentum transfer cross section (i.e. we assume $\sigma_{l \geq 2} = \sigma_1$) and those where the full differential cross section is considered. The differences are less than 1% (usually less than 0.1%) indicating the distribution function is not sufficiently anisotropic to couple in higher-order partial cross sections. Equivalently, anisotropy in the differential cross sections has only a minimal impact on the anisotropy in the velocity distribution function.

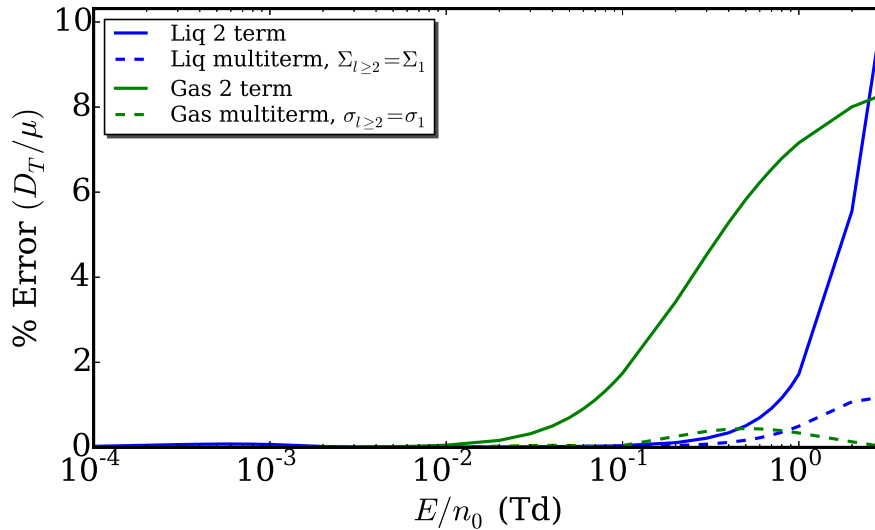


Figure 7.11: Percentage differences between the two-term and multi-term values of the characteristic energy for the gas and liquid phases using the full differential cross sections (solid lines), and percentage differences between the multi-term results with using only the momentum transfer cross section and the full differential cross section (dashed lines). All percentages are relative to the converged multi-term result using the full differential cross section.

7.3 Conclusion

We have extended the approach of Lekner and Cohen [2,3], overcoming some of its limitations, to calculate the effective cross sections and transport properties of electrons in liquid argon. For the first time an accurate multipole polarizability in the electron-atom potential, and a fully non-local treatment of exchange were included in the calculation of liquid-phase cross sections using the full machinery of the Dirac-Fock scattering equations. The accuracy of the potential implemented and associated cross sections calculated was confirmed by comparison with experiment in the gas-phase, and the importance of a fully non-local treatment of exchange was demonstrated. The result calls into question cross sections (gas, liquid or clusters) which assume a local treatment of the exchange. Sensitivity to the radial cut-off for the electron-atom potential was presented, and while the maximum in the potential was shown to be a suitable choice, enhanced accuracy may be achieved with an energy dependent choice of the cutoff.

The calculation of the drift velocity and characteristic energies were performed for the first time using a multi-term solution of Boltzmann's equation accounting for coherent scattering. The full anisotropy of the liquid-phase differential cross section was considered including anisotropy arising from both the interaction and from the structure factor. The multi-term framework enabled an assessment of the sensitivity to this anisotropy in the differential cross section and in the velocity distribution function. While the two-term approximation was found to be sufficient for accuracies to within 1% for the drift velocity, errors of the order of 10% or more were found in the characteristic energy. The latter was found to be the dominant contribution to the differences in the two and multi term results. It was found that both coherent scattering and screening of the electron-atom potential are required to reproduce the measured transport coefficient values. We emphasize that there are no free parameters in the current theory and its implementation, and hence the high level of agreement between the calculated and measured transport coefficients yields confidence that the essential physics has been captured in the theory.

8

Non-hydrodynamic space-time dependent transport

This chapter contains material that has been submitted to the following journal article:

G. J. Boyle, D. G. Cocks, W. J. Tattersall, R. P. McEachran, and R. D. White. A multi-term solution of the space-time Boltzmann equation for electrons in gaseous and liquid Argon. *Submitted to Physical Review E*.

8.1 Introduction

In the previous chapter, the scattering and transport of excess electrons in liquid argon in the hydrodynamic regime was investigated, generalizing the seminal works of Lekner and Cohen [2, 3] with modern scattering theory techniques and kinetic theory. Transport coefficients such as drift velocities and characteristic energies calculated in the hydrodynamic regime with our hydrodynamic multi-term Boltzmann equation solution were in good agreement with swarm experiment measurements in both gas- and liquid-phase argon. In this chapter, the discussion is extended to the non-hydrodynamic regime.

The solution of the the full temporal-, spatial- and energy-dependent Boltzmann equation is formidable, both mathematically and computationally. Historically, the majority of kinetic theory investigations have focused on the hydrodynamic regime where spatial gradients are small, and have considered increasingly complex space- and time-dependent hydrodynamic behaviours and field configurations (see reviews [248, 254, 269, 271, 519]). In situations where the hydrodynamic regime is not applicable, the space-time dependence of the phase-space distribution function can not be projected onto the number density and a density gradient expansion is no longer valid. Instead the configuration-space dependence of the Boltzmann equation must be treated on equal footing with the energy-space dependence, which makes for a difficult problem even for simple geometries [278–280]. It is no surprise that systematic studies of non-hydrodynamic phenomena

lag behind their hydrodynamic counterparts. The prototypical example of non-hydrodynamic phenomena is the Frank-Hertz experiment [281,282], which helped lay the foundations for quantum and atomic physics. Extensive theoretical studies of non-hydrodynamic electron phenomena have been performed including field free spatial relaxation [290], and spatial relaxation in the presence of uniform [291–293], non-uniform [294] and periodic electric fields [295–297]. Similar kinetic studies on the spatial relaxation of electrons in uniform and spatially periodic fields have been performed by Golubovskii et al. [298–301]. Li and co-workers have considered arbitrary electric and magnetic field configurations with a multi-term analysis [254,303,520]. Solution of the Boltzmann equation for electrons including both the space and time dependence have also recently been performed [304–306], however these authors restricted their calculations to a two-term approximation in Legendre polynomials in order to make the problem computationally feasible. Limitations of the two-term approximation for molecular gases are well known [512]. Prior to the study in [8], all studies of electron transport in liquids were in the hydrodynamic or spatially homogeneous regimes, and restricted to the two-term approximation.

In this chapter, we present a full multi-term space-time dependent solution of Boltzmann’s equation, capable of handling highly non-equilibrium electron transport in dilute gases, dense gases and liquids under non-hydrodynamic conditions. To our knowledge, this is the first time such a complete solution of Boltzmann’s equation has been developed. In addition, by solving for the spatio-temporal evolution of the Boltzmann equation Green’s function, the technique is quite general in its application, enabling various experimental configurations (temporal and spatial initial and boundary conditions) and practical devices to be modelled from a single solution. This work extends the Boltzmann equation framework to applications and accuracies comparable to those achieved using the Monte-Carlo simulations of Petrović, Dujko and co-workers [149–151].

The operator splitting treatment of the space, time and energy dependence is detailed in Section 8.2. In Section 8.3 we present solutions for a model hard-sphere liquid system with a Percus-Yevick structure factor used to simulate a prototypical liquid with realistic pair correlations. A simple inelastic channel is included to induce periodic oscillatory structures (an idealized version of the well known Frank-Hertz experiment [282]) which can act as a non-hydrodynamic benchmark. Lastly, in Section 8.4 we investigate the temporal and spatial evolution of the phase-space distribution for electrons in liquid argon, using microscopic cross sections which have been derived previously [8]. The issues with treating liquid systems as gaseous systems with increased density, and the implications for various applications including liquid argon time projection chambers, are highlighted.

8.2 Solution technique

The Boltzmann equation, (2.2), consists of two parts; an advective component (in phase-space) and a component representing collisions. It is a formidable task to solve the Boltzmann equation numerically, using a single numerical scheme for both components and a single time-stepping method. Because of the complexity, we choose to replace the task of solving the full Boltzmann equation by the task of solving the configuration-space transport, the energy-space transport and the contributions due to collisions separately, then combining the results in a manner that appropriately approximates the full solution. This can be achieved via the technique known as operator splitting [356].

8.2.1 Operator splitting

As discussed in Chapter 2, the Legendre polynomial expansion of Boltzmann's equation in plane parallel geometry given in equation (2.9) can be represented as

$$\frac{\partial f_l}{\partial t} + S_Z(f_l) + S_U(f_l) = 0, \quad (8.1)$$

where

$$S_Z(f_l) = \sum_{p=\pm 1} \Delta_l^{(p)} \left(\frac{2}{m}\right)^{\frac{1}{2}} U^{\frac{1}{2}} \frac{\partial}{\partial z} f_{l+p}, \quad (8.2)$$

$$S_U(f_l) = \sum_{p=\pm 1} \Delta_l^{(p)} \left(\frac{2}{m}\right)^{\frac{1}{2}} eE \left(U^{\frac{1}{2}} \frac{\partial}{\partial U} + p \frac{(l + \frac{3p+1}{2})}{2} U^{-\frac{1}{2}} \right) f_{l+p} + J_l(f_l). \quad (8.3)$$

The simplest method of operator splitting, and the method employed in this work, is Lie-Trotter splitting [521, 522], which employs two separate operators, e.g. S_Z and S_U , in a sequential order.

If

$$\frac{\partial f}{\partial t} + S_Z(f) + S_U(f) = 0, \quad (8.4)$$

then the Lie-Trotter algorithm is

$$\frac{\partial f^*}{\partial t} + S_Z(f^*) = 0, \text{ with } t \in [t^n, t^{n+1}] \text{ and } f^*(t^n) = f(t^n), \quad (8.5)$$

$$\frac{\partial f^\#}{\partial t} + S_U(f^\#) = 0, \text{ with } t \in [t^n, t^{n+1}] \text{ and } f^\#(t^n) = f^*(t^{n+1}), \quad (8.6)$$

so that $f(t^{n+1}) = f^\#(t^{n+1})$, where t^n and t^{n+1} are successive times. This simple method can be shown to be only accurate to first order in time, and there are many other methods available that offer higher order accuracy and often include additional advantageous properties [355, 522–526]. The major reason for this particular choice of operator splitting algorithm is that if S_Z is treated in an explicit manner, and S_U is treated in an implicit manner, then the result is essentially the Douglas class of the Alternating Direction Implicit schemes [527, 528], which is particularly successful at accurately capturing the steady-state solution. Accurately and consistently determining the steady-state solution can be a problem for general operator splitting methods [529].

The isolation of the configuration-space dependence to the operator S_Z makes this particular scheme an example of dimensional splitting. We can now investigate in detail how to treat the configuration-space advection, energy-space advection, and collision components numerically.

8.2.2 Configuration-space advection

The operator involving the configuration-space dependence, S_z , is given by equation (8.2), which represents a coupled homogeneous advection equation. As there are no derivatives of U present in S_z , the configuration-space dependence can be solved independently for different values of U which is huge simplification when a discretization in energy space is used. The coupled advection equation can be simplified as follows:

$$\frac{\partial}{\partial t} f_l + \left(\frac{2U}{m}\right)^{\frac{1}{2}} \Delta_l^{(-)} \frac{\partial}{\partial z} f_{l-1} + \left(\frac{2U}{m}\right)^{\frac{1}{2}} \Delta_l^{(+)} \frac{\partial}{\partial z} f_{l+1} = 0, \quad (8.7)$$

which can be written in matrix form,

$$\frac{\partial}{\partial t} \mathbf{f} + \mathbf{A} \frac{\partial}{\partial z} \mathbf{f} = \mathbf{0}, \quad (8.8)$$

where $\mathbf{f} = [f_0, f_1, \dots, f_{l_{\max}}]$ and

$$\mathbf{A} = \left(\frac{2U}{m} \right)^{\frac{1}{2}} \begin{bmatrix} 0 & \Delta_0^{(+)} & & & & \\ \Delta_1^{(-)} & 0 & \Delta_1^{(+)} & & & \\ & \ddots & \ddots & \ddots & & \\ & & \Delta_{l_{\max}-1}^{(+)} & 0 & \Delta_{l_{\max}-1}^{(+)} & \\ & & & \Delta_{l_{\max}}^{(-)} & 0 & \\ & & & & & 0 \end{bmatrix}. \quad (8.9)$$

By letting $\mathbf{A} = \mathbf{R}\mathbf{\Lambda}\mathbf{R}^{-1}$, where $\mathbf{\Lambda}$ is a matrix of eigenvalues of \mathbf{A} on the diagonal, and \mathbf{R} are the associated eigenvectors, then

$$\frac{\partial}{\partial t} \mathbf{g} + \mathbf{\Lambda} \frac{\partial}{\partial z} \mathbf{g} = \mathbf{0}, \quad (8.10)$$

where $\mathbf{g} = \mathbf{R}^{-1}\mathbf{f}$, which now represents a set of uncoupled, homogeneous advection equations. It follows from the method of characteristics [530], that

$$\mathbf{g}(t, z) = \mathbf{g}(0, z - \mathbf{\Lambda}t). \quad (8.11)$$

Even in this extremely simple form, the solution can be troublesome. When discretized, the set of values $z - \mathbf{\Lambda}t$ are unlikely to align with existing z values, and hence some form of interpolation is required. It can be shown that linear interpolation is equivalent to a first order upwind finite volume method scheme [531]. First order methods have the advantage of being well behaved and can be used to conserve mass etc. with no unwanted, unphysical oscillations, but have the disadvantage of introducing extra numerical diffusion, particularly around regions of sharp variation [357]. Higher order methods perform better at controlling unwanted diffusion but can lead to problematic, oscillatory and unphysical solutions. Rather than straightforward interpolation, we choose to employ a variation of a technique well known in fluid transport, the SHASTA algorithm of Boris and Book [532]. The SHASTA algorithm approach, termed flux-corrected transport (FCT), leads to a class of Eulerian finite-difference algorithms which strictly enforce the non-negative property of realistic mass and energy densities. As a result, steep gradients and shocks can be handled particularly well, which is a useful property when modelling transport under non-hydrodynamic conditions. A FCT algorithm consists conceptually of two major stages, a transport or convective stage, followed by an anti-diffusive or corrective stage.

We employ a simplified version of the full FCT algorithm to numerically approximate $\mathbf{g}(0, z - \mathbf{\Lambda}t)$. Let us consider the evolution of $\mathbf{g}(t, z)$ for a single $\mathbf{\Lambda}$, i.e., $g(t, z; \mathbf{\Lambda})$, over a time interval of Δt , with a uniform configuration-space mesh with spacing Δz . By discretizing in this way, $z_j = j\Delta z$ for $j = 1, 2, \dots, n_z - 1$, and $t_{n+1} = t_n + \Delta t$. The algorithm is as follows:

1. **Shift** The elements of $g(t, z; \mathbf{\Lambda})$ are shifted to the node closest to $z - \beta$, where $\beta = \frac{\Delta t}{\Delta z} \mathbf{\Lambda}$. This may result in an ‘overshoot’, but we can then propagate the shifted solution (in step 2) either forwards or backwards in time as appropriate. The purpose of this step is to overcome time step limitations due to the Courant-Friedrichs-Levy (CFL) condition [533], which allows us to choose arbitrary time step sizes with respect to the configuration-space convergence (sufficiently small time steps are still necessary for the operator splitting accuracy etc.). By

shifting to the nearest node, the CFL condition

$$|\beta| = \frac{\Delta t}{\Delta z} |\Lambda| \leq 1 \quad (8.12)$$

for the remaining advection is always satisfied.

2. Advection with additional diffusion The advection algorithm employed is given by

$$g_j^{n+1} = g_j^n - \frac{\beta'}{2} (g_{j+1}^n - g_{j-1}^n) + \left(\gamma + \frac{\beta'^2}{2} \right) (g_{j+1}^n - 2g_j^n + g_{j-1}^n), \quad (8.13)$$

where $g_j^{n+1} = g(t_{n+1}, z_j)$, and

$$\gamma = \left[0, \frac{\beta'}{2} \right], \quad (8.14)$$

is the additional numerical diffusion. The dimensionless advancement $\beta' = \beta - \lfloor \beta \rfloor$ accounts for the shift that has been applied in step 1. Note that β' may be opposite in sign to β , which corresponds to an overshoot in step 1. However, this does not adversely affect the procedure. If $\gamma = 0$, then equation (8.13) is the well known Lax-Wendroff scheme [357], which is accurate to second order. Historically, the inclusion of an extra diffusion term, γ , has been used to ensure that a density function (i.e. a function that is non-negative by definition) remains positive, which is unconditionally enforced everywhere if $\gamma = \frac{\beta'}{2}$. In our case, the g_j^n include contributions from $f_{l \geq 1}$, which are expected to be negative in some regions of space. However, the presence of γ ensures the stability of g_j^{n+1} , which can be defined by the requirement that $\Delta g_j^{n+1} < \max(\Delta g_{j-1}^n, \Delta g_j^n, \Delta g_{j+1}^n)$ where $\Delta g_j^n = g_{j+1}^n - g_j^n$. When the solution g_j^n is sharply varying or, in the extreme case, a discontinuity, the additional diffusion is necessary to suppress unphysical oscillatory behaviour in g_j^{n+1} .

3. Anti-diffusion An ‘anti-diffusion’ step is employed to reduce the extra numerical diffusion introduced in (8.13) i.e.,

$$\bar{g}_j^{n+1} = g_j^{n+1} - \left(\gamma + \frac{\beta'^2}{2} \right) (g_{j+1}^{n+1} - 2g_j^{n+1} + g_{j-1}^{n+1}). \quad (8.15)$$

The inclusion of this extra diffusion in step 2 assures that the solution is positive and physically realistic, and the straightforward application of step 3 undoes this which can re-introduce a negative solution. Boris and Book [532] suggested modifying the removal of the erroneous diffusion by just enough to maintain positivity, in a non-linear way (note that they worked with non-negative densities, as we have remarked on above in step 2). This is an early example and precursor of the modern technique of flux limiting [534–538]. In this work the full anti-diffusion step is applied in general, except in regions where a sharp variation or discontinuity is known *a priori* (e.g. configuration-space boundaries), in which case no anti-diffusion is applied. Unphysical oscillations can now occur, but we have found that for the situations considered they are negligibly small. The natural extension is to include flux limiting to prevent this unphysical behaviour but this introduces extra computational complexity. The anti-diffusion step could also be solved implicitly rather than explicitly, but we found that this had no significant impact on the results.

It should be noted that the shift step can be performed after the advection and anti-diffusion stages with no change in the result. We have assumed that the boundaries are absorbing, in that

the elements of $g(t, z)$ that move outside the computational domain are lost, and no information is introduced from outside the domain. Although perfectly absorbing boundaries are notoriously difficult to implement numerically, in our calculations we avoid this problem by keeping the swarm density negligible at the simulation edges, through the use of an adaptive mesh, see Section 8.2.4. In practice we pre-calculate a transformation matrix (for a given set of parameters) which combines the above three steps for each of the grid energies.

8.2.3 Green's function solution

In our formalism and associated code, we solve for the Boltzmann equation Green's function

$$\mathcal{L}f_l = \delta(z - z_0)\delta(t - t_0), \quad (8.16)$$

where

$$\mathcal{L}f_l = \frac{\partial f_l}{\partial t} + \left(\frac{2}{m}\right)^{\frac{1}{2}} \sum_{p=\pm 1} \Delta_l^{(p)} \left[U^{\frac{1}{2}} \frac{\partial}{\partial z} + \frac{eE}{m} \left(U^{\frac{1}{2}} \frac{\partial}{\partial U} + p \frac{(l + \frac{3p+1}{2})}{2} U^{-\frac{1}{2}} \right) \right] f_{l+p} + J_l(f_l), \quad (8.17)$$

for $l = 0, 1, 2, \dots, \infty$. The Green's function solution, f_l , can then be used to find the solution of the more general space-time Boltzmann equation, i.e.

$$\mathcal{L}\tilde{f}_l = S(z, t), \quad (8.18)$$

where $S(z, t)$ is a source term, then

$$\tilde{f}_l(U, z, t) = \int dt_0 \int dz_0 f_l(U, z - z_0, t - t_0) S(z_0, t_0). \quad (8.19)$$

We do this by choosing an initial distribution in configuration-space that is a good approximation to a delta-function, which, for this study, is a narrow Gaussian,

$$\delta_a(z) = \frac{1}{a\sqrt{\pi}} \exp\left(-\frac{z^2}{a^2}\right), \quad (8.20)$$

where a is a parameter controlling the width of the Gaussian, representing the temporal-spatial relaxation profile of a single pulse centred on z_0 and released at t_0 . In the limit of $a \rightarrow \infty$, $\delta_a(z) \rightarrow \delta(z)$. The formalism is quite general, enabling the treatment of various experiments (e.g. Pulsed Townsend (PT), Steady-State Townsend (SST) and other drift tube configurations [50] - detailed in Section 8.2.5), as well as various source and spatial/energy space/temporal distributions, through a single solution. This approach extends the functionality and accuracy of Boltzmann equation solutions to those routinely achieved by Monte Carlo simulations [9, 149, 539].

8.2.4 Numerical considerations and adaptive meshing

The matrix system of linear equations that result from the discretization of the Legendre-decomposed Boltzmann equation in energy- and configuration-space at each time step are of the size $(n_z n_U (l_{\max} + 1)) \times (n_z n_U (l_{\max} + 1))$, where n_z and n_U are the number of nodes in configuration and energy space respectively. Due to the discretization schemes, the matrix is sparse and sparse techniques are employed to exploit this property. Each of these parameters are free to be increased

until some convergence criterion is met. It should be noted that, although the two-term approximation ($l_{\max} = 1$) has been used extensively, it is well known that it can be insufficient in many situations [512].

In order to model the spatio-temporal relaxation of a narrow Gaussian source distribution in configuration-space with a distribution of energies as computationally efficiently as possible, we have developed a configuration-space node-mesh that adaptively follows the size of the distribution throughout the simulation. In this way a small configuration-space window is used around the original narrow Gaussian source which can then be sufficiently resolved with a small n_z . As the initial pulse drifts and diffuses, a small amount of information reaches and then leaks out of the window boundaries. Before the amount of information lost to the system exceeds some small tolerance, the window is extended and the solution at the previous time-step calculated on the new configuration-space mesh. We have found that the most convenient way to quantify the amount of information on the boundary is by the relative number density, and impose the condition that when

$$\int_{t_0}^t dt' \frac{n(z_L \text{ or } z_R, t')}{\int dz n(z, t')} \geq 10^{-5}, \quad (8.21)$$

then the configuration-space window is doubled (while the number of nodes is kept the same). Here t_0 is the time of the last window adjustment, z_L and z_R are locations of the left and right configuration-space boundaries respectively. The choice to extend the window by doubling is to make it so that the new mesh lines up exactly with nodes of the old mesh, hence requiring no interpolation. The accuracy of the modified Lax-Wendroff scheme used to model the configuration-space advection [357] is related to the parameter $\beta = \frac{\Delta t}{\Delta z} \Lambda$, hence by doubling Δz after a re-adjustment, the value of Δt can also be doubled. This effectively allows us to use smaller time steps when our solution is sharp and diffusing quickly, and larger time steps once the solution has spread out and is varying less quickly. A maximum value for the time step size still needs to be enforced however, since with bigger time step sizes less mixing between the configuration-space and energy-space components of the operator splitting occurs, leading to errors.

There is one extra complication to be discussed. Since the boundaries are absorbing, when they are re-adjusted, the number density profiles (and distribution functions) drop directly from the built-up value at the previous boundaries location to zero in a single Δz , which can lead to problematic, unphysical, oscillatory solutions when treated with the method described in Section 8.2.2. In order to combat this, we simply apply the procedure without the final anti-diffusion step for a small amount of time on the edge and in the newly opened regions. The extra diffusion added ensures that the solution remains positive and give physical results, which, after a small amount of time, ensures that the profiles decrease smoothly to zero at the boundary. After this short correction time, we again apply the full procedure. By not removing the added extra diffusion we have increased the overall diffusion, but since it is only applied for a small time and to a region where there is necessarily only a small proportion of particles, this does not significantly affect the transport profiles.

8.2.5 Transport properties

The cross sections and collision operator terms represent the microscopic picture of electron interactions with the medium. The macroscopic picture, e.g. transport properties that represent experimental measurables, are obtained as averages of certain quantities with respect to the distribution function, f . Among the transport properties of interest in the current manuscript are the number density, n , particle flux, Γ , and average energy, ϵ , of the electron swarm, which can

be calculated via

$$n(z, t) = 2\pi \left(\frac{2}{m}\right)^{\frac{3}{2}} \int dU U^{\frac{1}{2}} f_0(U, z, t), \quad (8.22)$$

$$\Gamma(z, t) = \frac{2\pi}{3} \left(\frac{2}{m}\right)^2 \int dU U f_1(U, z, t), \quad (8.23)$$

$$\epsilon(z, t) = \frac{1}{n(z, t)} 2\pi \left(\frac{2}{m}\right)^{\frac{3}{2}} \int dU U^{\frac{3}{2}} f_0(U, z, t). \quad (8.24)$$

Likewise, we can sample the traditional hydrodynamic transport coefficients in this non-hydrodynamic framework, e.g. the drift velocity, W , and the (longitudinal) diffusion coefficient, D_L :

$$W(t) = \frac{d}{dt} \left[\frac{1}{N(t)} \left(\int dz z n(z, t) \right) \right], \quad (8.25)$$

$$D_L(t) = \frac{1}{2} \frac{d}{dt} \left[\frac{1}{N(t)} \left(\int dz z^2 n(z, t) \right) - \left(\frac{1}{N(t)} \int dz z n(z, t) \right)^2 \right], \quad (8.26)$$

where $N(t)$ is the total number of particles:

$$N(t) = \int dz n(z, t). \quad (8.27)$$

When the above properties are calculated from the Green's function solution, which corresponds to a simulation of a PT experiment, then the transport properties for other experimental systems can also be calculated in a straightforward manner. In this work we are also interested in the results of a SST simulation, for which there have been previous calculations performed for benchmark systems. Similar to [149, 278, 282, 317], the SST transport properties can be determined from the Green's function transport properties via

$$f_i^{\text{SST}}(U, z) = \int_0^\infty dt_0 f_i(U, z, t_0), \quad (8.28)$$

$$n_{\text{SST}}(z) = \int_0^\infty dt_0 n(z, t_0), \quad (8.29)$$

$$\Gamma_{\text{SST}}(z) = \int_0^\infty dt_0 n(z, t_0) v_z(z, t_0), \quad (8.30)$$

$$\epsilon_{\text{SST}}(z) = \frac{1}{n_{\text{SST}}(z)} \int_0^\infty dt_0 n(z, t_0) \epsilon(z, t_0). \quad (8.31)$$

In practice the upper limit of the integrals is not ∞ , but a sufficiently long time for the SST transport properties to have converged over the z range considered.

8.2.6 Reduced variables

Henceforth, it is convenient to work with rescaled reduced variables. In particular, the space and time variations will be presented as functions of

$$z^* = n_0 \sigma_0 z, \quad (8.32)$$

$$t^* = n_0 \sigma_0 \sqrt{\frac{2e}{m}} t, \quad (8.33)$$

where $\sigma_0 = 10^{-20} \text{ m}^2$. Likewise, the electric field dependence arises through the reduced electric field E/n_0 in units of Townsend ($1 \text{ Td} = 10^{-21} \text{ Vm}^2$). By presenting results in this manner

scales out the n_0 dependence, and hence allows comparisons between the dilute gas phase and the liquid/dense gas phase, to give a true reflection of the impact of coherent and other scattering effects.

8.3 Electron transport in a modified Percus-Yevick hard-sphere benchmark liquid model

In order to investigate the effects of medium structure on charged particle transport, a model for the structure function is required. The Percus-Yevick model introduced in Section 4.6 is once again used to emulate the structure of a real liquid. The remaining details required of the benchmark hard-sphere model implemented for electron sized particles are

$$\begin{aligned}
 \sigma_m &= 6 \text{ \AA}^2, \\
 \sigma^{\text{exc}} &= \begin{cases} 0, & U < 2 \text{ eV} \\ 0.1 \text{ \AA}^2, & U \geq 2 \text{ eV} \end{cases} \\
 \Phi &= 0, 0.2, 0.3, 0.4, \\
 E/n_0 &= 3 \text{ Td}, \\
 m_0 &= 4 \text{ amu}, \\
 T_0 &= 0 \text{ K}.
 \end{aligned} \tag{8.34}$$

A step-like inelastic process has been included in addition to the standard Percus-Yevick hard-sphere benchmark system in model (8.34). The inelastic channel introduces a periodic oscillatory non-hydrodynamic behaviour, similar to those observed in the well-known Frank-Hertz experiment, and can hence determine whether the numerical code is accurately capturing the non-hydrodynamic phenomena. The variation of the momentum transfer cross section with Φ for model (8.34) was shown in Chapter 4 in Figure 4.5.

The source distribution is given by

$$f(U, z, 0) = A f_U(U) f_z(z), \tag{8.35}$$

where $f_z(z)$ is a narrow Gaussian in configuration-space, i.e.,

$$f_z(z) = \frac{1}{\Delta z_0 \sqrt{2\pi}} \exp\left(-\frac{1}{2} \left(\frac{z}{\Delta z_0}\right)^2\right), \tag{8.36}$$

(we take $\Delta z_0 = 0.1$), while $f_U(U)$ corresponds to drifted Maxwellian distribution with $T = 10^5 \text{ K}$, and $\mathbf{W} = 10^4 \text{ ms}^{-1} \hat{\mathbf{E}}$, i.e.,

$$f(\mathbf{v}) = n \left(\frac{m}{2\pi k_b T}\right)^{\frac{3}{2}} \exp\left[-\frac{m}{2k_b T} (\mathbf{v} - \mathbf{W})^2\right], \tag{8.37}$$

and A is a normalization constant such that $\int U^{\frac{1}{2}} f(U, z, 0) dU = 1$.

8.3.1 Transport coefficients in the long-time limit

The asymptotic values of the drift velocity and longitudinal diffusion coefficient calculated from the spatial moments (8.25) and (8.26) respectively using the full non-hydrodynamic code are displayed

in Table 8.1 for various volume fractions. Here we compare these values with those determined from a purely hydrodynamic formalism and associated code [7,8]. The zeroth order hydrodynamic transport coefficients, i.e., the mean energy and drift velocity, agree to within 0.2% with the asymptotic non-hydrodynamic values for the volume fractions considered. The hydrodynamic and non-hydrodynamic calculations of the longitudinal diffusion coefficient agree to within 0.7%. As the volume fraction increases, both the mean energy, drift velocity and diffusion coefficient increase monotonically, a consequence of the coherent scattering where, at low energies, increasing volume fractions leads to decreasing structure factors at low Δk , and hence decreased momentum-transfer cross sections. A discussion on the physical variation of the hydrodynamic transport coefficients with volume fraction is given in Appendix A from the perspective of fluid modelling.

Table 8.1: Comparison of the transport quantities calculated from non-hydrodynamic (first row) and time asymptotic hydrodynamic (second row) formalisms for model (8.34) at various volume fractions Φ .

Φ	ϵ [eV]	W [10^4 ms^{-1}]	$n_0 D_L$ [$10^{24} \text{ m}^{-1} \text{ s}^{-1}$]
0	0.8335	1.385	2.386
	0.8337	1.385	2.387
0.2	0.9765	3.397	6.333
	0.9772	3.391	6.328
0.3	1.080	5.929	11.22
	1.080	5.921	11.24
0.4	1.233	10.52	19.51
	1.233	10.51	19.63

8.3.2 Space-time evolution of the phase-space distribution and its velocity moments

In Figure 8.1 the space-time evolution of the f_0 and f_1 velocity distribution function components are compared for $\Phi = 0$ and $\Phi = 0.4$ at three different times. The space-time evolution of the integral moments of f_0 (electron density $n(z, t)$) and velocity moment of f_1 (flux Γ) are displayed in Figure 8.2. The timescale for variation of f_0 is governed by $\sim \left(2 \frac{m}{m_0} \nu_m\right)^{-1}$, and hence there is no explicit Φ dependence in the timescale, however differences arise due to the implicit energy dependence in the collision frequency (which does depend on Φ) and the coupling to higher order moments with different timescales. The timescale for variation of f_1 on the other hand is governed by $\tilde{\nu}_m^{-1}$, which has an explicit Φ dependence. The timescale for momentum exchange is significantly decreased for increasing Φ at low energies, as shown in Figure 4.5, however they approach the same value at higher energies. We will show that this is reflected in the evolution of the profiles.

At small times (e.g. $t^* = 0.2$), there are only small differences in the f_0 contours between the two volume fractions, and this is also highlighted in the density $n(z, t)$. At higher energies ($> 5\text{-}6 \text{ eV}$) there are also very little differences in the f_1 contours (reflecting the similarity in the momentum relaxation times at these energies), however at low energies, the $\Phi = 0.4$ contours for f_1 are significantly displaced in both energy and configuration-space relative to the $\Phi = 0$ case. This indicates significantly higher advective and diffusive fluxes in this energy regime at this time, which is evidenced in the flux profiles of Figure 8.2. Given the sharp initial pulse with large spatial gradients, we observe large positive and negative diffusive fluxes, along with a large positive advective contribution.

At larger times, the f_0 and f_1 contours in the $\Phi = 0.4$ case depart significantly from the $\Phi = 0$ case, initially in the low energy regime and then finally over the entire energy regime as the higher energy electrons relax from the initial condition. The peaks in each of the distribution components at larger times for the $\Phi = 0.4$ case are significantly displaced in the z -direction from the $\Phi = 0$ case. This is reflected in both the density and flux profiles at larger times, which highlight the enhanced drift and diffusion due to the reduced momentum transfer cross section associated with coherent scattering for this model and field. Interestingly, at sufficiently long times, the $\Phi = 0.4$ contours have predominantly positive values, and only very small negative excursions at low energies, in contrast to the $\Phi = 0$ contours. At these times, the flux is positive over the entire swarm indicating that the advective contribution dominates the diffusion contribution, since the density gradients are much more rapidly dissipated in the $\Phi = 0.4$ case, as seen in Figure 8.2.

Strikingly, both the $\Phi = 0$ and $\Phi = 0.4$ contours for both f_0 and f_1 demonstrate periodic structures in both configuration space and in energy space at sufficiently long times and sufficiently downstream from the source. The periodic structures manifest themselves earlier for the $\Phi = 0.4$ case. These are the well known Franck-Hertz oscillations [281,282]. A simplistic picture of this non-hydrodynamic phenomena is that the electrons in the swarm are being repeatedly accelerated by the electric field to an energy above the inelastic process threshold whereby they undergo an inelastic collision losing their energy. This simple physics is evidenced in the f_0 and f_1 distributions. By integrating over the energy to obtain the density and flux, shown in Figure 8.2, much of the periodic structures observed in the distribution function is masked, however some non-Gaussian spatial structure is still observed. We will explore the Φ -dependence of the wavelengths of oscillations further in Section 8.3.3.

8.3.3 Steady-state Townsend configuration

The solution detailed in Section 8.3.2 is essentially equivalent to solving for the Boltzmann equation Green's function for the model (8.34). A strict validation of this approach and associated numerical code is to be able to reproduce the Steady-State Townsend (SST) transport properties from the Green's function solution, as described in Section 8.2.3. The average energy (8.31) and average velocity (8.30) for SST simulations of various volume fractions are shown in Figure 8.3. In the spatially asymptotic regime, the average energy and the average velocity are equal to the hydrodynamic and pulsed-Townsend values given in Table 8.1. It can be seen that the SST properties demonstrate damped spatially periodic structures similar to those observed in the Frank-Hertz experiment and other investigations [281, 282, 287, 292, 540, 541]. They are a manifestation of the energy and spatial periodic structures in the distribution function components, and in the spatially periodic structures in the density and flux profiles of Figure 8.2. By assuming the elastic scattering is weak, the width between the peaks in the transport property profiles, λ , is directly related to the threshold energy of the inelastic process, U_I in eV, via [542]

$$\lambda = \frac{U_I}{(0.1)_{\text{eV/Td}} (E/n_0)_{\text{Td}}}, \quad (8.38)$$

where the reduced electric field is in Townsend (Td). For model (8.34), the theoretical spacing is 6.6. In Figure 8.3 it is possible to see that there are variations in the wavelength of the spatial structures with Φ , as well as significant differences in the decay rates of the oscillation amplitudes. For $\Phi = 0$, the wavelength is approximately 8.24 ± 0.02 and this decreases to 6.67 ± 0.02 for $\Phi = 0.4$. The differences arise explicitly due the differences in the elastic momentum transfer cross section, as well as implicit variations associated with the modification to the swarm's energy with

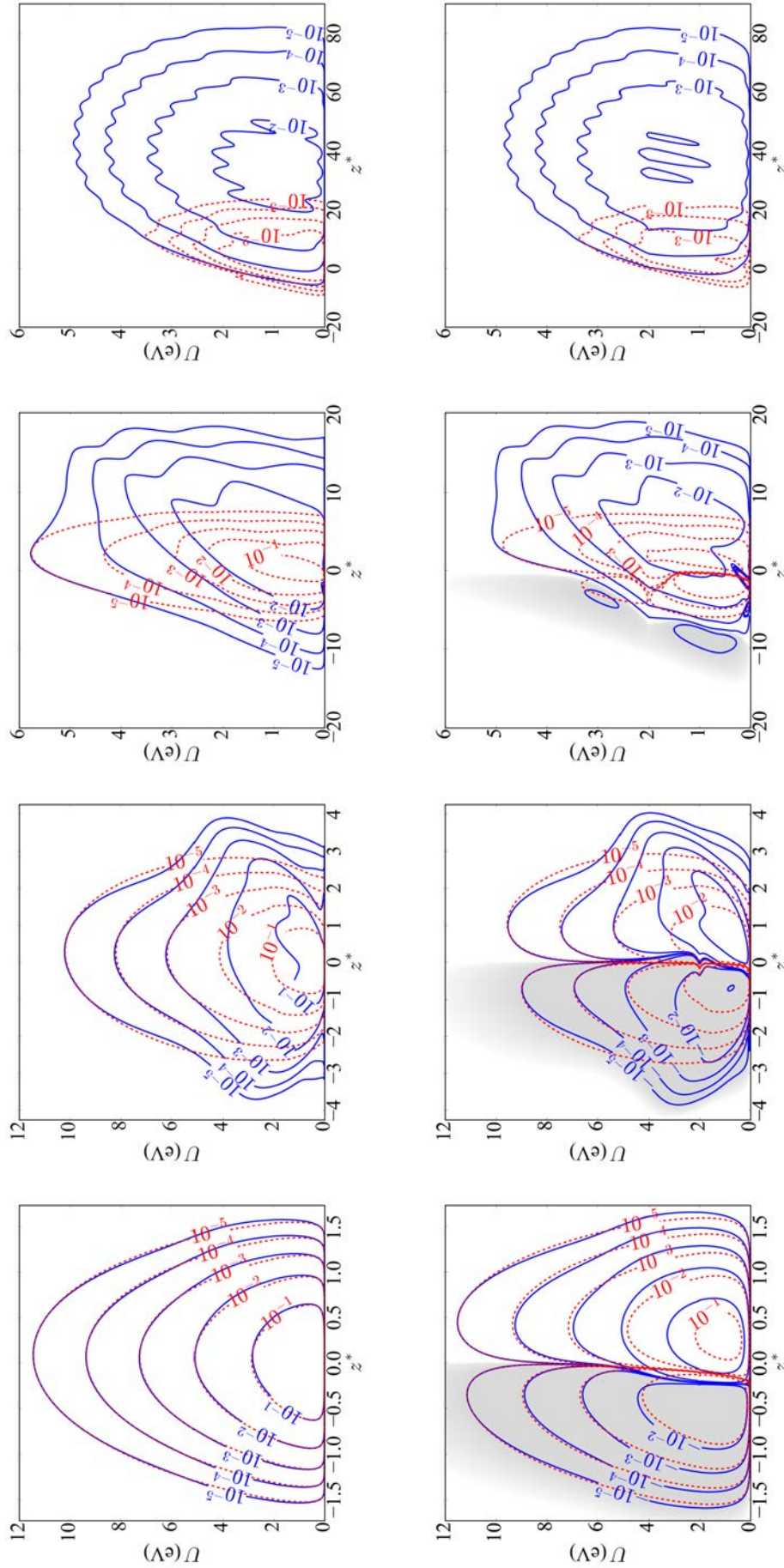


Figure 8.1: Temporal evolution of the distribution function components for model (8.34) with $\Phi = 0.4$ (solid lines) and $\Phi = 0.4$ (dashed lines) and $\Phi = 0.4$ (solid lines). The first row are $U^{\frac{1}{2}} f_0/n_0$ (eV^{-1}) contours while the second row are $|U f_1/n_0|$ ($\text{eV}^{-1/2}$) contours. The shaded contours indicate $U f_1 < 0$. The four columns represent the times, $t^* = 0.2, 2, 20, \text{ and } 200$ respectively.

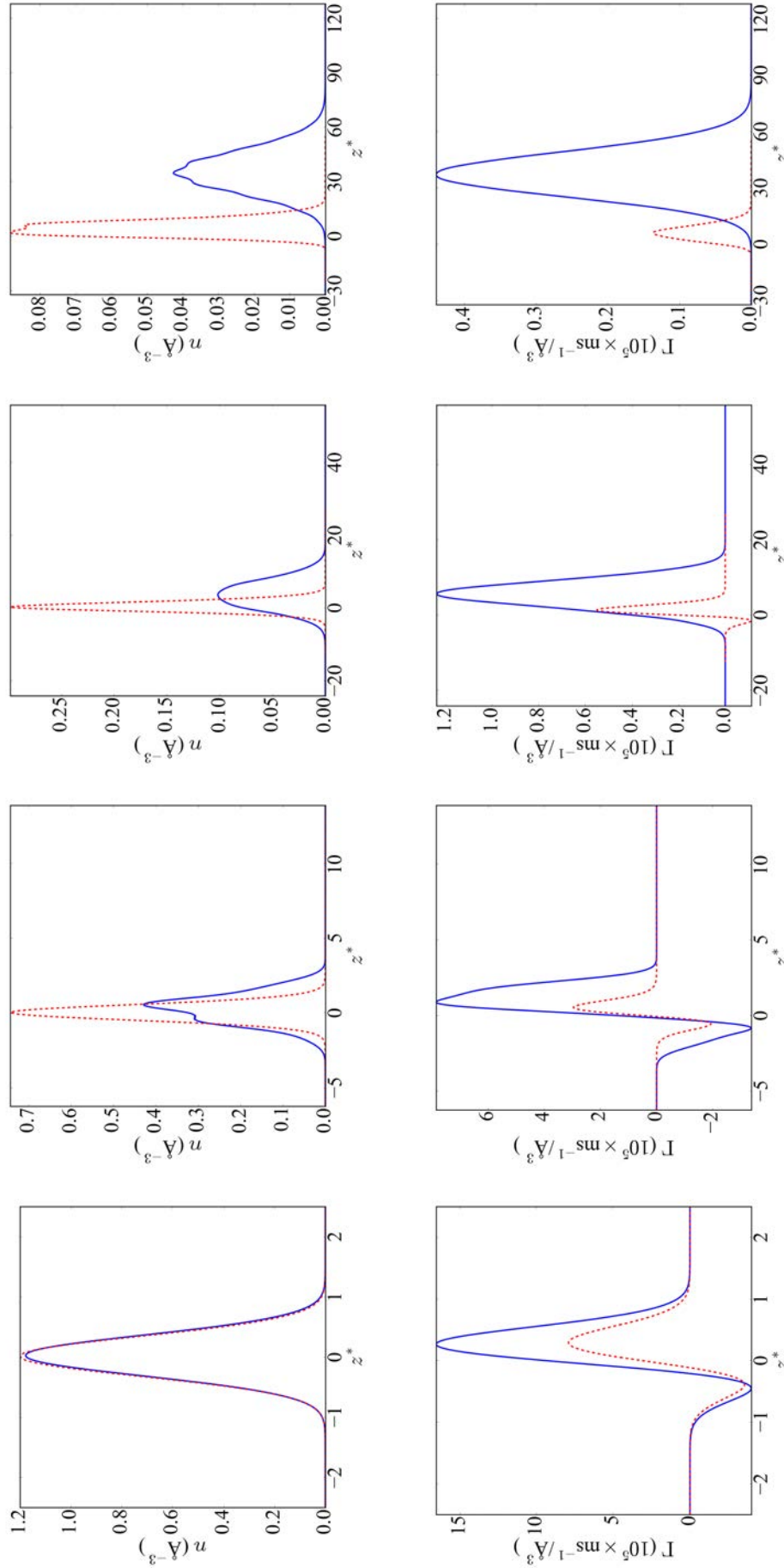


Figure 8.2: Temporal evolution of the spatially varying density and flux for model (8.34) with $\Phi = 0$ (dashed lines) and $\Phi = 0.4$ (solid lines). The four columns represent the times, $t^* = 0.2, 2, 20,$ and 200 respectively.

Φ . For $\Phi = 0.4$, the momentum transfer cross section for elastic scattering is significantly reduced compared to the $\Phi = 0$ case. Hence, the randomizing collisions that dampen the oscillations [282] are reduced for $\Phi = 0.4$ as compared to other Φ , and the variation of damping with Φ then follows. Likewise, it should not be surprising that the wavelength for the $\Phi = 0.4$ case is closest to the analytic value of (8.38), since the reduced momentum transfer associated with the $\Phi = 0.4$, more closely approximates the weak elastic scattering assumption used in deriving it.

We must also point out that the validity of these profiles are dependent on the discretization of the distributions in configuration-space. If the spatial discretization is of the same order as the Frank-Hertz wavelength, then it will be very difficult to resolve these features in the distributions and consequently the time-averaged profiles. Of course, our initial choice for the discretization is small enough to easily resolve these features, but as the simulation progresses and the distribution diffuses, our adaptive mesh will increase in range and also increase the spatial discretization step size. After a point, the coarseness of the discretization causes the distribution to slowly lose its features, which is visible in the time-averaged quantities by the suppression of the amplitude of the oscillations. In our simulations we expect our results for $z^* \gtrsim 30$ deviate from the true spatially dependent steady-state values, however the fully relaxed values agree with the hydrodynamic values. It is simple to address this issue by increasing the number of points in configuration-space but this is also significantly more computationally intensive

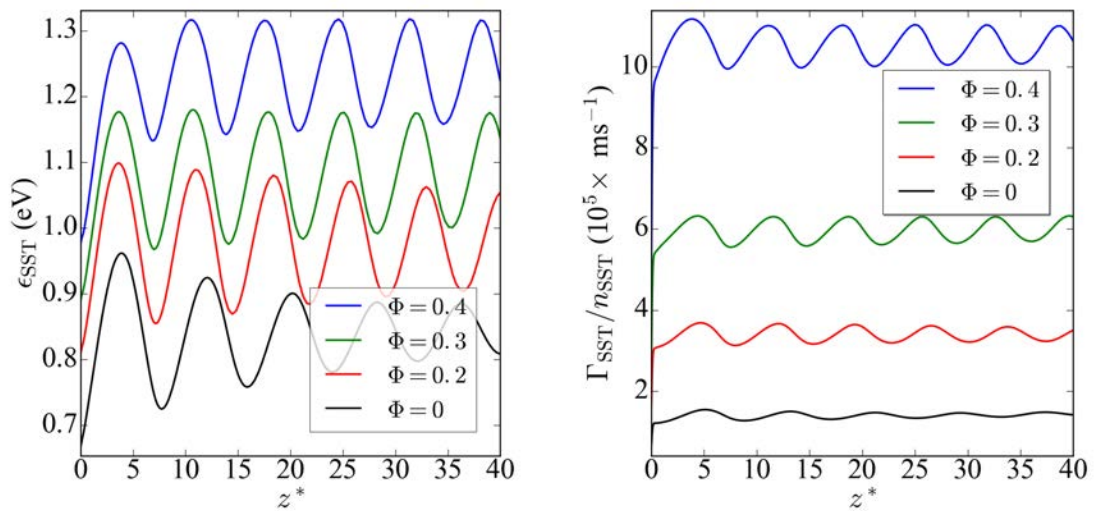


Figure 8.3: Spatial variation of the average energy and average velocity under SST conditions for model (8.34) with various volume fractions Φ .

8.4 Spatio-temporal relaxation of electrons in liquid argon

Electron transport in liquid argon is an essential component in the function of Liquid Argon Time Projection Chambers (LArTPC) which are currently being used for high energy particle detection [88]. Ionized electrons in liquid argon originating from the high energy particles are accelerated under the action of an electric field to generate a current and consequently reconstruct the path of the high energy particle. Typically these chambers operate with electric field strengths

of less than 500 kV/cm. The aim of this component is to follow the spatio-temporal evolution of these ionized electrons in liquid argon, relevant to the operation of these detectors. Foxe et al. [543] have measured the energy distribution of the electrons ionized by high energy particles in liquid argon, and have shown that the majority of the ionized electrons have energies below 1 eV. Consequently in this study we employ an initial source energy-distribution that is constant in energy space up to 1 eV, i.e.,

$$f_U(U) = CU^{-\frac{1}{2}}\Theta(U - 1 \text{ eV}), \quad (8.39)$$

where Θ is the Heaviside step function, and U is in eV and C is a normalisation constant. The mean energy of this distribution is 0.5 eV. The swarm is released from a narrow Gaussian in configuration-space,

$$f_z(z) = \frac{1}{\Delta z_0 \sqrt{2\pi}} \exp\left(-\left(\frac{z}{\Delta z_0}\right)^2\right) \quad (8.40)$$

so that the full initial phase-space distribution is $f(U, z, 0) = Af_U(U)f_z(z)$, where A is a normalization constant such that $\int U^{\frac{1}{2}} f(U, z, 0) dU = 1$. For argon, we take $\Delta z_0 = 10$, a larger initial spread than for the Percus-Yevick model, reflecting the smaller cross sections of argon, and hence a larger mean free path. The aim of this component is to follow the spatio-temporal evolution of these ionized electrons in liquid argon, relevant to the operation of these detectors.

8.4.1 Cross sections, potentials and screening

In Chapter 7, the modifications required to treat transport of electrons in dense gaseous and liquid argon was investigated, with our simulations focused purely on the hydrodynamic regime. The potentials, screening factor, and cross sections derived in Chapter 7 are used once again here. The momentum transfer cross section calculated from the dilute gaseous and liquid argon potentials are shown in Figure 8.4. It is significant to note the absence of the Ramsauer minimum in the liquid-phase cross section.

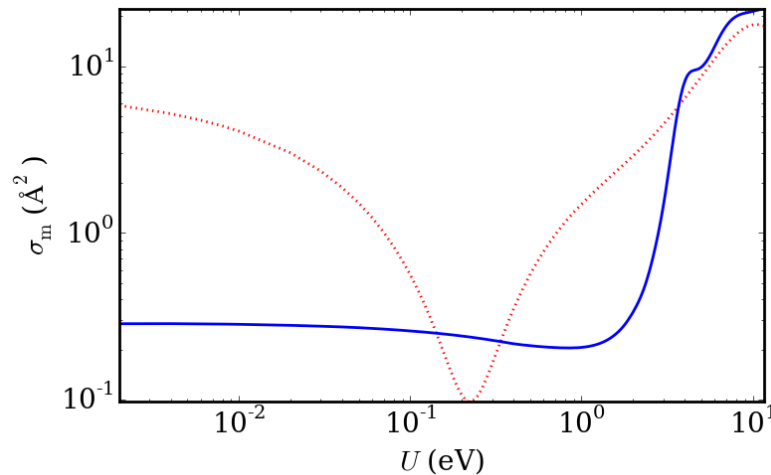


Figure 8.4: The momentum transfer cross sections in the gas-phase (dashed line) and liquid-phase (solid line) for electrons in argon.

8.4.2 Results

To consider conditions representative of those in liquid state particle detectors, we simulate electron transport in liquid argon under the following conditions:

$$\begin{aligned} E/n_0 &= 2.5 \times 10^{-3} \text{ Td}, \\ T_0 &= 85 \text{ K}, \\ m_0 &= 40 \text{ amu}. \end{aligned} \tag{8.41}$$

The reduced field is equivalent to 500 kV/cm with a density corresponding to liquid argon, $n_0 = 0.0213 \text{ \AA}^{-3}$. For this reduced electric field and source distribution, given in (8.39)–(8.40), the electron swarm energies are generally well below the first inelastic channel threshold energy (8.9 eV), so that there is no inelastic channel operative, and hence the periodic spatial structures observed in the Percus-Yevick hard-sphere liquid model above are not present.

The relaxation of the f_0 distribution function component are compared for the gas and liquid phases at three different times in Figure 8.5. At $t^* = 1$, there are only small differences between the contours reflecting similar energy relaxation rates between the two phases initially. At $t^* = 10$, a bulge is beginning to develop in the gas-phase contour in the energy region between 0.1 – 0.5 eV while no such bulge appears in the liquid-phase contour. This corresponds to the presence of a Ramsauer minimum in the gas-phase momentum transfer cross section only. In this region, the gas-phase momentum transfer cross section dips below the liquid cross section, which has resulted in this enhancement of the diffusive flux in this range. At higher energies the liquid cross section is less than the gas-phase cross section, which has resulted in enhanced diffusive flux. At $t^* = 100$ these effects are even more pronounced.

In Figure 8.5 the f_1 component contours for the gas and liquid phases of argon are compared for the same three times. At the first time, $t^* = 1$, there is already significant differences in the f_1 contours, with the largest change occurring in the Ramsauer minimum range in the gas-phase case. This highlights again the difference in the timescales of the energy and momentum relaxation between the two phases. As time increases, greater differences develop between the f_1 contours particularly around the Ramsauer minimum and at the high energy range for the reasons previously discussed.

The number density as a function of time is shown in Figure 8.6. The behaviour of the number density profiles is consistent with the behaviour of the f_0 and f_1 profiles. At $t^* = 1$ there is no noticeable difference in the two number density profiles. At later times it is clear that, despite the Ramsauer minimum in the gas-phase, the liquid-phase experiences the greater diffusion rate overall. For the electric field and initial source distribution considered, the average drift velocity for both the gas and liquid phases is small compared to the diffusion rates.

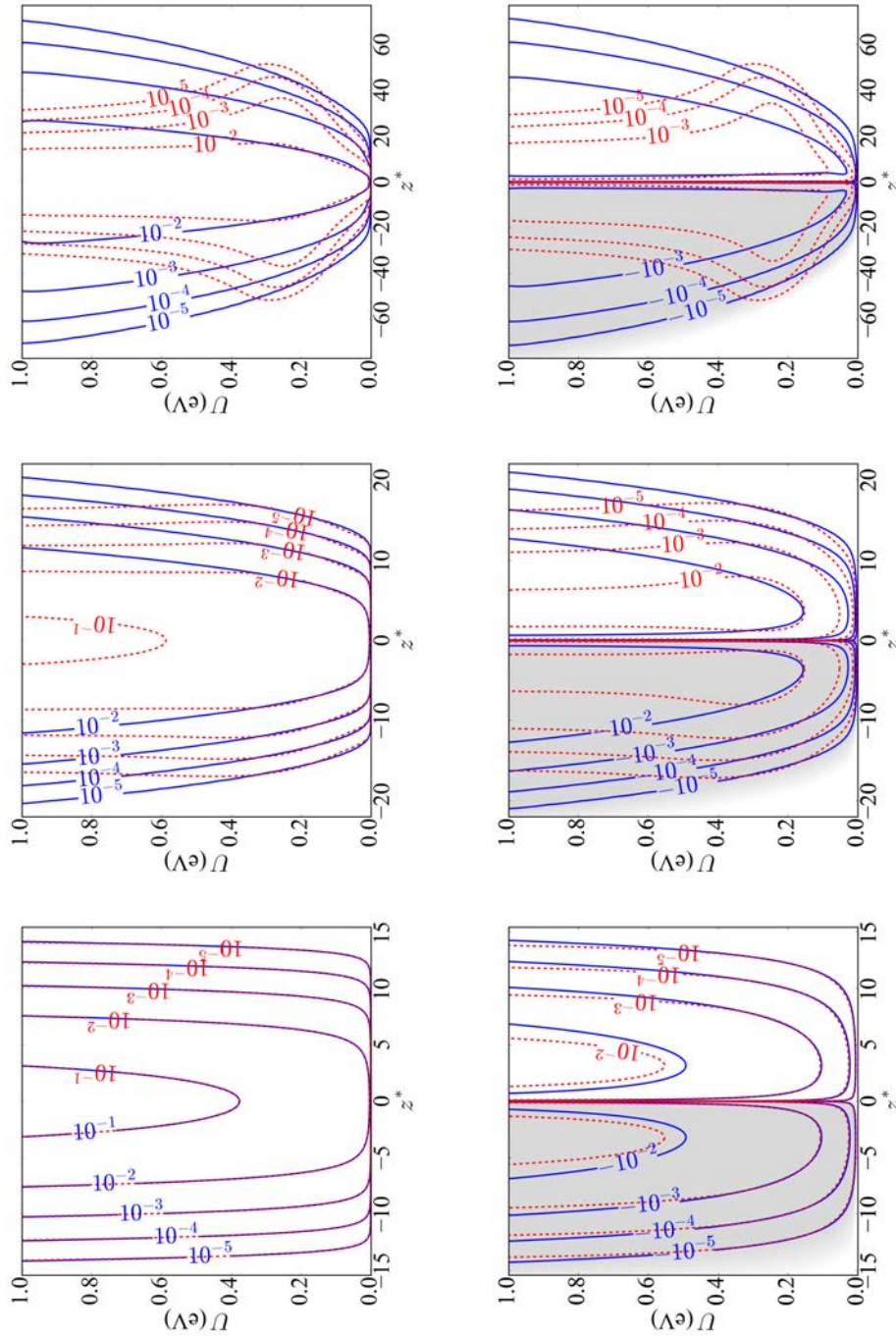


Figure 8.5: Temporal evolution of the distribution function components for gas-phase (dashed lines) and liquid-phase (solid lines) argon. The first row are $U^{1/2} f_0 / n_0$ (eV⁻¹) contours, the second row are $|U f_1 / n_0|$ (eV^{-1/2}) contours. The shaded contours indicate $U f_1 < 0$. The three columns represent the times, $t^* = 1, 10, \text{ and } 100$ respectively.

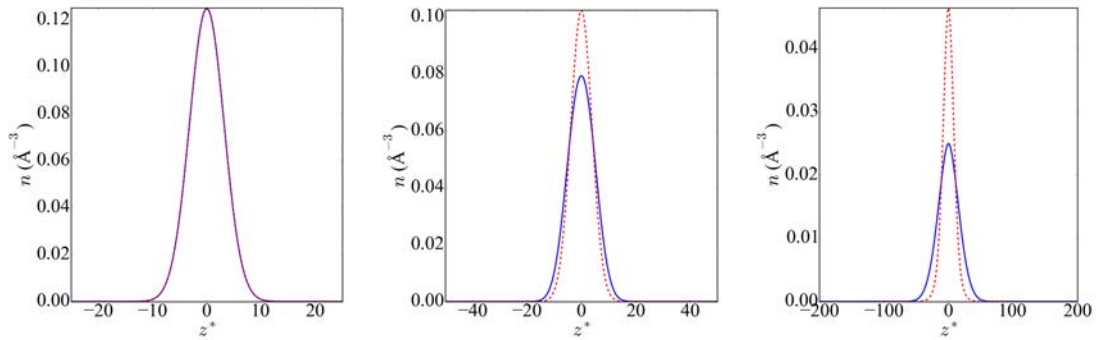


Figure 8.6: Temporal evolution of the number density profiles for gas-phase (dashed lines) and liquid-phase (solid lines) argon. The three columns represent the times, $t^* = 1, 10,$ and 100 respectively.

8.5 Conclusion

In this chapter, a full multi-term, space-time dependent solution of the electron Boltzmann equation in gases and liquids capable of modelling non-hydrodynamic conditions has been developed. The flexibility of the algorithm lies in solving the Boltzmann equation's Green's function, knowledge of which allows one to construct the solution for other experimental configurations e.g. the SST experiment and similar applications. Operator splitting has been employed to efficiently evolve the energy-space and configuration-space components individually with tailored numerical schemes.

The theory and associated code was first applied to a simple hard-sphere benchmark model liquid, where structure effects were simulated by the Percus-Yevick structure factor as a function of the volume fraction, Φ . The inclusion of an inelastic channel was a key test of the algorithm's ability to reproduce non-hydrodynamic phenomena. Periodic spatial structures developed in the space-time and steady-state profiles for the distribution function components and associated transport properties, the periodicity of which is directly related to the threshold energy of the inelastic process. We observed that these periodic structures arose on shorter times scales when coherent scattering effects became important. The steady-state profiles constructed for various volume fractions also reproduced the non-hydrodynamic oscillatory structures expected. The asymptotic transport coefficients calculated from the non-hydrodynamic solution of Boltzmann's equation were also shown to be consistent with the values calculated from a hydrodynamic solution of Boltzmann's equation.

Finally, the cross sections calculated in Chapter 7 were used to investigate the spatio-temporal evolution of electrons in gas-phase and liquid-phase argon. The two momentum-transfer cross sections feature different qualitative and quantitative behaviours. Striking differences in the evolution of the components of the phase-space distribution were apparent, reflecting the differences in the gas-phase and liquid-phase cross sections, particularly the absence of a Ramsauer minimum in the liquid-phase. This highlights the problems associated with treating liquid systems as gaseous systems with increased density, which has implications for various applications including liquid argon time projection chambers.

9

Concluding remarks

9.1 Summary

An understanding of the temporal and spatial behaviour of electrons and positrons (as well as other species) in gases and soft-condensed matter underpins a variety of technologies and applications. Electron applications are ubiquitous in modern life: plasma processing of microelectronic devices, radiation therapy, dosimetry, plasma medicine and liquid particle detectors all depend on electron-driven processes. Positrons have the unique property of annihilating with electrons, a process which is exploited in positron-annihilation spectroscopy, positron therapy and positron emission tomography. Particularly for applications involving the human body, there is a need to be able to accurately quantify the biological consequences of ionizing-radiation, including damage to DNA, with the aim of minimizing the negative effects. The scope of this thesis has been to develop a systematically benchmarked model for lepton transport in gases and simple atomic liquids valid under hydrodynamic and non-hydrodynamic conditions. This has been achieved via a numerical solution to the space-time dependent Boltzmann equation. An expansion of the velocity-space in terms of Legendre polynomials has been performed with no limitation placed on the number of terms included, i.e., a *multi-term* solution.

Under hydrodynamic conditions, the numerical scheme has been benchmarked for a variety of model and real systems over a wide range of electric field strengths, chosen to validate the relevant collisional processes. Swarm experiments, which generally operate in the hydrodynamic regime, provide a stringent test on the accuracy and completeness of scattering cross section sets. The Boltzmann equation provides a connection between microscopic information such as cross sections, and macroscopic information including swarm experiment measurements, which has allowed us to work closely with scattering theoreticians to comment on the accuracy and validity of new and existing cross section sets. In this role, we have investigated and made recommendations for the low-energy elastic cross section for the electron-neon system and the elastic and annihilation cross sections for the positron-helium system.

At higher energies, additional inelastic channels, such as ionization, become available. Ionization by positron impact (PII) is a fundamentally different process than ionization by electron impact (EII). In this work, a PII kinetic theory collision operator has been derived for the first time, as well as a simple energy-partition function model that qualitatively captures the underlying physics of high energy and near-threshold PII. We have shown that PII is much more sensitive to the energy-partitioning than EII. In our investigation of the role of ionization on thermalization in H_2 , different treatments of the energy-partitioning lead to differences of more than an order of magnitude in the mean energy profiles, with implications to the energy deposition and number of secondary particles generated.

Transport in tissue or biological matter requires a model of transport in soft-condensed matter. The seminal works of Lekner and Cohen, which describe how to modify the scattering potentials for dense fluids and include coherent scattering effects, have been generalized with modern scattering theory. An effective liquid-phase argon cross section for elastic scattering has been calculated, and the transport coefficients calculated agree closely with swarm experiment measurements in both the gaseous and liquid states. The importance of an accurate treatment of the exchange and polarization potentials has been highlighted.

Finally, a full, multi-term Boltzmann equation solver describing the non-equilibrium spatio-temporal evolution of swarms under non-hydrodynamic conditions has been developed. To our knowledge, this is the first time such a complete solution of Boltzmann's equation has been developed. We have presented solutions for a model hard-sphere liquid with the addition of an inelastic channel to induce periodic oscillatory structures, which can act as a non-hydrodynamic benchmark. The spatio-temporal evolution of the phase-space distribution for electrons in liquid argon has been investigated, using the microscopic cross sections derived previously. The gas phase and liquid phase momentum-transfer cross sections demonstrated quantitative and qualitative differences, which were reflected in the phase-space distribution evolution, and highlights the problems associated with treating liquid systems as gaseous systems with increased density.

9.2 Recommendations for future work

This is a very broad field of research with many applications and opportunities that arise naturally from this work. The analytic, mathematical and numerical tools and framework developed, together with the results obtained, suggest several avenues of research that can be further developed.

First, our Boltzmann equation solution can be generalized beyond plane-parallel geometry to other geometries and symmetries. A spherically-symmetric system in configuration-space and velocity-space can also be adequately described with the same Legendre polynomial expansion considered here. Cylindrical geometry in configuration-space or the presence of magnetic fields that destroy the spherical symmetry of the velocity-space cannot be adequately represented in this simple way. In general, an expansion of the velocity-space in terms of spherical harmonics is required [330]. These extensions are particularly important to PET applications, as the positrons are emitted from a spherically symmetric radioactive source, the development of combined PET-MRI scanners involve magnetic fields, and the ionized electrons arising from the thermalization spur are produced with a cylindrical geometry. Similarly, the ionized electrons produced in the emerging field of ion-beam therapy [544] are produced with a cylindrical geometry.

Second, a number of other important microscopic effects need to be included in our models on the path to biological matter, for both electrons and positrons. The generalized Cohen and Lekner procedure developed for electrons in atomic liquids can be adapted to positrons in atomic liquids.

Quantum self-interference [158, 159], the formation of localized states such as bubbles and clusters [160, 163], accounting for orientational correlations due to dipoles in polar liquids [333, 545] and the transition to solvation are effects that need to be included. Further investigation of scattering from biomolecules including H₂O, THF, pyrimidine, Uracil and other simple DNA analogues is warranted [546] to generate complete sets of differential cross sections for tissue analogues.

Finally, in this work, a general framework has been developed for tracking the drift and diffusion of a pulse-like source during thermalization, via an adaptive configuration-space mesh. For many applications, a high energy source of particles must be followed as it thermalizes, often through many orders of magnitude with respect to the mean energy. An adaptive energy-space mesh has been applied in our hydrodynamic relaxation studies, but has not yet been used in conjunction with the adaptive configuration space mesh for non-hydrodynamic investigations.

A

Fluid modelling in dilute and dense atomic gases

This appendix contains material that has been published in the following journal article:

[4] G. J. Boyle, R. D. White, R. E. Robson, S. Dujko and Z. Lj. Petrović. On the approximation of transport properties in structured materials using momentum-transfer theory. *New Journal of Physics*, **14**, 045011 (2012). doi:10.1088/1367-2630/14/4/045011.

This chapter includes reference Boltzmann equation solutions results which were performed by R. D. White. All other work described in this appendix is my own.

It should be noted that a scaling error was made [9] in the calculation of the Percus-Yevick structure factor, which is evident when comparing Figure A.1 to Figure 4.5 in Chapter 7. However, since both the fluid model described here and the reference Boltzmann equation solver both used the same (erroneous) structure factor, the comparisons made and associated comments are still valid.

A.1 Introduction

The integro-differential nature of the Boltzmann kinetic equation, (2.2), makes finding a general solution for the velocity (phase-space) distribution function a computationally expensive task. In previous chapters, a multi-term Legendre polynomial expansion, (2.4), (2.6)–(2.8), has been employed and numerical schemes developed to find the distribution function directly (see Chapters 2 and 3). In this appendix, the task of finding the phase-space distribution function is set aside, and instead the focus is on the kinetic theory at a semi-quantitative level, by considering a fluid approach. Fluid equations are generated by taking low-order moments of the kinetic equation, which essentially represent continuity, momentum and energy balance equations [251, 266, 404, 547]. Whereas it is difficult to gain physical insight directly from the full Boltzmann equation,

the moment approach allows one to obtain analytic relations between measurable quantities and hence direct physical understanding of the relationships between these properties. This procedure has a long history in the kinetic theory of gases [243, 548]. While there are many and varied techniques to close the set of moment equations and approximate the moments of the collision integral (see [269, 549] for discussions), we believe momentum transfer theory (MTT) (see the textbook discussion [328]) represents the most transparent and internally consistent method to approximate the moments of the collision operator. It is exact in the benchmark case of point-charged induced dipole interactions, and the prescriptions for improved accuracy are clear [327, 404]. While the primary aim of MTT initially was to furnish relationships between measurable quantities (e.g. Wannier energy relations, generalized Einstein relations (GER), etc.), more recently it has been demonstrated to provide transport properties in good qualitative and semi-quantitative agreement with more rigorous treatments such as Boltzmann equation solutions and Monte-Carlo simulations [31, 171, 266, 269, 270, 327, 549–551].

While there exists a large body of literature dedicated to the measurement and calculation of scattering cross sections and transport properties for the dilute gas phase, the same cannot be said for the structured and soft-condensed phase. One aim of this work is to capitalize on this body of literature in the gas phase by adapting and applying it where possible to consider transport in structured and soft-condensed phases. In Chapter 7, an effective liquid scattering cross section was calculated *ab initio* from the Dirac-Fock equation, which involved both coherent scattering effects and a modification to the dilute gas-phase potential. The aim of this appendix is to approximately calculate transport coefficients in structured and soft-condensed materials directly from transport properties measured or calculated in the dilute gas phase limit.

A.2 Fluid equations and momentum-transfer theory

A full and general solution to the Boltzmann equation, (2.2), can be achieved only numerically [1, 269]. A fluid equation treatment, however, can yield approximate quantitative results and, importantly, can furnish analytic relationships between physically measurable properties. The problem of solving the Boltzmann equation for f in phase-space is replaced by a low order set of approximate (velocity) moment equations of f [34, 251, 252, 263, 266, 404]. The set of moment equations is found by multiplying the modified Boltzmann equation (2.2) by an arbitrary property of swarm particle velocity, $\Psi(\mathbf{v})$, and integrating over all velocities,

$$\begin{aligned} \frac{\partial}{\partial t} [n \langle \Psi(\mathbf{v}) \rangle] + \nabla \cdot [n \langle \mathbf{v} \Psi(\mathbf{v}) \rangle] - n \frac{q}{m} \left\langle \mathbf{E} \cdot \frac{\partial}{\partial \mathbf{v}} \Psi(\mathbf{v}) \right\rangle &= - \int \Psi(\mathbf{v}) J(f) d\mathbf{v}, \\ &= C_{\Psi}, \end{aligned} \quad (\text{A.1})$$

where $\langle \rangle$ represents the average over swarm particle velocity, and the negative on the right hand side of (A.1) indicates the rate of loss of that quantity due to collisions with the medium. If one takes $\Psi(\mathbf{v})$ equals 1, $m\mathbf{v}$ and $\frac{1}{2}m\mathbf{v}^2$, etc. in succession the above generates an infinite chain, a full solution of which would be equivalent to knowing f . In practice, one must truncate the chain, and generally for light particles only the first three moment equations are required. Setting $\Psi(\mathbf{v})$ equal

to 1, $m\mathbf{v}$ and $\frac{1}{2}mv^2$, yields the continuity, momentum and energy balance equations respectively:

$$\frac{\partial n}{\partial t} + \nabla \cdot n\mathbf{v} = C_1, \quad (\text{A.2})$$

$$\frac{\partial}{\partial t}[nm\langle\mathbf{v}\rangle] + \nabla \cdot [nm\langle\mathbf{v}\mathbf{v}\rangle] - nma = C_{m\mathbf{v}}, \quad (\text{A.3})$$

$$\frac{\partial}{\partial t}[n\langle\frac{1}{2}mv^2\rangle] + \nabla \cdot [n\langle\frac{1}{2}mv^2\mathbf{v}\rangle] - nma \cdot \langle\mathbf{v}\rangle = C_{\frac{1}{2}mv^2}. \quad (\text{A.4})$$

Momentum transfer theory (MTT) provides a way of evaluating the collision terms [328], and the exact form will be detailed below. For now, it suffices to say that the collision frequencies are assumed to be slow-varying functions of energy. The Taylor series representation,

$$\nu(U) = \nu(\epsilon) + (U - \epsilon)\nu'(\epsilon) + \dots, \quad (\text{A.5})$$

about some reference energy, ϵ , at which the dominant contribution to the average occurs, can then be assumed to converge rapidly. It is assumed that the appropriate reference energy is the average energy $\langle U \rangle$. For conservative collisional processes such as elastic and inelastic scattering, only the first term of the expansion (A.5) is generally considered. However, when energy-dependent non-conservative processes, such as positronium formation, positron annihilation, and electron induced ionization, are required in the description then the derivative term in (A.5) become leading term and must be kept.

The connection between experiment and theory is generally given by the continuity equation (2.86):

$$\frac{\partial n(\mathbf{r}, t)}{\partial t} + \nabla \cdot \Gamma(\mathbf{r}, t) = S(\mathbf{r}, t), \quad (\text{A.6})$$

where $\Gamma = n\langle\mathbf{v}\rangle$ denotes the swarm particle flux, n the charged particle density and S represents a source or sink term arising from the presence of non-conservative collisional processes. If the gradient of the swarm number density is also assumed to be small, and we are far from boundaries, sources or sinks, the ‘hydrodynamic regime’ applies, and one can apply the density gradient expansion of the phase-space distribution function [263]. The space-time dependence of all properties is then effectively been projected onto functionals of the number density. Projecting out the space and time dependence average energy, $\epsilon(\mathbf{r}, t)$ and flux in the same manner, we have respectively

$$\epsilon(\mathbf{r}, t) = \langle\frac{1}{2}mv^2\rangle = \epsilon + \gamma \cdot \frac{\nabla n}{n} + \dots, \quad (\text{A.7})$$

$$\Gamma(\mathbf{r}, t) = n\langle\mathbf{v}\rangle = n\mathbf{W} - \mathbf{D} \cdot \nabla n + \dots, \quad (\text{A.8})$$

where ϵ is the mean energy of the swarm and γ is the gradient energy parameter [272]. Fick’s law (A.8) defines the ‘flux drift velocity’ \mathbf{W} and ‘flux diffusion tensor’ \mathbf{D} . These are distinct from the ‘bulk’ transport coefficients [264, 549] which are not considered in this appendix. If the hydrodynamic regime has not been reached, then the space-time dependence of the distribution function cannot be projected onto the number density, and transport coefficients are not meaningful quantities. A complete, non-hydrodynamic solution is then required.

Using the explicit form of the collision operators used in [1, 315] and applying the relevant approximations from MTT, the set of moment equations (A.3) in the hydrodynamic regime yield

for a steady-state swarm of light particles, $m \ll m_0$, the following hierarchy of coupled equations [4]:

$$\mathbf{W} = \frac{q\mathbf{E}}{m(\tilde{\nu}_m + \frac{2}{3}\epsilon\nu'_A)}, \quad (\text{A.9})$$

$$\epsilon = \frac{3}{2}k_b T_0 + \frac{1}{2}m_0 \mathbf{W}^2 \frac{\tilde{\nu}_m}{\nu_m} - \frac{\Omega}{\nu_e} - \frac{2}{3}\epsilon^2 \frac{\nu'_A}{\nu_e}, \quad (\text{A.10})$$

$$\left(\tilde{\nu}_m + \frac{2}{3}\epsilon\nu'_A\right) \mathbf{D} = \frac{d}{d\epsilon} \left(\tilde{\nu}_m + \frac{2}{3}\epsilon\nu'_A\right) \mathbf{W}\gamma + \frac{2}{3} \frac{\epsilon}{m} \mathbf{I}, \quad (\text{A.11})$$

$$\begin{aligned} \left[1 + \frac{\nu'_m}{\nu_m} \left(\epsilon - \frac{3}{2}k_b T_0 - \frac{1}{2}m_0 \mathbf{W}^2 \frac{\tilde{\nu}'_m}{\nu'_m}\right) + \frac{\Omega'}{\nu_e} + \frac{1}{\nu_e} \frac{d}{d\epsilon} \left(\frac{2}{3}\epsilon^2 \nu'_A\right)\right] \gamma \\ = -m_0 \frac{\tilde{\nu}_m}{\nu_m} \mathbf{W} \cdot \mathbf{D} - \mathbf{Q}. \end{aligned} \quad (\text{A.12})$$

The effect of attachment enters the balance equations through the derivative, ν'_A . It has also been assumed that, for light particles, random motion dominates directed motion, i.e., $\langle v^2 \rangle \geq \langle \mathbf{v} \rangle^2$. The average momentum and transfer collision frequencies,

$$\begin{aligned} \nu_m(\epsilon) &= \nu_m^{\text{elas}}(\epsilon) + \nu_m^{\text{inel}}(\epsilon), \\ &= \sum_j n_{0j} \sqrt{\frac{2\epsilon}{m}} \sigma_m(j, j; \epsilon) + \sum_{\substack{j, j' \\ j \neq j'}} n_{0j} \sqrt{\frac{2\epsilon}{m}} \sigma_m(j, j'; \epsilon), \\ &= \sum_{j, j'} n_{0j} \sqrt{\frac{2\epsilon}{m}} \sigma_m(j, j'; \epsilon), \end{aligned} \quad (\text{A.13})$$

$$\nu_e(\epsilon) = \frac{2m}{m_0} \nu_m(\epsilon), \quad (\text{A.14})$$

$$\begin{aligned} \tilde{\nu}_m(\epsilon) &= \tilde{\nu}_m^{\text{elas}}(\epsilon) + \nu_m^{\text{inel}}(\epsilon), \\ &= \sum_j n_{0j} \sqrt{\frac{2\epsilon}{m}} \tilde{\sigma}_m(j, j; \epsilon) + \sum_{\substack{j, j' \\ j \neq j'}} n_{0j} \sqrt{\frac{2\epsilon}{m}} \sigma_m(j, j'; \epsilon), \end{aligned} \quad (\text{A.15})$$

$$\nu_A(\epsilon) = \sum_{j, j'} n_{0j} \sqrt{\frac{2\epsilon}{m}} \sigma_A(j, j'; \epsilon), \quad (\text{A.16})$$

represent the dilute gas phase momentum and energy transfers, soft-condensed momentum transfer, and attachment collision frequencies respectively, and are all prescribed functions of the mean energy defined in the centre of mass frame. The terms σ_m , $\tilde{\sigma}_m$ and σ_A represent the momentum-transfer cross sections for dilute gaseous and soft-condensed mediums, and the attachment cross section respectively. Ω represents the energy lost in inelastic collisions in one elastic energy transfer collisional time, ν_e^{-1} , and is given by

$$\Omega(U) = \sum_I \Delta U_I (\langle \vec{\nu}_I(U) \rangle + \langle \hat{\nu}_I(U) \rangle). \quad (\text{A.17})$$

The inelastic channels I are governed by threshold energies U_I , and collision frequencies for inelastic and super-elastic processes, $\vec{\nu}_I(U)$ and $\hat{\nu}_I(U)$, respectively.

Equations (A.9) and (A.10) represent coupled non-linear differential equations for the drift

velocity \mathbf{W} and mean energy ϵ , which serve as inputs into the linear coupled differential equations (A.11) and (A.12) for the diffusion coefficients and gradient energy parameter. The heat flux, \mathbf{Q} , is found from higher order moments, and so an assumption needs to be made to achieve closure. In this work we neglect \mathbf{Q} , which is generally a safe assumption under hydrodynamic conditions, but not always [267]. For further discussion on the heat flux the reader is referred to [549].

From this system of equations structure-modified generalizations of well known dilute gas phase results such as Wannier's energy relation [243], generalized Einstein relations [327], and others can be made, as detailed below.

A.3 Standard MTT

In the preceding section, the system of equations (A.9)–(A.12) were derived for homogeneous and first order inhomogeneous transport coefficients valid in soft-condensed matter. The aim of this section is to develop semi-analytic relationships between dilute gas phase microscopic information, such as cross sections and medium structure factor, and soft-condensed phase macroscopic transport coefficients. To illustrate the technique, we limit ourselves to the simple case of a steady, spatially uniform swarm subject to an electric field, undergoing elastic and particle-loss processes only with a background medium. In this case, $\nu_m = \nu_m^{\text{elas}}$, $\tilde{\nu}_m = \tilde{\nu}_m^{\text{elas}}$ and $\Omega = 0$.

A.3.1 Drift velocity and mean energy

If 'effective collision frequencies' are defined by

$$\tilde{\nu}_{\text{eff}} = \tilde{\nu}_m + \frac{2}{3}\epsilon\nu'_A, \quad (\text{A.18})$$

$$\nu_{\text{eff}} = \nu_m + \frac{2}{3}\epsilon\nu'_A, \quad (\text{A.19})$$

then the equations (A.9) and (A.10) simplify to

$$W = \frac{qE}{m\tilde{\nu}_{\text{eff}}}, \quad (\text{A.20})$$

and

$$\epsilon = \frac{3}{2}k_bT_0 + \frac{1}{2}m_0W^2\frac{\tilde{\nu}_m}{\nu_m} - \frac{2}{3}\epsilon^2\frac{\nu'_A}{\nu_e}, \quad (\text{A.21})$$

which can be combined as

$$\epsilon = \frac{3}{2}k_bT_0 + \frac{1}{2}m_0\left(\frac{qE}{m}\right)^2\frac{\tilde{\nu}_m}{\tilde{\nu}_{\text{eff}}^2\nu_m} - \frac{2}{3}\epsilon^2\frac{\nu'_A}{\nu_e}. \quad (\text{A.22})$$

Equation (A.21) is a generalization of the well known Wannier energy relation [243] in dilute gas transport theory, which is frequently used empirically to produce the approximate mean energy from measured drift velocities [328]. From (A.22), it is clear that given knowledge of the dilute gas phase cross sections for the necessary processes and the structure factor of the medium, the above non-linear expressions can be solved for the soft-condensed phase mean energy and drift velocity numerically by any number of methods [552, 553].

It is well known in gas transport theory that, for some energy profiles, the inclusion of inelastic or non-conservative scattering cross sections can cause regions in which the flux drift velocity decreases despite an increase in the applied electric field [267, 328, 414]. The conditions for the occurrence of this phenomena, known as 'negative differential conductivity' (NDC), have been

investigated previously [31, 266, 267, 414]. For a structured media there is a new type of NDC [315] which does not require inelastic collisions or non-conservative processes, i.e. purely a consequence of the medium structure. NDC is characterized by a decrease in the drift velocity W despite an increase in the magnitude of applied electric field E , i.e.

$$\frac{dW}{dE} < 0. \quad (\text{A.23})$$

For simplicity, we assume elastic collisions only and take the cold gas approximation, $T_0 = 0$ K, such the drift and mean energy equations (A.20) and (A.21) respectively become

$$W = \frac{qE}{m\tilde{\nu}_m}, \quad (\text{A.24})$$

$$\epsilon = \frac{1}{2}m_0W^2\frac{\tilde{\nu}_m}{\nu_m}. \quad (\text{A.25})$$

From these relations it can be shown that

$$\frac{d\epsilon}{d \ln E} \left[1 - \frac{d \ln \left(\frac{\tilde{\nu}_m}{\nu_m} \right)}{d \ln \epsilon} \right] = m_0W \frac{\tilde{\nu}_m}{\nu_m} \frac{dW}{d \ln E}. \quad (\text{A.26})$$

Considering the signs of the left hand side and right hand side constituents of (A.26), it is evident that for structure induced NDC to occur, the following condition must be met,

$$\frac{d \ln \left(\frac{\tilde{\nu}_m}{\nu_m} \right)}{d \ln \epsilon} > 1. \quad (\text{A.27})$$

In Section A.3.3 this condition is further explored through numerical investigations, and can be confirmed graphically.

A.3.2 Diffusion coefficients

The homogenous transport coefficients found in Section A.3.1 can be used to find first order inhomogeneous transport coefficients. For the electric field only case considered here, there are two non-zero components of the diffusion tensor; those parallel to the electric field, D_L , and those perpendicular, D_T , given by:

$$D_T = \frac{2}{3} \frac{\epsilon}{m\tilde{\nu}_{\text{eff}}}, \quad (\text{A.28})$$

$$D_L = \frac{2}{3} \frac{\epsilon}{m\tilde{\nu}_{\text{eff}}} + \frac{\tilde{\nu}'_{\text{eff}}}{\tilde{\nu}_{\text{eff}}} W \gamma, \quad (\text{A.29})$$

where dashed quantity represents energy derivatives. Substituting in the parallel component of expression (A.12) (neglecting the heat flux) into (A.29) and re-arranging ,

$$D_L = \frac{2}{3} \frac{\epsilon}{m\tilde{\nu}_{\text{eff}}} \left[1 + \frac{m_0W^2 \frac{\tilde{\nu}'_{\text{eff}}}{\nu_{\text{eff}}} \frac{\tilde{\nu}_m}{\nu_m}}{1 - \frac{1}{2}m_0W^2 \frac{\partial}{\partial \epsilon} \left(\frac{\tilde{\nu}_m}{\nu_m} \right) + \frac{\partial}{\partial \epsilon} \left(\frac{2}{3} \epsilon^2 \frac{\tilde{\nu}_A}{\nu_e} \right)} \right]^{-1}. \quad (\text{A.30})$$

This result can expressed in terms of the mobility, μ ,

$$\mu = \frac{W}{E} = \frac{q}{m\tilde{\nu}_{\text{eff}}}, \quad (\text{A.31})$$

which can then be used in combination with (A.21) to prove the following identity;

$$\frac{\frac{\partial \ln \mu}{\partial \ln E}}{\left(1 + \frac{\partial \ln \mu}{\partial \ln E}\right)} = \frac{-m_0 W^2 \frac{\nu_{\text{eff}}'}{\nu_{\text{m}}} \frac{\bar{z}_{\text{m}}}{\nu_{\text{m}}}}{1 - \frac{1}{2} m_0 W^2 \frac{\partial}{\partial \epsilon} \left(\frac{\bar{z}_{\text{m}}}{\nu_{\text{m}}}\right) + \frac{\partial}{\partial \epsilon} \left(\frac{2}{3} \epsilon^2 \frac{\bar{z}_{\text{A}}}{\nu_{\text{e}}}\right)}. \quad (\text{A.32})$$

It follows that equation (A.30) can be written as

$$\frac{D_{\text{L}}}{D_{\text{T}}} = 1 + \frac{\partial \ln \mu}{\partial \ln E}, \quad (\text{A.33})$$

which is valid in soft-condensed matter and is of the same form as the well-known generalized Einstein relation in dilute gas transport theory [243, 267]. The inclusion of a non-zero heat flux, Q , manifests itself as a correction term in (A.33).

A.3.3 Benchmark model

The benchmark model for coherent scattering was introduced in Section 4.6. For a system of hard-spherical particles, the model of Percus and Yevick (with the Verlet-Weiss correction) [411, 412] provides the appropriate structure behaviour. The important factor is the volume fraction, Φ , which is a measure of how tightly packed the particulates of the media are. Low volume fractions indicate a larger inter-particle spacing, whereas higher volume fractions indicate a smaller inter-particle spacing. Figure A.1 shows the static structure value, $S(K)$, for different values of Φ . The details of the model parameters was given in model (4.21).

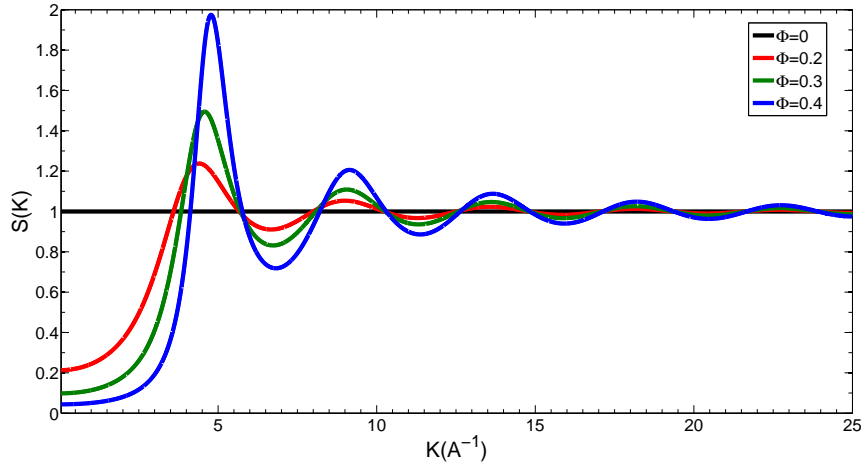


Figure A.1: The variation of the static structure factor with momentum exchange K for the Percus-Yevick model (with Verlet-Weiss correction) for various volume fractions, Φ .

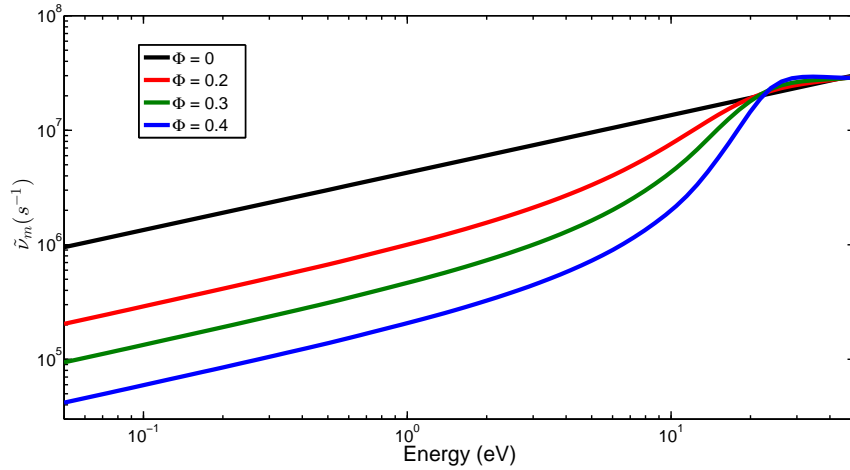


Figure A.2: The energy variation of elastic the collision frequency, $\tilde{\nu}_m$, for various volume fractions Φ , for a dense gas of hard spheres.

Mean energy and drift velocity

The spatially homogeneous transport coefficients, i.e. mean energy and drift velocity, were calculated from (A.9) and (A.10) for the hard-sphere model. In Figures A.3 and A.4, the variation of swarm mean energy and drift velocity, respectively, with reduced electric field E/n_0 is displayed for the fluid model approach and compared with those of the Boltzmann solution. The fluid model predictions are qualitatively correct and exhibit satisfactory quantitative agreement, generally to within 10 to 20 percent of the Boltzmann equation solution results. In regions where the structure-modified momentum transfer collision frequency varies rapidly with energy, the associated errors are increased. This is consistent with the approximations associated with the low-order truncation of (A.5) associated with momentum transfer theory. It is evident that the presence of structure in the medium causes a significant difference between the two sets of coefficients. Coherent scattering effects generally act to reduce the momentum transfer thus enhancing the field's ability to pump energy and momentum into the system. The enhancements in the mean energy and drift velocity due to enhanced coherent scattering effects then follows. At high fields the profiles converge to the dilute gas phase profile, a reflection of the decrease in the associated de Broglie wavelength and subsequent suppression of coherent scattering effects.

Importantly, in Figure A.4, the fluid model successfully predicts the phenomenon of structure-induced negative differential conductivity (NDC) [1,315], i.e., a decrease in drift velocity despite an increase in electric field. While NDC has been demonstrated in the past as a consequence of inelastic [267] or non-conservative [266] processes, its occurrence here is purely a result of including structure effects. In certain regions an increase in energy leads to a sharp increase in the momentum-transfer cross section (a reflection of sharp increases in the structure factor) and hence a decrease in drift velocity (for further details on structure-induced NDC see [1,315]). A condition for the occurrence of NDC was given in (A.27), restated differently using equation (4.19),

$$\frac{d \ln s}{d \ln \epsilon} > 1. \quad (\text{A.34})$$

Figure A.5 shows a log-log plot of energy versus s , as defined in 7, superimposed with straight lines of slope one. It is evident that there are energies for $\Phi = 0.3$ and $\Phi = 0.4$ profiles for which the slope of $\log s / \log \epsilon$ exceeds one, but for lower Φ there are not. This coincides with the occurrence of NDC in Figure A.4 for $\Phi = 0.3$ and $\Phi = 0.4$ and not in the smaller volume fraction profiles. It

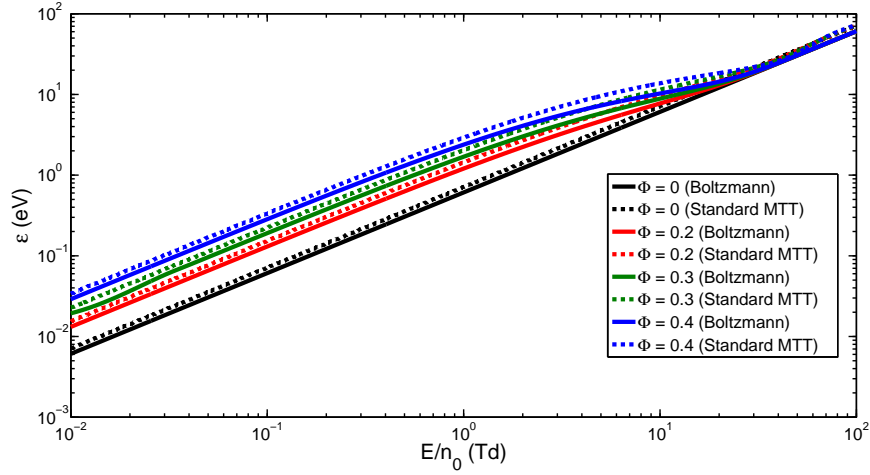


Figure A.3: Variation of the swarm mean energy with reduced electric field, for various volume fractions Φ , for a dense gas of hard spheres. Fluid results are compared with those from a multi-term Boltzmann equation solution [1].

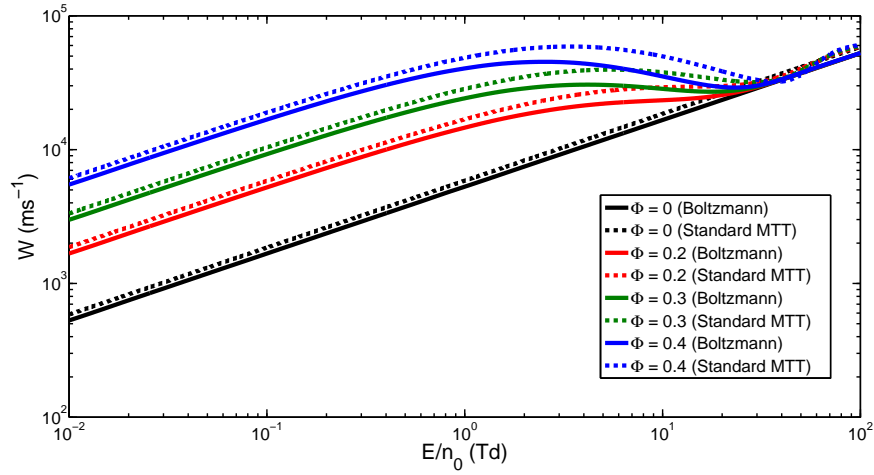


Figure A.4: Variation of the swarm flux drift velocity with reduced electric field, for various volume fractions Φ , for a dense gas of hard spheres. Fluid results are compared with those from a multi-term Boltzmann equation solution [1].

can be deduced from (A.24) that during NDC, a small increase E is accompanied by a rapid increase in $\tilde{\nu}_m$ resulting in an overall decrease in the drift velocity.

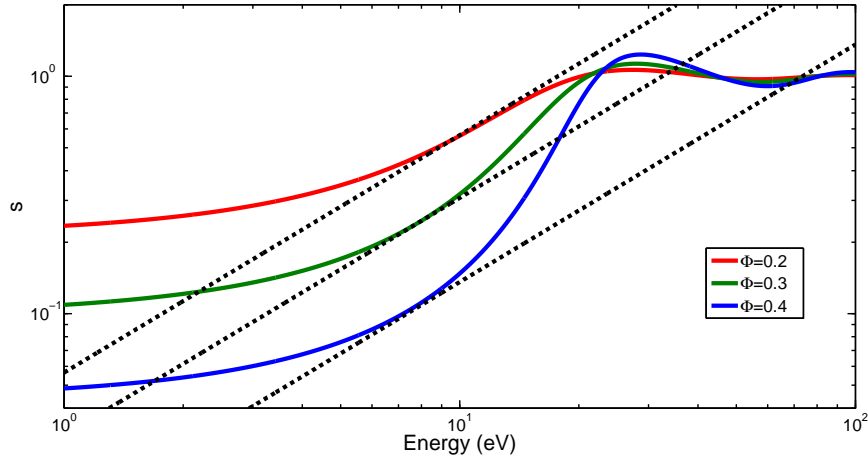


Figure A.5: Variation of s , as defined in (4.20), with reduced electric field, for various volume fractions Φ , for a dense gas of hard spheres.

Diffusion coefficients

The phenomenon of anisotropic diffusion is well known for charged particles of all masses in dilute gaseous systems is now textbook material [328]

$$\frac{D_L}{D_T} = 1 + \frac{\partial \ln \mu}{\partial \ln E} = \frac{\partial \ln W}{\partial \ln E}. \quad (\text{A.35})$$

For charged particles interacting with a dilute gas of hard spheres with a constant collision cross section, $W \sim E^{\frac{1}{2}}$, and hence

$$\frac{D_L}{D_T} \simeq 0.5. \quad (\text{A.36})$$

In Figures A.6 and A.7 the variation is presented in the transverse and longitudinal diffusion coefficients respectively with reduced electric field as a function of the volume fraction Φ . Figure A.6 highlights the effect of coherent scattering on the transverse diffusion coefficient. For low fields, the dense gas diffusion is about two orders of magnitude greater than the dilute gas equivalent, which is successfully predicted by the fluid equations. As the field increases, the fluid approximations departs significantly from the Boltzmann solution, reflecting the regions in the structure factor which vary quickly and violate the assumption made in (A.5) of a slowly-varying collision frequency and subsequent low-order truncation. Extra correction terms may need to be included to account for this. Once the field increases to a point where the collision frequency is less varying with energy, the fluid approximations return to the dense gas phase Boltzmann equation profiles, which converge on the dilute gas profile.

Figure A.7 shows the variation of the longitudinal diffusion coefficient with reduced electric field. Comparing with Figure A.6, the dilute profile for the longitudinal diffusion coefficient is half the value of the transverse diffusion coefficient when considering hard spheres, as predicted by the generalized Einstein relation (A.36). When coherent scattering effects are included the ratio of 0.5 is still retained at high and low field strengths. In between the two extremes, the oscillatory nature of the structure factor effects in the momentum transfer collision frequency is exhibited, causing the fluid model to break down entirely for the two largest volume fractions, $\Phi = 0.3$ and $\Phi = 0.4$, in the region between about 10 Td and 20 Td where the dense gas collision frequency varies sharpest. In this region we observe that the drift profiles predicted by the fluid approximation in A.4 exhibit

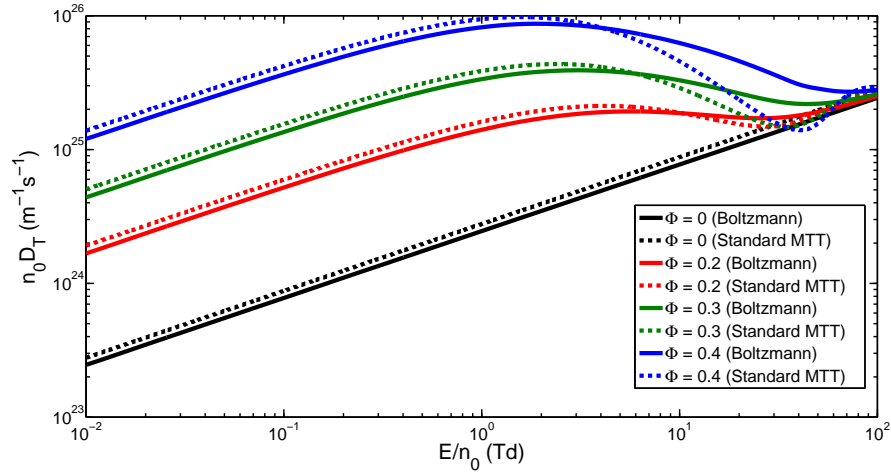


Figure A.6: Variation of the transverse diffusion coefficient with reduced electric field for various volume fractions Φ , for a dense gas of hard spheres. Fluid results are compared with those from a multi-term Boltzmann equation solution [1].

NDC. Consequently, the right hand side of relation (A.33) becomes negative and the relation breaks down. Again, extra correction terms in MTT are required to remedy this [267].

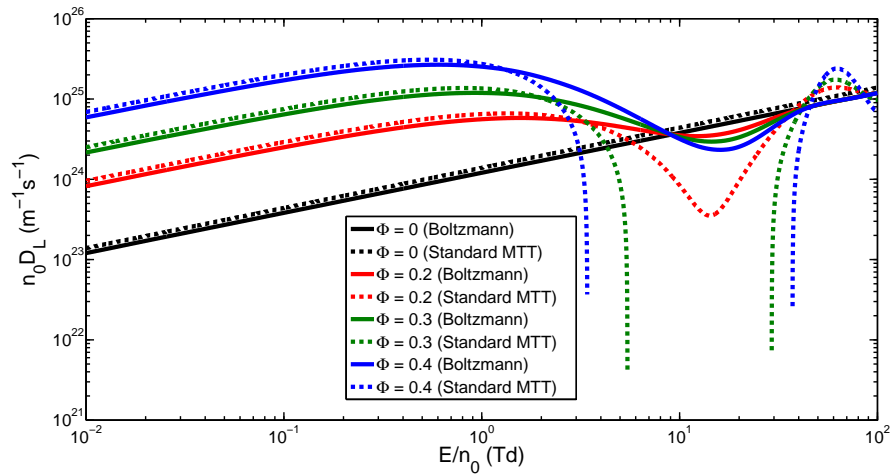


Figure A.7: Variation of the longitudinal diffusion coefficient with reduced electric field for various volume fractions Φ , for a dense gas of hard spheres. Fluid results are compared with those from a multi-term Boltzmann equation solution [1].

A.3.4 Liquid argon

The fluid model theory is now applied to the case of positrons in liquid argon at 84 K. This application has been considered previously and data is available for both the dilute gaseous and liquid phases [1, 31, 315]. The semi-analytic expressions (A.9)-(A.11), include only elastic and attachment collision effects. As such, it is expected that these will give less accurate results for liquid argon than for the hard-sphere test case, particularly at fields where inelastic effects become significant, but there is a range of fields where these equations are suitable.

Figure A.8 details the variation of positron swarm mean energy with the reduced electric field in gaseous and liquid argon. The fluid model gives much less accurate predictions in this scenario as compared to the hard-sphere test model case. The fluid predictions demonstrate peculiar,

unphysical behaviour; there are regions in which multiple steady-state mean energies can result from a single reduced electric field strength. Given the occurrence of this behaviour in the dilute gas phase situation as well, it is clearly a consequence of the cross section behaviour rather than purely a structure effect. Low-order MTT is not sufficient to account for the variation of the collision frequencies. As the field strength increases, the fluid profiles diverge significantly from that of the Boltzmann solution results as neglected inelastic processes become significant.

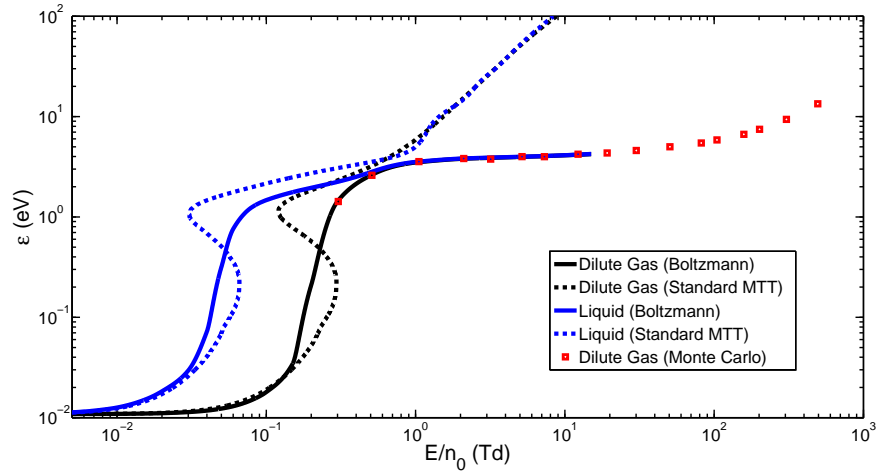


Figure A.8: Variation of the swarm mean energy with reduced electric field, for dilute gaseous and liquid argon at 84 K. Fluid results are compared with those from a multi-term Boltzmann equation solution [1] and Monte-Carlo simulation [31].

The same issues are echoed by the drift velocities shown in Figure A.9; generally bigger errors than the hard-sphere model scenario, peculiar profile behaviour and degeneracy, and large discrepancies when inelastic processes become significant.

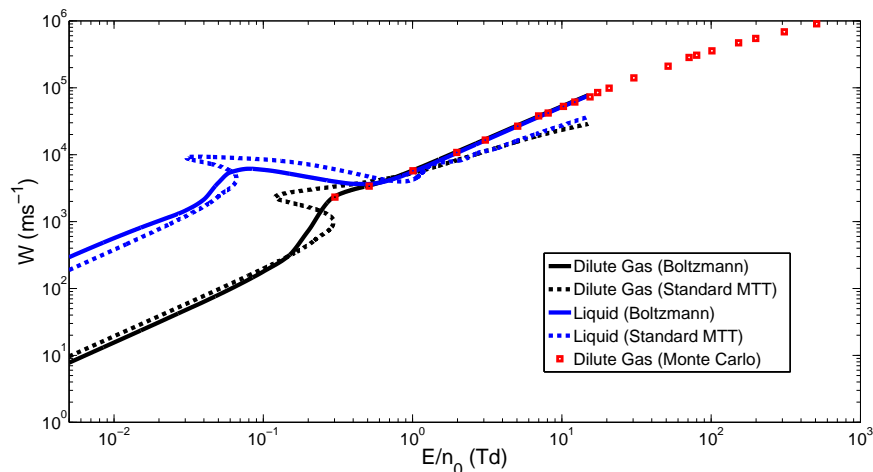


Figure A.9: Variation of the swarm flux drift velocity with reduced electric field, for dilute gaseous and liquid argon at 84 K. Fluid results are compared with those from a multi-term Boltzmann equation solution [1] and Monte-Carlo simulation [31].

Given the inadequacy of the spatially homogeneous transport property predictions, the higher order moments, for which these serve as inputs, are not derived. Extra terms in the Taylor series expansion (A.5) will be required to sufficiently describe positron transport in liquid argon using the standard MTT technique.

In light of the issues experienced using a standard MTT approach, a modified approach has been developed, which utilizes the existing dilute gas phase transport coefficient literature to predict transport in the soft-condensed phase, and is outlined in the following section.

A.4 Modified MTT

In the preceding section, relations between dilute gas phase *microscopic* quantities and soft-condensed phase *macroscopic* transport coefficients were derived. The aim of this section is to develop semi-analytic relationships between sets of transport coefficients in the dilute gas phase and in the soft-condensed phase, facilitating the prediction of the latter directly from knowledge of the former and structure information of the medium. From here forth, tildes will represent transport properties in dense and soft-condensed phases while those without will represent quantities in the dilute gas phase limit.

The steady-state, spatially homogeneous balance equations, (A.20) and (A.21), are restated here for clarity:

$$\tilde{W} = \frac{qE}{m\tilde{\nu}_{\text{eff}}}, \quad (\text{A.37})$$

$$\tilde{\epsilon} = \frac{3}{2}k_{\text{b}}T_0 + \frac{1}{2}m_0\tilde{W}^2\frac{\tilde{\nu}_{\text{m}}}{\nu_{\text{m}}} - \frac{2}{3}\tilde{\epsilon}^2\frac{\nu'_{\text{A}}}{\nu_{\text{e}}}. \quad (\text{A.38})$$

If the inter-particle spacing is large compared to the de Broglie wavelength of the swarm particle, then the static structure factor $S(\Delta\mathbf{k})$ reduces to unity and subsequently $\tilde{\nu}_{\text{m}} \rightarrow \nu_{\text{m}}$, regaining the gas phase relations,

$$W = \frac{qE}{m\nu_{\text{eff}}}, \quad (\text{A.39})$$

$$\epsilon = \frac{3}{2}k_{\text{b}}T_0 + \frac{1}{2}m_0W^2 - \frac{2}{3}\epsilon^2\frac{\nu'_{\text{A}}}{\nu_{\text{e}}}. \quad (\text{A.40})$$

Comparing (A.37) and (A.39),

$$\tilde{W} = W\frac{\nu_{\text{eff}}(\epsilon)}{\tilde{\nu}_{\text{eff}}(\tilde{\epsilon})}, \quad (\text{A.41})$$

which immediately links the drift velocities and mean energies in the two types of media. Substituting (A.41) into (A.38) it follows that

$$\tilde{\epsilon} = \frac{3}{2}k_{\text{b}}T_0 + \frac{1}{2}m_0W^2\left(\frac{\nu_{\text{eff}}(\epsilon)}{\tilde{\nu}_{\text{eff}}(\tilde{\epsilon})}\right)^2\frac{\tilde{\nu}_{\text{m}}(\tilde{\epsilon})}{\nu_{\text{m}}(\tilde{\epsilon})} - \frac{2}{3}\tilde{\epsilon}^2\frac{\nu'_{\text{A}}(\tilde{\epsilon})}{\nu_{\text{e}}(\tilde{\epsilon})}, \quad (\text{A.42})$$

which gives the sought after expression: a non-linear relation for the soft-condensed phase mean energy $\tilde{\epsilon}$ purely in terms of the dilute gas phase mean energy ϵ , drift W , and medium structure factor $s(\epsilon)$. In general this relation must be solved numerically, and results are presented in Section A.4.1. The process for finding soft-condensed phase transport coefficients from dilute gas phase information is then as follows;

1. Find ν_{m} and ν'_{A} by fitting dilute gas phase mean energy, ϵ , and drift velocity, W , according to the functional forms (A.39) and (A.40).
2. Include coherent scattering effects which, for isotropic scattering, is found simply from $\tilde{\nu}_{\text{m}} = \nu_{\text{m}}s$.

3. Solve (A.42) for soft-condensed phase mean energy, $\tilde{\epsilon}$, which can then be used to find other condensed-phase transport coefficients.

In the spirit of other popular approaches used in transport physics [548, 554] we seek to represent equation (A.42) in terms of an ‘effective electric field’, E_{eff} , i.e. what is the electric field needed in the dilute gas phase limit, to generate the same average energy in the soft-condensed phase:

$$\tilde{\epsilon}(E) = \epsilon(E_{\text{eff}}) \equiv \epsilon. \quad (\text{A.43})$$

Using (A.39), (A.40) becomes

$$\epsilon = \frac{3}{2}k_{\text{b}}T_0 + \frac{1}{2}m_0 \left(\frac{qE_{\text{eff}}}{m\nu_{\text{eff}}} \right)^2 - \frac{2}{3}\epsilon^2 \frac{\nu'_{\text{A}}}{\nu_{\text{e}}}. \quad (\text{A.44})$$

Combining (A.44) with (A.38) yields an expression for the effective electric field strength in terms of the actual applied electric field strength and various collision frequencies evaluated at ϵ :

$$E_{\text{eff}} = E \frac{\nu_{\text{eff}}(\epsilon)}{\tilde{\nu}_{\text{eff}}(\epsilon)} \sqrt{\frac{\tilde{\nu}_{\text{m}}(\epsilon)}{\nu_{\text{m}}(\epsilon)}}, \quad (\text{A.45})$$

$$= E \frac{\nu_{\text{eff}}(\epsilon)}{\tilde{\nu}_{\text{eff}}(\epsilon)} \sqrt{s(\epsilon)}, \quad (\text{A.46})$$

where (A.46) is a simplification for isotropic scattering. The effective field is non-linearly dependent on the mean energy, and solving (A.45) with (A.44) is mathematically equivalent to solving (A.42). Effective fields calculated for a simplistic test model and real liquid are presented in Section A.4.1.

Once the mean energy and drift velocity valid in soft-condensed matter have been found, diffusion coefficients can then be derived from the relations given in Section A.3.2. It should be emphasized that the relations for diffusion in the soft-condensed phase require only energy and drift velocity data in the dilute gas phase. This is in the spirit of MTT, however relations could be derived which facilitate more direct computation between the diffusion coefficient sets.

A.4.1 Benchmark model

The benchmark model of a system of hard spheres described in Section A.3.3 is once again employed.

Mean energy and drift velocity

The spatially homogeneous transport coefficients, i.e. mean energy and drift velocity, were calculated from (A.42) and (A.41) for the hard-sphere model. Figures A.10 and A.11 compare the variation of swarm mean energy and drift velocity with reduced electric field of the modified MTT approach with those of the standard MTT and Boltzmann solutions. The modified MTT technique generally gives better prediction than the standard MTT. This is a consequence of using ‘effective collision frequencies’ fitted from the Boltzmann dilute gas phase transport coefficients, which serve to reduce some of the errors involved with MTT. Comments from Section A.3.3 regarding the qualitative behaviour of the standard MTT mean energy and drift velocity are all still appropriate here.

In Figure A.12 the relationship between the actual reduced electric field strength and the effective electric field strength as described by (A.45), for the two MTT approaches. Generally transport in a structured medium requires a lower electric field to generate the same energies and

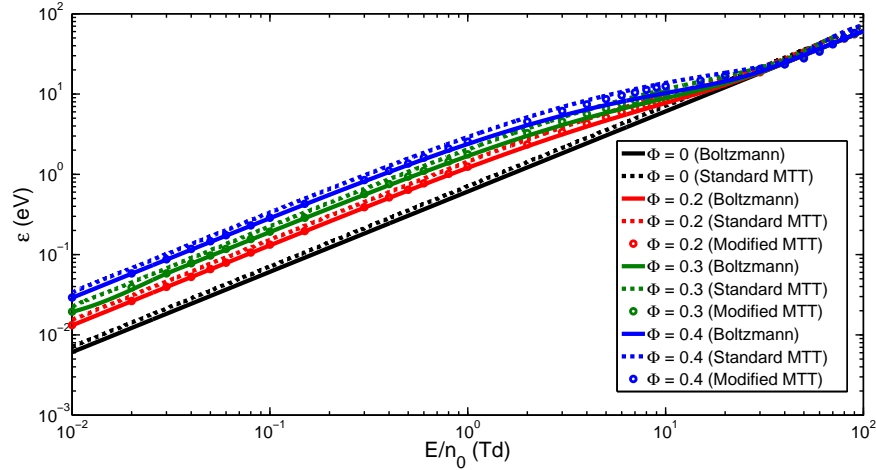


Figure A.10: Variation of the swarm mean energy with reduced electric field, for various volume fractions Φ , for a dense gas of hard spheres. Fluid results are compared with those from a multi-term Boltzmann equation solution [1].

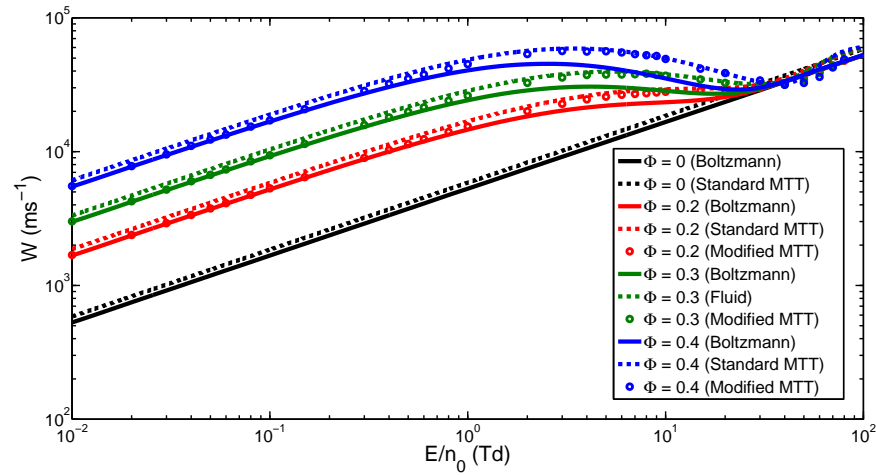


Figure A.11: Variation of the swarm flux drift velocity with reduced electric field, for various volume fractions Φ , for a dense gas of hard spheres. Fluid results are compared with those from a multi-term Boltzmann equation solution [1].

drift velocity as transport in a dilute gas, which is a reflection of the reduction in the momentum transfer due to coherent scattering effects. At high fields, E_{eff} approaches E as expected. Although E_{eff} is calculated from the same expression, there are small differences evident between the standard and modified MTT results. This is due to (A.45) being evaluated at slightly different dilute gas phase energies; the former using a MTT calculation while the latter uses the Boltzmann solution information directly. It is thus expected that modified MTT predictions are more accurate.

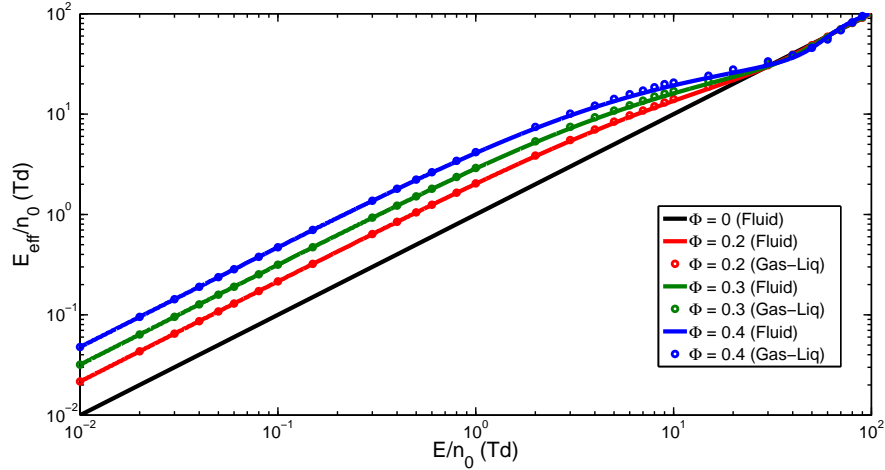


Figure A.12: Variation of the reduced effective electric field, E_{eff} , with reduced electric field for various volume fractions Φ , for a dense gas of hard spheres.

Diffusion coefficients

The diffusion coefficients can then be found from (A.28) and (A.33) using the homogeneous transport quantities as inputs, and are shown in Figures A.6 and A.7. The diffusion coefficients found from the modified MTT are generally more accurate than the standard MTT, which is to be expected from using more accurate inputs. Phenomenologically, comments made in Section A.3.3 still apply here. A breakdown of the low order fluid model entirely for the two largest volume fractions, $\Phi = 0.3$ and $\Phi = 0.4$, in the region where the dense gas phase collision frequency varies sharpest is again seen.

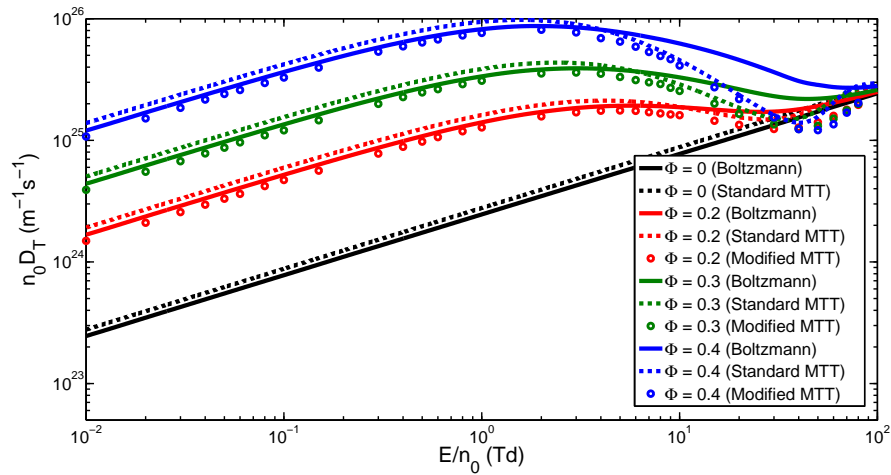


Figure A.13: Variation of the transverse diffusion coefficient with reduced electric field for various volume fractions Φ , for a dense gas of hard spheres. Fluid results are compared with those from a multi-term Boltzmann equation solution [1].

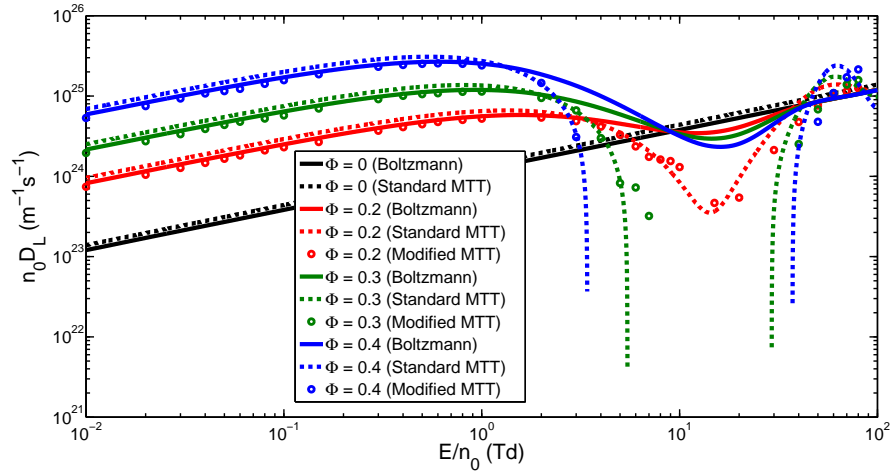


Figure A.14: Variation of the longitudinal diffusion coefficient with reduced electric field for various volume fractions Φ , for a dense gas of hard spheres. Fluid results are compared with those from a multi-term Boltzmann equation solution [1].

A.4.2 Liquid argon

We now apply the modified MTT technique to the case of positrons in liquid argon at 84 K.

Drift velocity and mean energy

Figure A.15 details the variation of positron swarm mean energy with the reduced electric field in gaseous and liquid argon. Previously, when using the standard MTT approach, the mean energy exhibited peculiar, inaccurate and unphysical behaviour. Here the modified MTT approach yields results with accuracy comparable to the test hard-sphere case. The dilute gas and liquid profiles also now converge at high field strengths. Although the effects of inelastic processes become significant at approximately 100 Td, the inaccuracies that one would expect from neglecting inelastic processes are suppressed in Figure A.15 by the collision frequency fitting process. This is somewhat fortuitous as the coherent scattering effects are becoming suppressed in this region, and the approximation of a coherent effective collision frequency model is minimized.

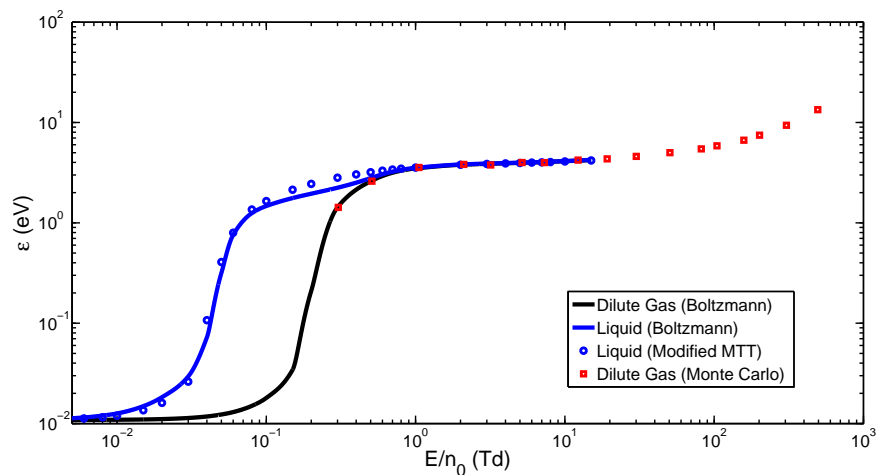


Figure A.15: Variation of the swarm mean energy with reduced electric field, for dilute gaseous and liquid argon at 84 K. Fluid results are compared with those from a multi-term Boltzmann equation solution [1] and Monte-Carlo simulation [31].

The variation of the drift velocity with reduced electric field is highlighted in Figure A.16. The new model used to obtain liquid phase drift velocities from the dilute gas phase drift velocities is shown to produce the required qualitative behaviour, again successfully demonstrating structure-induced NDC. The accuracy is generally within the 10 to 20 percent expected from using a MTT approximation. The discrepancy in the low field region we believe to be a consequence of different extrapolation methods used by the Boltzmann and fluid numerical algorithms to evaluate the structure factor and process cross sections at low energies.

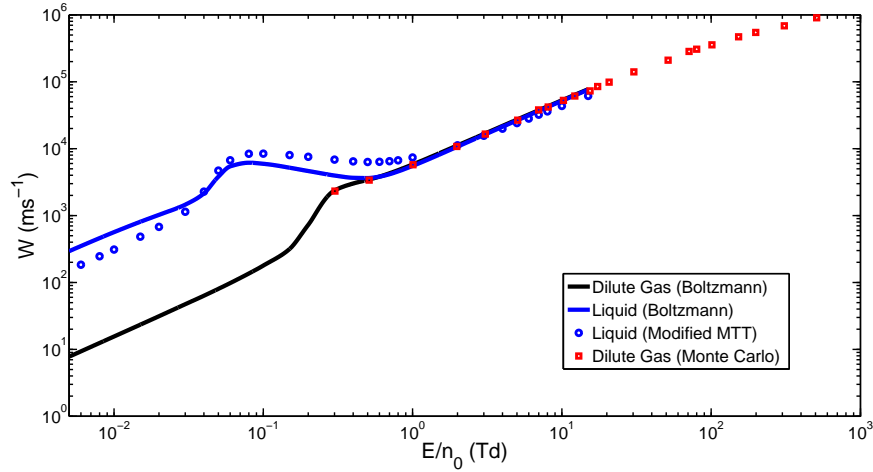


Figure A.16: Variation of the swarm flux drift velocity with reduced electric field, for dilute gaseous and liquid argon at 84 K. Fluid results are compared with those from a multi-term Boltzmann equation solution [1] and Monte-Carlo simulation [31].

The relationship between the actual reduced electric field strength and effective reduced electric field for liquid argon are shown in Figure A.17. The largest difference between the two profiles occurs at the lowest field strengths, which then converge as the field increases as required. Again the effective field is generally greater than the actual, reflecting the mostly increased mean energy and drift velocity exhibited by swarm in the liquid phase in Figures A.8 and A.9, reflecting the enhanced efficiency of the field to pump energy into the swarm due to the reduced momentum exchange associated with coherent scattering.

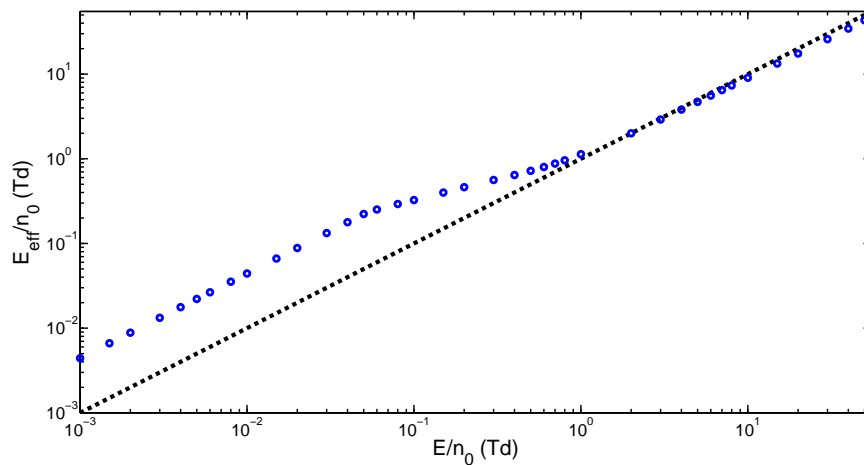


Figure A.17: Variation of the reduced effective electric field, E_{eff} , with reduced electric field, for dilute gaseous and liquid argon at 84 K. Fluid results are compared with those from a multi-term Boltzmann equation solution [1] and Monte-Carlo simulation [31].

Diffusion coefficients

The variation of the transverse and longitudinal diffusion coefficients with reduced electric field are detailed in Figures A.18 and A.19. Although the accuracy of these higher order quantities has decreased, the modified MTT approach still yields a good qualitative description of the liquid phase diffusion behaviour. Despite significant discrepancies between the predicted and expected transverse diffusion coefficients at high field strengths, the longitudinal diffusion coefficients do behave qualitatively well in this region. However, similar to the behaviour observed for the test hard-sphere situation, for regions in which NDC occurs, our low order MTT theory breaks down, as evident in Figure A.19. Extra correction terms may once again need to be included to account for this.

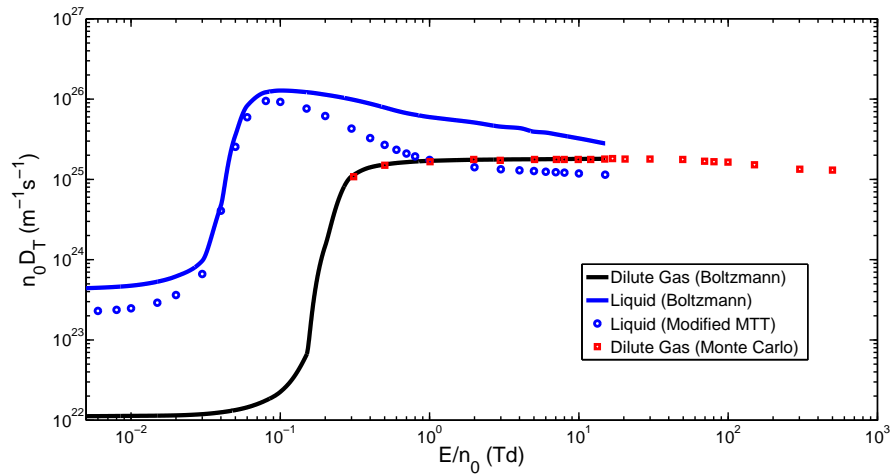


Figure A.18: Variation of the transverse diffusion coefficient with reduced electric field, for dilute gaseous and liquid argon at 84 K. Fluid results are compared with those from a multi-term Boltzmann equation solution [1] and Monte-Carlo simulation [31].

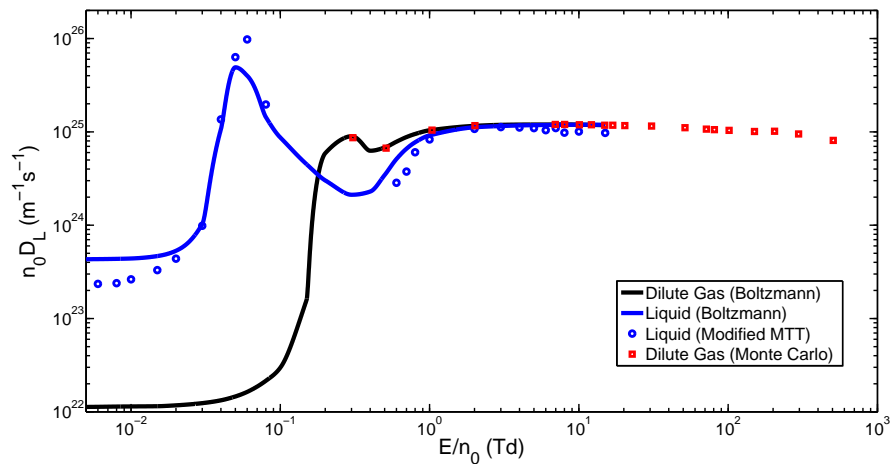


Figure A.19: Variation of the longitudinal diffusion coefficient with reduced electric field, for dilute gaseous and liquid argon at 84 K. Fluid results are compared with those from a multi-term Boltzmann equation solution [1] and Monte-Carlo simulation [31].

A.5 Summary

In this appendix, a fluid model has been developed primarily to gain physical insight as well as simplify computations, which generalizes many of the relations for dilute gas phase systems to soft-condensed systems, including the Wannier energy relation and the generalized Einstein relations for diffusion. We have applied these relations to a benchmark model and to positrons in liquid argon, and compared favourably the results with a full multi-term Boltzmann solution [1, 315]. The low-order momentum-transfer theory approximation was shown to break down in argon, and a modified approach was developed using simple relations that evaluate soft-condensed phase transport properties from a knowledge of transport properties in the dilute gas phase and structure factors for the medium. The modified fluid model relations provide excellent qualitative agreement and generally good quantitative agreement. Given the ease of implementation and ability to capitalize on existing transport literature, the fluid models developed will be beneficial tools for predicting the transport properties in soft-condensed matter from existing gas phase data.

References

- [1] R. D. White and R. E. Robson. Multiterm solution of a generalized Boltzmann kinetic equation for electron and positron transport in structured and soft condensed matter. *Phys. Rev. E*, **84**, 031125 (2011).
- [2] J. Lekner. Motion of electrons in liquid argon. *Phys. Rev.*, **158**, 130 (1967).
- [3] M. H. Cohen and J. Lekner. Theory of hot electrons in gases, liquids, and solids. *Phys. Rev.*, **158**, 305 (1967).
- [4] G. J. Boyle, R. D. White, R. E. Robson, S. Dujko, and Z. Lj. Petrović. On the approximation of transport properties in structured materials using momentum-transfer theory. *New J. Phys.*, **14**, 045011 (2012).
- [5] G. J. Boyle, M. J. E. Casey, R. D. White, Y. Cheng, and J. Mitroy. Transport properties of electron swarms in gaseous neon at low values of E/N. *J. Phys. D: Appl. Phys.*, **47**, 345203 (2014).
- [6] G. J. Boyle, M. J. E. Casey, R. D. White, and J. Mitroy. Transport theory for low-energy positron thermalization and annihilation in helium. *Phys. Rev. A*, **89**, 022712 (2014).
- [7] G. J. Boyle, W. J. Tattersall, D. G. Cocks, S. Dujko, and R. D. White. Kinetic theory of positron-impact ionization in gases. *Phys. Rev. A*, **91**, 052710 (2015).
- [8] G. J. Boyle, R. P. McEachran, D. G. Cocks, and R. D. White. Electron scattering and transport in liquid argon. *J. Chem. Phys.*, **142**, 154507 (2015).
- [9] W. J. Tattersall, D. G. Cocks, G. J. Boyle, S. J. Buckman, and R. D. White. Monte Carlo study of coherent scattering effects of low energy charged particle transport in Percus-Yevick liquids. *Phys. Rev. E*, **91**, 043304 (2015).
- [10] T. Koizumi, H. Murakoshi, S. Yamamoto, and I. Ogawa. The characteristic energy and momentum transfer cross section for low-energy electrons in neon. *J. Phys. B: At. Mol. Phys.*, **17**, 4387 (1984).
- [11] P. G. Coleman, T. C. Griffith, G. R. Heyland, and T. L. Killeen. Positron lifetime spectra for noble gases. *J. Phys. B: At. Mol. Phys.*, **8**, 1734 (1975).
- [12] R. I. Campeanu and J. W. Humberston. Diffusion of positrons in helium gas. *J. Phys. B: At. Mol. Phys.*, **10**, 239 (1977).
- [13] C. Y. Leung and D. A. L. Paul. Positron diffusion and annihilation in helium. *J. Phys. B: At. Mol. Phys.*, **2**, 1278 (1969).

- [14] G. F. Lee, P. H. R. Orth, and G. Jones. Electric field dependence of the annihilation rate of positrons in helium. *Phys. Lett. A*, **28**, 674 (1969).
- [15] S. A. Davies, M. Charlton, and T. C. Griffith. Free positron annihilation in gases under the influence of a static electric field. *J. Phys. B: At. Mol. Opt. Phys.*, **22**, 327 (1989).
- [16] B. Shizgal and K. Ness. Thermalisation and annihilation of positrons in helium and neon. *J. Phys. B: At. Mol. Phys.*, **20**, 847 (1987).
- [17] A. Kover and G. Laricchia. Triply differential study of positron impact ionization of H₂. *Phys. Rev. Lett.*, **80**, 5309 (1998).
- [18] S. J. Buckman, J. W. Cooper, M. T. Elford, and M. Inokuti. Momentum transfer cross sections. In *Photon and Electron Interactions with Atoms, Molecules and Ions*, edited by Y. Itikawa, volume 17A, 2–35. Springer, Darmstadt (2003).
- [19] J. B. Furness and I. E. McCarthy. Semiphenomenological optical model for electron scattering on atoms. *J. Phys. B*, **6**, 2280 (1973).
- [20] B. H. Bransden and C. J. Noble. Electron impact excitation of atomic hydrogen and hydrogenic ions. *J. Phys. B*, **9**, 1507 (1976).
- [21] J. Yarnell, M. Katz, R. Wenzel, and S. Koenig. Structure factor and radial distribution function for liquid argon at 85 K. *Phys. Rev. A*, **7**, 2130 (1973).
- [22] A. G. Robertson. Drift velocities of low energy electrons in argon at 293 and 90 K. *Aust. J. Phys.*, **30**, 39 (1977).
- [23] A. G. Robertson. Laplace Database. www.lxcat.net (1977). Accessed 29 January, 2015.
- [24] R. W. Warren and J. H. Parker. Ratio of the diffusion coefficient to the mobility coefficient for electrons in He, Ar, N₂, H₂, D₂, CO, and CO₂ at low temperatures and low E/p. *Phys. Rev.*, **128**, 2661 (1962).
- [25] R. W. Warren and J. H. Parker. Dutton Database. www.lxcat.net (1962). Accessed 29 January, 2015.
- [26] J. S. Townsend and V. A. Bailey. The motion of electrons in argon and in hydrogen. *Phil. Mag.*, **44**, 1033 (1922).
- [27] J. S. Townsend and V. A. Bailey. Dutton Database. www.lxcat.net (1922). Accessed 29 January, 2015.
- [28] L. Miller, S. Howe, and W. Spear. Charge transport in solid and liquid Ar, Kr, and Xe. *Phys. Rev.*, **166**, 871 (1968).
- [29] B. Halpern, J. Lekner, S. A. Rice, and R. Gomer. Drift velocity and energy of electrons in liquid argon. *Phys. Rev.*, **156**, 351 (1967).
- [30] E. Shibamura, T. Takahashi, S. Kubota, and T. Doke. Ratio of diffusion coefficient to mobility for electrons in liquid argon. *Phys. Rev. A*, **20**, 2547 (1979).
- [31] M. Suvakov, Z. Lj. Petrović, J. P. Marler, S. J. Buckman, R. E. Robson, and G. Malović. Monte Carlo simulation of non-conservative positron transport in pure argon. *New J. Phys.*, **10**, 053034 (2008).

- [32] R. D. White. *Multi-term solution of the Boltzmann equation for electron swarms in DC and AC electric fields*. Honours thesis, James Cook University, Australia (1993).
- [33] R. D. White. *Time-dependent multi-term solution of Boltzmann's equation for charged particle swarms in temporally varying electric fields*. Ph.D. thesis, James Cook University, Australia (1996).
- [34] K. F. Ness and R. E. Robson. Velocity distribution function and transport coefficients of electron swarms in gases. II. Moment equations and applications. *Phys. Rev. A*, **34**, 2185 (1986).
- [35] L. C. Pitchford, S. V. O'Neil, and J. R. Rumble. Extended Boltzmann analysis of electron swarm experiments. *Phys. Rev. A*, **23**, 294 (1981).
- [36] B. M. Penetrante, J. N. Bardsley, and L. C. Pitchford. Monte Carlo and Boltzmann calculations of the density gradient expanded energy distribution functions of electron swarms in gases. *J. Phys. D: Appl. Phys.*, **18**, 1087 (1985).
- [37] D. R. A. MacMahon. *Ion Diffusion Unit, Internal Rept. ANU (unpublished)* (1983).
- [38] P. Segur, M. Yousfi, and M. C. Bordage. Comparisons between different methods of solution of the Boltzmann equation adapted to the calculation of swarm parameters in a weakly ionised medium. *J. Phys. D: Appl. Phys.*, **17**, 2199 (1984).
- [39] I. D. Reid. An investigation of the accuracy of numerical solutions of Boltzmann's equation for electron swarms in gases with large inelastic cross sections. *Aust. J. Phys.*, **32**, 231 (1979).
- [40] G. L. Braglia, L. Romano, and M. Diligenti. Comment on "Comparative calculations of electron-swarm properties in N₂ at moderate E/N values". *Phys. Rev. A*, **26**, 3689 (1982).
- [41] T. Taniguchi, H. Tagashira, and Y. Sakai. Validity of a Boltzmann equation method for predicting the effect of ionization and attachment. *J. Phys. D: Appl. Phys.*, **10**, 2301 (1977).
- [42] J. Lucas and H.T. Saelee. A comparison of a Monte Carlo simulation and the Boltzmann solution for electron swarm motion in gases. *J. Phys. D: Appl. Phys.*, **8**, 640 (1975).
- [43] A. G. Robertson. The momentum transfer cross section for low energy electrons in neon. *J. Phys. B: At. Mol. Opt. Phys.*, **5**, 648 (1972).
- [44] J. Mitroy, M. S. Safronova, and C. W. Clark. Theory and applications of atomic and ionic polarizabilities. *J. Phys. B: At. Mol. Opt. Phys.*, **43**, 202001 (2010).
- [45] K. Becker, H. Deutsch, and M. Inokuti. Opportunities and challenges for atomic, molecular, and optical physics in plasma chemistry. *Adv. At. Mol. Opt. Phys.*, **43**, 399 (2000).
- [46] T. Makabe and Z. Lj. Petrović. *Plasma Electronics: Applications to Microelectronic Device Fabrication*. Taylor and Francis, New York (2006).
- [47] W. C. Röntgen. On a new kind of rays. *Science*, **3**, 227 (1896).
- [48] P. F. Dahl. *Flash of the Cathode Rays: A History of J J Thomson's Electron*. CRC Press, Boca Raton (1997).
- [49] L. B. Loeb. *Basic Processes of Gaseous Electronics*. University of California Press, Los Angeles (1955).

- [50] L. G. H. Huxley and R. W. Crompton. *The Drift and Diffusion of Electrons in Gases*. Wiley, New York (1974).
- [51] L. G. Christophorou and J. K. Olthoff. *Fundamental Electron Interactions with Plasma Processing Gases*. Physics of Atoms and Molecules. Springer Science & Business Media, New York (2004).
- [52] J. F. Ward. DNA damage produced by ionizing radiation in mammalian cells: Identities, mechanisms of formation, and reparability. In *Progress in Nucleic Acid Research and Molecular Biology*, volume 35, 95. Academic Press, San Diego (1988).
- [53] R. K. Sachs, P. L. Chen, P. J. Hahnfeldt, and L. R. Hlatky. DNA damage caused by ionizing radiation. *Math. Biosci.*, **112**, 271 (1992).
- [54] J. T. Bushberg, J. A. Siebert, E. M. Leidholdt Jr., and J. M. Boone. *The Essential Physics of Medical Imaging*. Lippincott Williams & Wilkins, Philadelphia (2002).
- [55] E. J. Hall and D. J. Brenner. Cancer risks from diagnostic radiology. *Brit. J. Radiol.*, **81**, 362 (2008).
- [56] I. Abril, R. Garcia-Molina, C. D. Denton, I. Kyriakou, and D. Emfietzoglou. Energy loss of hydrogen- and helium-ion beams in DNA: Calculations based on a realistic energy-loss function of the target. *Radiat. Res.*, **175**, 247 (2011).
- [57] V. Cobut, Y. Frongillo, J. P. Patau, T. Goulet, M. J. Fraser, and J. P. Jay-Gerin. Monte Carlo simulation of fast electron and proton tracks in liquid water - I. Physical and physicochemical aspects. *Rad. Phys. Chem.*, **51**, 229 (1998).
- [58] E. Surdutovich, O. I. Obolensky, E. Scifoni, I. Pshenichnov, I. Mishustin, A. V. Solov'yov, and W. Greiner. Ion-induced electron production in tissue-like media and DNA damage mechanisms. *Eur. Phys. J. D*, **51**, 63 (2009).
- [59] B. Boudaiffa, P. Cloutier, D. Hunting, M. A. Huels, and L. Sanche. Resonant formation of DNA strand breaks by low-energy (3 to 20 eV) electrons. *Science*, **287**, 1658 (2000).
- [60] F. Martin, P. D. Burrow, Z. Cai, P. Cloutier, D. Hunting, and L. Sanche. DNA strand breaks induced by 0-4 eV electrons: The role of shape resonances. *Phys. Rev. Lett.*, **93**, 068101 (2004).
- [61] R. Loevinger, T. F. Budinger, and E. E. Watson. *MIRD Primer for Absorbed Dose Calculations, Revised*. The Society of Nuclear Medicine, New York (1991).
- [62] W. J. Snyder, M. R. Ford, G. G. Warner, and B. B. Watson. Medical Internal Radiation Dose Committee (MIRD) Pamphlet No. 5. *J. Nucl. Med.*, **10**, 7 (1969).
- [63] M. G. Stabin. MIRDOSE: personal computer software for internal dose assessment in nuclear medicine. *J. Nucl. Med.*, **37**, 538–546 (1996).
- [64] M. G. Kong, G. Kroesen, G. Morfill, T. Nosenko, T. Shimizu, J. van Dijk, and J. L. Zimmermann. Plasma medicine: an introductory review. *New J. Phys.*, **11**, 115012 (2009).
- [65] W. Tian and M. J. Kushner. Atmospheric pressure dielectric barrier discharges interacting with liquid covered tissue. *J. Phys. D: Appl. Phys.*, **47**, 165201 (2014).

- [66] S. A. Norberg, W. Tian, E. Johnsen, and M. J. Kushner. Atmospheric pressure plasma jets interacting with liquid covered tissue: Touching and not-touching the liquid. *J. Phys. D: Appl. Phys.*, **47**, 475203 (2014).
- [67] C. Chen, D. X. Liu, Z. C. Liu, A. J. Yang, H. L. Chen, G. Shama, and M. G. Kong. A model of plasma-biofilm and plasma-tissue interactions at ambient pressure. *Plas. Chem. Plas. Proc.*, **34**, 403 (2014).
- [68] M. Laroussi. Non-thermal decontamination of biological media by atmospheric pressure plasmas: review, analysis and prospects. *IEEE Trans. Plasma Sci.*, **30**, 1409 (2002).
- [69] B. Halliwell and J. Gutteridge. *Free Radicals in Biology and Medicine (4th Ed.)*. Oxford University Press, Oxford (2007).
- [70] D. B. Graves. The emerging role of reactive oxygen and nitrogen species in redox biology and some implications for plasma applications to medicine and biology. *J. Phys. D: Appl. Phys.*, **45**, 263001 (2012).
- [71] D. B. Graves. Low temperature plasma biomedicine: A tutorial review. *Phys. Plasmas*, **21**, 080901 (2014).
- [72] R. E. Sladek and E. Stoffels. Deactivation of Escherichia coli by the plasma needle. *J. Phys. D: Appl. Phys.*, **38**, 1716 (2005).
- [73] H. W. Lee, G. J. Kim, J. M. Kim, J. K. Park, J. K. Lee, and G. C. Kim. Tooth bleaching with nonthermal atmospheric pressure plasma. *J. Endod.*, **35**, 587 (2009).
- [74] I. E. Kieft, E. P. van der Laan, and E. Stoffels. Electrical and optical characterization of the plasma needle. *New J. Phys.*, **6**, 149 (2004).
- [75] R. Foest, E. Kindel, A. Ohl, M. Stieber, and K. D. Weltmann. Non-thermal atmospheric pressure discharges for surface modification. *Plasma Phys. Control. Fusion*, **47**, B525 (2005).
- [76] K. D. Weltmann, R. Brandenburg, T. Woetke, J. Ehlbeck, R. Foest, M. Stieber, and E. Kindel. Antimicrobial treatment of heat sensitive products by miniaturized atmospheric pressure plasma jets (APPJs). *J. Phys. D: Appl. Phys.*, **41**, 194008 (2008).
- [77] K. D. Weltmann, R. Brandenburg, J. Ehlbeck, R. Foest, M. Stieber, and T. Woetke. Plasma decontamination at atmospheric pressure - basics and applications. *Proc. IEEE 35th Int. Conf. on Plasma Science* (2008).
- [78] J. L. Walsh and M. G. Kong. Contrasting characteristics of linear-field and cross-field atmospheric plasma jets. *Appl. Phys. Lett.*, **93**, 111501 (2008).
- [79] T. Shimizu, B. Steffes, R. Pompl, F. Jamitzky, W. Bunk, K. Ramrath, M. Georgi, W. Stolz, H.-U. Schmidt, T. Urayama, S. Fujii, and G. E. Morfill. Characterization of microwave plasma torch for decontamination. *Plasma Process Polym.*, **5**, 577 (2008).
- [80] A. V. Pipa, T. Bindemann, R. Foest, E. Kindel, J. Roepcke, and K. D. Weltmann. Non-thermal atmospheric pressure discharges for surface modification. *J. Phys. D: Appl. Phys.*, **41**, 194011 (2008).
- [81] T. Woedke, A. Kramer, and K. D. Weltmann. Plasma sterilization: what are the conditions to meet this claim? *Plasma Process Polym.*, **5**, 534 (2008).

- [82] S. Samukawa, M. Hori, S. Rauf, K. Tachibana, P. Bruggeman, G. Kroesen, et al. The 2012 plasma roadmap. *J. Phys. D: Appl. Phys.*, **45**, 253001 (2012).
- [83] M. J. Potter, R. Harrison, A. Ramsden, B. Bryan, P. Andrews, and D. Gault. Facial acne and fine lines: transforming patient outcomes with plasma skin regeneration. *Ann. Plast. Surg.*, **58**, 608 (2007).
- [84] S. Kilmer, R. Fitzpatrick, E. Bernstein, and D. Brown. Long term follow-up on the use of plasma skin regeneration (PSR) in full facial rejuvenation procedures. *Lasers Surg. Med.*, **36**, 22 (2005).
- [85] G. Farin and K. E. Grund. Technology of argon plasma coagulation with particular regard to endoscopic applications. *Endosc. Surg. Allied Technol.*, **2**, 71 (1994).
- [86] D. Dobrynin, G. Fridman, G. Friedman, and A. Fridman. Physical and biological mechanisms of direct plasma interaction with living tissue. *New J. Phys.*, **11**, 115020 (2009).
- [87] M. Witzke, P. Rumbach, D. B. Go, and R. M. Sankaran. Evidence for the electrolysis of water by plasmas formed at the surface of aqueous solutions. *J. Phys. D: Appl. Phys.*, **45**, 442001 (2012).
- [88] A. Marchionni. Status and new ideas regarding liquid argon detectors. *Ann. Rev. Nucl. Part. Sci.*, **63**, 269 (2013).
- [89] C. Regenfus and the ArDM collaboration. The Argon Dark Matter Experiment (ArDM). *J. Phys. Conf. Ser.*, **203**, 012024 (2010).
- [90] E. Aprile, J. Angle, F. Arneodo, L. Baudis, A. Bernstein, A. Bolozdynya, et al. Design and performance of the XENON10 dark matter experiment. *Astropart. Phys.*, **34**, 679 (2011).
- [91] G. J. Alner, H. M. Araújo, A. Bewick, C. Bungau, B. Camanzi, M. J. Carson, et al. First limits on WIMP nuclear recoil signals in ZEPLIN-II: A two-phase xenon detector for dark matter detection. *Astropart. Phys.*, **28**, 287 (2007).
- [92] B. Baller, C. Bromberg, N. Buchanan, F. Cavanna, H. Chen, E. Church, et al. Liquid argon time projection chamber research and development in the United States. *J. Instrum.*, **9**, T05005 (2014).
- [93] S. Amerio, S. Amoruso, M. Antonello, P. Aprili, M. Armenante, F. Arneodo, et al. Design, construction and tests of the ICARUS T600 detector. *Nucl. Instr. Meth. Phys. Res. A*, **527**, 329 (2004).
- [94] C. Rubbia, M. Antonello, P. Aprili, B. Baibussinov, M Baldo Ceolin, L. Barzé, et al. Underground operation of the ICARUS T600 LAr-TPC: first results. *J. Instrum.*, **6**, P07011 (2011).
- [95] The ATLAS collaboration. Monitoring and data quality assessment of the ATLAS liquid argon calorimeter. *J. Instrum.*, **9**, P07024 (2014).
- [96] S. Weinberg. *The quantum theory of fields, Volume 1: Foundations*. Cambridge University Press, Cambridge (1995).
- [97] P. A. M. Dirac. The quantum theory of the electron. *Proc. R. Soc. Lond. A.*, **117**, 610 (1928).

- [98] P. A. M. Dirac. A theory of electrons and protons. *Proc. R. Soc. Lond. A*, **126**, 360 (1930).
- [99] C. D. Anderson. The positive electron. *Phys. Rev.*, **43**, 491 (1933).
- [100] P. M. S. Blackett and G. P. S. Occhialini. Some photographs of the tracks of penetrating radiation. *Proc. Roy. Soc. Lond. A*, **139**, 699 (1933).
- [101] M. Charlton and J. W. Humberston. *Positron Physics, Volume II of Cambridge Monographs on Atomic, Molecular and Chemical Physics*. Cambridge University Press, Cambridge (2001).
- [102] K. Iwata, R. G. Greaves, T. J. Murphy, M. D. Tinkle, and C. M. Surko. Measurements of positron-annihilation rates on molecules. *Phys. Rev. A*, **51**, 473 (1995).
- [103] A. Ore and J. L. Powell. Three-photon annihilation of an electron-positron pair. *Phys. Rev.*, **75**, 1696 (1949).
- [104] S. DeBenedetti, C. E. Cowan, and W. R. Konneker. Angular distribution of annihilation radiation. *Phys. Rev.*, **76**, 440 (1949).
- [105] S. DeBenedetti, C. E. Cowan, W. R. Konneker, and H. Primakoff. On the angular distribution of two-photon annihilation radiation. *Phys. Rev.*, **77**, 205 (1950).
- [106] S. Mohorovičić. Möglichkeit neuer elemente und ihre bedeutung für die astrophysik. *Astronomische Nachrichten*, **253**, 94 (1934).
- [107] M. Deutsch. Evidence for the formation of positronium in gases. *Phys. Rev.*, **82**, 455 (1951).
- [108] S. G. Karsheboim. Precision study of positronium: testing bound state QED theory. *Int. J. Mod. Phys. A*, **19**, 3879 (2004).
- [109] A. Rich. Recent experimental advances in positronium research. *Rev. Mod. Phys.*, **53**, 127 (1981).
- [110] M. Charlton. Positron transport in gases. In *J. Phys.: Conf. Ser.*, volume 162, 012003. IOP Publishing (2009).
- [111] R. W. Siegel. Positron annihilation spectroscopy. *Ann. Rev. Mater. Sci.*, **10**, 393 (1980).
- [112] R. M. Moadel, R. H. Weldon, E. B. Katz, P. Lu, J. Mani, M. Stahl M. D. Blaufox, R. G. Pestell, M. J. Charron, and E. Dadachova. Positherapy: Targeted nuclear therapy of breast cancer with 18F-2-deoxy-2-fluoro-D-glucose. *Cancer Res.*, **65**, 698 (2005).
- [113] S. R. Cherry, J. A. Sorensen, and M. E. Phelps. *Physics in Nuclear Medicine*. Saunders, Philadelphia (2003).
- [114] J. Knuuti. Positron emission tomography-molecular imaging of biological processes. *International Congress Series*, **1265**, 248 (2004). Quantitation in Biomedical Imaging with PET and MRI. Proceedings of the International Workshop on Quantitation in Biomedical Imaging with PET and MRI.
- [115] J. G. Webster, J. W. Clark, M. R. Neuman, W. H. Olson, R. A. Peura, F. P. Primiano, M. P. Siedband, and L. A. Wheeler. *Medical Instrumentation*. John Wiley & Sons, Inc., New York (1998).
- [116] M. E. Juweid and B. D. Cheson. Positron-emission tomography and assessment of cancer therapy. *N. Eng. J. Med.*, **354**, 496 (2006).

- [117] G. L. Brownell, C. A. Burnham, C. W. Stearns, D. A. Chesler, A. L. Brownell, and M. R. Palmer. Developments in high resolution positron emission tomography at MGH. *Int. J. Imag. Sys. Tech.*, **2**, 207 (1989).
- [118] J. Wang and L. Maurer. Positron emission tomography: applications in drug discovery and drug development. *Curr. Top. in Med. Chem.*, **5**, 1053 (2005).
- [119] W. Vaalburg, N. H. Hendrikse, and E. F. de Vries. Drug development, radiolabelled drugs and PET. *Ann. Med.*, **31**, 432 (1999).
- [120] S. R. Cherry. Fundamentals of positron emission tomography and applications in preclinical drug development. *J. Clin. Pharmacol.*, **41**, 482 (2001).
- [121] P. Price. Monitoring response to treatment in the development of anticancer drugs using PET. *Nucl. Med. Biol.*, **27**, 691 (2000).
- [122] R. Katz, H. N. Wagner, M. Fauntleroy, T. Kuwert, and R. Frank. The use of imaging as biomarkers in drug development: Regulatory issues worldwide. *J. Clin. Pharmacol.*, **41**, 118S (2001).
- [123] J. S. Fowler, N. D. Volkow, G. J. Wang, Y. S. Ding, and S. L. Dewey. PET and drug research and development. *J. Nucl. Med.*, **40**, 1154 (1999).
- [124] W. M. Moses. Fundamental Limits of Spatial Resolution in PET. *Nucl. Instr. Meth. Phys. Res. A*, **21**, 648 (2012).
- [125] C. S. Levin and E. J. Hoffman. Calculation of positron range and its effect on the fundamental limit of positron emission tomography system spatial resolution. *Phys. Med. Biol.*, **44**, 781 (1998).
- [126] G. R. Massoumi, P. J. Schultz, W. N. Lennard, and J. Ociepa. Positron emission yields for encapsulated ^{22}Na sources. *Nucl. Instr. Meth. B*, **30**, 592 (1988).
- [127] S. V. Smith. Positrons as imaging agents and probes in nanotechnology. *J. Phys.: Conf. Ser.*, **185**, 012044 (2009).
- [128] B. J. Pichler, M. S. Judenhofer, and H. F. Wehri. PET/MRI hybrid imaging: devices and initial results. *Eur. Radiol.*, **18**, 1077 (2008).
- [129] N. Metropolis, N. Rosenbluth, M. Rosenbluth, A. Teller, and E. Teller. Equation of state calculations by fast computing machines. *J. Chem. Phys.*, **21**, 1087 (1953).
- [130] B. J. Alder and T. E. Wainwright. *Transport Processes in Statistical Mechanics: Proceedings of the International Symposium Held in Brussels, August 21-31, 1956*. Interscience Publishers Inc., New York (1958).
- [131] E. Cohen and W. Thirring. *The Boltzmann Equation: Theory and Applications*. Springer-Verlag, Wien New York (1973).
- [132] S. Agostinelli, J. Allison, K. Amako, J. Apostolakis, H. Araujo, P. Arce, et al. GEANT4 - a simulation toolkit. *Nucl. Instr. Meth. Phys. Res. A*, **506**, 250 (2003).
- [133] A. F. Bielajew, H. Hirayama, W. R. Nelson, and D. W. O. Rogers. History, overview and recent improvements of EGS4. Presented at Radiation Transport Calculations Using The EGS4, Capri, Italy, June 28 - July 1, 1194 (1994).

- [134] I. Kawrakow. Accurate condensed history Monte Carlo simulation of electron transport. I. EGSnrc, the new EGS4 version. *Med. Phys.*, **27**, 485 (2000).
- [135] J. A. Halbleib and T. A. Mehlhorn. ITS: The integrated TIGER series of coupled electron/photon Monte Carlo transport codes. Technical report, Sandia National Labs., Albuquerque, NM (USA) (1984).
- [136] F. B. Brown. MCNP - A general Monte Carlo N-particle transport code, version 5. *Los Alamos National Laboratory, Oak Ridge, TN* (2003).
- [137] F. Salvat, J. M. Fernandez-Varea, and J. Sempau. PENELOPE - A code system for Monte Carlo simulation of electron and photon transport. *OECD-Nuclear Energy Agency* (2003).
- [138] W. Friedland, P. Jacob, and P. Kundrat. Stochastic simulation of DNA double-strand break repair by non-homologous end joining based on track structure calculations. *Radiat. Res.*, **173**, 677 (2010).
- [139] C. Champion, C. Le Loirec, and B. Stosic. EPOTRAN: A full-differential Monte Carlo code for electron and positron transport in liquid and gaseous water. *Int. J. Radiat. Biol.*, **88**, 54 (2012).
- [140] A. Muñoz, J. M. Pérez, G. García, and F. Blanco. An approach to Monte Carlo simulation of low-energy electron and photon interactions in air. *Nucl. Instr. Meth. A*, **536**, 176 (2005).
- [141] A. Muñoz, F. Blanco, J. C. Oller, J. M. Pérez, and G. García. Energy deposition models at the molecular level in biological systems. *Adv. Quan. Chem.*, **52**, 21 (2007).
- [142] I. Buvat and I. Castiglioni. Monte Carlo simulations in SPET and PET. *Q. J. Nucl. Med.*, **46**, 48 (2002).
- [143] C. J. Thompson, J. M. Cantu, and Y. Picard. PETSIM: Monte Carlo program simulation of all sensitivity and resolution parameters of cylindrical positron imaging systems. *Phys. Med. Biol.*, **37**, 731 (1992).
- [144] S. Jan, G. Santin, D. Strul, S. Staelens, K. Assié, D. Autret, et al. GATE: a simulation toolkit for PET and SPECT. *Phys. Med. Biol.*, **49**, 4543 (2004).
- [145] H. Zaidi, C. Labbé, and C. Morel. EIDOLON: Implementation of an environment for Monte Carlo simulation of fully 3D positron tomography on a high performance parallel platform. *Parallel Comput.*, **24**, 1523 (1998).
- [146] I. Castiglioni, O. Cremonesi, M. C. Gilardi, V. Bettinardi, G. Rizzo, A. Savi, E. Bellotti, and F. Fazio. Scatter correction techniques in 3D PET: a Monte Carlo evaluation. *IEEE Trans. Nucl. Sci.*, **46**, 2053 (1999).
- [147] A. Reilhac, M. C. Gregoire, N. Costes, F. Lavenne, C. Pierre, A. Diou, and J. F. Pujol. A PET Monte Carlo simulator from numerical phantoms: validation against the EXACT ECAT HR+ scanner. *Proc. IEEE Nucl. Sci. Symp.*, 1527–1531 (1998).
- [148] G. Garcia, Z. Lj. Petrović, R. D. White, and S. Buckman. Monte Carlo model of positron transport in water: Track structures based on atomic and molecular scattering data for positrons. *IEEE Trans. Plasma Sci.*, **39**, 2962 (2011).

- [149] S. Dujko, R. D. White, and Z. Lj. Petrović. Monte Carlo studies of non-conservative electron transport in the steady-state Townsend experiment. *J. Phys. D: Appl. Phys.*, **41**, 245205 (2008).
- [150] Z. Lj. Petrović, S. Marjanović, S. Dujko, A. Banković, G. Malović, S. J. Buckman, G. García, R. D. White, and M. J. Brunger. On the use of Monte Carlo simulations to model transport of positrons in gases and liquids. *Appl. Radiat. Isot.*, **83**, 148 (2013).
- [151] S. Dujko, Z. M. Raspopović, R. D. White, T. Makabe, and Z. Lj. Petrović. Monte Carlo analysis of ionization effects on spatiotemporal electron swarm development. *Eur. Phys. J. D*, **68**, 166 (2014).
- [152] M. Inokuti. Inelastic collisions of fast charged particles with atoms and molecules - the Bethe theory revisited. *Rev. Mod. Phys.*, **43**, 297 (1971).
- [153] M. Inokuti and M. R. C. McDowell. Elastic scattering of fast electrons by atoms. I. Helium to neon. *J. Phys. B: Atom. Molec. Phys.*, **7**, 2382 (1974).
- [154] F. Manero, F. Blanco, and G. García. Electron-scattering cross sections of fluoromethanes in the energy range from 0.1 to 10 keV. *Phys. Rev. A*, **66**, 032714 (2002).
- [155] C. Le Loirec and C. Champion. Track structure simulation for positron emitters of medical interest. Part I: The case of the allowed decay isotopes. *Nucl. Instr. Meth. Phys. Res. B*, **582**, 644 (2007).
- [156] Z. Lj. Petrović, A. Banković, S. Dujko, S. Marjanović, G. Malović, J. P. Sullivan, and S. J. Buckman. Data for modeling of positron collisions and transport in gases. *AIP Conf. Proc.*, **1545**, 115 (2013).
- [157] Y. Sakai. Quasifree electron transport under electric field in nonpolar simple-structured condensed matters. *J. Phys. D: Appl. Phys.*, **40**, R441 (2007).
- [158] V. M. Atrazhev and I. T. Iakubov. The electron drift velocity in dense gases. *J. Phys. D: Appl. Phys.*, **10**, 2155 (1977).
- [159] A. Y. Polischuk. Theory of electron mobilities in dense gases with small polarizability. *Physica B+C*, **124**, 91 (1984).
- [160] A. G. Khrapak and I. T. Iakubov. Electrons and positrons in dense gases. *Usp. Fiz. Nauk.*, **45**, 129 (1979).
- [161] J. P. Hernandez. Electron self-trapping in liquids and dense gases. *Rev. Mod. Phys.*, **63**, 1007 (1991).
- [162] I. T. Iakubov. Excess electron coupled with dense gases and liquid. *Contrib. Plasma Phys.*, **33**, 544 (1993).
- [163] I. T. Iakubov and A. G. Khrapak. Self-trapped states of positrons and positronium in dense gases in liquids. *Rep. Prog. Phys.*, **45**, 697 (1982).
- [164] E. W. McDaniel and M. R. C. McDowell. *Case Studies in Atomic Collision Physics II*. North-Holland Publishing Company, Amsterdam (1972).
- [165] L. G. Christophorou and S. R. Hunter (Vol. 2). *Electron Molecule Interactions and their Applications*. Academic Press, New York (1984).

- [166] H. S. W. Massey, E. H. S. Burhop, and H. B. Gilbody. *Electronic and Ionic Impact Phenomena, Vol. 5*. University Press, Oxford (1974).
- [167] D. Griffiths. *Introduction to Elementary Particles*. John Wiley & Sons Inc., Toronto (1987).
- [168] S. J. Buckman, M. J. Brunger, D. S. Newman, G. Snitchler, S. Alston, D. W. Norcross, M. A. Morrison, B. C. Saha, G. Danby, and W. K. Trail. Near-threshold vibrational excitation of H₂ by electron impact: Resolution of discrepancies between experiment and theory. *Phys. Rev. Lett.*, **65**, 3253 (1990).
- [169] M. Charlton. Experimental studies of positron scattering in gases. *Rep. Prog. Phys.*, **48**, 737 (1985).
- [170] R. W. Crompton. Benchmark Measurements of Cross Sections for Electron Collisions: Electron Swarm Methods. *Adv. Atomic Molecular and Optical Physics*, **33**, 97 (1994).
- [171] Z. Lj. Petrović, M. Suvakov, Z. Nikitović, S. Dujko, O. Šašić, J. Jovanović, G. Malović, and V. Stojanović. *Plasma Sources Sci. Technol.*, **16**, S1 (2007).
- [172] M. Yamaji, Y. Nakamura, and Y. Morokuma. Measurements of ionization and attachment coefficients in 0.468% and 4.910% c-C₄F₈/Ar mixtures and pure c-C₄F₈. *J. Phys. D: Appl. Phys.*, **37**, 432 (2004).
- [173] Y. Nakamura. Drift velocity and longitudinal diffusion coefficient of electrons in nitrogen and carbon monoxide. *J. Phys. D: Appl. Phys.*, **20**, 933 (1987).
- [174] H. Date, K. Kondo, and H. Tagashira. Transport coefficients defined by arrival time spectra of electron swarms in krypton gas. *J. Phys. D: Appl. Phys.*, **23**, 1384 (1990).
- [175] H. Date, S. Yachi, K. Kondo, and H. Tagashira. Transport coefficients defined by arrival-time spectra of electron swarms in methane gas. *J. Phys. D: Appl. Phys.*, **25**, 42 (1992).
- [176] J. de Urquijo, C. A. Arriaga, C. Cisneros, and I. Alvarez. A time-resolved study of ionization, electron attachment and positive-ion drift in methane. *J. Phys. D: Appl. Phys.*, **32**, 41 (1999).
- [177] J. C. Bowe. Drift velocity of electrons in nitrogen, helium, neon, argon, krypton, and xenon. *Phys. Rev.*, **117**, 1411 (1960).
- [178] Y. Sakai, T. Okumura, and H. Tagashira. Measurement of electron impact ionisation and attachment coefficients in NO₂/He gas mixtures and estimated electron collision cross sections for no₂*. *Aust. J. Phys.*, **48**, 419 (1995).
- [179] Y. Sakai, S. Sawada, and H. Tagashira. Effect of Penning ionisation on the Townsend first ionisation coefficient of pulsed and steady-state Townsend experiments in Ar/Ne mixtures. *J. Phys. D: Appl. Phys.*, **19**, 2393 (1986).
- [180] G. Cavalleri, E. Gatti, and P. Principi. Experimental measurement of the diffusion coefficients for thermal electrons in pure neon. *Nuovo Cimento*, **31**, 318 (1964).
- [181] G. Cavalleri, E. Gatti, and A. M. Interlenghi. Improvements in the measurement of electron diffusion coefficients by the light chamber technique. *Nuovo Cimento B*, **40**, 450 (1965).
- [182] B. Schmidt, K. Berkhan, B. Götz, and M. Müller. New experimental techniques in the study of electron swarms in gases and their impact on the determination of low energy electron scattering cross sections. *Phys. Scr.*, **T53**, 30 (1994).

- [183] A. N. Goyette, J. de Urquijo, Y. Wang, L. G. Christophorou, and J. K. Olthoff. Electron transport, ionization, and attachment coefficients in C_2F_4 and C_2F_4/Ar mixtures. *J. Chem. Phys.*, **114**, 8932 (2001).
- [184] J. L. Hernandez-Avila, E. Basurto, and J. de Urquijo. Electron transport and swarm parameters in CO_2 and its mixtures with SF_6 . *J. Phys. D: Appl. Phys.*, **35**, 2264 (2002).
- [185] O. Šašić, J. V. Jovanović, Z. Lj. Petrović, J. de Urquijo, J. R. Castrejón-Pita, J. L. Hernández-Avila, and E. Basurto. Electron impact ionization and transport in nitrogen–argon mixtures. *Phys. Rev. E*, **71**, 046408 (2005).
- [186] J. V. Jovanović, O. Šašić, J. L. Hernández-Avila, Z. Lj. Petrović, and J. de Urquijo. Electron impact ionization and transport in nitrogen–argon mixtures. *J. Phys. D: Appl. Phys.*, **42**, 045202 (2009).
- [187] D. A. Dahl, T. H. Teich, and C. M. Franck. Obtaining precise electron swarm parameters from a pulsed townsend setup. *J. Phys. D: Appl. Phys.*, **45**, 485201 (2012).
- [188] D. A. Dahl and C. M. Franck. Response analysis of electron attachment rates to c_3f_8 and sf_6 in buffer gases. *J. Phys. D: Appl. Phys.*, **46**, 445202 (2013).
- [189] S. Kawaguchi, K. Satoh, and H. Itoh. Electron transport in CF_3I and CF_3I-N_3 mixtures*. *Eur. Phys. J. D*, **68**, 100 (2014).
- [190] T. C. Griffith and G. R. Heyland. Experimental aspects of the study of the interaction of low-energy positrons with gases. *Phys. Rep.*, **39**, 169 (1978).
- [191] J. W. Shearer and M. Deutsch. The lifetime of positronium in matter. *Phys. Rev.*, **76**, 462 (1949).
- [192] W. R. Falk and G. Jones. Experimental studies of the annihilation of positrons in the noble gases. *Can. J. Phys.*, **42**, 1751 (1964).
- [193] S. J. Tao, J. Bell, and J. H. Green. Fine structure in the delayed coincidence lifetime curves for positrons in argon. *Proc. Phys. Soc.*, **83**, 453 (1964).
- [194] D. A. L. Paul. The velocity-dependent annihilation rate of slow positrons in argon. *Proc. Phys. Soc.*, **84**, 563 (1964).
- [195] K. Wright. Chebyshev collocation methods for ordinary differential equations. *Comput. J.*, **6**, 358 (1964).
- [196] P. J. Curry and M. Charlton. Evidence for Ps formation in spurs in high-density gaseous CO_2 . *Chem. Phys.*, **95**, 313 (1985).
- [197] G. R. Heyland, M. Charlton, T. C. Griffith, and G. L. Wright. Positron lifetime spectra for gases. *Can. J. Phys.*, **60**, 503 (1982).
- [198] D. A. L. Paul and C. Y. Leung. On the thermalization times of positrons in polyatomic gases. *Can. J. Phys.*, **46**, 2779 (1968).
- [199] P. H. R. Orth and G. Jones. Annihilation of positrons in argon I. Experimental. *Phys. Rev.*, **183**, 7 (1969).
- [200] G. F. Lee and G. Jones. Electric field and temperature dependence of positron annihilation in argon gas. *Can. J. Phys.*, **52**, 17 (1974).

- [201] J. D. McNutt, V. B. Summerour, A. D. Ray, and P. H. Huang. Complex dependence of the positron annihilation rate on methane gas density and temperature. *J. Chem. Phys.*, **62**, 1777 (1975).
- [202] A. C. Mao and D. A. L. Paul. Positron annihilation in methane. *Can. J. Phys.*, **55**, 235 (1977).
- [203] P. M. Smith and D. A. L. Paul. Positron annihilation in methane gas. *Can. J. Phys.*, **48**, 2984 (1970).
- [204] E. A. G. Armour and D. J. Baker. An improved theoretical value for Z_{eff} for low-energy positron-hydrogen-molecule scattering. *J. Phys. B: At. Mol. Phys.*, **19**, L871 (1985).
- [205] T. J. Murphy and C. M. Surko. Positron trapping in an electrostatic well by inelastic collisions with nitrogen molecules. *Phys. Rev. A*, **46**, 5696 (1992).
- [206] R. G. Greaves, M. D. Tinkle, and C. M. Surko. Creation and uses of positron plasmas*. *Phys. Plasmas*, **1**, 1439 (1994).
- [207] D. A. L. Paul and J. S. Tsai. On the theory of positron drift in a uniform electric field. *Can. J. Phys.*, **57**, 1667 (1979).
- [208] D. A. L. Paul and N. Bose. Positron drift and diffusion in gases. In *Electron and Ion Swarms: Proceedings of the Second International Swarm Seminar, Oak Ridge, Tennessee, USA, July 22-23, 1981*, edited by L. G. Christophorou. Pergamon Press, Oxford (1982).
- [209] N. Bose, D. A. L. Paul, and J. S. Tsai. Positron drift in molecular hydrogen. *J. Phys. B: At. Mol. Phys.*, **14**, L227 (1981).
- [210] W. Schmidt. *Liquid state electronics of insulating liquids*. Taylor & Francis, Boca Raton (1997).
- [211] D. W. Swan. Drift velocity of electrons in liquid argon, and the influence of molecular impurities. *Proc. Phys. Soc.*, **83**, 659 (1964).
- [212] K. Yoshino, U. Sowada, and W. F. Schmidt. Effect of molecular solutes on the electron drift velocity in liquid Ar, Kr, and Xe. *Phys. Rev. A*, **14**, 438 (1976).
- [213] E. M. Gushchin, A. A. Kruglov, and I. M. Obodovsky. Dynamics of electrons in condensed argon and xenon. *Sov. Phys. JETP*, **82**, 1114 (1982).
- [214] H. Schnyders, S. A. Rice, and L. Meyer. Electron drift velocities in liquefied argon and krypton at low electric field strengths. *Phys. Rev.*, **150**, 127 (1966).
- [215] S. Kubota, T. Takahashi, and J. Ruan. Hot electron relaxation in solid and liquid argon, krypton and xenon. *J. Phys. Soc. Jpn.*, **51**, 3274 (1982).
- [216] L. G. Christophorou. Mobilities of slow electrons in low- and high-pressure gases and liquids. *Int. J. Radiat. Phys. Chem.*, **7**, 205 (1975).
- [217] J. M. Warman, U. Sowada, and D. A. Armstrong. Concerning the density and temperature dependence of the electron mobility in high-pressure CO_2 . *Chem. Phys. Lett.*, **82**, 458 (1981).
- [218] P. Krebs. Excess electrons as a probe for polar "fluid structure". *Chem. Phys. Lett.*, **70**, 465 (1980).

- [219] P. Krebs and M. Wantschik. Mobility of electrons in ammonia vapor at various densities. *J. Phys. Chem.*, **84**, 1155 (1980).
- [220] P. Krebs, V. Giraud, and M. Wantschik. Electron localization in dense ammonia vapor. *Phys. Rev. Lett.*, **44**, 211 (1980).
- [221] P. Krebs and M. Heintze. Migration of excess electrons in high density supercritical ammonia. *J. Chem. Phys.*, **76**, 5484 (1982).
- [222] V. Giraud and P. Krebs. The onset of electron localization in subcritical water vapor. *Chem. Phys. Lett.*, **86**, 85 (1982).
- [223] V. M. Atrazhev and E. G. Dmitriev. Hot electrons in atomic non-polar liquids with molecular impurities. *J. Phys. C: Solid State Phys.*, **19**, 4329 (1986).
- [224] D. A. L. Paul and R. L. Graham. Annihilation of positrons in liquid helium. *Phys. Rev.*, **106**, 16 (1957).
- [225] J. Wackerle and R. Stump. Annihilation of positrons in liquid helium. *Phys. Rev.*, **106**, 18 (1957).
- [226] T. B. Daniel and R. Stump. Positron annihilation in helium. *Phys. Rev.*, **115**, 1599 (1959).
- [227] P. Hautojarvi, M. T. Lojonen, and R. Rytola. Positronium bubble in liquid helium. *J. Phys. B: Appl. Phys.*, **9**, 411 (1976).
- [228] D. A. L. Paul. Long τ_2 lifetimes from positronium annihilations in liquid argon and liquid nitrogen. *Can. J. Phys.*, **36**, 640 (1958).
- [229] D. M. Spektor, D. A. L. Paul, and J. R. Stevens. Positron and positronium lifetimes in liquid argon. *Can. J. Phys.*, **49**, 939 (1971).
- [230] I. Pepe, D. A. L. Paul, J. Deutsch, and R. Prieels. Positronium formation in liquid nitrogen as a function of electric field. *J. Phys. B: At. Mol. Opt. Phys.*, **26**, L373 (1994).
- [231] I. Pepe, D. A. L. Paul, J. Steyaert, F. Gimeno-Nogues, J. Deutsch, and R. Prieels. Positron annihilation in liquid helium and liquid argon under an electric field. *J. Phys. B: At. Mol. Opt. Phys.*, **28**, 3643 (1995).
- [232] I. Pepe, D. A. L. Paul, F. Gimeno-Nogues, J. Deutsch, and R. Prieels. Positron annihilation in helium, argon and nitrogen liquids under an electric field. *Hyperfine Interact.*, **89**, 425 (1994).
- [233] N. N. Bogoliubov. Kinetic Equations. *Journal of Physics USSR*, **10**, 265 (1946).
- [234] M. Born and H. S. Green. *A General Kinetic Theory of Liquids*. Cambridge University Press, Cambridge (1949).
- [235] J. G. Kirkwood. The statistical mechanical theory of transport processes I. General theory. *J. Chem. Phys.*, **14**, 180 (1946).
- [236] J. G. Kirkwood. The statistical mechanical theory of transport processes II. Transport in gases. *J. Chem. Phys.*, **15**, 72 (1947).
- [237] J. Yvon. La theorie statistique des fluides. *Actualites Scientifiques et Industrielles*, **203** (1935).

- [238] L. Boltzmann. Weitere studien über das wärmeleichgewicht unter gasmolekülen. *Wiener Berichte*, **66**, 275 (1872).
- [239] C. Cercignani. *The Boltzmann Equation and Its Applications*. Springer-Verlag, New York (1988).
- [240] H. A. Lorentz. *The theory of electrons*. G.E. Stechert and Co., New York (1909).
- [241] F. B. Pidduck. The abnormal kinetic energy of an ion in a gas. *Proc. Roy. Soc. A*, **88**, 296 (1913).
- [242] F. B. Pidduck. A treatise on electricity. *Proc. Lond. Math. Soc.*, **15**, 89 (1916).
- [243] G. H. Wannier. The threshold law for single ionization of atoms or ions by electrons. *Phys. Rev.*, **90**, 817 (1953).
- [244] W. P. Allis. *Handbuch der Physik*, volume XXI. Springer-Verlag, Berlin (1956).
- [245] L. Waldmann. *Handbuch der Physik*, volume XII. Springer-Verlag, Berlin (1958).
- [246] S. Chapman and T. G. Cowling. *The Mathematical Theory of Non-Uniform Gases (2nd Ed.)* (1952).
- [247] K. F. Ness. Spherical-harmonics decomposition of the Boltzmann equation for charged-particle swarms in the presence of both electric and magnetic fields. *Phys. Rev. E*, **47**, 327 (1993).
- [248] R. D. White, K. F. Ness, and R. E. Robson. Development of swarm transport theory in radio-frequency electric and crossed electric and magnetic fields. *Appl. Surf. Sci.*, **192**, 26 (2002).
- [249] K. Kumar. The Chapman-Enskog solution of the Boltzmann equation: A reformulation in terms of irreducible tensors and matrices. *Aust. J. Phys.*, **20**, 205 (1967).
- [250] K. Kumar. Polynomial expansions in kinetic theory of gases. *Ann. Phys.*, **37**, 113 (1967).
- [251] L. A. Viehland and E. A. Mason. Gaseous ion mobility in electric fields of arbitrary strength. *Ann. Phys.*, **91**, 499 (1975).
- [252] L. A. Viehland and E. A. Mason. Gaseous ion mobility and diffusion in electric fields of arbitrary strength. *Ann. Phys.*, **110**, 287 (1978).
- [253] S. L. Lin, R. E. Robson, and E. A. Mason. Moment theory of electron drift and diffusion in neutral gases in an electrostatic field. *J. Chem. Phys.*, **71**, 3483 (1979).
- [254] R. D. White, K. F. Ness, R. E. Robson, and B. Li. Charged-particle transport in gases in electric and magnetic fields crossed at arbitrary angles: Multiterm solution of Boltzmann's equation. *Phys. Rev. E*, **60**, 2231 (1999).
- [255] K. Maeda and T. Makabe. Radiofrequency electron swarm transport in reactive gases and plasmas. *Phys. Scr.*, **T53**, 61 (1994).
- [256] K. Maeda and T. Makabe. Time-dependent RF swarm transport by direct numerical procedure of the Boltzmann equation. *Jap. J. Appl. Phys.*, **33**, 4173 (1994).

- [257] D. Loffhagen and R. Winkler. Time-dependent multi-term approximation of the velocity distribution in the temporal relaxation of plasma electrons. *J. Phys. D: Appl. Phys.*, **29**, 618 (1996).
- [258] F. Sigeneger and R. Winkler. Study of the electron kinetics in cylindrical hollow cathodes by a multi-term approach. *Eur. Phys. J. Appl. Phys.*, **19**, 211 (2002).
- [259] D. Trunec, Z. Bonaventura, and D. Necas. Solution of time-dependent Boltzmann equation for electrons in non-thermal plasma. *J. Phys. D: Appl. Phys.*, **39**, 2544 (2006).
- [260] L. C. Pitchford and A. V. Phelps. Comparative calculations of electron-swarm properties in N_2 at moderate E/N values. *Phys. Rev. A*, **25**, 540 (1982).
- [261] G. J. M. Hagelaar and L. C. Pitchford. Solving the Boltzmann equation to obtain electron transport coefficients and rate coefficients for fluid models. *Plasma Sources Sci. Technol.*, **14**, 722 (2005).
- [262] LXCat. www.lxcat.net.
- [263] K. Kumar, H. R. Skullerud, and R. E. Robson. Kinetic theory of charged particle swarms in neutral gases. *Aust. J. Phys.*, **33**, 343 (1980).
- [264] Y. Sakai, H. Tagashira, and S. Sakamoto. The development of electron avalanches in argon at high E/N values. I. Monte Carlo simulation. *J. Phys. D: Appl. Phys.*, **10**, 1035 (1977).
- [265] H. Tagashira, Y. Sakai, and S. Sakamoto. The development of electron avalanches in argon at high E/N values. II. Boltzmann equation analysis. *J. Phys. D: Appl. Phys.*, **10**, 1051 (1977).
- [266] S. B. Vrhovac and Z. L. Petrović. Momentum transfer theory of nonconservative charged particle transport in mixtures of gases: General equations and negative differential conductivity. *Phys. Rev. E*, **53**, 4012 (1996).
- [267] R. E. Robson. Generalized Einstein relation and negative differential conductivity in gases. *Aust. J. Phys.*, **37**, 35 (1984).
- [268] R. E. Robson, Z. Lj. Petrović, Z. M. Raspopović, and D. Loffhagen. Negative absolute electron mobility, Joule cooling and the second law. *J. Chem. Phys.*, **119**, 11249 (2003).
- [269] R. D. White, R. E. Robson, S. Dujko, P. Nicoletopoulos, and B. Li. Recent advances in the application of Boltzmann equation and fluid equation methods to charged particle transport in non-equilibrium plasmas. *J. Phys. D: Appl. Phys.*, **42**, 194001 (2009).
- [270] R. E. Robson, P. Nicoletopoulos, B. Li, and R. D. White. Kinetic theoretical and fluid modelling of plasmas and swarms: the big picture. *Plasma Sources Sci. Technol.*, **17**, 024020 (2008).
- [271] R. E. Robson and K. F. Ness. Velocity distribution function and transport coefficients of electron swarms in gases: Spherical-harmonics decomposition of Boltzmann's equation. *Phys. Rev. A*, **33**, 2068 (1986).
- [272] R. D. White, R. E. Robson, and K. F. Ness. Anomalous anisotropic diffusion of electron swarms in AC electric fields. *Aust. J. Phys.*, **48**, 925 (1995).

- [273] R. D. White, R. E. Robson, and K. F. Ness. Nonconservative charged-particle swarms in AC electric fields. *Phys. Rev. E*, **60**, 7457 (1999).
- [274] R. E. Robson, K. Maeda, T. Makabe, and R. D. White. Frequency variation of the mean energy of RF electron swarms. *Aust. J. Phys.*, **48**, 35 (1995).
- [275] S. Dujko, R. D. White, Z. Lj. Petrović, and R. E. Robson. Benchmark calculations of non-conservative charged-particle swarms in DC electric and magnetic fields crossed at arbitrary angles. *Phys. Rev. E*, **81**, 046403 (2010).
- [276] Z. Lj. Petrović, S. Dujko, D. Marić, G. Malović, Z. Nikitović, O. Šašić, J. Jovanović, V. Stojanović, and M. Radmilović-Radenović. Measurement and interpretation of swarm parameters and their application in plasma modelling. *J. Phys. D: Appl. Phys.*, **42**, 194002 (2009).
- [277] Z. Donko, P. Hartmann, and K. Kutasi. On the reliability of low-pressure DC glow discharge modelling. *Plasma Sources Sci. Technol.*, **15**, 178 (2006).
- [278] B. Li, R. D. White, and R. E. Robson. Spatially periodic structures in electron swarms: Ionization, NDC effects and multi-term analysis. *J. Phys. D: Appl. Phys.*, **35**, 1 (2002).
- [279] I. A. Porokhova, Y. B. Golubovskii, J. Bretagne, M. Tichy, and J. F. Behnke. Anisotropy of the electron component in a cylindrical magnetron discharge. I. Theory of the multiterm analysis. *Phys. Rev. E*, **71**, 066406 (2005).
- [280] I. A. Porokhova, Y. B. Golubovskii, J. Bretagne, M. Tichy, and J. F. Behnke. Anisotropy of the electron component in a cylindrical magnetron discharge. II. Application to real magnetron discharge. *Phys. Rev. E*, **71**, 066407 (2005).
- [281] J. Frank and G. Hertz. Über die erregung der quecksilberresonanzlinie 253.6 durch elektronenstöße. *Verh. Deutsche Phys. Ges.*, **16**, 512 (1914).
- [282] R. E. Robson, B. Li, and R. D. White. Spatially periodic structures in electron swarms and the Franck-Hertz experiment. *J. Phys. B: At. Mol. Opt. Phys.*, **33**, 507 (2000).
- [283] P. M. Morse, W. P. Allis, and E. S. Lamar. Velocity distributions for elastically colliding electrons. *Phys. Rev.*, **48**, 412 (1935).
- [284] R. W. L. Thomas and W. R. L. Thomas. Monte Carlo simulation of electrical discharges in gases. *J. Phys. B: At. Mol. Phys.*, **2**, 562 (1969).
- [285] P. Segur and R. Keller. A numerical method of solution of the Boltzmann equation in a weakly ionized heterogeneous gas. *J. Comput. Phys.*, **24**, 43 (1977).
- [286] P. Segur, M. C. Bordage, J. P. Balaguer, and M. Yousfi. The application of a modified form of the s_n method to the calculation of swarm parameters of electrons in a weakly ionised equilibrium medium. *J. Comput. Phys.*, **50**, 116 (1983).
- [287] P. Segur, A. Alkaa, S. Pineau, A. Zaharaoui, A. Chouki, C. Moutarde, and S. Laffront. Kinetic description of electrons in inhomogeneous electric fields. *Plasma Sources Sci. Technol.*, **4**, 183 (1995).
- [288] J. V. Dicarlo and M. J. Kushner. Solving the spatially dependent Boltzmann's equation for the electron-velocity distribution using flux corrected transport. *J. Appl. Phys.*, **66**, 5763 (1989).

- [289] M. J. Kushner and M. J. Hartig. Radially dependent solutions of Boltzmann's equation in low-temperature plasmas using a modified two-term expansion. *J. Appl. Phys.*, **73**, 1080 (1993).
- [290] R. Winkler and F. Sigeneger. Relaxation of the electron gas in spatially decaying plasmas. *J. Phys. D: Appl. Phys.*, **34**, 3407 (2001).
- [291] R. Winkler, F. Sigeneger, and D. Uhrlandt. Nonlocal behaviour of the electron component in nonequilibrium plasmas. *Pure Appl. Chem.*, **68**, 1065 (1996).
- [292] F. Sigeneger and R. Winkler. Spatial electron relaxation in nonisothermal plasmas. *Plasma Chem. Plasma Process.*, **17**, 1 (1997).
- [293] R. Winkler, G. Petrov, F. Sigeneger, and D. Uhrlandt. Strict calculation of electron energy distribution functions in inhomogeneous plasmas. *Plasma Sources Sci. Technol.*, **6**, 118 (1997).
- [294] D. Loffhagen, F. Sigeneger, and R. Winkler. Spatial transition of the electron gas from the active to the remote plasma state. *Plasma Chem. Plasma Process.*, **23**, 415 (2003).
- [295] F. Sigeneger, Y. B. Golubovskii, I. A. Porokhova, and R. Winkler. On the nonlocal electron kinetics in s-and p-striations of DC glow discharge plasmas: I. Electron establishment in striation-like fields. *Plasma Chem. Plasma Process.*, **18**, 153 (1998).
- [296] F. Sigeneger and R. Winkler. On the nonlocal electron kinetics in s and p striations of DC glow discharge plasmas: II. Electron properties in periodic states. *Plasma Chem. Plasma Process.*, **20**, 429 (2000).
- [297] F. Sigeneger, G. I. Sukhinin, and R. Winkler. Kinetics of the electrons in striations of spherical glow discharges. *Plasma Chem. and Plasma Process.*, **20**, 87 (2000).
- [298] Y. B. Golubovskii, R. V. Kozakov, V. A. Maiorov, J. Behnke, and J. F. Behnke. Nonlocal electron kinetics and densities of excited atoms in S and P striations. *Phys. Rev. E*, **62**, 2707 (2000).
- [299] Y. B. Golubovskii, A. Y. Skoblo, V. A. Maiorov, and V. O. Nekutchayev. On the formation of electron velocity distribution functions in striation-like fields. *Plasma Sources Sci. Technol.*, **11**, 309 (2002).
- [300] Y. B. Golubovskii, I. A. Porokhova, J. Behnke, and V. O. Nekutchayev. On the bunching effect of electrons in spatially periodic resonance fields. *J. Phys. D: Appl. Phys.*, **31**, 2447 (1998).
- [301] Y. B. Golubovskii, V. A. Maiorov, I. A. Porokhova, and J. Behnke. On the non-local electron kinetics in spatially periodic striation-like fields. *J. Phys. D: Appl. Phys.*, **32**, 1391 (1999).
- [302] B. Li. *Hydrodynamic and non-hydrodynamic charged particle swarms*. Ph.D. thesis, James Cook University (1999).
- [303] B. Li, R. E. Robson, and R. D. White. Magnetic field effects on spatial relaxation of swarm particles in the idealized steady-state Townsend experiment. *Phys. Rev. E*, **74**, 026405 (2006).
- [304] W. J. Goedheer and P. M. Meijer. Numerical simulation of RF discharges for plasma processing. *J. Nucl. Mater.*, **200**, 282 (1993).

- [305] M. O. M. Mahmoud and M. Yousfi. Boltzmann equation analysis of spatiotemporal electron swarm development. *J. Appl. Phys.*, **81**, 5935 (1997).
- [306] D. Loffhagen and R. Winkler. Spatiotemporal relaxation of electrons in non-isothermal plasmas. *J. Phys. D: Appl. Phys.*, **34**, 1355 (2001).
- [307] A. F. Borghesani. Electron and ion transport in dense rare gases. *IEEE Trans. Dielectr. Electr. Insul.*, **13**, 492 (2006).
- [308] G. Braglia and V. Dallacasa. Theory of electron mobility in dense gases. *Phys. Rev. A*, **26**, 902 (1982).
- [309] V. M. Atrazhev and I. T. Iakubov. Hot electrons in non-polar liquids. *J. Phys. C: Solid State Phys.*, **14**, 5139 (1981).
- [310] V. M. Atrazhev, I. T. Iakubov, and V. V. Pogosov. Evolution of the Ramsauer effect on scattering of electrons in liquids. *Phys. Lett. A*, **204**, 393 (1995).
- [311] V. M. Atrazhev and I. V. Timoshkin. Electron scattering by a cut-off atomic potential: Application to electron properties in atomic liquids. *Phys. Rev. B*, **54**, 11252 (1996).
- [312] V. M. Atrazhev and I. V. Timoshkin. Transport of electrons in atomic liquids in high electric fields. *IEEE Trans. Dielectr. Electr. Insul.*, **5**, 450 (1998).
- [313] M. Lax. Multiple scattering of waves. *Rev. Mod. Phys.*, **23**, 287 (1951).
- [314] L. Van Hove. Correlations in space and time and Born approximation scattering in systems of interacting particles. *Phys. Rev.*, **95**, 249 (1954).
- [315] R. D. White and R. E. Robson. Positron kinetics in soft condensed matter. *Phys. Rev. Lett.*, **102**, 230602 (2009).
- [316] A. V. Vasenkov and M. J. Kushner. Angular anisotropy of electron energy distributions in inductively coupled plasmas. *J. Appl. Phys.*, **94**, 5522 (2003).
- [317] H. Sugawara, Y. Sakai, and H. Tagashira. Analyses of electron swarms in gases under steady-state Townsend conditions. *J. Phys. D: Appl. Phys.*, **27**, 90 (1994).
- [318] H. Sugawara, Y. Sakai, and H. Tagashira. Position-dependent electron swarm behaviour in steady-state Townsend discharges. *J. Phys. D: Appl. Phys.*, **25**, 1483 (1992).
- [319] Y. Sakai, K. Sukegawa, S. Nakamura, and H. Tagashira. Monte Carlo simulation of electron transport behavior in liquid argon. *IEEE Trans. Elec. Ins.*, **23**, 609 (1988).
- [320] Z. Donko. Particle simulation methods for studies of low-pressure plasma sources. *Plasma Sources Sci. Technol.*, **20**, 024001 (2011).
- [321] T. J. Sommerer, W. N. G. Hitchon, and J. E. Lawler. Electron heating mechanisms in helium rf glow discharges: A self-consistent kinetic calculation. *Phys. Rev. Lett.*, **63**, 2361 (1989).
- [322] A. Bogaerts, R. Gijbels, and W. Goedheer. Hybrid modeling of a capacitively coupled radio frequency glow discharge in argon: Combined Monte Carlo and fluid model. *Jpn. J. Appl. Phys.*, **38**, 4404 (1999).
- [323] E. E. Kunhardt. Electron kinetics in simple liquids at high electric fields. *Phys. Rev. B*, **44**, 4235 (1991).

- [324] H. M. Jones and E. E. Kunhardt. Monte Carlo investigation of electron-impact ionization in liquid xenon. *Phys. Rev. B*, **48**, 9382 (1993).
- [325] E. E. Kunhardt and Y. Tzeng. Monte Carlo technique for simulating the evolution of an assembly of particles increasing in number. *J. Comp. Phys.*, **67**, 279 (1986).
- [326] M. Wojcik and M. Tachiya. Electron transport and electron-ion recombination in liquid argon: simulation based on the Cohen-Lekner theory. *Chem. Phys. Lett.*, **363**, 381 (2002).
- [327] E. A. Mason and E. W. McDaniel. *Transport Properties of Ions in Gases*. Wiley, New York (1988).
- [328] R. E. Robson. *Introductory Transport Theory for Charged Particles in Gases*. World Scientific, Singapore (2006).
- [329] J. W. Gibbs. *Elementary Principles in Statistical Mechanics*. Scribner, New York (1902).
- [330] R. E. Robson, R. Winkler, and F. Sigener. Multiterm spherical tensor representation of Boltzmann's equation for a nonhydrodynamic weakly ionized plasma. *Phys. Rev. E*, **65**, 056410 (2002).
- [331] U. Fano and G. Racah. *Irreducible Tensorial Sets*. Academic Press, New York (1959).
- [332] M. Abramowitz and I. A. Stegun. *Handbook of Mathematical Functions*. Dover Publications Inc., New York (1972).
- [333] J. P. Hansen and I. R. McDonald. *Theory of Simple Liquids (2nd Edition)*. Academic Press Limited, San Diego (1990).
- [334] H. Goldstein. *Classical Mechanics*. Addison Wesley, San Francisco (2002).
- [335] F. B. Pidduck. Energy distribution of electrons in a gas. *Q. J. Math.*, **7**, 199 (1936).
- [336] B. I. Davydov. Uber Die Geschwindigkeitsverteilung Der Sich Im Elektrischen Felde Bewegenden Elektronen. *Phys. Z. Sowj. Un.*, **8**, 59 (1935).
- [337] C. S. Wang-Chang, G. E. Uhlenbeck, and J. DeBoer. In *Studies in Statistical Mechanics*, volume II, 241. Wiley, New York (1964).
- [338] L. S. Frost and A. V. Phelps. Rotational excitation and momentum transfer cross sections for electrons in H₂ and N₂ from transport coefficients. *Phys. Rev.*, **127**, 1621 (1962).
- [339] T. Holstein. Energy distribution of electrons in high frequency gas discharges. *Phys. Rev.*, **70**, 367 (1946).
- [340] D. V. Schroeder. *An Introduction to Thermal Physics*. Addison Wesley Longman, San Francisco (2000).
- [341] A. Hochstim. *Kinetic Processes in Gases and Plasmas*. Academic Press, New York (1969).
- [342] K. F. Ness. *Kinetic Theory for Charged Particle Swarms in Gases with Application to Electron*. Ph.D. thesis, James Cook University, Australia (1985).
- [343] J. P. Marler, Z. Lj. Petrović, A. Banković, S. Dujko, M. Suvakov, G. Malović, and S. J. Buckman. Positron transport: The plasma-gas interface. *Phys. Plasmas*, **16**, 057101 (2009).

- [344] A. Banković, S. Dujko, R. D. White, S. J. Buckman, S. Marjanović, G. Malović, G. García, and Z. Lj. Petrović. Positron transport in water vapour. *New J. Phys.*, **14**, 035003 (2012).
- [345] A. Banković, S. Dujko, R. D. White, S. J. Buckman, and Z. Lj. Petrović. Monte Carlo simulation and Boltzmann equation analysis of non-conservative positron transport in H₂. *Nucl. Instr. Meth. Phys. Res. B*, **279**, 92 (2012).
- [346] J. S. Townsend. *Electricity in Gases*. Oxford University Press, London (1915).
- [347] L. G. H. Huxley. XXXVI. The lateral diffusion of a stream of ions in a gas. *Phil. Mag.*, **30**, 396 (1940).
- [348] G. Cavalleri. Measurements of lateral diffusion coefficients and first Townsend coefficients for electrons in helium by an electron-density sampling method. *Phys. Rev.*, **179**, 186 (1969).
- [349] R. E. Robson. Transport phenomena in the presence of reactions: Definition and measurement of transport coefficients. *Aust. J. Phys.*, **44**, 685 (1991).
- [350] N. A. Dyatko, A. P. Napartovich, Z. Lj. Petrović, and Z. M. Raspopović. On the possibility of negative electron mobility in a decaying plasma. *J. Phys. D: Appl. Phys.*, **33**, 375 (2000).
- [351] S. Dujko, Z. Raspopović, Z. Lj. Petrović, and T. Makabe. Negative mobilities of electrons in radio frequency fields. *IEEE Trans. Plasma Sci.*, **31**, 711 (2003).
- [352] D. Blake and R. E. Robson. Negative differential conductivity in gases: The “true origin”. *J. Phys. Soc. Jpn.*, **70**, 3556 (2001).
- [353] R. Winkler, G. L. Braglia, A. Hess, and J. Wilhelm. Fundamentals of a technique for determining electron distribution functions by multi-term even-order expansion in Legendre polynomials 1. Theory. *Beitr. Plasmaphys.*, **24**, 657 (1984).
- [354] H. Leyh, D. Loffhagen, and R. Winkler. A new multi-term solution technique for the electron Boltzmann equation of weakly ionized steady-state plasmas. *Comp. Phys. Comm.*, **113**, 33 (1998).
- [355] L. Pareschi and G. Russo. Numerical solution of the Boltzmann equation I. Spectrally accurate approximation of the collision operator. *SIAM J. Numer. Anal.*, **37**, 1217 (2000).
- [356] J. G. Verwer and B. Sportisse. A note on operator splitting analysis in the stiff linear case. *Technical Report MAS-R9830, CWI* (1998).
- [357] R. J. LeVeque. *Finite Difference Methods for Ordinary and Partial Differential Equations*. SIAM, Philadelphia (2007).
- [358] T. Liszka and J. Orkisz. The finite difference method at arbitrary irregular grids and its application in applied mechanics. *Comput. Struct.*, **11**, 83 (1980).
- [359] H. Johansen and P. Colella. A cartesian grid embedded boundary method for Poisson’s equation on irregular domains. *J. Comput. Phys.*, **147**, 60 (1998).
- [360] S. K. Lele. Compact finite difference schemes with spectral-like resolution. *J. Comp. Phys.*, **103**, 16 (1992).
- [361] A. Harten, J. M. Hyman, P. D. Lax, and B. Keyfitz. On finite-difference approximations and entropy conditions for shocks. *Commun. Pure Appl. Math.*, **29**, 297 (1976).

- [362] S. O. Unverdi and G. Tryggvason. A front-tracking method for viscous, incompressible, multi-fluid flows. *J. Comput. Phys.*, **100**, 25 (1992).
- [363] D. Gottlieb and S. A. Orszag. *Numerical Analysis of Spectral Methods: Theory and Applications*. Society for Industrial and Applied Mathematics (1977).
- [364] C. Canuto, M. Y. Hussaini, A. Quarteroni, and T. A. Zhang. *Spectral Methods in Fluid Dynamics*. Springer-Verlag, Heidelberg (1988).
- [365] J. P. Boyd. *Chebyshev and Fourier Spectral Methods Second Edition*. Dover Publications Inc., Mineola (2001).
- [366] N. L. Trefethen. *Spectral Methods in MATLAB*. SIAM, Philadelphia (2000).
- [367] B. Fornberg. *A Practical Guide to Pseudospectral Methods*. Cambridge University Press, Cambridge (1998).
- [368] N. Kovvali. *Theory and Applications of Gaussian Quadrature Methods*. Morgan and Claypool, San Rafael (2011).
- [369] K. Ito. *Encyclopedic dictionary of mathematics*. MIT Press, Cambridge (1993).
- [370] R. E. Robson and A. Prytz. The discrete ordinate/pseudo-spectral method: Review and application from a physicist's perspective. *Aust. J. Phys.*, **46**, 465 (1993).
- [371] J. C. Slater. Electronic energy bands in metal. *Phys. Rev.*, **45**, 794 (1934).
- [372] L. V. Kantorović. On a new method of approximate solution of partial differential equations. *Dokl. Akad. Nauk SSSR*, **4**, 532 (1934).
- [373] C. Lanczos. Trigonometric interpolation of empirical and analytical functions. *J. Math. Phys.*, **17**, 123 (1938).
- [374] C. W. Clenshaw. The numerical solution of linear differential equations in Chebyshev series. *Math. Proc. Cambridge Philos. Soc.*, **53**, 134 (1957).
- [375] S. A. Orszag. Comparison of pseudospectral and spectral approximations. *Stud. Appl. Math.*, **50**, 293 (1972).
- [376] B. Shizgal. A Gaussian quadrature procedure for use in the solution of the Boltzmann equation and related problems. *J. Comput. Phys.*, **41**, 309 (1981).
- [377] B. Shizgal and R. Blackmore. A discrete ordinate method of solution of linear boundary value and eigenvalue problems. *J. Comput. Phys.*, **55**, 313 (1984).
- [378] B. Shizgal and T. Nishigori. A uniform WKB approach to electron thermalization in gases. *Chem. Phys. Lett.*, **171**, 493 (1990).
- [379] B. A. Finlayson and L. E. Scriven. The method of weighted residuals - a review. *Appl. Mech. Rev.*, **19**, 735 (1966).
- [380] R. Eymard, T. R. Gallouët, and R. Herbin. Finite volume methods. *Handb. Numer. Anal.*, **7**, 713 (2000).
- [381] G. Strang and G. Fix. *An Analysis of The Finite Element Method*. Prentice Hall, Englewood Cliffs (1973).

- [382] J. C. Strikwerda. *Finite Difference Schemes and Partial Differential Equations*. Chapman and Hall, New York (1989).
- [383] J. P. Boyd. *Chebyshev and Fourier Spectral Methods (Lecture Notes in Engineering)*. Springer-Verlag, Heidelberg (1989).
- [384] N. D. Jewell. *The Development and Stability of Some Non-Planar Boundary-Layer Flows*. Ph.D. thesis, University of Adelaide, Australia (2009).
- [385] G. W. Stewart. *Afternotes on Numerical Analysis*. SIAM, Philadelphia (1996).
- [386] J. Berrut and N. Trefethen. Barycentric Lagrange interpolation. *SIAM Review*, **46**, 501 (2004).
- [387] E. Weisstein. *CRC Concise Encyclopedia of Mathematics, 2nd Ed.* CRC Press, Boca Raton (2003).
- [388] J. Shen. Stable and efficient spectral methods in unbounded domains using Laguerre functions. *SIAM J. Num. Anal.*, **38**, 1113 (2000).
- [389] B. Fornberg. *A Practical Guide to Pseudospectral Methods*. Cambridge University Press, Cambridge (1996).
- [390] R. L. Burden and J. D. Faires. *Numerical Analysis (3rd Ed.)*. Prindle, Weber and Schmidt, Boston (1985).
- [391] J. Parker. Position- and time-dependent diffusion modes for electrons in gases. *Phys. Rev.*, **139**, A1792 (1965).
- [392] N. L. Trefethen and D. Bau. *Numerical Linear Algebra*. SIAM, Philadelphia (1997).
- [393] G. H. Golub and C. F. Van Loan. *Matrix Computations*. JHU Press, Maryland (2013).
- [394] R. B. Lehoucq, D. C. Sorenson, and C. Yang. *ARPACK Users Guide: Solution of Large-Scale Eigenvalue Problems with Implicitly Restarted Arnoldi Methods*. SIAM, Philadelphia (1998).
- [395] S. A. Orszag. Accurate solution of the Orr-Sommerfeld stability equation. *J. Fluid Mech.*, **50**, 689 (1971).
- [396] R. Sincovec, A. Erisman, E. Yip, and M. Epton. Analysis of descriptor systems using numerical algorithms. *J. Fluid Mech.*, **26**, 139 (1981).
- [397] M. L. Manning, B. Bamieh, and J. M. Carlson. Descriptor approach for eliminating spurious eigenvalues in hydrodynamic equations. *arXiv preprint arXiv:0705.1542* (2008).
- [398] W. E. Schiesser. *Partial Differential Equation Analysis in Biomedical Engineering: Case Studies with Matlab*. Cambridge University Press, Cambridge (2012).
- [399] W. E. Schiesser. *The Numerical Method of Lines*. Academic Press, San Diego (1991).
- [400] L. F. Shampine. ODE solvers and the method of lines. *Numer. Meth. Part. D. E.*, **10**, 739 (2005).
- [401] M. N. O. Sadiku and C. N. Obiozor. A simple introduction to the method of lines. *Int. J. Elec. Eng. Educ.*, **37**, 282 (2000).

- [402] M. B. Carver and H. W. Hinds. The method of lines and the advection equation. *Simulation*, **31**, 59 (1978).
- [403] J. C. Butcher. *Numerical Methods for Ordinary Differential Equations*. John Wiley and Sons, Inc., New Jersey (2003).
- [404] R. E. Robson. Physics of reacting particle swarms in gases. *J. Chem. Phys.*, **85**, 4486 (1986).
- [405] E. Hewitt and R. Hewitt. The Gibbs-Wilbraham phenomenon: An episode in Fourier analysis. *Arch. Hist. Exact Sci.*, **21**, 129 (1979).
- [406] D. Loffhagen, F. Sigeneger, and R. Winkler. Study of the electron kinetics in the anode region of a glow discharge by a multiterm approach and Monte Carlo simulations. *J. Phys. D: Appl. Phys.*, **35**, 1768 (2002).
- [407] R. Winkler, D. Loffhagen, and F. Sigeneger. Temporal and spatial relaxation of electrons in low temperature plasmas. *Appl. Surf. Sci.*, **192**, 50 (2002).
- [408] F. Sigeneger, N. A. Dyatko, and R. Winkler. Spatial electron relaxation: Comparison of Monte Carlo and Boltzmann equation results. *Plasma Chem. Plasma Process.*, **23**, 103 (2003).
- [409] M. Wertheim. Exact solution of the Percus-Yevick integral equation for hard spheres. *Phys. Rev. Lett.*, **10**, 321 (1963).
- [410] E. Thiele. Equation of state for hard spheres. *J. Chem. Phys.*, **39**, 474 (1963).
- [411] L. Verlet and J.-J. Weis. Equilibrium theory of simple liquids. *Phys. Rev. A*, **5**, 939 (1972).
- [412] W. Meegen and P. Pusey. Dynamic light-scattering study of the glass transition in a colloidal suspension. *Phys. Rev. A*, **43**, 5429 (1991).
- [413] E. Koehler, E. Brown, and S. J.-P. A. Haneuse. On the assessment of Monte Carlo error in simulation-based statistical analyses. *Am. Stat.*, **63**, 155 (2009).
- [414] Z. Lj. Petrović, R. W. Crompton, and G. N. Haddad. Model calculations of negative differential conductivity in gases. *Aust. J. Phys.*, **37**, 23 (1984).
- [415] S. J. Buckman and M. J. Brunger. A critical comparison of electron scattering cross sections measured by single collision and swarm experiments. *Aust. J. Phys.*, **50**, 483 (1997).
- [416] L. L. Alves, K. Bartschat, S. F. Biagi, M. C. Bordage, L. C. Pitchford, C. M. Ferreira, G. J. M. Hagelaar, W. L. Morgan, S. Pancheshnyi, A. V. Phelps, V. Puech, and O. Zatsarinny. Comparisons of sets of electron-neutral scattering cross sections and swarm parameters in noble gases: II. Helium and neon. *J. Phys. D: Appl. Phys.*, **46**, 334002 (2013).
- [417] K. Bartschat, E. T. Hudson, M. P. Scott, P. G. Burke, and V. M. Burke. Differential cross sections and electron-impact coherence parameters for electron scattering from helium atoms. *J. Phys. B: At. Mol. Opt. Phys.*, **29**, 2875 (1996).
- [418] D. V. Fursa and I. Bray. Convergent close-coupling calculations of electron - helium scattering. *J. Phys. B: At. Mol. Opt. Phys.*, **30**, 757 (1997).
- [419] O. Zatsarinny and K. Bartschat. Benchmark calculation of total cross sections for ionization-excitation of helium. *J. Phys. B: At. Mol. Opt. Phys.*, **47**, 061001 (2014).

- [420] Y. Cheng, L. Y. Tang, J. Mitroy, and M. S. Safronova. All-order relativistic many-body theory of low-energy electron-atom scattering. *Phys. Rev. A*, **89**, 012701 (2014).
- [421] R. K. Nesbet. Variational calculations of accurate e-He cross sections below 19 eV. *Phys. Rev. A*, **20**, 58 (1979).
- [422] O. Zatsarinny and K. Bartschat. Large-scale pseudostate calculations for electron scattering from neon atoms. *Phys. Rev. A*, **85**, 062710 (2012).
- [423] O. Zatsarinny and K. Bartschat. BSR Database. www.lxcat.net (2014). Accessed 29 January, 2015.
- [424] M. S. Safronova, W. R. Johnson, and A. Derevianko. Relativistic many-body calculations of energy levels, hyperfine constants, electric-dipole matrix elements, and static polarizabilities for alkali-metal atoms. *Phys. Rev. A*, **60**, 4476 (1999).
- [425] M. S. Safronova and W. R. Johnson. All-order methods for relativistic atomic structure calculations. *Adv. At. Mol. Opt. Phys.*, **55**, 191 (2008).
- [426] R. A. Nielsen. Absolute values of the electron drift velocity in nitrogen, helium, neon and argon. *Phys. Rev.*, **50**, 950 (1936).
- [427] J. L. Pack and A. V. Phelps. Drift velocities of slow electrons in helium, neon, argon, hydrogen, and nitrogen. *Phys. Rev.*, **121**, 798 (1961).
- [428] H. N. Kucukarpaci, H. T. Saelee, and J. Lucas. Electron swarm parameters in helium and neon. *J. Phys. D: Appl. Phys.*, **14**, 9 (1981).
- [429] L. S. Frost and A. V. Phelps. Momentum-transfer cross sections for slow electrons in He, Ar, Kr, and Xe from transport coefficients. *Phys. Rev.*, **136**, 1538 (1964).
- [430] R. O. Berger, T. F. O'Malley, and L. Spruch. Extrapolation of cross-section data to zero energy for long-range effective potentials. *Phys. Rev.*, **137**, 1068 (1965).
- [431] P. S. Hooper, W. Franzen, and R. Gupta. Analysis of low-energy electron scattering by helium, neon, and argon. *Phys. Rev.*, **168**, 50 (1968).
- [432] T. F. O'Malley and R. W. Crompton. Electron-neon scattering length and S-wave phaseshifts from drift velocities. *J. Phys. B: At. Mol. Phys.*, **13**, 3451 (1980).
- [433] D. R. Nelson and F. J. Davis. Determination of diffusion coefficients of thermal electrons with a time-of-flight swarm experiment. *J. Chem. Phys.*, **51**, 2322 (1969).
- [434] T. Rhymes, R. W. Crompton, and G. Cavalleri. Diffusion coefficient for thermal electrons in neon at 295 K. *Phys. Rev. A*, **12**, 776 (1975).
- [435] T. Rhymes, R. W. Crompton, and G. Cavalleri. Erratum: Diffusion coefficient for thermal electrons in neon at 295 K. *Phys. Rev. A*, **14**, 898 (1976).
- [436] J. L. Pack, R. E. Voshall, A. V. Phelps, and L. E. Kline. Longitudinal electron diffusion coefficients in gases: Noble gases. *J. Appl. Phys.*, **71**, 5363 (1992).
- [437] R. P. McEachran and A. D. Stauffer. Relativistic effects in low-energy electron-argon scattering. *Aust. J. Phys.*, **50**, 511 (1997).

- [438] T. F. O'Malley. Low-energy scattering of a charged particle by a neutral polarizable system. *Phys. Rev.*, **125**, 1300 (1962).
- [439] T. F. O'Malley. Extrapolation of electron-rare gas atom cross sections to zero energy. *Phys. Rev.*, **130**, 1020 (1963).
- [440] S. J. Buckman and J. Mitroy. Analysis of low-energy electron scattering cross sections via effective-range theory. *J. Phys. B: At. Mol. Opt. Phys.*, **22**, 1365 (1989).
- [441] H. P. Saha. Accurate *ab initio* calculation of scattering length and phase shifts at very low energies for electron-neon scattering. *Phys. Rev. Lett.*, **65**, 2003 (1990).
- [442] S. Pancheshnyi, S. Biagi, M. C. Bordage, G. J. M. Hagelaar, W. L. Morgan, A. V. Phelps, and L. C. Pitchford. The LXCat project: Electron scattering cross sections and swarm parameters for low temperature plasma modeling. *Chem. Phys.*, **398**, 148 (2012).
- [443] S. J. Buckman and M. T. Elford. *Momentum Transfer Cross Sections*, 2–35. Springer, Darmstadt (2003).
- [444] D. F. Register and S. Trajmar. Differential, integral, and momentum-transfer cross sections for elastic electron scattering by neon - 5 to 100 eV. *Phys. Rev. A*, **29**, 1785 (1984).
- [445] R. J. Gulley, D. T. Alle, M. J. Brennan, M. J. Brunger, and S. J. Buckman. TOF neon. *J. Phys. B: At. Mol. Opt. Phys.*, **27**, 2593 (1994).
- [446] H. P. Saha. Low-energy elastic scattering of electrons from neon atoms. *Phys. Rev. A*, **39**, 5048 (1989).
- [447] W. L. Morgan. Morgan (Kinema Research and Software) database. www.lxcat.net (2014). Accessed 30 April, 2014.
- [448] J. Meunier, P. Belenguer, and J. P. Boeuf. Numerical model of an AC plasma display panel cell in neon-xenon mixtures. *J. Appl. Phys.*, **78**, 731 (1995).
- [449] J. Meunier and P. Belenguer and J. P. Boeuf. The SIGLO database. www.lxcat.net (2014). Accessed 30 April, 2014.
- [450] I. Shimamura. Neon cross sections. *Sci. Papers Inst. Phys. Chem. Res.*, **82**, 1 (1989).
- [451] S. F. Biagi. A multiterm Boltzmann analysis of drift velocity, diffusion, gain and magnetic-field effects in argon-methane-water-vapour mixtures. *Nucl. Instr. Meth. Phys. Res. A*, **283**, 716 (1989).
- [452] S. F. Biagi. Magboltz - transport of electrons in gas mixtures. <http://consult.cern.ch/writeup/magboltz/> (2012). Accessed 30 April, 2014.
- [453] S. F. Biagi. Biagi database. www.lxcat.net (2014). Accessed 30 April, 2014.
- [454] V. Puech and S. Mizzi. Collision cross sections and transport parameters in neon and xenon. *J. Phys. D: Appl. Phys.*, **24**, 1974 (1991).
- [455] V. Puech and S. Mizzi. Puech database. www.lxcat.net (2014). Accessed 30 April, 2014.
- [456] D. R. Lide (Editor). *CRC Handbook of Chemistry and Physics*. CRC Press, Boca Raton (2008).

- [457] P. G. Coleman, T. C. Griffith, G. R. Heyland, and T. L. Killeen. Positronium formation in noble gases. *J. Phys. B: At. Mol. Phys.*, **8**, L185 (1975).
- [458] P. A. Fraser. Positrons and positronium in gases. *Adv. At. Mol. Phys.*, **4**, 63 (1968).
- [459] S. J. Tao and T. M. Kelly. Theoretical and experimental positron annihilation and scattering cross sections in helium. *Phys. Rev.*, **185**, 135 (1969).
- [460] R. I. Campeanu. Positron diffusion in krypton and xenon. *Can. J. Phys.*, **60**, 615 (1982).
- [461] J. Mitroy and I. A. Ivanov. Semi-empirical model of elastic scattering and annihilation. *Phys. Rev. A*, **65**, 042705 (2002).
- [462] V. A. Dzuba, V. V. Flambaum, G. F. Gribakin, and W. A. King. Many-body calculations of positron scattering and annihilation from noble-gas atoms. *J. Phys. B: At. Mol. Opt. Phys.*, **29**, 3151 (1996).
- [463] H. Nakanishi and D. M. Schrader. Polarization potentials for positron- and electron-atom systems. *Phys. Rev. A*, **34**, 1810 (1986).
- [464] H. Nakanishi and D. M. Schrader. Simple but accurate calculations of elastic scattering of electrons and positrons from neon and argon. *Phys. Rev. A*, **34**, 1823 (1986).
- [465] S.-W. Chiu and D. M. Schrader. Semiempirical diabatic potential for low-energy positron-atom elastic scattering. *Phys. Rev. A*, **33**, 2339 (1986).
- [466] F. A. Gianturco and T. Mukherjee. Positron annihilation in simple molecular gases: A study of vibrational effects. *Nucl. Instr. Meth. Phys. Res. B*, **171**, 17 (2000).
- [467] J. E. Sienkiewicz and W. E. Baylis. Low-energy elastic scattering of positrons on argon. *Phys. Rev. A*, **40**, 3662 (1989).
- [468] D. D. Reid and J. M. Wadehra. Low-energy differential scattering of electrons and positrons from noble gases. *Phys. Rev. A*, **50**, 4859 (1994).
- [469] L. T. Sin Fai Lam. Elastic scattering of low-energy positrons by krypton and xenon. *J. Phys. B: At. Mol. Phys.*, **15**, 143 (1982).
- [470] G. G. Ryzhikh and J. Mitroy. *T*-matrix theory of positron annihilation on hydrogen. *J. Phys. B: At. Mol. Opt. Phys.*, **33**, 2229 (2000).
- [471] R. P. McEachran, D. L. Morgan, A. G. Ryman, and A. D. Stauffer. Positron scattering from noble gases. *J. Phys. B: At. Mol. Phys.*, **10**, 663 (1977).
- [472] J. P. Carbotte and S. Kahana. Positron annihilation in an interacting electron gas. *Phys. Rev.*, **139**, 213 (1965).
- [473] K. G. Lynn, J. R. MacDonald, R. A. Boi, L. C. Feldman, J. D. Gabbe, M. F. Robbins, E. Bonderup, and J. Golovchenko. Positron-annihilation momentum profiles in aluminum: Core contribution and the independent-particle model. *Phys. Rev. Lett.*, **38**, 241 (1977).
- [474] M. J. Puska and R. M. Nieminen. Theory of positrons in solids and on solid surfaces. *Rev. Mod. Phys.*, **66**, 841 (1994).
- [475] J. Mitroy and B. Barbiellini. Enhancement factors for positron annihilation studies. *Phys. Rev. B: At. Mol. Opt. Phys.*, **65**, 235103 (2002).

- [476] G. K. Ivanov. Resonance annihilation of slow positrons on molecules. *Dokl. Akad. Nauk. SSSR*, **291**, 622 (1986).
- [477] G. F. Gribakin. Mechanisms of positron annihilation on molecules. *Phys. Rev. A*, **61**, 022720 (2000).
- [478] J. Mitroy and M. W. J. Bromley. Convergence of CI single center calculations of positron-atom interactions. *Phys. Rev. A*, **73**, 052712 (2006).
- [479] G. F. Gribakin and J. Ludlow. Many-body theory of positron-atom interactions. *Phys. Rev. A*, **70**, 032720 (2004).
- [480] S. A. Novikov, M. W. J. Bromley, and J. Mitroy. Positron scattering and annihilation from hydrogen-like ions. *Phys. Rev. A*, **69**, 052702 (2004).
- [481] D. G. Green and G. F. Gribakin. Positron scattering and annihilation for hydrogen-like ions. *Phys. Rev. A*, **88**, 032708 (2013).
- [482] P. Van Reeth and J. W. Humberston. Elastic scattering and positronium formation in low-energy positron-helium collisions. *J. Phys. B: At. Mol. Opt. Phys.*, **32**, 3651 (1999).
- [483] J. Y. Zhang and J. Mitroy. Stochastic variational calculation of zero-energy positron scattering from H, He, and H₂. *Phys. Rev. A*, **83**, 022711 (2011).
- [484] P. Van Reeth, J. W. Humberston, K. J. Iwata, R. J. Greaves, and C. M. Surko. Annihilation in low-energy positron-helium scattering. *J. Phys. B: At. Mol. Opt. Phys.*, **29**, L465 (1996).
- [485] H. Wu, I. Bray, D. V. Fursa, and A. T. Stelbovics. Low-energy positron-helium convergent close coupling calculations. *J. Phys. B: At. Mol. Opt. Phys.*, **37**, L1 (2004).
- [486] R. P. McEachran, D. L. Morgan, A. G. Ryman, and A. D. Stauffer. Positron scattering from noble gases: corrected results for helium. *J. Phys. B: At. Mol. Phys.*, **11**, 951 (1978).
- [487] J. P. Sullivan, C. Makocheke, A. Jones, P. Caradonna, and S. J. Buckman. High-resolution, low-energy positron scattering from helium: measurements of the total scattering cross section. *J. Phys. B: At. Mol. Opt. Phys.*, **41**, 081001 (2008).
- [488] T. Mizogawa, Y. Nakayama, T. Kawaratani, and M. Tosaki. Precise measurements of positron-helium total cross sections from 0.6 to 22 eV. *Phys. Rev. A*, **31**, 2171 (1985).
- [489] K. F. Canter, P. G. Coleman, T. C. Griffith, and G. R. Heyland. The measurement of total cross sections for positrons of energies 2-400 eV in He, Ne, Ar, and Kr. *J. Phys. B: At. Mol. Phys.*, **6**, L201 (1973).
- [490] T. S. Stein, W. E. Kauppila, V. Pol, J. H. Smart, and G. Jesion. Measurements of total scattering cross sections for low-energy positrons and electrons colliding with helium and neon atoms. *Phys. Rev. A*, **17**, 1600 (1978).
- [491] J. Y. Zhang, J. Mitroy, and K. Varga. Development of a confined variational method for elastic scattering. *Phys. Rev. A*, **78**, 042705 (2008).
- [492] J. Mitroy. Effective range description of annihilating collisions. *Phys. Rev. A*, **66**, 022716 (2002).
- [493] J. W. Humberston and P. Van Reeth. Annihilation in low energy positron-helium scattering. *Nucl. Instr. Meth. Phys. Res. B*, **143**, 127 (1998).

- [494] R. I. Campeanu and J W Humberston. Theoretical aspects of positron collisions in gases. *J. Phys. B: At. Mol. Phys*, **10**, L153 (1977).
- [495] J. Czernin and M. Phelps. Positron emission tomography scanning: Current and future applications. *Annu. Rev. Med.*, **53**, 89 (2002).
- [496] L. Sanche. Low-energy electron damage to DNA and its basic constituents. *Phys. Scr.*, **68**, C108 (2003).
- [497] L. Sanche. Low energy electron-driven damage in biomolecules. *Eur. Phys. J. D: At. Mol. Opt. Plas. Phys.*, **35**, 367 (2005).
- [498] L. Sanche. *Radiation Induced Molecular Phenomena in Nucleic Acid: A Comprehensive Theoretical and Experimental Analysis*. Springer, Netherlands (2008).
- [499] L. Sanche. *Radical and Radical Ion Reactivity in Nucleic Acid Chemistry*. Wiley, New Jersey (2009).
- [500] K. F. Ness and A. M. Nolan. Flux and reactive contributions to electron transport in methane. *Aust. J. Phys.*, **53**, 437 (2000).
- [501] G. K. Grubert and D. Loffhagen. Boltzmann equation and Monte Carlo analysis of the electrons in spatially inhomogeneous, bounded plasmas. *J. Phys. D: Appl. Phys.*, **47**, 025204 (2014).
- [502] K. F. Ness and T. Makabe. Electron transport in argon in crossed electric and magnetic fields. *Phys. Rev. E*, **62**, 4083 (2000).
- [503] M. Brauner and J. S. Briggs. Ionisation to the projectile continuum by positron and electron collisions with neutral atoms. *J. Phys. B: At. Mol. Phys.*, **19**, L325 (1986).
- [504] H. Klar. Threshold ionisation of atoms by positrons. *J. Phys. B: At. Mol. Phys.*, **14**, 4165 (1981).
- [505] P. N. Ashley, J. Moxom, and G. Laricchia. Near-threshold ionization of He and H₂ by positron impact. *Phys. Rev. Lett.*, **77**, 1250 (1996).
- [506] W. Ihra, J. H. Macek, F. Mota-Furtado, and P. F. O'Mahoney. Threshold law for positron impact ionization of atoms. *Phys. Rev. Lett.*, **78**, 4027 (1997).
- [507] C. Arcidiacono, A. Kover, and G. Laricchia. Energy-sharing asymmetries in ionization by positron impact. *Phys. Rev. Lett.*, **95**, 223202 (2005).
- [508] M. Brauner, J. S. Briggs, and H. Klar. Triply-differential cross sections for ionisation of hydrogen atoms by electrons and positrons. *J. Phys. B: At. Mol. Opt. Phys.*, **22**, 2265 (1989).
- [509] M. C. Zammit, D. V. Fursa, and I. Bray. Convergent-close-coupling formalism for positron scattering from molecules. *Phys. Rev. A*, **87**, 020701 (2013).
- [510] P. Bruggeman and C. Leys. Non-thermal plasmas in and in contact with liquids. *J. Phys. D: Appl. Phys.*, **42**, 053001 (2009).
- [511] R. A. Buckingham. The classical equation of state of gaseous helium, neon and argon. *Proc. Roy. Soc. London A Mat.*, **168**, 264 (1938).

- [512] R. D. White, R. E. Robson, B. Schmidt, and M. A. Morrison. Is the classical two-term approximation of electron kinetic theory satisfactory for swarms and plasmas? *J. Phys. D: Appl. Phys.*, **36**, 3125 (2003).
- [513] S. Chen, R. P. McEachran, and A. D. Stauffer. *Ab initio* optical potentials for elastic electron and positron scattering from the heavy noble gases. *J. Phys. B: At. Mol. Opt. Phys.*, **41**, 025201 (2008).
- [514] R. P. McEachran and A. D. Stauffer. Dynamic distortion effects in electron-atom scattering. *J. Phys. B: At. Mol. Opt. Phys.*, **23**, 4605 (1990).
- [515] D. J. R. Mimmagh, R. P. McEachran, and A. D. Stauffer. Elastic electron scattering from the noble gases including dynamic distortion. *J. Phys. B: At. Mol. Opt. Phys.*, **26**, 1727 (1993).
- [516] A. Dorn, A. Elliot, J. C. Lower, S. F. Mazevet, R. P. McEachran, I. E. McCarthy, and E. Weigold. The elastic scattering of spin-polarized electrons from xenon. *J. Phys. B: At. Mol. Opt. Phys.*, **31**, 547 (1998).
- [517] R. P. McEachran, A. G. Ryman, and A. D. Stauffer. Polarisabilities and shielding factors for He, Ne and Ar. *J. Phys. B: At. Mol. Phys.*, **10**, L681 (1977).
- [518] M. J. Brennan and K. F. Ness. Comments on electron transport in gases with particular reference to argon. *Nuovo Cimento D*, **14**, 933 (1992).
- [519] D. Loffhagen and F. Sigeneger. Advances in Boltzmann equation based modelling of discharge plasmas. *Plasma Sources Sci. Technol.*, **18**, 034006 (2009).
- [520] S. Dujko, R. D. White, Z. Lj. Petrović, and R. E. Robson. A multi-term solution of the nonconservative Boltzmann equation for the analysis of temporal and spatial non-local effects in charged-particle swarms in electric and magnetic fields. *Plasma Sources Sci. Tech.*, **20**, 024013 (2011).
- [521] K. A. Bagrinovskii and S. K. Godunov. Difference schemes for multidimensional problems. *Dokl. Akad. Nauk. SSSR*, **115**, 431 (1957).
- [522] G. Strang. On the construction and comparison of different splitting schemes. *SIAM J. Numer. Anal.*, **5**, 506 (1968).
- [523] B. O. Dia and M. Schatzman. Commutateur de certains semi-groupes holomorphes et applications aux directions alternées. *Math. Mod. Numer. Anal.*, **30**, 343 (1996).
- [524] T. Ohwada. High order approximation methods for the Boltzmann equation. *J. Comp. Phys.*, **139**, 1 (1998).
- [525] A. Gerisch and R. Weiner. The positivity of low-order explicit Runge-Kutta schemes applied in splitting methods. *Comp. Math. App.*, **45**, 53 (2003).
- [526] S. Gottlieb and C.-W. Shu. Total variation diminishing Runge-Kutta schemes. *Math. Comp.*, **67**, 73 (1998).
- [527] J. Douglas. Alternating direction method for three space variables. *Numer. Math.*, **4**, 41 (1962).
- [528] J. Douglas and J. E. Gunn. A general formulation of alternating direction methods. *Numer. Math.*, **6**, 428 (1964).

- [529] W. Hundsdorfer. Accuracy and stability of splitting with stabilizing corrections. *Appl. Numer. Math.*, **42**, 213 (2002).
- [530] A. D. Polyanin. *Handbook of Linear Partial Differential Equations for Engineers and Scientists*. Chapman and Hall, Boca Raton (2002).
- [531] M. Morales-Hernandez, P. Garcia-Navarro, and J. Murillo. A large time step 1D upwind explicit scheme (CFL > 1): Application to shallow water equations. *J. Comp. Phys.*, **231**, 6532 (2012).
- [532] J. P. Boris and D. L. Book. Flux-corrected transport. I. SHASTA, a fluid algorithm that works. *J. Comp. Phys.*, **11**, 38 (1973).
- [533] R. Courant, K. Friedrichs, and H. Lewy. On the partial difference equations of mathematical physics. *IBM J. Res. Dev.*, **11**, 215 (1967).
- [534] A. Harten. High resolution schemes for hyperbolic conservation laws. *J. Comp. Phys.*, **49**, 357 (1983).
- [535] S. Osher and S. Chakravarthy. High resolution schemes and the entropy condition. *SIAM J. Numer. Anal.*, **21**, 955 (1984).
- [536] P. L. Roe. Numerical algorithms for the linear wave equation. *Royal Aircraft Establishment Technical Report 81047* (1981).
- [537] S. T. Zalesak. Fully multidimensional flux corrected transport algorithms for fluids. *J. Comp. Phys.*, **31**, 335 (1979).
- [538] P. K. Sweby. High resolution schemes using flux limiters for hyperbolic conservation laws. *SIAM J. Numer. Anal.*, **21**, 995 (1984).
- [539] S. Dujko, Z. M. Raspopović, and Z. Lj. Petrović. Monte Carlo studies of electron transport in crossed electric and magnetic fields in CF₄. *J. Phys. D: Appl. Phys.*, **38**, 2952 (2005).
- [540] J. Fletcher. Non-equilibrium in low pressure rare gas discharges. *J. Phys. D: Appl. Phys.*, **18**, 221 (1985).
- [541] G. Petrov and R. Winkler. Multi-term treatment of electron kinetics in inhomogeneous nonequilibrium plasmas. *J. Phys. D: Appl. Phys.*, **30**, 53 (1997).
- [542] R. D. White, R. E. Robson, P. Nicoletopoulos, and S. Dujko. Periodic structures in the Franck-Hertz experiment with neon: Boltzmann equation and Monte-Carlo analysis. *The European Physical Journal D*, **66**, 117 (2012).
- [543] M. Foxe, C. Hagmann, I. Jovanović, A. Bernstein, K. Kazkaz, V. Mozin, S. V. Pereverzev, S. Sangiorgio, and P. Sorensen. Low-energy (<10 keV) electron ionization and recombination model for a liquid argon detector. *Nucl. Instr. Meth. Phys. Res. A*, **771**, 88 (2015).
- [544] A. V. Solov'yov, E. Surdutovich, E. Scifoni, I. Mishustin, and W. Greiner. Physics of ion beam cancer therapy: A multiscale approach. *Phys. Rev. E*, **79**, 011909 (2009).
- [545] N. Veglio, F. J. Bermejo, L. C. Prado, J. Ll. Tamarit, and G. J. Cuello. Direct experimental assessment of the strength of orientational correlations in polar liquids. *Phys. Rev. E*, **72**, 031502 (2005).

- [546] Carl Winstead and Vincent McKoy. Electron-biomolecule collision studies using the schwinger multichannel method. In *Radiation Damage in Biomolecular Systems*, edited by G. García Gómez-Tejedor and M. C. Fuss, Biological and Medical Physics, Biomedical Engineering, 87–113. Springer Netherlands, Dordrecht (2012).
- [547] R. E. Robson. Physics of reacting particle swarms. II. The muon-catalyzed cold fusion cycle. *J. Chem. Phys.*, **88**, 198 (1988).
- [548] L. Tonks. Drift of ions and electrons in a magnetic field. *Phys. Rev.*, **51**, 744 (1937).
- [549] R. E. Robson, R. D. White, and Z. Lj. Petrović. Colloquium: Physically based fluid modeling of collisionally dominated low-temperature plasmas. *Rev. Mod. Phys.*, **77**, 1303 (2005).
- [550] Z. Lj. Petrović, A. Banković, S. Dujko, S. Marjanović, M. Suvakov, G. Malović, J. P. Marler, S. J. Buckman, R. D. White, and R. E. Robson. On new developments in the physics of positron swarms. *J. Phys. Conf. Ser.*, **199**, 012016 (2010).
- [551] R. E. Robson, R. D. White, and T. Makabe. Charged particle transport in harmonically varying electric fields: Foundations and phenomenology. *Ann. Phys.*, **261**, 74 (1997).
- [552] R. P. Brent. *Algorithms for Minimization without Derivatives*. Prentice-Hall, Englewood Cliffs (1973).
- [553] W. H. Press, B. P. Flannery, S. A. Teukolsky, and W. T. Vetterling. *Numerical Recipes in FORTRAN: The Art of Scientific Computing (2nd Ed.)*. Cambridge University Press, England (1992).
- [554] H. Margeneau. Conduction and dispersion of ionized gases at high frequencies. *Phys. Rev.*, **69**, 508 (1946).